Advances in Meteorology and Geophysics

2023

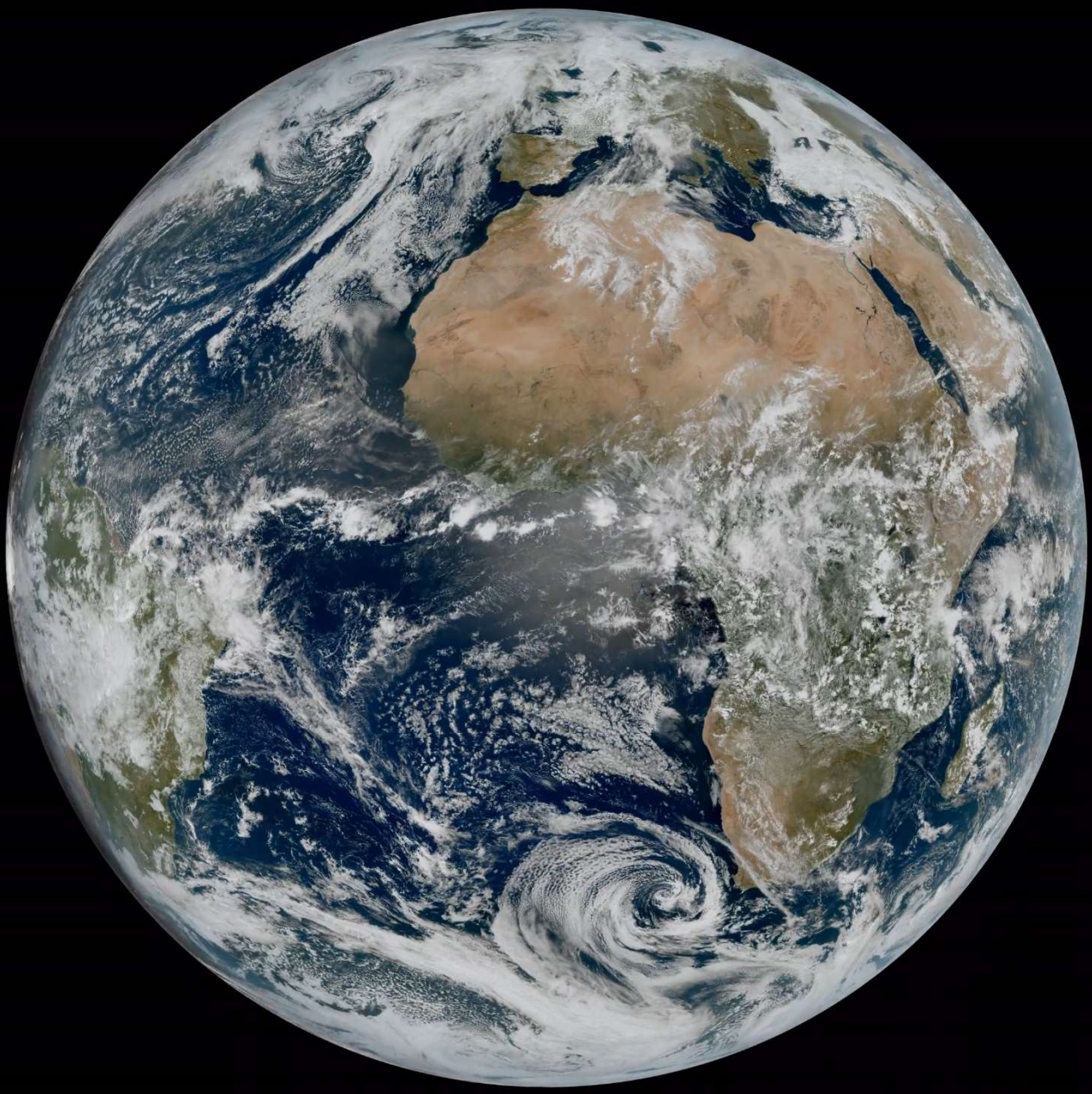

EDITED BY
Mário Gonzalez Pereira, Rui Oliveira, Patrícia Navarro, Lourdes Bugalho

Advances in Meteorology and Geophysics

2023

Advances in Meteorology and Geophysics 2023

ADVANCES IN METEOROLOGY AND GEOPHYSICS 2023
DOI: https://doi.org/10.60620/he5s-8x66

COVER CREDIT:
©EUMETSAT 2023 – The first image from EUMETSAT's newest satellite, Meteosat Third Generation – Imager 1 (MTG-I1), released on 4 May 2023. The satellite's Flexible Combined Imager instrument captured the image at 11:50 UTC on 18 March 2023. The image reveals an extraordinary level of detail.

EDITORIAL AND PRODUCTION TEAM
Mário Gonzalez Pereira
Centre for the Research and Technology of Agro-environmental and Biological Sciences, Inov4Agro, University of Trás-os-Montes and Alto Douro, Vila Real, Portugal

Rui Oliveira
Physics Department (ECT), Institute of Earth Sciences (ICT/IIFA), Earth Remote Sensing Laboratory (EaRSLab), University of Évora

Patrícia Navarro
Portuguese Institute of the Sea and Atmosphere (Instituto Português do Mar e da Atmosfera), Ponta Delgada, Portugal

Lourdes Bugalho
Portuguese Institute of the Sea and Atmosphere (Instituto Português do Mar e da Atmosfera), Lisboa, Portugal

The editorial and production teams are members of the Governing Board of the Portuguese Association of Meteorology and Geophysics (*Associação Portuguesa de Meteorologia e Geofísica*, APMG).

Associação Portuguesa de Meteorologia e Geofísica
Instituto Português do Mar e da Atmosfera - Rua C do Aeroporto de Lisboa
1749-077 Lisboa
Portugal
http://www.apmg.pt | geral@apmg.pt

Universidade de Trás-os-Montes e Alto Douro
Quinta de Prados
5000-801 Vila Real
Portugal
https://www.utad.pt/

Advances in Meteorology and Geophysics

2023

edited by

MÁRIO GONZALEZ PEREIRA
University of Trás-os-Montes and Alto Douro

RUI OLIVEIRA
University of Évora

PATRÍCIA NAVARRO
Portuguese Institute of the Sea and Atmosphere

LOURDES BUGALHO
Portuguese Institute of the Sea and Atmosphere

DOI: https://doi.org/10.60620/he5s-8x66

ADVANCES IN METEOROLOGY AND GEOPHYSICS 2023
Advances in Meteorology and Geophysics 2023 / [ed. lit.] Mário Gonzalez Pereira... [et al.]. - Vila Real, 2023. - Contém referências bibliográficas

ISBN : 978-989-704-543-1
1. Meteorology / 2. Geophysics

CDU 551.5
550.3

 DOI: https://doi.org/10.60620/he5s-8x66

Contents

Preface 10
Acknowledgements 11
List of contributors 12
PART I: ADVANCES IN METEOROLOGY 16
Aethalometer Measurements During Cumbre Vieja Volcano Eruption 17
Machine Learn Estimates of Downward Surface Long-Wave Fluxes (Dslf) Based on Reanalysis and Satellite Observations 22
Evaluation of Eolic Potential in Portugal 29
On the Convenience of the Use of Seasonal and Monthly Climatic Indices in Correlation Studies 35
Drought Assessment in Southern Africa Using Remote Sensing Vegetation Indices 42
The Impact of Multiple Atmospheric Rivers on The Extreme Precipitation Events in December 2022 in Portugal 52
Concurrent Marine and Atmospheric Heatwaves and Droughts and their Influence on Fire Activity in the Mediterranean Region 60
Formation of Pyrocumulus During a Megafire Event in Portugal Using the Coupled Atmosphere-Fire Spread Model Wrf-Sfire 66
Smoke Dispersion in the October 2017 Forest Fires in Mainland Portugal: Validation of Numerical Simulations 77
Implementation of a Statistical Post-Processing Method for Significant Wave Height Forecasting 86
A Coupled Ecophysiological and Meteorological Model for the Grapevine Simulation Under Agroforestry Conditions 90
PART II: ADVANCES IN GEOPHYSICS 94
The Analysis of the Seismic Tacana Volcanic Complex in 2017 – 2018 95
Density Variations, Thermodynamic Properties and Earthquakes in the Horseshoe Basin 105
Preliminary Results of the Macroseismic Survey on the 28 February 1969 (7.9 Ms) Earthquake that Occurred at SW St. Vincent Cape 111
Advancements in the LouMu Project–Muography for Geophysical Surveys 117
Characterization of the Gravitational Mass Movements by Seismic Signals 123

Preface

The Portuguese Association of Meteorology and Geophysics (*Associação Portuguesa de Meteorologia e Geofísica*, APMG), has among its main objectives to cooperate with any organizations that carry out activities in the areas of meteorological and geophysical sciences, with all institutions that fight for the protection of the climate system and for the prevention against natural catastrophes as well as to foster unity, mutual help and fellowship among the associates. To achieve these objectives, every two years the APMG organizes a Symposium of Meteorology and Geophysics and co-organises the Portuguese-Spanish Meteorology Meeting, which is co-organized with the Spanish Meteorological Association (AME), since its inception. In 2023, this important objective of the APMG was achieved with the holding of its 12th Symposium on Meteorology and Geophysics and the 21st Portuguese-Spanish Meteorology Meeting (APMG2023), from the 20th to the 22nd of March 2023, with the support of the Portuguese Institute of the Sea and Atmosphere (*Instituto Português do Mar e da Atmosfera*, IPMA).

The previous Symposium was held in 2019 as the APMG2021 Symposium was not organized in 2021 due to pandemic restrictions. These last few years have been characterized by limitations on travel and face-to-face meetings. As the popular saying goes, "necessity sharpens ingenuity" and new forms of communication and meetings were found with the advantage of bringing people together more easily, saving money and time, and preserving the environment. However, it was also noticed that online meetings do not replace face-to-face meetings, where personal ties are built and, in our view, help to build a community, in this case, a meteorological and geophysical one. For this reason, APMG decided to organize the Symposium traditionally.

On the other hand, after almost four years, the organization could not fail to choose IPMA as the host of the APMG2023 Symposium for several reasons. First, the National Meteorological Service (SNM), created in 1946, gave rise to the National Institute of Meteorology and Geophysics (INMG), then the Meteorology Institute (IM) and finally to the IPMA. Second, APMG's headquarters are at the IPMA. Finally, in third place, IMPA is where all the operational work in Meteorology and Geophysics was carried out, the workplace of most meteorologists and geophysicists in Portugal, which facilitated the participation of these professionals in the Symposium. APMG intends to continue to make every effort to unite the scientific community in these areas.

The APMG2023 Symposium offered all participants the possibility to contribute to this book by publishing their new results and most recent findings in the form of a chapter. This contribution should preferably, but not exclusively, be based on your papers presented at the Symposium, with the sole purpose of describing your most recent conclusions and contributions to the advancement of knowledge in meteorology and geophysics. A significant number of participants decided to accept our challenge and submit their manuscripts on a vast and diverse set of topics, so we decided to divide the book into two parts: Part I: Advances in Meteorology and Part II: Advances in Geophysics.

Finally, the APMG Governing Board (*Conselho Dirigiente*) thanks all associates, participants and colleagues in Meteorology, Geophysics and related fields for their significant contributions to the success of the APMG2023 Symposium and this book.

Lourdes Bugalho
President of APMG

 DOI: https://doi.org/10.60620/he5s-8x66

Acknowledgements

This work is supported by National Funds from FCT ‑ Portuguese Foundation for Science and Technology, under the project UIDB/04033/2020 (CITAB – Centre for the Research and Technology of Agro-Environmental and Biological Sciences), and the project UIDB/04683/2020 (ICT – Institute of Earth Sciences).

The editorial team is grateful to the editorial sector of UTAD, especially Rui Pires, Maria Rodrigues, and Carmen Taborda.

This book is supported by the following institutions:

- Universidade de Trás-os-Montes e Alto Douro
- Universidade de Évora
- Instituto Português do Mar e da Atmosfera, I.P.

List of contributors

Diamantino Henriques
Instituto Português do Mar e da Atmosfera (IPMA)
Observatório Afonso Chaves,
Rua Mãe de Deus – Relvão, 9500-321 Ponta Delgada, Portugal
diamantino.henriques@ipma.pt

África Barreto
Izaña Atmospheric Research Centre (CIAI), AEMET,
Santa Cruz de Tenerife, 38001, Spain
abarretov@aemet.es

Sergio Rodríguez
Institute of Natural Products and Agrobiology (IPNA)
CSIC, Tenerife, Spain
sergio.rodriguez@csic.es

José Pacheco
Instituto de Investigação em Vulcanologia e Avaliação de Riscos (IVAR)
Rua da Mãe de Deus, 9500-321 Ponta Delgada, Portugal
jose.mr.pacheco@azores.gov.pt

Emanuel Dutra
Instituto Português do Mar e da Atmosfera (IPMA)
Rua C do Aeroporto, 1749-077, Lisbon, Portugal
emanuel.dutra@ipma.pt

Claudia Victoria Campos Rubio
Centre for the Research and Technology of Agro-environmental and Biological Sciences (CITAB), Inov4Agro, University of Trás-os-Montes and Alto Douro (UTAD)
Quinta de Prados, 5000-801 Vila Real, Portugal
claudia.campos.rubio@gmail.com

Mário Gonzalez Pereira
Centre for the Research and Technology of Agro-environmental and Biological Sciences (CITAB), Inov4Agro, University of Trás-os-Montes and Alto Douro (UTAD)
Quinta de Prados, 5000-801 Vila Real, Portugal
gpereira@utad.pt

Raúl Rodríguez-Solà
Physics Department, ETSEIB, Universitat Politècnica de Catalunya·BarcelonaTech
Diagonal 647, 08028 Barcelona, Spain
raul.rodriguez@upc.edu

Marta Alarcón
Physics Department, EEBE, Universitat Politècnica de Catalunya BarcelonaTech
Eduard Maristany 16, 08019 Barcelona, Spain
marta.alarcon@upc.edu

Jordina Belmonte
Department of Animal Biology, Plant Biology and Ecology, Faculty of Bioscience, Universitat Autònoma de Bellaterra, 08193 Bellaterra, Spain
jordina.belmonte@uab.cat

Paulo Fialho
Instituto de Investigação em Vulcanologia e Avaliação de Riscos (IVAR)
Rua da Mãe de Deus, 9500-321 Ponta Delgada, Portugal
fialho.paulo@gmail.com

Yenny González
CIMEL Electronique,
Paris, 75011, France
y-gonzalez@cimel.fr

Emilio Cuevas
Izaña Atmospheric Research Centre (CIAI), AEMET,
Santa Cruz de Tenerife, 38001, Spain
ecuevasa@aemet.es

Francisco M. Lopes
Instituto Dom Luiz (IDL), University of Lisbon
Campo Grande, 1749-016 Lisbon, Portugal
fmtlopes@fc.ul.pt

Isabel Trigo
Instituto Português do Mar e da Atmosfera (IPMA)
Rua C do Aeroporto, 1749-077, Lisbon, Portugal
isabel.trigo@ipma.pt

Lourdes Bugalho
Instituto Português do Mar e da Atmosfera, I. P.
Rua C do Aeroporto, 1749-077 Lisboa, Portugal
lourdes.bugalho@ipma.pt

M. Carmen Casas-Castillo
Physics Department, ESEIAAT, Universitat Politècnica de Catalunya·BarcelonaTech
Colom 1, 08222 Terrassa, Spain,
m.carmen.casas@upc.edu

Ricard Kirchner
Physics Department, ESEIAAT, Universitat Politècnica de Catalunya·BarcelonaTech
Colom 1, 08222 Terrassa, Spain,
ricard.kirchner@upc.edu

Cristina Periago
Physics Department, EEBE, Universitat Politècnica de Catalunya BarcelonaTech
Eduard Maristany 16, 08019 Barcelona, Spain
cristina.periago@upc.edu

Fernando Maliti Chivangulula
Centre for the Research and Technology of Agro-environmental and Biological Sciences (CITAB), Inov4Agro, University of Trás-os-Montes and Alto Douro (UTAD)
Quinta de Prados, 5000-801 Vila Real, Portugal
fmality@yahoo.com.br

 DOI: https://doi.org/10.60620/he5s-8x66

Malik Amraoui
Centre for the Research and Technology of Agro-environmental and Biological Sciences (CITAB), Inov4Agro, University of Trás-os-Montes and Alto Douro (UTAD)
Quinta de Prados, 5000-801 Vila Real, Portugal
malik@utad.pt

Alexandre M. Ramos
Inst. of Meteo. & Clim. Res. Karlsruhe Institute of Technology (KIT), Karlsruhe, Germany

Paulo J. Pinto
Instituto Português do Mar e da Atmosfera, I. P.
Rua C do Aeroporto, 1749-077 Lisboa, Portugal

Raquel Santos
Instituto Português do Mar e da Atmosfera (IPMA),
Rua C do Aeroporto, 1749-077, Lisboa, Portugal
raquel.santos@ipma.pt

Célia M. Gouveia
Instituto Português do Mar e da Atmosfera (IPMA),
Rua C do Aeroporto, 1749-077, Lisboa, Portugal

Rui Silva
CESAM, Department of Physics, University of Aveiro,
Campus Universitário de Santiago, 3810-193 Aveiro Portugal

Ana Cristina Carvalho
Swedish Meteorological and Hydrological Institute. Research Department. FoUmmk group.
Folkborgsvägen 17, 603 80, Norrköping

Alfredo Rocha
CESAM, Department of Physics, University of Aveiro,
Campus Universitário de Santiago, 3810-193 Aveiro Portugal

João Rio
Instituto Português do Mar e da Atmosfera, I. P.
Rua C do Aeroporto, 1749-077 Lisboa, Portugal
joao.rio@ipma.pt

André Barreirinha
Instituto Português do Mar e da Atmosfera, I. P.
Rua C do Aeroporto, 1749-077 Lisboa, Portugal

Maria José Monteiro
Instituto Português do Mar e da Atmosfera, I. P.
Rua C do Aeroporto, 1749-077 Lisboa, Portugal

Ana Miranda
CESAM & Departamento de Ambiente e Ordenamento, Universidade de Aveiro
Campus Universitário de Santiago, 3810-193 Aveiro, Portugal

Pedro Silva
Instituto Português do Mar e da Atmosfera, I. P.
Rua C do Aeroporto, 1749-077 Lisboa, Portugal
pedro.silva@ipma.pt

Mário Santos
Centre for the Research and Technology of Agro-Environment and Biological Sciences (CITAB), Inov4Agro, University of Trás-os-Montes and Alto Douro
Quinta de Prados, 5000-801 Vila Real, Portugal
mgsantos@utad.pt

Tomás Gaspar
Instituto Dom Luiz, Faculdade de Ciências, Universidade de Lisboa
Campo Grande Edifício C1, Piso 1, 1749-016 Lisboa, Portugal

Ricardo Deus
Instituto Português do Mar e da Atmosfera, I. P.
Rua C do Aeroporto, 1749-077 Lisboa, Portugal

Ricardo M. Trigo
Instituto Dom Luiz, Faculdade de Ciências, Universidade de Lisboa
Campo Grande Edifício C1, Piso 1, 1749-016 Lisboa, Portugal

Ana Russo
Instituto Dom Luiz, Faculdade de Ciências, Universidade de Lisboa
Campo Grande Edifício C1, Piso 1, 1749-016 Lisboa, Portugal

Ricardo Vaz
CESAM, Department of Physics, University of Aveiro,
Campus Universitário de Santiago, 3810-193 Aveiro Portugal
ricardojorgevaz@ua.pt

Susana Cardoso Pereira
CESAM, Department of Physics, University of Aveiro,
Campus Universitário de Santiago, 3810-193 Aveiro Portugal

David Carvalho
CESAM, Department of Physics, University of Aveiro,
Campus Universitário de Santiago, 3810-193 Aveiro Portugal

Paulo Pinto
Instituto Português do Mar e da Atmosfera, I. P.
Rua C do Aeroporto, 1749-077 Lisboa, Portugal

Carla Gama
CESAM & Departamento de Ambiente e Ordenamento, Universidade de Aveiro
Campus Universitário de Santiago, 3810-193 Aveiro, Portugal

Manuel Lopes
Instituto Português do Mar e da Atmosfera, I. P.
Rua C do Aeroporto, 1749-077 Lisboa, Portugal

Tobias Osswald
CESAM & Departamento de Ambiente e Ordenamento, Universidade de Aveiro
Campus Universitário de Santiago, 3810-193 Aveiro, Portugal

Ricardo Ramos
Instituto Português do Mar e da Atmosfera, I. P.
Rua C do Aeroporto, 1749-077 Lisboa, Portugal
ricardo.ramos@ipma.pt

Isilda Cunha Menezes
Centre for Environmental and Marine Studies (CESAM), University of Aveiro, Department of Environment and Planning
Campus Universitário de Santiago, 3810-193 Aveiro, Portugal
isildacm@ua.pt

Alan Yair Alarcón Pacheco
Geophysics Institute, UNAM
Avenida Universidad 3000, Mexico City, Mexico
a.alarcon@igeofisica.unam.mx

Maria Rosa Alves Duque
Universidade de Évora, Departamento de Física, Escola de Ciências e Tecnologia
Rua Romão Ramalho 59, Évora, Portugal
mrad@uevora.pt

Paulo M. Alves
Instituto Português do Mar e da Atmosfera, I. P.
Rua C do Aeroporto, 1749-077 Lisboa, Portugal
paulo.alves@ipma.pt

Susana Custódio
Instituto Dom Luiz, Faculdade de Ciências, Universidade de Lisboa
Campo Grande Edifício C1, Piso 1, 1749-016 Lisboa, Portugal
sicustodio@fc.ul.pt

Pedro Teixeira
Physics Department (ECT), Institute of Earth Sciences (ICT/IIFA), Earth Remote Sensing Laboratory (EaRSLab), University of Évora
Rua Romão Ramalho n.º 59 7000-671 Évora, Portugal
pmmt@uevora.pt

Bento Caldeira
Physics Department (ECT), Institute of Earth Sciences (ICT/IIFA), Earth Remote Sensing Laboratory (EaRSLab), University of Évora
Rua Romão Ramalho n.º 59 7000-671 Évora, Portugal

Isabel Alexandre
Instituto Superior Técnico (IST)
Av. Rovisco Pais, 1, 1049-001 Lisboa

João Costa
Mina de Ciência – Lousal Ciência Viva Center
Avenida Frédéric Velge, 7570-006, Lousal, Portugal

José Borges
Physics Department (ECT), Institute of Earth Sciences (ICT/IIFA), Earth Remote Sensing Laboratory (EaRSLab), University of Évora
Rua Romão Ramalho n.º 59 7000-671 Évora, Portugal

Lorenzo Cazon
Instituto Galego de Física de Altas Enerxías (IGFAE) - Universidade de Santiago de Compostela
Rúa de Xoaquín Díaz de Rábago, 15705 Santiago de Compostela, Spain

Luis Lopes
Laboratory of Instrumentation and Experimental Particle Physics (LIP)
Av. Prof. Gama Pinto, 2, 1649-003 Lisboa

Mário Pimenta
Laboratory of Instrumentation and Experimental Particle Physics (LIP)
Av. Prof. Gama Pinto, 2, 1649-003 Lisboa

Paolo Dobrilla
Laboratory of Instrumentation and Experimental Particle Physics (LIP)
Av. Prof. Gama Pinto, 2, 1649-003 Lisboa

Célia Marreiros
Instituto Português do Mar e da Atmosfera, I. P.
Rua C do Aeroporto, 1749-077 Lisboa, Portugal
celia.marreiros@ipma.pt

Carlos S. Oliveira
Instituto Superior Técnico, CERIS
Av. Rovisco Pais 1049-001 Lisboa, Portugal
csoliv@civil.ist.utl.pt

Fernando Carrilho
Instituto Português do Mar e da Atmosfera, I. P.
Rua C do Aeroporto, 1749-077 Lisboa, Portugal
fernando.carrilho@ipma.pt

Alberto Blanco
Laboratory of Instrumentation and Experimental Particle Physics (LIP)
Av. Prof. Gama Pinto, 2, 1649-003 Lisboa

Bernardo Tomé
Laboratory of Instrumentation and Experimental Particle Physics (LIP)
Av. Prof. Gama Pinto, 2, 1649-003 Lisboa

João Matos
Nacional Laboratory of Energy and Geology (LNEG), Campus de Aljustrel
Bairro da Vale d'Oca, Apartado 14, 7601-909 Aljustrel, Portugal

Jorge Silva
Physics Department (DF), University of Coimbra
Rua Larga, 3004-516 Coimbra, Portugal

Josué Figueira
Physics Department (ECT), Institute of Earth Sciences (ICT/IIFA), Earth Remote Sensing Laboratory (EaRSLab), University of Évora
Rua Romão Ramalho n.º 59 7000-671 Évora, Portugal

Luis Afonso
Laboratory of Instrumentation and Experimental Particle Physics (LIP)
Av. Prof. Gama Pinto, 2, 1649-003 Lisboa

Magda Duarte
University of Minho, Gualtar Campus, CP3, 3.02,
R. da Universidade, 4710-057 Braga

Mourad Bezzeghoud
Physics Department (ECT), Institute of Earth Sciences (ICT/IIFA), Earth Remote Sensing Laboratory (EaRSLab), University of Évora
Rua Romão Ramalho n.º 59 7000-671 Évora, Portugal

Pedro Assis
Laboratory of Instrumentation and Experimental Particle Physics (LIP)
Av. Prof. Gama Pinto, 2, 1649-003 Lisboa

 DOI: https://doi.org/10.60620/he5s-8x66

Raul Sarmento
Laboratory of Instrumentation and Experimental Particle Physics (LIP)
Av. Prof. Gama Pinto, 2, 1649-003 Lisboa

Sofia Andringa
Laboratory of Instrumentation and Experimental Particle Physics (LIP)
Av. Prof. Gama Pinto, 2, 1649-003 Lisboa

Karla Guadalupe Ramírez Veja
UNAM
Circuito Instituto S/N, Coyoacán 04510, México
karlup@comunidad.unam.mx

Emma Suriñach Cornet
Department RISKNAT Avalanches Research Group- Institut Geomodels. DPY. Dinàmica de la Terra i de l'Oceà, Facultat de Ciències de la Terra.
c/Martí i Franquès s/n, Universitat de Barcelona (UB). Barcelona 28008, Spain

Rui Oliveira
Physics Department (ECT), Institute of Earth Sciences (ICT/IIFA), Earth Remote Sensing Laboratory (EaRSLab), University of Évora
Rua Romão Ramalho n.º 59 7000-671 Évora, Portugal

Vanessa Pais
Mina de Ciência – Lousal Ciência Viva Center
Avenida Frédéric Velge, 7570-006, Lousal, Portugal

Elsa Leticia Flores Márquez
Departamento de Geomagnetísmo y Exploración, Instituto de Geofísica, UNAM
Circuito Instituto S/N, Coyoacán 04510, México
leticia@igeofisica.unam.mx

PART I: ADVANCES IN METEOROLOGY

 DOI: https://doi.org/10.60620/he5s-8x66

Aethalometer Measurements During Cumbre Vieja Volcano Eruption

Diamantino Henriques [1], Paulo Fialho [2], África Barreto [3], Yenny González [4], Sergio Rodríguez [5], Emilio Cuevas [3], José Pacheco [2]

[1] *Instituto Português do Mar e da Atmosfera (IPMA), Observatório Afonso Chaves, Rua Mãe de Deus – Relvão, 9500–321 Ponta Delgada, Portugal, diamantino.henriques@ipma.pt*
[2] *Instituto de Investigação em Vulcanologia e Avaliação de Riscos (IVAR), Rua da Mãe de Deus, 9500-321 Ponta Delgada, Portugal, fialho.paulo@gmail.com, jose.mr.pacheco@azores.gov.pt*
[3] *Izaña Atmospheric Research Centre (CIAI), AEMET, Santa Cruz de Tenerife, 38001, Spain, abarretov@aemet.es, ecuevasa@aemet.es.*
[4] *CIMEL Electronique, Paris, 75011, France, y-gonzalez@cimel.fr*
[5] *Institute of Natural Products and Agrobiology (IPNA), CSIC, Tenerife, Spain, sergio.rodriguez@csic.es*

SUMMARY

Aethalometer measurements were carried out at the Atmospheric Observatory of Izaña (IZO) during the eruption of the Cumbre Vieja volcano on the island of La Palma to study the impact of volcanic ash in aethalometer signals. Principal Component Analyses of the back trajectories arriving at IZO showed that more than 53% of the variance of equivalent BC (eBC) concentration is explained by the two first components, being 33% explained by the first component and about 20%) explained by the second one. Backward trajectories passing over Africa represent the largest contribution to PC1 during the campaign period.

Keywords: Aethalometer; Black Carbon; Dust; Volcanic Ash; Principal Components Analysis.

1. Introduction

The aethalometer is an optical instrument specially designed for the continuous measurement of Black Carbon in ambient air (Hansen, Anthony D.A. et al., 1984). Black Carbon (BC) is a type of carbonaceous material, with significant absorption in the visible range, and is one of the products formed from the combustion of carbon-based fuel (Seinfeld & Pandis, 2016). The measurement method is based on the attenuation of the radiation coming from a monochromatic radiation source, through a filter where the material is collected during sampling. The attenuation suffered may not only be due to absorption but also to possible reflected/scattered components. Thus, the attenuation observed during measurement may not be due only to the presence of carbonaceous particles but to other particles that may also attenuate the radiation at the same wavelengths. The dependence of attenuation on wavelength along the visible spectrum allows the evaluation of the degree of "purity" of the BC present in the sample. Thus, the so-called Angstrom absorption coefficient (Moosmüller et al., 2009) in this study Ångström (attenuation) exponent α_{ATN} can be written as:

$$\frac{\sigma_{\lambda_2}}{\sigma_{\lambda_1}} = \left(\frac{\lambda_2}{\lambda_1}\right)^{-\alpha_{ATN}} \quad (1)$$

were σ_{λ_1} and σ_{λ_2} are the attenuation coefficients at wavelengths λ_1 and λ_2 respectively, calculated from the aethalometer radiation attenuation measurements. For fossil fuel, biomass burning and dust (iron oxides) application of equation (1) to the aethalometer data is expected to give the aerosol absorption Ångström exponent, α_{abs} (the multi-scattering correction applicable to convert the attenuation coefficient into the absorption coefficient is wavelength independent). Fossil fuel BC aerosols are

expected to show α_{abs} of one, whereas biomass-burning aerosols and dust are typically larger than 1 (Fialho et al., 2006; Kirchstetter et al., 2004; Moosmüller et al., 2009; Sandradewi et al., 2008).

Volcanoes are the most important geochemical source of trace constituents in the atmosphere (Hobbs, 2000) and have long been implicated as a possible cause of weather and climate variations (Robock, 2000). According to the latest IPCC report (IPCC, 2021), the radiative effects of volcanic aerosols are a dominant natural driver of climate variability at the interannual scale. Overall, the effective radiative forcing of volcanic aerosols, consisting mainly of sulphate, is negative, thus counteracting the warming effect of greenhouse gases, but insufficient to cancel it out over a scale of more than a few years. However, the residence times of aerosols in the middle and low troposphere are generally about 10 days (Hobbs, 2000). Volcanic ash (VA) particles can be released into the atmosphere during explosive eruptions and transported hundreds to thousands of kilometres away (Vogel et al., 2017).

The available information on the optical properties of VA is still scarce. However, available data estimated from samples, show that the imaginary part of the complex refractive indices of VA in visible and near IR range (Vogel et al., 2017) is in the range of 0.0002 – 0.0027, much lower than for BC: 0.6 – 0.8 (Bond & Bergstrom, 2006) and mineral dust: 0.006 – 0.79 (Seinfeld & Pandis, 2016), indicating a lower absorption component. However, the real part of the complex refractive indices of VA has values of the same order, of magnitude as BC, ranging 1from .4 to 1.7 (Vogel et al., 2017), indicating that they also attenuate radiation and may therefore interfere with the aethalometer measurements.

The eruption of the Cumbre Vieja volcano on the island of La Palma (19 Sep. to 13 Dec. 2021) provided an opportunity to analyze the impact of volcanic ash on the attenuation signals measured by the aethalometer. In this sense, a sampling campaign was carried out, between 2nd November 2021 and 28th April 2022, at the Atmospheric Observatory of Izaña (IZO). IZO is located on the island of Tenerife (28.31°N, 16.50°W), approximately 140 km SE of La Palma, and at an altitude of 2373 m. The impact of the volcanic eruption on air quality at the island of La Palma was naturally high and also affected the neighbouring island of Tenerife. Sulphur dioxide concentrations observed at IZO were higher than 7700 μgm^{-3}, being in the range of concentrations recorded in the largest tropospheric volcanic eruptions worldwide (Milford et al., 2023).

2. Methods and materials

An aethalometer mod. AE43 was installed in one of the IZO facilities called PARTILAB (Cuevas Agulló et al., 2015). The AE43 (Magee Scientific, 2020) uses 7 wavelengths distributed over the ultraviolet (370 nm), visible (470 nm, 520 nm, 590 nm and 660 nm) and near-infrared (880 nm and 950 nm) and two "spots" with different sampling rates for loading effect correction. Each pair of spots corresponds to an air sample of 24 h (**Figure 1**).

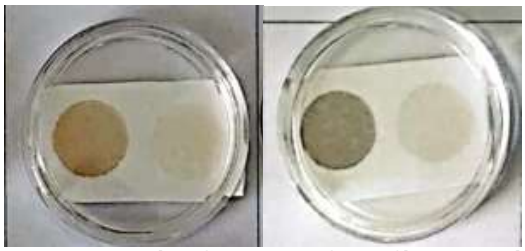

Figure 1. Examples of two pieces of AE43 filter tape with dual spot samples collected with AE43.

The left spot of **Figure 1** was obtained with a flow rate of 3.8 l/min (high flow) while the right spot was obtained with 1.2 l/min (low flow). Each pair of spots was analyzed visually and classified according to two qualitative criteria, colour (Red, Brown, Gray) and hue (dark, light, very light). For each 24h spot, nine back trajectories were computed using the FLEXTRA three-dimensional trajectory model (Stohl et al., 2015; Stohl & Seibert, 1998), based on ERA5 reanalysis (Hersbach et al., 2020) and at one-hour intervals. The spatial domain of the model was between latitudes 20°N and 40°N and longitudes 0 and 25°W. The trajectories had as a destination a point close to IZO (28.3°N, 16.5°W, 2400 m). Each trajectory has a duration of 120 h, i.e. each trajectory represents the history of the air mass during

 DOI: https://doi.org/10.60620/r6q2-h293

the last five days before arrival at the IZO. Each parcel of air arriving at a given point should carry some of the properties acquired along its route. It is therefore of interest to find out how long each parcel has remained over certain areas of interest. For this case, five zones representing possible aerosol sources have been defined: La Palma, Tenerife, Africa and Europe (**Figure 2**).

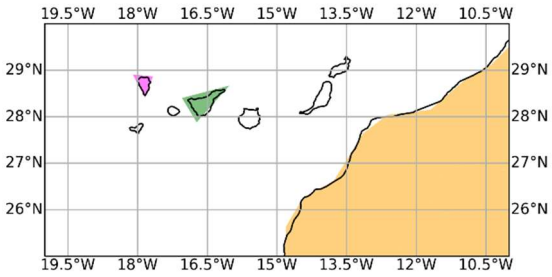

Figure 2. Some source zones selected for this study: La Palma (magenta), Tenerife (green), and Africa (beige).

For each trajectory, the number of hours that the air parcel remained over each of the 5 selected zones was calculated. The results were aggregated to assess the potential contribution of each zone to the composition of each spot (**Figure 3**).

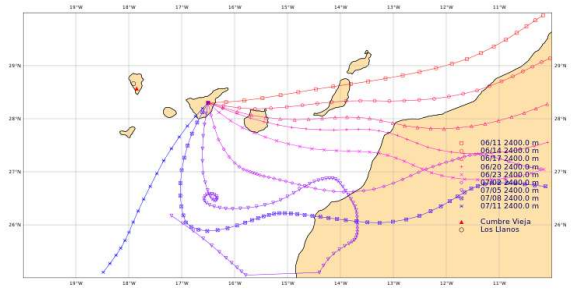

Figure 3. 3D FLEXTRA backward trajectories 120 h before 12-07-2021 00:00 UTC arriving at IZO (28.30N, -16.50E, 2400m). Steps intervals: 1h.

To evaluate the importance of each zone in the BC signals recorded by the aethalometer, a Principal Component Analysis (PCA) was performed using the available data for the samples/spots: mean and standard deviation values of the equivalent Black Carbon (eBC) concentration over wavelengths; Ångström exponent (α_{ATN}) for visible range (470 nm to 660 nm); residence times in each of the five defined zones.

3. Results

The results are presented as biplot graphs of the 2 first PCA, using as the label for each point the colour or hue of the corresponding sample. **Figure 4** shows that the particles spent around 78% of the campaign time over the ocean, close to 15% over Africa and less than 0.1% over the La Palma zone.

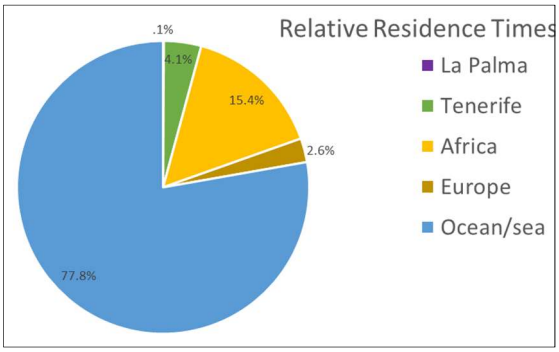

Figure 4. Relative residence times of air masses arriving at IZO during the campaign period for the five selected zones.

3.1. Mean and Standard Deviation values of the Black Carbon concentration over wavelength.

The first principal component (PC1) explains about 33% of the variance while the first two components explain more than 53% of that variance (**Figure 5**). The backward trajectories that pass over Africa contribute only to PC1. On the other hand, the remaining trajectories contribute both to the PC1 and PC2 and are practically independent, being also practically parallel and therefore highly correlated among themselves. The mean values and standard deviations of BC are practically parallel (highly correlated), with some relation with backward trajectories passing over Africa, but weak relationship with the others. Most of the samples are on the negative side of PC1. Most of the samples with B (brown) and U (undefined colours are clustered along the same direction as the trajectories over the islands, Ocean/Sea and Europe.

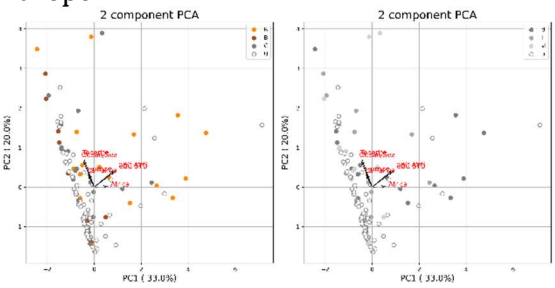

Figure 5. Biplot of the two first PC for mean and standard deviation of eBC measured on the samples and residence times for the 5 selected source zones. Colour target (left): R (red), B (brown), G (green), U (unknown); Hue target (right): d (dark), l (light), vl (very light), u (unknown).

3.2. Angstrom exponent for the visible range wavelengths

The PC1 explains 30% of the variance while the first two components explain 50% of that variance. The trajectories crossing Africa contribute almost equally to both PC1 and PC2 (**Figure 6**). On the other hand, the remaining trajectories contribute more to PC2, and those that pass over Tenerife are almost independent of those passing through Africa. $\alpha_{abs}$is well correlated with the trajectories through Africa and has a weak correlation with the others. The backward trajectory through La Palma contributes the least to the components. Most of the coloured and dark samples are on the positive side of PC2.

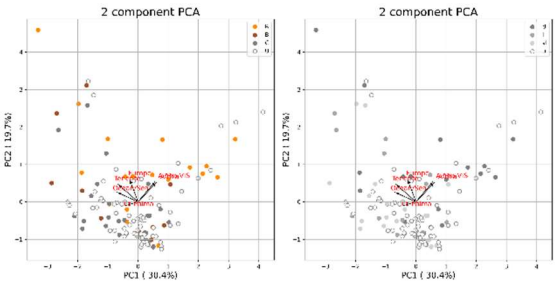

Figure 6. Biplot of the two first PC for mean and standard deviation of α_{ATN} on the visible range (AlphaVIS) measured on the samples and residence times for the 5 selected source zones. Colour target (left): R (red), B (brown), G (green), U (unknown); Hue target (right): d (dark), l (light), vl (very light), u (unknown).

4. Conclusions

Between November 2nd, 2021, and April 29th, 2022, a total of 178 aerosol filter samples were collected at IZO by using the aethalometer AE43 they were analyzed for their equivalent BC particle content and classified according to their colour and hue.

For the same period, air mass back trajectories arriving at the IZO were calculated and residence times in five defined zones were determined. Of the 1333 trajectories obtained (73931 hours), only 39 (66 hours) had passage through the island of La Palma and therefore episodes of possible ash collection directly from the Cumbre Vieja volcano were rare.

The principal component analyses show that the BC values of the trajectories with passage over La Palma are not significantly different from the others, except for those that passed through Africa, which contribute only to PC1.

These PCA also show that the trajectories that passed over the island of La Palma contribute the least to the principal components of the Ångström exponent, suggesting that any directly transported ash does not significantly affect the measurements done with the aethalometer.

5. Acknowledgements

The authors are grateful for the support provided by the AEMET team in the release of the IVAR equipment at customs, the installation and the network and communications setup that allowed the success of this campaign.

6. References

Bond, T. C., & Bergstrom, R. W. (2006). Light absorption by carbonaceous particles: An investigative review. Aerosol Science and Technology, 40(1), 27 – 67. DOI: https://doi.org/10.1080/02786820500421521

Cuevas Agulló, E., Milford, C., & Tarasova, O. (Eds.). (2015). Izaña Atmospheric Research Center. Activity Report 2012-2014. Agencia Estatal de Meteorología; Organización Meteorológica Mundial. DOI: https://doi.org/10.31978/281-15-004-2

Fialho, P., Freitas, M. C., Barata, F., Vieira, B., Hansen, A. D. A., & Honrath, R. E. (2006). The Aethalometer calibration and determination of iron concentration in dust aerosols. Journal of Aerosol Science, 37(11), 1497 – 1506. DOI: https://doi.org/10.1016/j.jaerosci.2006.03.002

Hansen, Anthony D.A., Rosen, H., & Novakov, T. (1984). The Aethalometer - An instrument for the real-time measurement of optical absorption by aerosol particles. The Science of The Total Environment, 36, 191–196.

Hersbach, H., Bell, B., Berrisford, P., Hirahara, S., Horányi, A., Muñoz-Sabater, J., Nicolas, J., Peubey, C., Radu, R., Schepers, D., Simmons, A., Soci, C., Abdalla, S., Abellan, X., Balsamo, G., Bechtold, P., Biavati, G., Bidlot, J., Bonavita, M., … Thépaut, J. N. (2020). The ERA5 global reanalysis. Quarterly Journal of the Royal Meteorological Society, 146(730), 1999–

 DOI: https://doi.org/10.60620/r6q2-h293

2049. DOI: https://doi.org/10.1002/qj.3803

Hobbs, P. V. (2000). Introduction to Atmospheric Chemistry. Cambridge University Press, Cambridge.

IPCC. (2021). Climate Change 2021: The Physical Science Basis. In V. , Masson-Delmotte, P. Zhai, A. Pirani, S. L. Connors, C. Péan, S. Berger, N. Caud, Y. Chen, L. Goldfarb, M. I. Gomis, M. Huang, K. Leitzell, E. Lonnoy, J. B. R. Matthews, T. K. Maycock, T. Waterfield, O. Yelekçi, R. Yu, & B. Zhou (Eds.), Cambridge University Press. In Press. Cambridge University Press. DOI: https://doi.org/https://doi.org/10.1017/9781009157896

Kirchstetter, T. W., Novakov, T., & Hobbs, P. V. (2004). Evidence that the spectral dependence of light absorption by aerosols is affected by organic carbon. Journal of Geophysical Research D: Atmospheres, 109(21). DOI: https://doi.org/10.1029/2004JD004999

Magee Scientific. (2020). Aethalometer ® Model AE43 User Manual (Issue November, pp. 1–145).

Milford, C., Torres, C., Vilches, J., Gossman, A. K., Weis, F., Suárez-Molina, D., García, O. E., Prats, N., Barreto, Á., García, R. D., Bustos, J. J., Marrero, C. L., Ramos, R., Chinea, N., Boulesteix, T., Taquet, N., Rodríguez, S., López-Darias, J., Sicard, M., … Cuevas, E. (2023). Impact of the 2021 La Palma volcanic eruption on air quality: Insights from a multidisciplinary approach. Science of the Total Environment, 869. DOI: https://doi.org/10.1016/j.scitotenv.2023.161652

Moosmüller, H., Chakrabarty, R. K., & Arnott, W. P. (2009). Aerosol light absorption and its measurement: A review. In Journal of Quantitative Spectroscopy and Radiative Transfer (Vol. 110, Issue 11, pp. 844–878). DOI: https://doi.org/10.1016/j.jqsrt.2009.02.035

Robock, A. (2000). Volcanic eruptions and climate. Reviews of Geophysics, 38(2), 191–219. DOI: https://doi.org/10.1029/1998RG000054

Sandradewi, J., Prévôt, A. S. H., Szidat, S., Perron, N., Alfarra, M. R., Lanz, V. A., Weingartner, E., & Baltensperger, U. R. S. (2008). Using aerosol light absorption measurements for the quantitative determination of wood burning and traffic emission contribution to particulate matter. Environmental Science and Technology, 42(9), 3316 – 3323. DOI: https://doi.org/10.1021/es702253m

Seinfeld, J. H. J. H., & Pandis, S. N. (2016). Atmospheric Chemistry and Physics. From Air Pollution to Climate Change. In Air pollution to climate (3rd ed.). Wiley.

Stohl, A., & Seibert, P. (1998). Accuracy of trajectories as determined from the conservation of meteorological tracers. Q. J. Roy. Met. Soc., 124, 1465–1484. DOI: https://doi.org/10.1002/qj.49712454907

Stohl, A., Wotawa, G., Seibert, P., & Kromp-Kolb, H. (2015). Interpolation errors in wind fields as a function of spatial and temporal resolution and their impact on different types of kinematic trajectories. Journal of Applied Meteorology, 34, 2149–2165.

Vogel, A., Diplas, S., Durant, A. J., Azar, A. S., Sunding, M. F., Rose, W. I., Sytchkova, A., Bonadonna, C., Krüger, K., & Stohl, A. (2017). Reference data set of volcanic ash physicochemical and optical properties. Journal of Geophysical Research: Atmospheres, 122(17), 9485–9514. DOI: https://doi.org/10.1002/2016JD026328

Machine Learn Estimates of Downward Surface Long-Wave Fluxes (Dslf) Based on Reanalysis and Satellite Observations

Francisco M. Lopes [1], Emanuel Dutra [1,2], Isabel Trigo [1,2]

[1] *Instituto Dom Luiz (IDL), University of Lisbon, Campo Grande, 1749-016, Lisbon, Portugal, fmtlopes@fc.ul.pt*
[2] *Instituto Português do Mar e da Atmosfera (IPMA), Rua C do Aeroporto, 1749-077, Lisbon, Portugal, emanuel.dutra@ipma.pt; isabel.trigo@ipma.pt*

SUMMARY

A machine learning approach based on multivariate adaptive regression splines (MARS) is explored to integrate reanalysis data, satellite cloud information and ground observations of Downward Surface Long-wave Radiation Fluxes (DSLF), to estimate hourly DSLF for all-sky conditions. The MARS estimates are shown to have lower errors than other models when tested against 23 stations (BSRN/ARM), outperforming other DSLF estimates, including the current LSA-SAF operational product. In this work, the proposed methodology is shown to be consistent when new validation is performed, particularly with an independent network of 52 stations (FLUXNET2015). Further assessment of MARS estimates for the whole MSG disk is carried out, showing the potential of the model for operational purposes.

Keywords: Downward Surface Long-wave Fluxes; All-weather; Multivariate Adaptive Regression Splines; EUMETSAT LSA-SAF; ECMWF-ERA5.

1. Introduction

Downward Surface Long-wave Fluxes (DSLF), i.e. the incoming thermal irradiance reaching the surface within the thermal infrared spectrum (3 – 100 μm), is one of the components of the Earth's surface radiative budget (Wild et al., 2013). DSLF is directly linked to the vertical profiles of atmospheric air temperature and water vapour, and cloud-base properties (i.e. height, temperature, and emissivity), obviously contributing to the net surface long-wave budget. When accurately estimated, DSLF can be used for heat exchange fluxes, climate variability and global warming calculations (Houghton et al., 2001). Over the last two decades, there has been a synergetic use of state-of-the-art numerical weather prediction models, in-situ and remote sensed data. However, the recent use of machine learning methods to estimate DSLF, as an alternative to simpler empirical formulations (e.g. Bilbao and H. de Miguel 2006; Josey, Pascal, and Yelland 2003; Trigo et al. 2010), has been gaining terrain, taking advantage of more flexible and complex approaches to solving complex nonlinear statistical problems between DSLF and its main modulators. For instance, some of these studies include extremely randomized trees (Cao et al., 2022), random forest (Wang et al., 2020; Q. Zhou et al., 2017), neural networks (Wang et al., 2012) and, more recently, multivariate adaptive regression splines (MARS) (Jung et al., 2019; Lopes et al., 2022; W. Zhou et al., 2018, 2019). In particular, the present work makes use of a machine learning model with an algorithm based on MARS, being previously calibrated and validated (Lopes et al., 2022) with Baseline Surface Radiation Network (BSRN) and Atmospheric Radiation Measurement (ARM) user facility observations. The MARS model uses as input near-surface temperature, dew point, and total column water vapour from the latest European Centre for Medium-range Weather Forecasts (ECMWF) reanalysis

 DOI: https://doi.org/10.60620/swxy-ct70

(ERA5), and cloud information from the Meteosat Second Generation (MSG), to estimate half-hourly values of DSLF under all-sky conditions. Validation results against 23 ground stations (BSRN/ARM) showed that MARS estimates have lower errors in comparison to the Exploitation of Meteorological Satellites (EUMETSAT) Satellite Application Facility on Land Surface Analysis (LSA-SAF) current operational algorithm (Trigo et al., 2010) and ERA5's downward long-wave fluxes. The results were supported by additional testing of the MARS model performance using an independent dataset of 52 FLUXNET2015 stations. It was concluded that due to the combination of its recursive partitioning and spline fitting in the form of a series of stepwise functions and knots with observations, reanalysis and cloud information, the MARS model provides significant improvements when compared with DSLF estimates from LSA-SAF based on least square fitting methods. Despite demonstrating overall improvements, the MARS model also indicated the presence of errors for extreme values of DSLF when compared to other product estimates. These were linked to the model adopted-calibration, which considers a random selection of 6 months of input data (or 40% of availability) from each of the 23 BSRN/ARM stations. Such model corrections are currently underway and should be implemented in future works.

The objective of the present study is focused on further evaluating the model for the whole MSG disk (i.e. longitude/latitude +/- 75° E/N), to assess the added value that the MARS model has for operational purposes in comparison to the current LSA-SAF DSLF product. In this context, BSRN and FLUXNET2015 ground stations are once again used to validate the model considering a different configuration of the input variables used to compute DSLF for the entire MSG disk. This includes ECMWF-ERA5 data and instantaneous cloud information from the MSG cloud mask, similar to the operational configuration used for the current LSA-SAF product. In the following sections, we describe the data and methods used to evaluate the MARS model estimates (section 2); results for the new BSRN and FLUXNET2015 validations, being followed by an application example with an overview of the DSLF product for the Iberian Peninsula (section 3); corresponding discussion for the obtained results (section 4); and conclusions (section 5).

2. Data and Methods

To validate model estimates, ground observations within the MSG disk are used, and most of these are located in Europe. The analyses include two separate networks, namely 22 stations from the BSRN (Driemel et al., 2018), comprising 16 years (from 2004 to 2019), and 53 stations from the FLUXNET2015 (Pastorello et al., 2020), comprising 11 years (from 2004 – 2014). All measured data is freely available at each designated website (https://bsrn.awi.de/ and https://fluxnet.org).

Models considered in this work include the MARS model, the LSA-SAF operational product for DSLF (MDSLF, (Trigo et al., 2011)), and ERA5 fluxes. The MARS model core algorithm follows the MARS methodology (Friedman, 1991; Friedman & Roosen, 1995), which incorporates a 2-stage building process: a forward and a backward pass. In the former, also known as the training procedure, the algorithm finds the best combination between the different pairs of base functions (composed of predictors and predictand) based on the maximum reduction in sum-of-squares residual error. Then, in the latter, also known as the pruning procedure, the algorithm removes the least effective terms at each step to avoid model overfitting. Similarly, to the MDSLF model, to produce instantaneous 30-minute estimates of DSLF over a 0.05° grid resolution for the whole MSG disk, the previous calibrated MARS model is now directly fed with ECMWF-ERA5 30-minute data of two-metre air and dewpoint temperatures (t2m and d2m, respectively), and total column water vapour (tcwv), and instantaneous (15-minute) cloud information from the MSG cloud mask. The MDSLF model uses an algorithm, previously calibrated (Trigo et al., 2010), based on ERA-40 atmospheric profiles and MODTRAN-4 (Berk et al., 2003) radiation fluxes, which are used within a bulk parameterization scheme followed by a piecewise regression to

estimate DSLF. Finally, the most recent ECMWF reanalysis (ERA5 (Hersbach et al., 2020)) hourly radiation fluxes projected on a coarser grid resolution (0.25°) are used for comparison, being extracted from the Copernicus Data Store. It should be noted that, for the proposed validations, ERA5 fluxes are adjusted to each location elevation, following a correction factor of -2.8 W.m^{-2} per 100 m, similar to (Marty et al., 2002). Moreover, both MARS and MDSLF models also include flux adjustments to calculate DSLF in the MSG disk.

The evaluation of each model against observations is performed using standard error metrics, such as the bias (μ), the standard deviation (σ), the root mean square error (RMSE), and the temporal correlation coefficient (R).

3. Results

The validation results against BSRN and FLUXNET2015 are shown for each model by the respective scatter density plots (**Figure 1, left panels and right panels**, respectively), where the colour scheme indicates the degree of point concentration for the hourly values. Moreover, additional information concerning the performance of each model under different conditions of observed DSLF from all stations is present in **Table A.1** and **Table A.2** of Appendix A.

MARS estimates of DSLF projected over the entire MSG disk generally show lower errors than other models. When compared against all 22 BSRN stations (**Figure 1, left panels**), the MARS model shows an RMSE of 19.60 W.m^{-2}, while higher values are found for MDSLF and ERA5 (23.79 and 22.07 W.m^{-2}, respectively). A similar behaviour is found for σ, while an overall overestimation (1.40 W.m^{-2}) is obtained with the MARS model towards observations, as opposed to the resulting underestimation obtained with MDSLF and ERA5. It is clear that, due to the nature of the MARS algorithm, the model performs better when higher samples are available, as for the case of values between 200 – 400 W.m^{-2} (**Table A.1**). Moreover, similar performances are found when computing DSLF at each station location, as shown by the corresponding median of the distribution of the metrics computed independently for each station. However, when estimating extreme values of DSLF, the MARS model shows an error increase in comparison to the MDSLF and ERA5, as shown for values above 400 W.m^{-2} and, particularly, for values below 200 W.m^{-2} where an RMSE of 31.05 W.m^{-2} is obtained, i.e. about 9 W.m^{-2} higher than the ones found for MDSLF and ERA5. The same validation analysis but considering the FLUXNET2015 stations shows very similar behaviours (**Figure 1, right panels**), with the MARS model outperforming other models, particularly when higher sampling is present (**Table A.2**). Although there is an overall error increase (in comparison to the previous validation against BSRN), this analysis shows the consistency of the applied methodology.

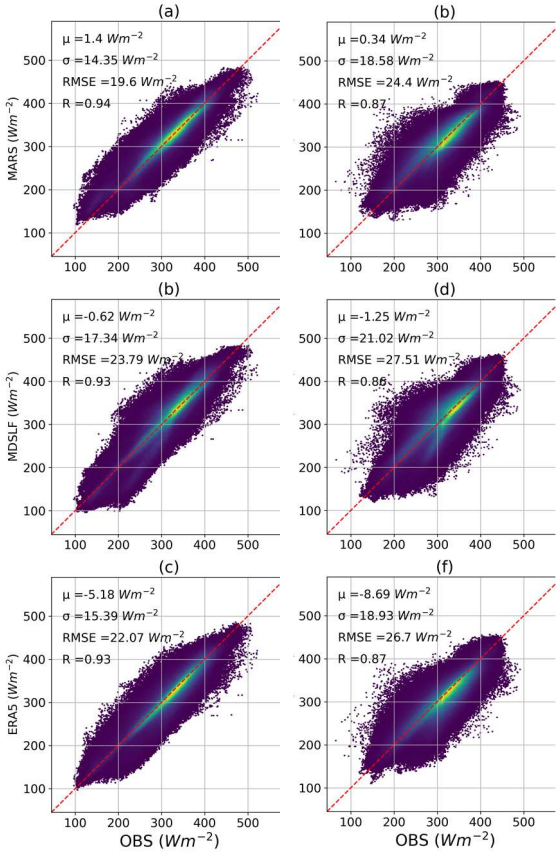

Figure 1. MARS, MDSLF and ERA5 hourly estimates of DSLF for all-sky conditions against (left panels) BSRN validation (2014 – 2019); and (right panels) FLUXNET2015 validation (2014 – 2014). Inside legends show standard error metrics, while the red dashed line corresponds to the identity line.

An application example of the DSLF hourly product over the Iberian Peninsula is shown for July 15th 2021 at 18 UTC (**Figure 2**). It is possible to notice the added value of using a high-resolution model in comparison to the

DOI: https://doi.org/10.60620/swxy-ct70

reanalysis. Taking advantage of a more detailed cloud field, both MARS and MDSLF provide a better characterization of the DSLF spatiotemporal variability, following up close to the cloud development throughout the day. Deviations between MARS and MDSLF are mainly related to DSLF magnitude differences, in which slightly higher values are found in the latter, reaching a maximum of about 390 W.m^{-2} in the southern region of the peninsula, where a cluster of clouds starts to form. In comparison, ERA5 shows a deviation of the fluxes more towards the southwestern most region (absent of clouds).

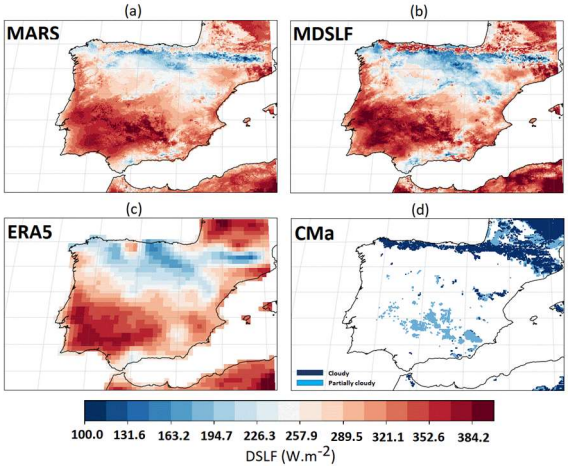

Figure 2. Snapshot of a 24-hour time-lapse video of the DSLF distribution over the Iberian Peninsula on July 15th 2021 at 18 UTC estimated with (a) MARS; (b) MDSLF; and (c) ERA5. Cloud cover information from the MSG cloud mask (CMa) MSG at 15-minute instantaneous values is also shown (d).

4. Discussion

The two validation analyses against BSRN and FLUXNET2015 ground stations show very similar results, in terms of the MARS model performance, to the results presented in (Lopes et al., 2022). This allows us to verify the consistency of the proposed model and adopted methodology since estimates of DSLF are now computed for the entire MSG disk using the ERA5 data and instantaneous cloud information from the MSG as inputs within the previous calibrated MARS model.

The MARS model's highest performance is found when compared with BSRN stations. This behaviour is expected since data from these stations were used to calibrate the model. Consequently, when performing an additional validation against an independent network of stations (FLUXNET2015), a general increase of the error occurs, demonstrating, however, that the MARS model continues to estimate DSLF better than MDSLF and ERA5 under such conditions. Despite the overall good results from MARS, particularly when higher samples are present, the model shows a degree of uncertainty in estimating extreme values of DSLF when compared with other models, especially within the lowest range. This is related to the adopted training procedure, namely to the input data selection method. Efforts to correct this aspect are currently underway, focusing on a more homogeneous selection of samples considering, at the same time, different ranges of observed DSLF and forecasted variables (t2m, d2m, tcwv). Such implementation is foreseen to be used in future works. Hourly estimates of DSLF produced by the MARS model show very small differences when directly compared with the MDSLF model, as shown for the Iberian Peninsula, being mainly related to the different core algorithms used within each model, since these use the same operational inputs compute DSLF over the entire MSG disk.

5. Conclusions

The present study is part of a sequential process that aims to establish a machine learning algorithm to serve an LSA-SAF operational product. To this end, a different method to estimate hourly DSLF under all-sky conditions within the MSG disk was presented and validated using ECMWF-ERA5 operational forecasts and instantaneous cloud information in the previously calibrated model to produce 30-minute outputs, as an alternative to the current LSA-SAF operational product (MDSLF). The new model takes advantage of its recursive partitioning and spline fitting, to combine reanalysis and observational data (in-situ and remote-sensed), enabling a more flexible approach to estimating DSLF. The multivariate adaptive regression splines (MARS) model was shown to provide better estimates within the MSG disk (i.e. longitude/latitude +/- 75° E/N), with lower errors and higher correlations against in situ observations, in comparison to the MDSLF and ERA5 outputs. These results were

verified using two separate networks of ground stations (BSRN and FLUXNET2015) within the MSG disk, which allowed us to demonstrate the added value of using BSRN for calibration and the consistency of the proposed methodology using an independent network of stations. The results clearly show significant improvements when compared with the LSA-SAF product, showing a comparable performance and consistent spatiotemporal variability, demonstrating the potential that the MARS model has for operational purposes.

6. References

Berk, A., Anderson, G. P., Acharya, P. K., Chetwynd, J. H., Bernstein, L. S., Shettle, E. P., Matthew, M. W., & Adler-Golden, S. M. (2003). MODTRAN4 Version 3 revision 1 USER ' S MANUAL. In Air Force Res. Lab; Space Vehicles Directorate, Air Force Material Command: Hanscom Air Force Base, MA, USA.

Bilbao, J., & H. de Miguel, A. (2006). Estimation of Daylight Downward Longwave Atmospheric Irradiance under Clear-Sky and All-Sky Conditions. Journal of Applied Meteorology and Climatology, 46, 878 – 889. DOI: https://doi.org/10.1175/JAM2503.1

Cao, Y., Li, M., & Zhang, Y. (2022). Estimating the Clear-Sky Longwave Downward Radiation in the Arctic from FengYun-3D MERSI-2 Data. Remote Sensing, 14(3), 1–13. DOI: https://doi.org/10.3390/rs14030606

Driemel, A., Augustine, J., Behrens, K., Colle, S., Cox, C., Cuevas-Agulló, E., Denn, F. M., Duprat, T., Fukuda, M., Grobe, H., Haeffelin, M., Hodges, G., Hyett, N., Ijima, O., Kallis, A., Knap, W., Kustov, V., Long, C. N., Longenecker, D., … König-Langlo, G. (2018). Baseline Surface Radiation Network (BSRN): Structure and data description (1992-2017). Earth System Science Data, 10(3), 1491–1501. DOI: https://doi.org/10.5194/essd-10-1491-2018

Friedman, J. H. (1991). Multivariate Adaptive Regression Splines. Annals of Statistics, 19(1), 1 – 67. DOI: https://doi.org/10.1214/aos/1176347963

Friedman, J. H., & Roosen, C. B. (1995). An introduction to multivariate adaptive regression splines. Statistical Methods in Medical Research, 4(3), 197–217. DOI: https://doi.org/10.1177/096228029500400303

Hersbach, H., Bell, B., Berrisford, P., Hirahara, S., Horányi, A., Muñoz-Sabater, J., Nicolas, J., Peubey, C., Radu, R., Schepers, D., Simmons, A., Soci, C., Abdalla, S., Abellan, X., Balsamo, G., Bechtold, P., Biavati, G., Bidlot, J., Bonavita, M., … Thépaut, J. N. (2020). The ERA5 global reanalysis. Quarterly Journal of the Royal Meteorological Society, 146(730), 1999–2049. DOI: https://doi.org/10.1002/qj.3803

Houghton, J. T., Ding, Y., Griggs, D. J., Noguer, M., Der, L. P. J. van, Dai, X., Maskell, K., & Johnson, C. A. (2001). Contribution of Working Group I to the Third Assessment Report of the Intergovernmental Panel on Climate Change. Cambridge University Press, 94. https://www.ipcc.ch/site/assets/uploads/2018/07/WG1_TAR_FM.pdf

Josey, S., Pascal, R. W., & Yelland, M. J. (2003). A new formula for determining the atmospheric longwave flux at the ocean surface at mid-high latitudes A New Formula For Determining the Atmospheric Longwave Flux at the Ocean Surface at Mid-High Latitudes. Journal of Geophysical Research Atmospheres. DOI: https://doi.org/10.1029/2002JC001418

Jung, M., Koirala, S., Weber, U., Ichii, K., Gans, F., Camps-Valls, G., Papale, D., Schwalm, C., Tramontana, G., & Reichstein, M. (2019). The FLUXCOM ensemble of global land-atmosphere energy fluxes. Scientific Data, 6(1), 74. DOI: https://doi.org/10.1038/s41597-019-0076-8

Lopes, F. M., Dutra, E., & Trigo, I. (2022). Integrating Reanalysis and Satellite Cloud Information to Estimate Surface Downward Long-Wave Radiation. Remote

 DOI: https://doi.org/10.60620/swxy-ct70

Sensing, 14(1704). DOI: https://doi.org/10.3390/rs14071704

Marty, C., Philipona, R., Frøhlich, C., & Ohmura, A. (2002). Altitude dependence of surface radiation fluxes and cloud forcing in the Alps: Results from the Alpine surface radiation budget network. Theoretical and Applied Climatology, 72(3–4), 137–155. DOI: https://doi.org/10.1007/s007040200019

Pastorello, G., Trotta, C., Canfora, E., Chu, H., Christianson, D., Cheah, Y. W., Poindexter, C., Chen, J., Elbashandy, A., Humphrey, M., Isaac, P., Polidori, D., Ribeca, A., van Ingen, C., Zhang, L., Amiro, B., Ammann, C., Arain, M. A., Ardö, J., … Papale, D. (2020). The FLUXNET2015 dataset and the ONEFlux processing pipeline for eddy covariance data. Scientific Data, 7(1), 225. DOI: https://doi.org/10.1038/s41597-020-0534-3

Trigo, I. F., Barroso, C., Viterbo, P., Freitas, S. C., & Monteiro, I. T. (2010). Estimation of downward long-wave radiation at the surface combining remotely sensed data and NWP data. Journal of Geophysical Research Atmospheres, 115(24), 1–14. DOI: https://doi.org/10.1029/2010JD013888

Trigo, I. F., Monteiro, I., & Freitas, S. C. (2011). The EUMETSAT Satellite Application Facility on Land Surface Analysis (LSA SAF). Validation Report. Down-welling Longwave Flux (MDSLF) (Issue I). https://nextcloud.lsasvcs.ipma.pt/s/JXNeANe6bgXE8Px

Wang, T., Shi, J., Ma, Y., Letu, H., & Li, X. (2020). All-sky longwave downward radiation from satellite measurements: General parameterizations based on LST, column water vapor and cloud top temperature. ISPRS Journal of Photogrammetry and Remote Sensing, 161(April 2019), 52–60. DOI: https://doi.org/10.1016/j.isprsjprs.2020.01.011

Wang, T., Yan, G., & Chen, L. (2012). Consistent retrieval methods to estimate land surface shortwave and longwave radiative flux components under clear-sky conditions. Remote Sensing of Environment, 124, 61–71. DOI: https://doi.org/10.1016/j.rse.2012.04.026

Wild, M., Folini, D., Scha, C., Loeb, N., Dutton, E. G., & Ko, G. (2013). The global energy balance from a surface perspective. 3107–3134. DOI: https://doi.org/10.1007/s00382-012-1569-8

Zhou, Q., Flores, A., Glenn, N. F., Walters, R., & Han, B. (2017). A machine learning approach to estimation of downward solar radiation from satellite-derived data products: An application over a semi-arid ecosystem in the U.S. PLoS ONE, 12(8), 1–19. DOI: https://doi.org/10.1371/journal.pone.0180239

Zhou, W., Shi, J., Wang, T., Peng, B., Zhao, R., & Yu, Y. (2019). Clear-Sky Longwave Downward Radiation Estimation by Integrating MODIS Data and Ground-Based Measurements. IEEE Journal of Selected Topics in Applied Earth Observations and Remote Sensing, 12(2), 450 – 459. DOI: https://doi.org/10.1109/JSTARS.2018.2878229

Zhou, W., Wang, T., Shi, J., Peng, B., Zhao, R., & Yu, Y. (2018). Remotely Sensed Clear-Sky Surface Longwave Downward Radiation by Using Multivariate Adaptive Regression Splines Method. State Key Laboratory of Remote Sensing Science, Jointly Sponsored by Institute of Remote Sensing and Digital Earth of Chinese Academy o. IEEE, 5575–5578.

Appendix A

Table A.1. BSRN validation between model estimates (MARS, MDSLF, ERA5) and observations from 22 ground stations between 2004 – 2019 under different conditions of observed DSLF: All (all hourly values); upper level (UL) for values above 400 W.m^{-2} middle level (ML) for values between 200 – 400 W.m^{-2} lower level (LL) for values below 200 W.m^{-2} and the median distribution of each error metric computed independently at each station. Standard error metrics are shown with units in W.m^{-2}, while correlations are between 0 and 1.

	MARS				MDSLF				ERA5			
Condition	μ	σ	RMSE	R	μ	σ	RMSE	R	μ	σ	RMSE	R
All	1.40	14.35	19.60	0.94	-0.62	17.34	23.79	0.93	-5.18	15.39	22.07	0.93
UL	-9.26	12.52	19.11	0.58	-3.84	13.80	18.47	0.55	-12.08	14.30	22.54	0.51
ML	1.12	13.86	19.00	0.91	-0.32	17.62	24.16	0.89	-5.25	15.36	22.05	0.90
LL	23.75	14.88	31.05	0.65	-3.21	15.00	21.81	0.70	6.42	15.51	21.72	0.69
MED	0.80	12.81	17.66	0.90	2.11	14.41	20.48	0.88	-5.46	13.86	20.51	0.88

Table A.2. FLUXNET2015 validation between model estimates (MARS, MDSLF, ERA5) and observations from 53 ground stations between 2004 – 2014 under different conditions of observed DSLF: All (all hourly values); upper level (UL) for values above 400 W.m^{-2} middle level (ML) for values between 200-400 W.m^{-2} lower level (LL) for values below 200 W.m^{-2} and the median distribution of each error metric computed independently at each station. Standard error metrics are shown with units in W.m^{-2}, while correlations are between 0 and 1.

	MARS				MDSLF				ERA5			
Condition	μ	σ	RMSE	R	μ	σ	RMSE	R	μ	σ	RMSE	R
All	0.34	15.58	24.40	0.87	-1.25	21.02	27.51	0.86	-8.69	18.93	26.70	0.87
UL	-16.82	15.81	26.66	0.40	-9.92	16.44	23.61	0.41	-20.90	17.74	30.77	0.37
ML	0.37	18.42	24.18	0.84	-1.25	21.19	27.68	0.82	-8.89	18.75	26.53	0.84
LL	20.24	16.65	30.64	0.38	9.42	16.32	24.40	0.47	15.55	18.21	28.90	0.38
MED	0.26	15.56	22.67	0.87	-2.03	19.01	26.26	0.85	-8.08	16.29	23.82	0.86

 DOI: https://doi.org/10.60620/swxy-ct70

Evaluation of Eolic Potential in Portugal

Claudia Victoria Campos Rubio [1], Lourdes Bugalho [2], Mário Gonzalez Pereira [1,3]

[1] *Centro de Investigação e Tecnologias Agroambientais e Biológicas (CITAB), Inov4Agro, Universidade de Trás-os-Montes e Alto Douro (UTAD), Quinta de Prados, 5000–801 Vila Real, Portugal, claudia.campos.rubio@gmail.com, gpereira@utad.pt*
[2] *Instituto Português do Mar e da Atmosfera, I. P., Rua C do Aeroporto, 1749–077 Lisboa, Portugal, lourdes.bugalho@ipma.pt*
[3] *Instituto Dom Luiz (IDL), FCUL, Campo Grande Edifício C1, Piso 1 1749–016 Lisboa, Portugal*

SUMMARY

The growth of the world population and technological and socioeconomic development motivates a growing energy demand. Fossil fuels continue to provide most of the energy consumed globally for different uses. This study aims to evaluate the onshore and offshore wind potential of the Portuguese territory, intending to map this energy resource. The wind potential will be assessed for a spatial domain that encompasses the mainland of Portugal and part of the adjacent Atlantic Ocean, to assess both onshore and offshore wind potential. The evaluation of the wind potential will be based on wind speed from different sources, namely ERA5 and identifying regions with the highest potential. The methodology includes a climatological analysis leading to a Wind Atlas and the identification of the regions with the highest potential and a comparative analysis of the results obtained with analysis and reanalysis data. This analysis was based on hourly and monthly wind values at different heights. The results of this analysis include the climatological characterization of the wind field and its power, including their spatiotemporal distribution at different scales.

Keywords: Eolic potential; Windspeed distribution; Onshore and offshore wind; Analysis and reanalysis; Portugal.

1. Introduction

The transition to a low-carbon society has promoted a growing interest in diversifying the energy mix (Couto & Estanqueiro, 2021). Renewable energies (RE) have been gaining strength in the market and attracting investments. The perceived benefit and development of the living creatures significantly mediates the connection between RE and investors willing to invest, as RE has more sustainable development goals with the use of and access to affordable and reliable green energy (Ali et al., 2023). In Europe, the main contributions to Europe's electricity supply are expected to come from solar and wind energy, which are already economically competitive, but have intermittent behaviour associated with their dependency on weather conditions (Couto et al., 2014; Couto & Estanqueiro, 2021). Wind energy was one of the country's first renewable energies to be explored and implemented (Lopes et al., 2018; Silva et al., 2007). Previous studies for the installation of wind farms are based on only one or a few years of data, measured in situ or simulated by regional atmospheric models or data-driven methods (Carvalho et al., 2014; Catalão et al., 2011; Cordeiro et al., 2000; Pousinho et al., 2010; Godinho & Castro, 2021). Most wind farms in the national territory are installed onshore, in mountainous regions (Cordeiro et al., 2000), but the interest in exploring this offshore resource has been increasing (Salvação et al., 2014). In this context, this study seeks to assess the wind potential in mainland Portugal and its adjacent Atlantic coast (**Figure 1**), with a focus on both onshore and offshore wind resources. This study also compares the assessed wind potential with data collected from weather stations and

gridded reanalysis datasets. The station data has the advantage of having been observed in situ. However, the reanalysis has several other advantages, including being long, flawless, consistent with the laws of physics of the atmosphere, and covering the entire territory with high spatial resolution, which better allows for identifying hotspots and patterns of space-time variability.

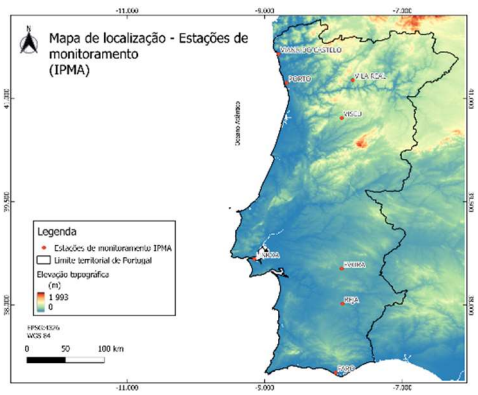

Figure 1 Location Map – Monitoring Stations (IPMA).

2. Data and methods

This study is based on two wind speed (WS) databases. The first is WS at 10 and 100 meters from the ERA5 (hereafter, ERA5 data) database, which provides gridded data with a spatial resolution of 0.25°×0.25° (31 km) (Hersbach et al., 2018. We download data for a 30-year climatological study period, defined from 1991 to 2020, for two reasons: (i) the 30 years is considered an adequate period by the World Meteorological Organization (WMO, 2017); and, (ii) be a period of the past but very recent, which could help to describe the wind regime in current climate conditions. For comparison, the WS measured at eight IPMA weather stations (hereafter, IPMA data), was also used (**Figure 1**). IPMA's eight meteorological stations are well distributed across the territory of mainland Portugal and four are located inland while the other four are on the coast (**Figure 1**).

The WS data processing included the assessment of the space-time distribution of the hourly and monthly wind at 10 m (WS10m) and 100 m (WS100m). This assessment is based on the computation and inspection of monthly arithmetic averages of hourly and monthly WS10m e WS100m which allowed us to assess the intra-annual variability of each of the wind speed fields. The WS10m and WS100m can be used to evaluate the specific kinetic energy (k_e, Eq. 1) and the wind power density (WPD, Eq. 2), at those heights (Claro et al., 2023).

$$k_e = \frac{K_e}{m} = \frac{1}{2}WS^2 \quad (1)$$

$$WPD = \frac{1}{2}\rho WS^3 \quad (2)$$

The dependence of k_e and WPD on the WS justifies focusing only on the results obtained for the WS, as the patterns of the k_e and WPD will be similar but with marked differences. The comparative analysis of the ERA5 WS was performed between the WS time series observed at each IPMA weather station and the WS time series at the ERA5 network points closest to the weather stations. The comparison was based on the graphical analysis of the WS series (ERA5 and IPMA) in each location and on a vast set of statistics: mean, standard deviation (STD), correlation coefficient (CORR), mean absolute error (MAE) and root mean square error (RMSE).

3. Results

The results obtained in the analysis of the space-time variability of the hourly WS reveal two main characteristics: high variability throughout the day of the wind potential and patterns characterized by higher values of wind speed over the sea (**Figure 2** and **Figure 3**).

Over the mainland, WS10m is essentially constant over the coast. Values increase from 8 am to 3 pm (coast inland, and from south to north) and then decrease in the opposite direction (**Figure 2**).

Over the national territory, in the southern region, the WS100m increases from 12h to 20h and decreases until 11h. However, in the northern region, WS100m is standardized from 21:00 to 7:00, decreasing until 11:00 and then increasing afterwards (**Figure 3**). In general, WS100m values are higher than WS10m, which can be explained by the effect of surface roughness.

DOI: https://doi.org/10.60620/m7ba-cq76

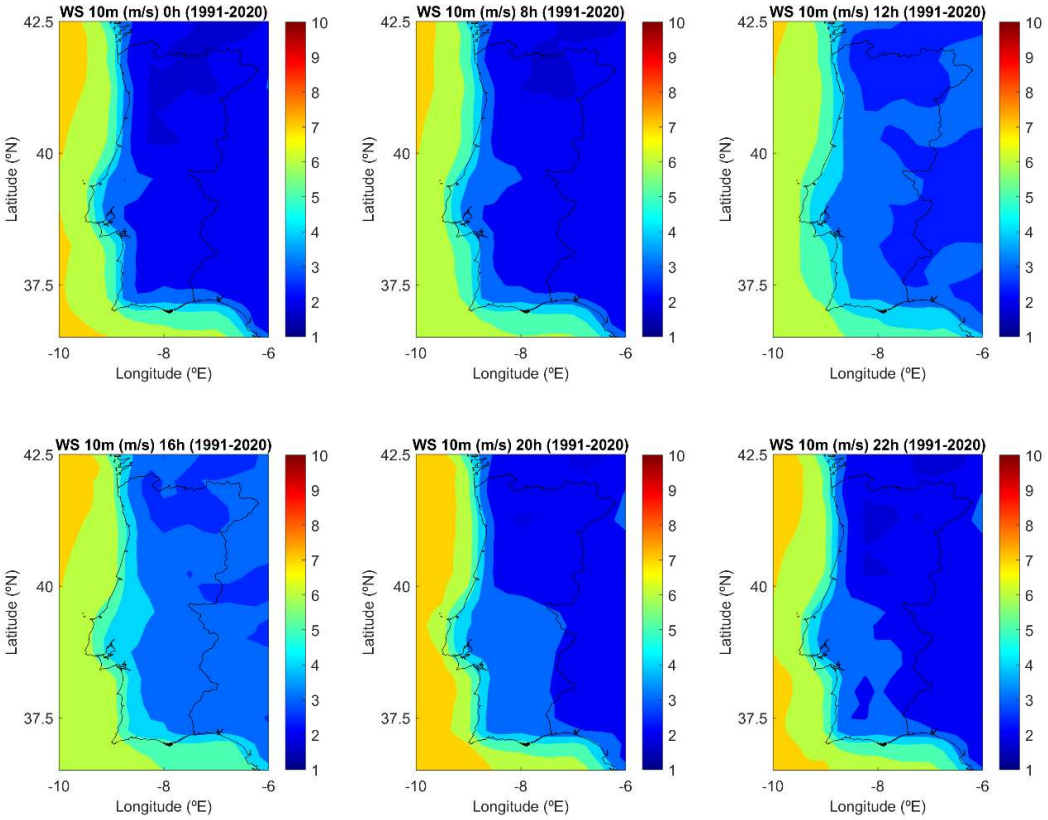

Figure 2. Hourly average (00h, 8h, 12h, 16h, 20h, 22h) of wind speed at 10 m (WS10m, left panels).

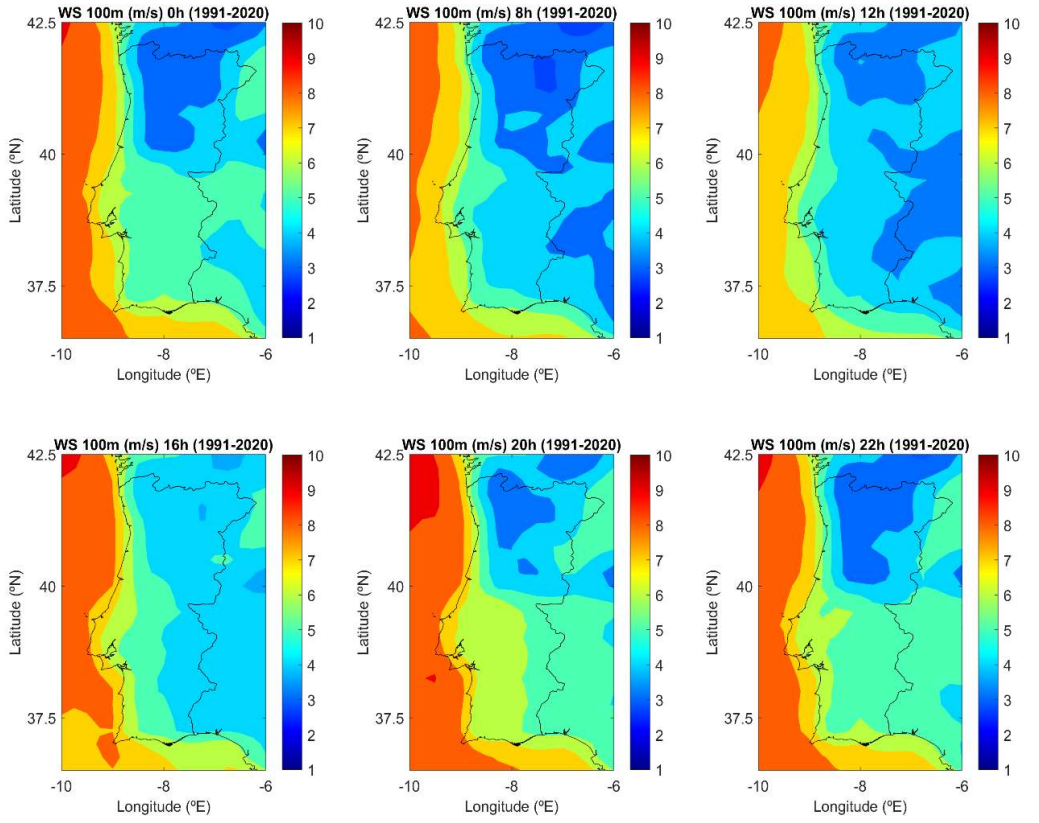

Figure 3. As **Figure** 2, but for the wind speed at 100 m.

In the case of the monthly average wind (**Figure 4**), the highest values continue to be observed over the sea, essentially constant on the coast, with higher values during the coldest semester (November to April) and a minimum value in September. The variability of the monthly WS10m is lower than that of the hourly WS10m. In general, WS10m is approximately constant throughout the year in the northern region and varies slightly in the southern region, with higher values in the coldest semester.

The spatial variability patterns of the WS100m are similar to those of the WS10m in the months of the coldest semester. Throughout the year, monthly WS100m is higher in the southern region than in the northern region. In the months of the hottest semester (May to October), the difference between WS100m in the north and south regions is smaller.

The values of the statistics computed for hourly and monthly ERA5 and IPMA WS are presented in **Table I** and **Table II**. Results of the comparative analysis of IPMA and ERA5 data reveal that for the hourly mean wind: (i) the ERA wind is considerably higher in the stations at the coast and Vila Real; the opposite happens in the other inland stations; values of the average, MAE and RMSE supports this result; (ii) the ERA wind variability (STD) is also higher at coastal stations, but lower at inland stations; (iii) the synchronous temporal variability (correlation coefficient, CORR) is smaller in coastal stations than in inland stations.

For the coastal stations, the CORR in Porto and Lisbon is similar (75%), lower in Faro (67%) and Viana do Castelo (53%). For inland stations, the CORR is similar and relatively high (84%) in the South (Évora and Beja) and also similar, but slightly lower (70%) in the North stations (Vila Real and Viseu). For the average daily wind, the patterns of variability are similar and, as expected, the variability (STD) is smaller, the errors are lower and the correlations are higher.

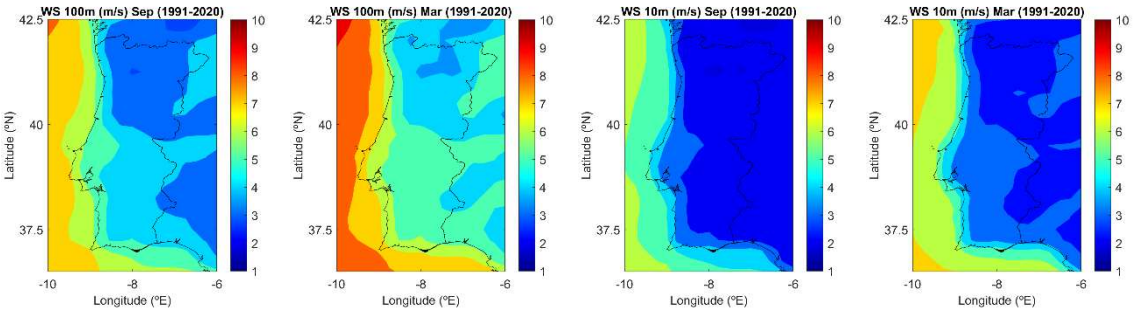

Figure 4. The monthly average for March and September of wind speed at 10 m (WS10m, two panels on the left) and 100 m (WS100m, two panels on the right).

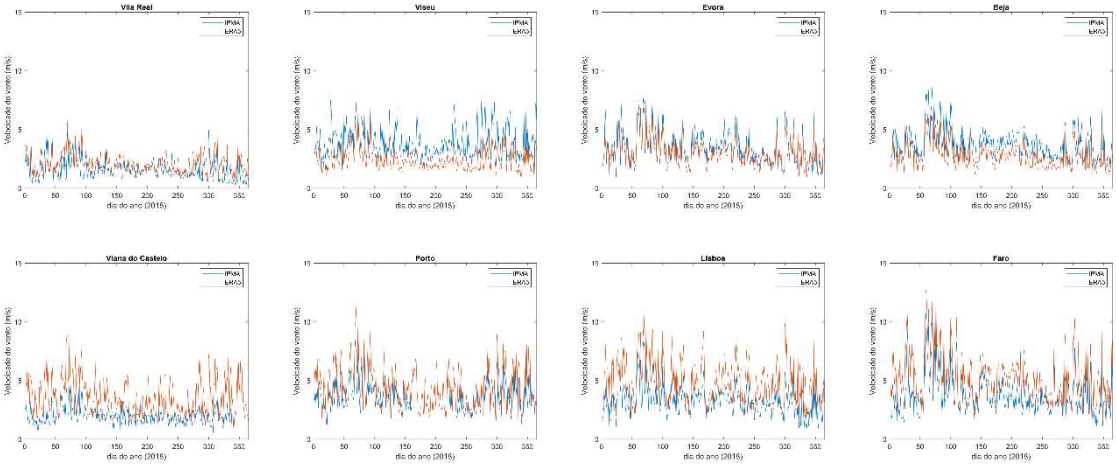

Figure 5. Wind speed at 10 m (WS10m) measured in IPMA weather stations and the ERA5 network points closest to the weather stations, for the year 2018.

DOI: https://doi.org/10.60620/m7ba-cq76

Table I. Mean, standard deviation (STD), correlation coefficient (CORR), mean absolute error (MAE) and root mean square error (RMSE) computed for the hourly wind speed at 10 m (WS10m) of ERA5 and IPMA data.

Statistic	Viana do Castelo	Porto	Lisboa	Faro	Vila Real	Viseu	Évora	Beja
Altitude	48	70	104	8	561	644	245	246
Mean IPMA	2.01	3.65	3.33	3.82	1.61	3.88	3.35	3.71
Mean ERA5	3.55	4.38	4.85	5.18	2.09	2.48	3.09	2.82
STD IPMA	1.20	2.00	1.78	2.45	1.33	1.93	1.99	1.77
STD ERA5	1.97	2.27	2.19	2.56	1.16	1.34	1.45	1.39
CORR	0.53	0.76	0.75	0.67	0.68	0.70	0.85	0.84
MAE	1.77	1.39	1.75	1.96	0.91	1.54	0.86	1.05
RMSE	2.25	1.74	2.12	2.46	1.12	1.96	1.12	1.31

Table II. As in **Table I**, but for daily wind speed.

Statistic	Viana do Castelo	Porto	Lisboa	Faro	Vila Real	Viseu	Évora	Beja
Altitude	48	70	104	8	561	644	245	246
Mean IPMA	2.01	3.65	3.33	3.82	1.61	3.88	3.35	3.71
Mean ERA5	3.55	4.38	4.85	5.18	2.09	2.48	3.09	2.82
STD IPMA	0.66	1.23	1.23	1.68	0.85	1.28	1.43	1.30
STD ERA5	1.57	1.78	1.83	2.07	0.81	0.93	1.13	1.07
CORR	0.59	0.86	0.84	0.83	0.74	0.75	0.92	0.91
MAE	1.60	1.04	1.58	1.47	0.61	1.41	0.49	0.90
RMSE	1.99	1.30	1.85	1.78	0.76	1.64	0.63	1.04

4. Conclusions

The study evaluates the space-time variability of the hourly and monthly wind speeds at 10 m and 100 m and, consequently, of the wind potential at those time scales and heights. The study also allowed us to analyse and compare the wind speed from different data sources and onshore and offshore Portugal. From the obtained results, we conclude that the wind potential: (i) is higher over the sea than over the land; (ii) higher at 100 m than at 10 m; (iii) presents high temporal variability throughout the day and tends to be higher in the colder period; (iv) is approximately constant on the coast, but varies inland; (v) presents high spatial variability between the south (lower altitude and more horizontal) and the north (higher altitude and irregular topography); (vi) is higher and with greater variability when calculated with reanalyses (ERA5) than with station data (IPMA), namely near the coast. The comparison of wind speed data from ERA5 and IPMA weather stations revealed (vii) a significant bias in location and dispersion statistics, especially on the coast, but similar and particularly synchronous variability in the interior region. Obtained results can support the decision of future investments in the area and are fundamental for future wind potential evaluation studies.

5. Acknowledgements

This work is supported by Nacional Funds from FCT – Portuguese Foundation for Science and Technology, under the project UIDB/04033/2020. We are grateful to the European Center for Medium-Range Weather Forecasts (ECMWF) for providing the ERA5 and to the *Instituto Português do Mar e da Atmosfera* (IPMA) for providing the wind speed data.

6. References

Ali, R., Hussain, R. I., & Hussain, D. S. (2023). How and when does renewable energy affect investors willing to invest? International Journal of Energy Sector Management, 17(1), 25-40. DOI: https://doi.org/10.1108/IJESM-06-2021-0025

Carvalho, D., Rocha, A., Gómez-Gesteira, M., & Santos, C. S. (2014). WRF wind simulation and wind energy production estimates forced by different reanalyses:

Comparison with observed data for Portugal. Applied Energy, 117, 116-126. DOI: https://doi.org/10.1016/j.apenergy.2013.12.001

Catalão, J. D. S., Pousinho, H. M. I., & Mendes, V. M. F. (2011). Short-term wind power forecasting in Portugal by neural networks and wavelet transform. Renewable energy, 36(4), 1245 - 1251. DOI: https://doi.org/10.1016/j.renene.2010.09.016

Claro, A., Santos, J. A., & Carvalho, D. (2023). Assessing the Future Wind Energy Potential in Portugal Using a CMIP6 Model Ensemble and WRF High-Resolution Simulations. Energies, 16(2), 661. DOI: https://doi.org/10.3390/en16020661

Cordeiro, M., Valente, A., & Leitao, S. (2000). Wind energy potential of the region of tras-os-montes and alto douro, Portugal. Renewable energy, 19(1-2), 185-191.

Couto, A., Costa, P., Rodrigues, L., Lopes, V. V., & Estanqueiro, A. (2014). Impact of weather regimes on the wind power ramp forecast in Portugal. IEEE Transactions on Sustainable Energy, 6(3), 934-942. DOI: https://doi.org/10.3390/10.1109/TSTE.2014.2334062

Couto, A., & Estanqueiro, A. (2021). Assessment of wind and solar PV local complementarity for the hybridization of the wind power plants installed in Portugal. Journal of Cleaner Production, 319, 128728. DOI: https://doi.org/10.1016/j.jclepro.2021.128728

Godinho, M., & Castro, R. (2021). Comparative performance of AI methods for wind power forecast in Portugal. Wind Energy, 24(1), 39 - 53. DOI: https://doi.org/10.1002/we.2556

Hersbach, H., Bell, B., Berrisford, P., Biavati, G., Horányi, A., Muñoz Sabater, J., ... & Thépaut, J. N. (2018). ERA5 hourly data on single levels from 1979 to present. Copernicus climate change service (c3s) climate data store (cds). DOI: https://doi.org/10.24381/cds.adbb2d47

Lopes, F., Sá, J., & Santana, J. (2018). Renewable generation, support policies and the merit order effect: a comprehensive overview and the case of wind power in Portugal. Electricity Markets with Increasing Levels of Renewable Generation: Structure, Operation, Agent-Based Simulation, and Emerging Designs, 227 - 263. DOI: https://doi.org/10.1007/978-3-319-74263-2_9

Pousinho, H. M. I., Mendes, V. M. F., & Catalão, J. P. S. (2010, March). Neuro-fuzzy approach to forecast wind power in Portugal. In International Conference on Renewable Energies and Power Quality (ICREPQ'10) (pp. 1 - 4). DOI: https://doi.org/10.24084/repqj08.244

Salvação, N., Bernardino, M., & Guedes Soares, C. (2014). Assessing the offshore wind energy potential along the coasts of Portugal and Galicia. Developments in Maritime Transportation and Exploitation of Sea Resources. Guedes Soares, C. & Lopez Pena F. (Eds.), Francis & Taylor Group London, UK, 995-1002.

Silva, B., Marques, M., Matos, J., & Rodrigues, Á. (2007). Review of the wind energy potential in Portugal. EWEC.

WMO (2017). WMO guidelines on the calculation of climate normals. WMO Technical Report

 DOI: https://doi.org/10.60620/m7ba-cq76

On the Convenience of the Use of Seasonal and Monthly Climatic Indices in Correlation Studies

M. Carmen Casas-Castillo [1], Raúl Rodríguez-Solà [2], Ricard Kirchner [1], Marta Alarcón [3], Cristina Periago [3], Jordina Belmonte [4,5]

[1] *Physics Department, ESEIAAT, Universitat Politècnica de Catalunya·BarcelonaTech, Colom 1, 08222 Terrassa, Spain, ricard.kirchner@upc.edu, m.carmen.casas@upc.edu*
[2] *Physics Department, ETSEIB, Universitat Politècnica de Catalunya·BarcelonaTech, Diagonal 647, 08028 Barcelona, Spain, raul.rodriguez@upc.edu*
[3] *Physics Department, EEBE, Universitat Politècnica de Catalunya·BarcelonaTech, Eduard Maristany 16, 08019 Barcelona, Spain, marta.alarcon@upc.edu, cristina.periago@upc.edu*
[4] *Department of Animal Biology, Plant Biology and Ecology, Faculty of Bioscience, Universitat Autònoma de Bellaterra, 08193 Bellaterra, Spain, jordina.belmonte@uab.cat*
[5] *Institute of Environmental Sciences and Technology (ICTA–UAB), Universitat Autònoma de Bellaterra, 08193 Bellaterra, Spain*

SUMMARY

Moderately extreme rainfall is usually characterized by a set of standardized indicators, the ETCCDI precipitation indices, useful to compare climate changes on a global scale. These indices quantify information to reflect some aspects of the state of the environment by aggregating data in annual amounts, simplifying the study of complex phenomena. There is extensive use of these annual standardized indices in many fields, such as agriculture, human health and water resources. In particular, a complex correlation between rainfall annual indices and pollination/sporulation parameters can be observed, being useful to describe, in a global way, their joint variations and trends over time. However, a direct cause-effect relationship cannot be established due to the time limitations of the pollen and fungal spore release seasons. To investigate this possible causality, the modification of the standardized annual indices by calculating them only for the autumn or winter before the release seasons, or even for a specific previous month, can be essential.

Keywords: Climatic indices; Precipitation; Airborne pollen; Aerobiology.

1. Introduction

Moderately extreme precipitation is usually characterized by a set of standardized indicators, the Expert Team on Climate Change Detection and Indices (ETCCDI) specific to rainfall (**Table** I), useful for comparing climate changes on a global scale (Klein-Tank et al. 2009, Zhang et al. 2011). These indices are intended to reflect some aspects of the state of the environment at a given time and place, and their standard calculation uses the aggregation of data in annual quantities, simplifying the study of certain complex phenomena.

Table I. ETCCDI rainfall indices

Rainfall ETCCDI	Description
RX1day	Maximum daily rainfall amount (mm)
RX5day	Maximum rainfall amount (mm) over 5 consecutive days
SDII	The ratio of total rainfall to the number of wet days
R10mm	Number of days with rainfall greater than 10 mm
R20mm	Number of days with rainfall greater than 20 mm
CWD	Maximum number of consecutive wet days (≥ 1 mm)
R95p	Total rainfall (mm) exceeding the 95th percentile
PRCPTOT	Total wet-day precipitation (mm)

There is extensive use of these annual indices, for example in the field of agriculture, human health and well-being, water resources, etc.
In particular, a complex correlation can be observed between annual rainfall indices and pollination/sporulation parameters (**Table II**), being useful to describe the possible joint variations and trends of both meteorological and pollen parameters over time globally (Ariano et al. 2010, Frei and Gassner 2008, Rojo et al. 2015).

Table II. Pollination/sporulation parameters

Pollen/spore variables	Description
APIn/ASIn	Annual Pollen/Spore Integral: Sum of the mean daily pollen and spore concentrations along the year (Pollen*day/m^3, Spore*day/m^3)
MPS/MSS	Main Pollen/Spore Season: the period comprised between the dates for which 2.5% and 97.5% of the APIn/ASIn is reached
SPIn/SSIn	Seasonal Pollen/Spore Integral: Sum of the mean daily pollen and spore concentrations during the MPS/MSS or another period defined in the MPS/MSS (Pollen*day/m^3, Spore*day/m^3)
Days P/S	Number of days with pollen/spores
Max	Maximum daily concentration (Pollen/m^3, Spore/m^3)
Peak	Date of the maximum daily concentration
Start	Date of Start of the MPS/MSS
End	Date of End of the MPS/MSS
Length	Number of days of the MPS/MSS

However, a direct cause-effect relationship cannot be established due, among other factors, to the temporary limitation of the periods of release of pollen and fungal spores. To investigate the possible causal relationship between rainfall and pollination/sporulation, it may be essential to modify the standardized annual indices by calculating them for the fall or winter season preceding the pollination/sporulation periods (as it is shown in **Figure 1**), or even for a particular previous month. When annual rainfall parameters are considered, a notable proportion of negative correlations caused by the rainfall wash-out effect are expected; this effect contributes to inhibiting pollen emission and removing airborne pollen as well as, to a lesser extent, fungal spores (Sofiev et al. 2013; Rathnayake et al. 2017; Majeed et al. 2018; Kluska et al. 2020; Rodríguez-Solà et al. 2022), even though rainfall previous to pollination might have a positive influence on pollen production (Makra et al. 2012). The use of seasonal, or even monthly, rainfall indices could be very convenient to refine the correlation analysis to get some results that might be masked in the annual approach.
With this purpose, Rodríguez-Solà et al. 2022 and Kirchner et al. 2023 compared the number of significant correlation values, as well as the ratio between positive and negative ones, between the pollen and spore parameters and the annual rainfall indices on the one hand, and with seasonal rainfall indices on the other. The precipitation data was provided by the Servei Meteorològic de Catalunya, under quality controls requirements (Llabrés-Brustenga et al. 2019). Both studies used the pollen and fungal spore data from twenty-five plant taxa and two fungal taxa (**Table III**), registered by the Catalan Aerobiological Network (Xarxa Aerobiològica de Catalunya, XAC) in six stations located in NE Spain for the period 2001 – 2019. Rodríguez-Solà et al. (2022) refined the analysis by the use of winter rainfall indices, while Kirchner et al. (2023) used autumn rainfall from the previous year.
It is important to understand how the ETCCDI indices are calculated, since the general expression "annual rainfall", usually used as a simplification, could be confusing in some cases. There are indices measured in mm (like PRCPTOT, total precipitation in the year/winter), while others are measured in the number of days (like CWD, the maximum number of consecutive wet days), and there is also the Simple Daily Intensity Index (SDII) which is computed considering both the rainfall amount and the number of rainy days. In the region of study of Rodríguez-Solà et al. 2022 and Kirchner et al. 2023, Catalonia (NE Spain), the months of the year contributing more to rainfall indicators are, in general, September and October for the second part of the year, and March and April for the first part of the year (Casas et al. 2004, Casas-Castillo et al. 2018, Llabres-Brustenga et al. 2020). Some of the contributing days for the calculation of the indices belong to the first part of the year, and others to the second part. For indices measured in mm, there is an approximate proportion of 40% – 45% belonging to the first semester and 55% – 60% for the second.

 DOI: https://doi.org/10.60620/5vpb-dt50

For indices measured in days, there is a similar proportion except for the index CWD, which corresponds to the first semester in 65% of the cases. Regarding the pollen seasons, only nine of the twenty-five studied taxa are limited to the first part of the year, seven of them concerning pollen from trees and two from shrubs; for the rest, pollen and fungal spore seasons cover part of the second part of the year, several of them reaching always September and October. The seasons of the studied fungal spores (*Cladosporium* and *Alternaria*) cover the entire year, with their daily peak always falling within the second part of the year, as it happens also for *Artemisia* and Poaceæ, and *Castanea* and Urticaceæ in 40% – 50% of the cases.

As an example, **Figure 1** shows the mean pollination levels of the Urticaceæ family measured between 2001 and 2019 at the Barcelona aerobiological station.

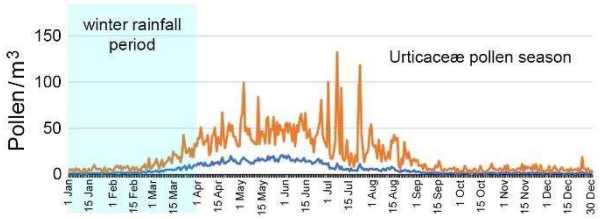

Figure 1. Average (blue line) and maximum (orange line) mean daily concentrations of Urticaceæ pollen in Barcelona, period 2001 – 2019.

Under those limiting circumstances to investigate the relationship between rainfall and pollination/sporulation parameters using annual indices, it seemed reasonable to refine the correlation analysis by considering the definition and calculation of autumn and winter indices. Rodríguez-Solà et al. (2022) performed a Spearman correlation analysis and found that not only did the total number of significant correlations grow, but the ratio between positive and negative correlations increased considerably. Among all the possible correlations between annual rainfall and aerobiological parameters, only between 4.2% and 4.5% were found to be significant at a confidence level of 95% (p-value < 0.05). This low percentage under 5% indicated that these results were within the margin of error, so in terms of the annual ETCCDI, there was no evidence of an influence of moderate to extreme rainfall on pollen and spore parameters. Furthermore, the ratio between the positive correlations, i.e., those that meant that a rainfall index favoured a pollen/spore parameter, and the negative ones (disfavoured) was almost 1: the number of positive and negative correlations was almost the same (**Figure 2**).

Table III. Pollens of different plants

Plants	Trees	Alnus Betula Castanea Cupressaceæ Fagus Fraxinus Olea Pinus Platanus Populus *Quercus* deciduous type *Quercus* evergreen type Quercus Total Ulmus
	Shrubs	Corylus Ericaceæ Pistacia
	Herbs	Amaranthaceæ Artemisia Mercurialis Plantago Poaceæ Polygonaceæ Urticaceæ
	Total Pollen	
Fungi		Alternaria Cladosporium

Despite these undefined results, the distinction between rainfall of the previous winter and annual rainfall showed some ability to discriminate different outcomes in most individual cases (Rodríguez-Solà et al. 2022). The total percentage of significant correlations slightly increased to 5.6% when only winter rainfall indices were considered, a value that could be considered still low due to the margin of error. However, this percentage is higher for some of the categories when considering them individually. For instance, regarding the rainfall ETCCDI, four of them obtained percentages of significant winter correlations above 5%: R10mm, 7.0%, R20mm, 6.6%, SDII, 6.2%, and PRCPTOT, 5.9%. Regarding the pollen and spore parameters, four of them also led to percentages above 5%: Days P/S (8.0%), End (6.9%), Start (6.3%), and Length (5.9%). All the studied locations but one revealed percentages above 5%, being prominently high for Lleida (9.0%). It is

remarkable that all herbs but one also showed similar percentages of significant correlations, being the highest ones: *Artemisia* 11.7%, *Plantago* 9.9%, Urticaceæ 9.9%, Poaceæ 9.1%, Amaranthaceæ 8.6%, and Polygonaceæ 7.8%, while for trees the highest were Cupressaceæ 7.0% and *Quercus* deciduous type 6.3%. Ericaceæ family obtained the highest percentage for all plants: 12.5%.

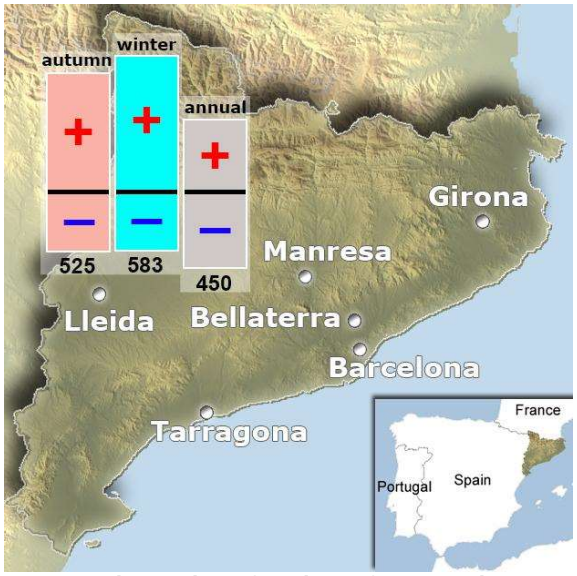

Figure 2. The number of total significant correlations in Catalonia, years 2001 to 2019.

Concerning the ratio of positive and negative significant correlations, Rodríguez-Solà et al. (2022) found a notable increase from the value for annual rainfall of 0.9, close to the unity, to a global 2.3 (see the blue column in **Figure 2**). Specifically, for the rainfall indices, the bigger ratios were found for the winter PRCPTOT, 3.5, and the indices related to rainfall intensity R10mm, and R20mm, with 3.3 and 2.7, respectively. This study concluded that moderate winter rainfall, represented by these three indices, had a greater impact on pollen/fungal spore production than extreme winter rainfall, which is more related to some of the rest of the rainfall indices. The aerobiological variables with the highest ratios were SPIn, 9.7, APIn, 8.7, and Days P/S, 8.5, all three related to the temporal extension of the MPS/MSS. Attending to the type of plant, Rodríguez-Solà et al. (2022) found a notable ratio of positive/negative significant correlations of 4.3 for herbs, more than double that for shrubs and trees (1.7), in line with the fact that herbaceous plants have a much quicker reaction than woody ones to an increased water availability, to prolong pollination or start new ones (Cariñanos et al. 2004; Galán et al. 2016), and a general higher ability to recover after water stress. Nevertheless, the low ratio value for the arboreal plants could be also explained in part by a winter rainfall washing-out effect, since in many cases, such as the Cupressaceæ family, *Fraxinus*, *Platanus*, and *Populus*, the pollination season already begins in winter. **Figure 3** shows how this differential behaviour can be also observed for the most allergenic taxa in Barcelona.

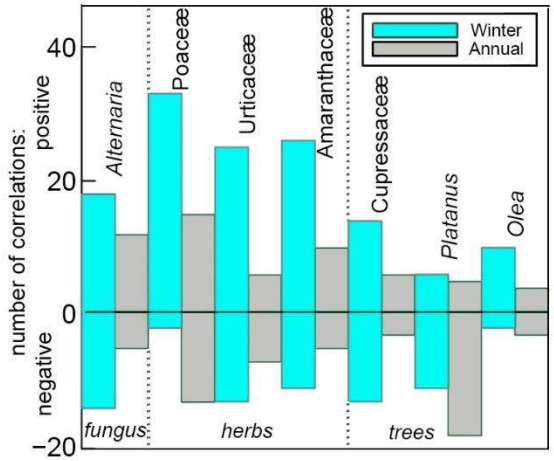

Figure 3. The number of total significant correlations for the most allergenic taxa in Barcelona.

Kirchner et al. (2023) went further back in time to investigate the correlation between aerobiological parameters and rainfall in the autumn ETCCDI of the previous year. As in the case of the previous winter, they found that the number of significant correlations, as well as the ratio between positive and negative ones, were higher for autumn than for annual rainfall, being the percentage of significant correlations of the total lower than for winter, 5.1% (see the pinkish column in **Figure 2**). The main differences, to the winter case, were that persistence and autumn rain events' duration seem to be more influential than rainfall amounts and intensity in the further pollination and sporulation. In contrast, while previous winter rainfall seems to influence more to the temporal extension of the subsequent pollen and spore seasons,

DOI: https://doi.org/10.60620/5vpb-dt50

autumn rainfall seemed to be more correlated to later pollen and spore amounts.

It could be argued that taking only into account whether a correlation is positive or negative, without considering the values of Spearman's coefficient (Eq. 1), could not be enough to estimate the overall differential. Including this information could be crucial in determining if, for instance, the positive correlations greatly outweigh the negative ones or not, apart from the counting numbers.

$$\rho = 1 - \frac{6\sum_{i=1}^{n} d_i^2}{n(n^2-1)} \qquad (1)$$

In Eq. 1, for two samples of n ranked elements, the coefficient ρ is calculated from the differences d_i^2 between the two ranks of each observation. In their study, Rodríguez-Solà et al. (2022) found mean values of the Spearman correlation coefficient around 0, both for the annual ETCCDI and for the aerobiological parameters with the rest of the variables, in an approximate range from -0.2 to $+0.1$, in line with the global ratio of 1 found for annual rainfall.

Instead, for winter rainfall the mean value of the Spearman coefficient grew to $+0.2$ for the ETCCDI, and even higher (between $+0.2$ and $+0.4$) for some of the aerobiological parameters, reinforcing the idea that the seasonal analysis managed to reveal correlations which remained masked in the annual case. These results are shown in **Figure 4**, together with the mean Spearman coefficient calculated for the autumn correlation study. **Figure 4** shows that the indices related to rainfall persistence, RX5day especially and CWD, have a relatively high correlation for the autumn rainfall of the previous year since persistent rainfall is the kind that could be responsible for storing water in the soil which could later affect the growing of plants and the subsequent pollen production (Matyasovszky et al. 2015).

In contrast, the winter correlations are more similar to each other, although in any case, they are all positive and higher than the annual ones. It is worth noting that the negative annual values with the highest coefficient are also those corresponding to persistent rainfall, which could be explained by the fact that prolonged rains are more effective in cleaning the air of pollen by wash-out than if they only occur during pollination.

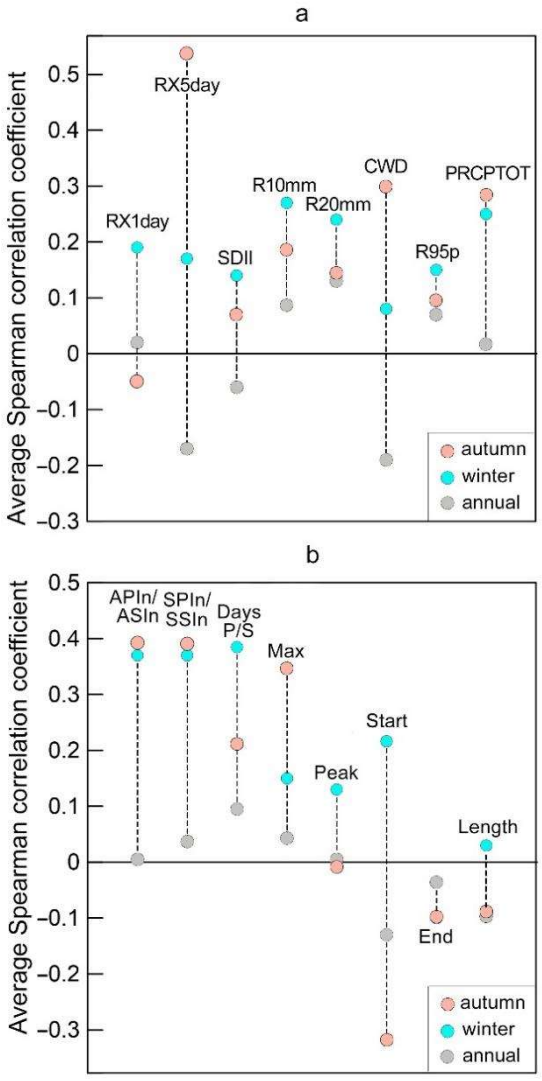

Figure 4. The mean value of the Spearman correlation coefficient for (a) every ETCCDI and (b) every pollen/fungal spore variable in the annual (grey), winter (blue), and autumn (pink) periods.

2. References

Ariano R, Canonica GW, Passalacqua G (2010) Possible role of climate changes in variations in pollen seasons and allergic sensitizations during 27 years. Ann Allergy Asthma Immunol 104:215–222. https://doi.org/10.1016/j.anai.2009.12.005

Cariñanos P, Galán C, Alcázar P, Domínguez E (2004) Airborne pollen records response to climatic conditions in arid areas of the Iberian Peninsula. Environmental and Experimental Botany

52(1): 11 – 22. DOI: https://doi.org/10.1016/j.envexpbot.2003.11.008

Casas, M.C., Codina, B., Redaño, Á., Lorente, J., 2004. A methodology to classify extreme rainfall events in the western Mediterranean area. Theoretical and Applied Climatology 77, 139–150. DOI: https://doi.org/10.1007/s00704-003-0003-x

Casas-Castillo MC, Llabrés-Brustenga A, Rius A, Rodríguez-Solà R, Navarro X (2018) A single scaling parameter as a first approximation to describe the rainfall pattern of a place: application on Catalonia. Acta Geophys 66(3): 415-424. DOI: https://doi.org/10.1007/s11600-018-0122-5

Frei T, Gassner E (2008) Climate change and its impact on birch pollen quantities and the start of the pollen season an example from Switzerland for the period 1969-2006. Int J Biometeorol 52(7):667-674. DOI: https://doi/org/10.1007/s00484-008-0159-2

Galán C, Alcázar P, Oteros J, García-Mozo H, Aira MJ, Belmonte J, Diaz de la Guardia C, Fernández-González D, Gutierrez-Bustillo M, Moreno-Grau S, Pérez-Badía R, Rodríguez-Rajo J, Ruiz-Valenzuela L, Tormo R, Trigo MM, Domínguez-Vilches E (2016) Airborne pollen trends in the Iberian Peninsula. Sci Total Environ 550:53 – 59. DOI: https://doi.org/10.1016/j.scitotenv.2016.01.069

Kirchner R, Casas-Castillo MC, Rodríguez-Solà R, Alarcón M, Periago C, De Linares C, Belmonte J (2023) Comparative Study Between the Effects of Autumn and Winter Rainfall on Aerobiological Variables in the NE of the Iberian Peninsula. In: Mensink, C., Jorba, O. (eds) Air Pollution Modeling and its Application XXVIII. ITM 2021. Springer Proceedings in Complexity. Springer, Cham. DOI: https://doi.org/10.1007/978-3-031-12786-1_36

Klein-Tank AMG, Zwiers FW, Zhang X (2009) Guidelines on Analysis of extremes in a changing climate in support of informed decisions for adaptation. Rep WCDMP-No. 72, WMO-TD no. 1500, World Meteorological Organization, Geneva, 55 pp.

Kluska K, Piotrowicz K, Kasprzyk I (2020) The impact of rainfall on the diurnal patterns of atmospheric pollen concentrations. Agric for Meteorol 291:108042. DOI: https://doi.org/10.1016/j.agrformet.2020.108042

Llabrés-Brustenga A, Rius A, Rodríguez-Solà R, Casas-Castillo MC (2020) Influence of regional and seasonal rainfall patterns on the ratio between fixed and unrestricted measured intervals of rainfall amounts. Theor Appl Climatol 140(1): 389–399. DOI: https://doi.org/10.1007/s00704-020-03091-w

Llabrés-Brustenga A, Rius A, Rodríguez-Solà R, Casas-Castillo MC, Redaño À (2019) Quality control process of the daily rainfall series available in Catalonia from 1855 to the present. Theor Appl Climatol 137(3–4): 2715 – 2729. DOI: https://doi.org/10.1007/s00704-019-02772-5

Majeed HT, Periago C, Alarcón M, Belmonte J (2018) Airborne pollen parameters and their relationship with meteorological variables in NE Iberian Peninsula. Aerobiologia 34:375 – 388. DOI: https://doi.org/10.1007/s10453-018-9520-z

Makra L, Matyasovszky I, Páldy A, Deák AJ (2012) The influence of extreme high and low temperatures and precipitation totals on pollen seasons of Ambrosia, Poaceæ and Populus in Szeged, southern Hungary. Grana 51:215 – 227. DOI: https://doi.org/10.1080/00173134.2012.661764

Matyasovszky I, Makra L, Csépe Z, Sümeghy Z, Deák ÁJ, Pál-Molnár E, Tusnády G (2015) Plants remember past weather: a study for atmospheric pollen concentrations of Ambrosia, Poaceæ and Populus. Theor Appl Climatol 122:181 – 193. DOI: https://doi.org/10.1007/s00704-014-1280-2

Rojo J, Rapp A, Lara B, Fernández-González F, Pérez-Badia R (2015) Effect of land uses and wind direction on the contribution of local sources to airborne pollen. Sci. Total Environ., 538: 672 - 682. DOI: https://doi/org/10.1016/J.SCITOTENV.2015.08.074

Sofiev M, Belmonte J, Gehrig R, Izquierdo R, Smith M, Dahl A, Siljamo P (2013) Airborne pollen transport. In M. Sofiev and K-C. Bergmann (eds.), Allergenic Pollen: A Review of the Production, Release, Distribution and Health Impacts, Springer Science+Business Media Dordrecht. DOI: https://doi.org/10.1007/978-94-007-4881-1_3

Rathnayake CM, Metwali N, Jayarathne T, Kettler J, Huang Y, Thorne PS, O'Shaughnessy PT, Stone EA (2017) Influence of rain on the abundance of bioaerosols in fine and coarse particles. Atmos Chem Phys 17:2459–2475. DOI: https://doi.org/10.5194/acp-17-2459-2017

Rodríguez-Solà R, Casas-Castillo MC, Ho-Zhang JJ, Kirchner R, Alarcón M, Periago C, De Linares C, Belmonte J (2022) A study on correlations between precipitation ETCCDI and airborne pollen/fungal spore parameters in the NE Iberian Peninsula. International Journal of Biometeorology 66: 1173 - 1187. DOI: https://doi.org/10.1007/s00484-022-02267-5

Zhang X, Alexander L, Hegerl GC, Jones P, Tank AK, Peterson TC, Trewin B, Zwiers FW (2011) Indices for monitoring changes in extremes based on daily temperature and precipitation data. Wires Clim Change 2:851 – 870. DOI: https://doi.org/10.1002/wcc.147

Drought Assessment in Southern Africa Using Remote Sensing Vegetation Indices

Fernando Maliti Chivangulula [1], Mário Gonzalez Pereira [1,2], Malik Amraoui [1]

[1] *Centro de Investigação e Tecnologias Agroambientais e Biológicas (CITAB), Inov4Agro, Universidade de Trás-os-Montes e Alto Douro (UTAD), Quinta de Prados, 5000–801 Vila Real, Portugal, fmality@yahoo.com.br, malik@utad.pt, gpereira@utad.pt.*
[2] *Instituto Dom Luiz (IDL), FCUL, Campo Grande Edifício C1, Piso 1 1749–016 Lisboa, Portugal*

SUMMARY

This work focused on the analysis of NDVI, EVI and VCI vegetation indices in Southern Africa over the two-year 2018 – 2019 period. The indices are computed with remote sensing data to provide useful information on drought patterns at regional and even global scales. The NDVI and EVI indices were obtained from the MODIS sensor information. The VCI index was calculated from the NDVI. The analysed data revealed the existence of a prominent annual vegetative cycle in the region during the study period. Between June and November 2019, the values of these indices are quite low, which follows the period of low rainfall. There is an extension of the dry period into the months known as rainy months, revealing the occurrence of a drought whose effects on vegetation lasted from November 2018 to December 2019. Obtained results confirm the usefulness of the three indices to study the drought regime, especially in vast regions, and VCI as the most sensitive index to assess the effects of drought on vegetation.

Keywords: Drought; Southern Africa; Vegetation indices; NDVI; EVI; VCI.

1. Introduction

The occurrence of extreme weather events such as droughts in Southern Africa (SA) has intensified. For example, in the last forty years, most of the extreme droughts in southern Angola occurred in recent years, namely in the years 1992 – 1993, 1998 – 1999, 2012 – 2013, 2015 – 2016 and 2018 – 2019. Additionally, the most recent event of 2018 – 2019 was the most extreme (Mateus & António, 2020). Drought seriously damages regional economies and causes social (e.g., disease, hunger, food insecurity, water shortages) and environmental problems (e.g., ecosystems' stability; ecological diversity) (Edwards et al., 2019; Funk et al., 2016).

More than two decades ago, scientific research began to use remote sensors onboard satellites to measure and map, among countless parameters, the density of green vegetation on the Earth's surface (Weier & Herring, 2000). Vegetation indices based on remote sensing data can provide useful information about drought patterns on regional and global scales, filling information gaps in regions with low density or a lack of in-situ meteorological data (Orimoloye et al., 2021; Shen et al., 2019).

One of the most widely used satellites for monitoring terrestrial phenomena with high spatial and temporal resolutions is the TERRA satellite, launched in 1999 by the National Aeronautics and Space Administration (NASA) (Anderson et al., 2016; Florenzano, 2008). The Moderate Resolution Imaging Spectroradiometer (MODIS) is one of the five sensors on NASA's polar orbit TERRA and AQUA satellites that have an overview of the entire surface of the Earth every 1 or 2 days. Its detectors feature 36 spectral bands between 0.405 and 14,385 μm. MODIS sensor data have spatial resolutions of 250 m, 500 m and 1 km and a 12-bit radiometric resolution. The information collected by sensors onboard satellites allows us to improve our global knowledge and to understand the processes that occur in the Atmosphere,

 DOI: https://doi.org/10.60620/mzh6-cy13

Earth's land and sea surface (Huete et al., 1999).

The World Meteorological Organization recommended 10 vegetation indices that use remote sensing data (WMO & GWP, 2016). The vegetation indices, based on remote sensing data, widely disseminated in the scientific community are the Normalized Difference Vegetation Index (NDVI), Enhanced Vegetation Index (EVI) and Vegetation Condition Index (VCI) (Weier & Herring, 2000). The NDVI measures the greenness and robustness of vegetation and can identify drought-related vegetation water stress (WMO & GWP, 2016). The EVI is more sensitive to the type, architecture and variations of the canopy and plant physiognomy (WMO & GWP, 2016).

The VCI is especially suited to detect and analyse changes in vegetation influenced by extreme weather events and changes in typical seasonal patterns that cannot be easily detected by NDVI and EVI (Moreira et al., 2015). These three indices provide consistent spatial and temporal comparisons of global vegetation conditions (Huete et al., 1999). Therefore, this study aims to assess the ability of those three remote-sensing vegetation indices to evaluate vegetation conditions and drought in SA.

In this work, the NDVI and EVI indices obtained from the MODIS sensor data on board the TERRA satellite will be presented on a monthly scale and at a spatial resolution of 1 km for the study period of 2018 and 2019. The VCI index is calculated using the values of the NDVI. The methodology included the production and analysis of monthly maps of NDVI, EVI and VCI indices, and the sensitivity analysis of these indices based on the variability and concordance of drought characteristics, annual vegetation and climate cycle (WMO & GWP, 2016).

2. Materials and methods

2.1. Study Area

SA is the part of the African continent south of the equator (Abiodun et al., 2019), located between the Atlantic Ocean to the west and the Indian Ocean to the east and includes semi-arid and desert areas, such as the Namib and Kalahari Deserts (**Figure 1**).

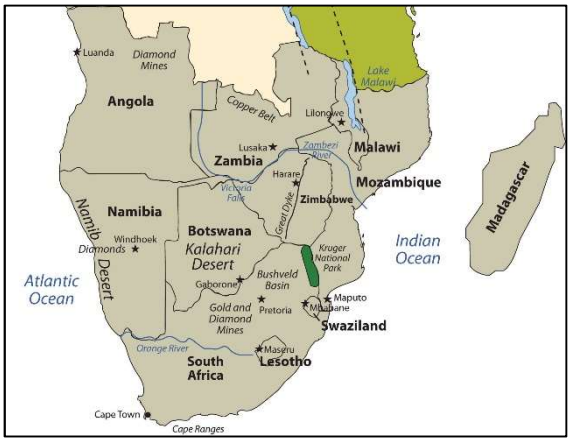

Figure 1. Map of Southern Africa. https://saylordotorg.github.io/

In general, the rural population practices rainfed agriculture for their subsistence (Uele, 2013). According to the Köppen-Geiger classification, the SA has three main climate types: arid or dry, tropical and temperate (Miranda, 2009; Peel et al., 2007). The SA is characterized by high climate variability, namely high space-time rainfall variability with recurrent floods and droughts. The climate of the region is also characterized by two distinct seasons: a rainy and hot season, in the summer, defined from November to March, and a cold and dry season during the winter, from April to October (Abiodun et al., 2019).

Long-term precipitation trends are of lesser intensity, but since 1970 there has been an increase in interannual precipitation variability (Jury, 2013). In the Kalahari desert, the daytime temperature is generally high and can exceed 40°C in some regions while, in contrast, the night temperature is much lower, reaching around 20°C (Abiodun et al., 2019).

2.2. Methodology

The work uses NDVI and EVI values from the NASA database obtained from the MODIS radiometer on board the TERRA satellite. The NDVI and EVI data of the study region were obtained in HDF format from the NASA ground data (MOD13A3 MODIS/Terra Vegetation Indices Monthly L3 Global 1km SIN Grid V006). The data were processed to obtain 2018 and 2019 monthly values of the vegetation conditions for SA with a spatial resolution of 1 km × 1 km. The VCI index is

calculated from the NDVI values for the same region and study period (Didan, 2015).

Vegetation indices based on MODIS data can allow consistent spatial and temporal comparisons of global vegetation conditions that serve to monitor all terrestrial vegetation activity on Earth through radiometric and structural parameters of vegetation.

The NDVI is obtained from the MODIS radiometer data and quantifies the fraction of photosynthetically active radiation absorbed by vegetation, that is, the greater the capacity of a plant to absorb visible sunlight, the more it performs photosynthesis and the more it is productive. On the other hand, the less sunlight the plant absorbs, the less the plant can carry out photosynthesis and the less it is productive (Didan, 2015; Larasati et al., 2020; Weier & Herring, 2000). The NDVI is a plant index that is based on reflectance by plants (**Figure 2**) in the wavelength band in the visible spectrum and near-infrared regions (0.7 – 1.9 μm). In visible light, chlorophyll strongly absorbs Electromagnetic Radiation (EMR) at visible wavelengths (0.5 – 0.7 μm), in near-infrared reflectance increases, vegetation absorbs very little radiation in this band (0.7 – 1.9 μm) of wavelengths (Carlson & Ripley, 1997).

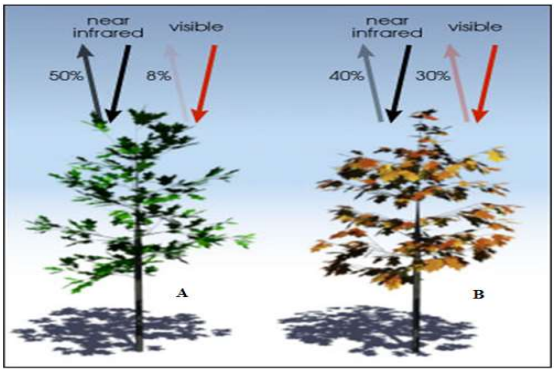

Figure 2. The visible and infrared light is reflected by vegetation. Healthy vegetation (A) absorbs most of the visible light that hits it and reflects a large part of the NIR light. Dry vegetation (B) reflects more visible light and less NIR light (Weier & Herring, 2000).

The NDVI is calculated by normalizing the per-pixel difference between the red and near-infrared (NIR) bands in the image, according to the equation below (Heath et al., 2016; Weier & Herring, 2000):

$$\mathrm{NDVI} = \frac{\mathrm{NIR} - \mathrm{red}}{\mathrm{NIR} + \mathrm{red}} \qquad (1)$$

The NDVI calculation for a given pixel always results in a number ranging from -1 to +1. A value close to -1 indicates that the area has very sparse vegetation to the point of no vegetation. A value close to 1 indicates that the area has dense to very dense vegetation (Weier & Herring, 2000). The NDVI is an index that uses satellite remote sensing data to monitor the health of vegetation including episodes of drought, forest fires, deforestation and desertification, with a high spatial resolution (WMO & GWP, 2016).

The EVI was elaborated to optimize the vegetation signal with improved sensitivity in regions of high biomass and vegetation monitoring through a canopy background signal linkage and a reduction in aerosol influences (Yamamoto et al., 2012). The EVI is characterized by high spatial resolution and allows the identification of plant water stress associated with drought (WMO & GWP, 2016).

EVI data provide robust comparisons of temporal and spatial data of global vegetation conditions to monitor the photosynthetic activity of vegetation allowing the detection of biophysical and phenological changes. The EVI is calculated similarly to the NDVI but corrects for some distortions in the light reflected by the vegetation caused by particles in the air (aerosols) as well as the ground cover below the vegetation.

The advantage of using EVI is that it does not saturate as easily as NDVI when viewing tropical forests and other surfaces with large amounts of chlorophyll (Didan, 2015; Weier & Herring, 2000). EVI is computed with the equation

$$\mathrm{EVI} = \mathrm{G}\frac{(\mathrm{NIR}-\mathrm{red})}{(\mathrm{L}+\mathrm{NIR}+\mathrm{C1\ red}-\mathrm{C2\ blue})} \qquad (2)$$

where L is the adjustment factor for the soil; C1 and C2 are adjustment coefficients for the effect of aerosols from the atmosphere. The values of the coefficients adopted by the EVI algorithm are L=1, C1=6, C2=7.5 and the gain factor G=2.5 (Anderson et al., 2016; Didan, 2015).

EVI can map vegetation states on cloudless images, standardize data according to the target sun-sensor position, ensure data quality and consistency, and describe and

DOI: https://doi.org/10.60620/mzh6-cy13

reconstruct phenological variation data (WMO & GWP, 2016). EVI data is decisive in helping scientists classify different types of vegetation in the world's landscapes, as well as detect changes in vegetation cover over time (Weier & Herring, 2000).

VCI analyses change in vegetation influenced by climate variability and change that cannot be easily detected using the NDVI. The VCI is used to identify drought situations and determine their onset, essentially in regions where localized and little-studied drought events occur (WMO & GWP, 2016). This index can determine the impact of drought on vegetation and can provide information on the onset of drought, its duration, intensity and dynamics (Parente et al., 2019; WMO & GWP, 2016). The VCI may be calculated by the following equation:

$$\mathrm{VCI} = \frac{(\mathrm{NDVI_{med}} - \mathrm{NDVI_{min}})}{(\mathrm{NDVI_{max}} - \mathrm{NDVI_{min}})} \qquad (3)$$

where $\mathrm{NDVI_{med}}$ is the mean value of NDVI for the period under study, $\mathrm{NDVI_{max}}$ and $\mathrm{NDVI_{min}}$ are the maximum and minimum values of NDVI for the same period.

The VCI values range from 0 to 1 and may be separated into different classes (Moreira et al., 2015): class 1, extremely dry (0 to 0.2); class 2, dry (0.2 to 0.4); class 3, normal condition (0.4 to 0.6); class 4, good condition (0.6 to 0.8); and, class 5, optimum condition (0.8 to 1.0). In summary, low VCI values indicate poor vegetation conditions and possible unfavourable climatic conditions while high VCI values describe the opposite situation. When VCI values are less than 0 or greater than 1, they indicate the existence of cloud, snow, ice or desert contaminating the NDVI data (Parente et al., 2019).

We used MATLAB software as a working tool that allows the efficient and fast handling of matrices (images) and the construction of maps and graphs.

Each processed monthly image of the study region consists of 16 grid cells, each grid cell consists of 1200 × 1200 pixels and each pixel has a spatial resolution of 1 km × 1 km. For the whole study period (2018 – 2019), 384 grid cells were used which allowed producing 24 maps per index and made a total of 72 maps for the three indices.

3. Results

The study carried out, presents the monthly values of the three indices, for the study period and the study area. **Figure 3** shows the maps of the NDVI, EVI and VCI for the characteristic months of the rainy and hot season, which include the months of November and December 2018 and January to March 2019. These months are characterized by high values of NDVI and EVI across the whole study area except the southeastern zone associated with the presence of the Kalahari Desert.

Similarly, to NDVI and EVI, and during the months of January, February and March of 2018 and 2019, the VCI index also presents high values throughout the study region and low values in the Kalahari Desert. In the months of November and December of 2018 and 2019, in contrast to the other two indices, the VCI shows low values across the southern zone and extending to the northeastern zone of SA.

Figure 4 presents the values of NDVI, EVI and VCI for the months of the beginning and the end of the dry season (April and October). These maps evidenced that the year 2019 was drier than 2018. In comparison with 2018, the values of the three indices are lower and the size of the region of lower values, i.e., the size of the area affected by the drought was greater. On the other hand, **Figure 4** shows that VCI is more sensitive than the other two indices, whose maps more clearly highlight vegetation response to water stress, and EVI is more sensitive than NDVI.

Figure 5 shows the annual cycle of the state of the vegetation, presenting a maximum value of VCI in the month of April and a minimum value in the month of September.

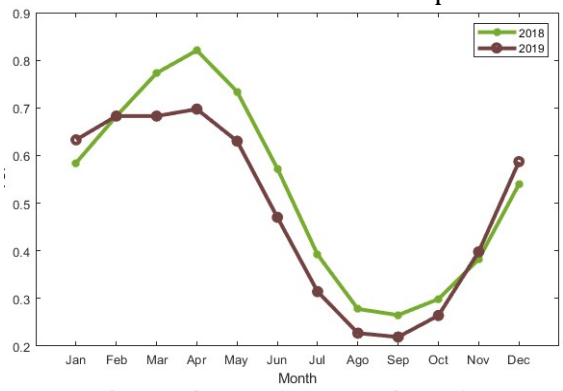

Figure 3. The spatial mean of VCI in Southern Africa in each month of the two-year study period 2018 – 2019.

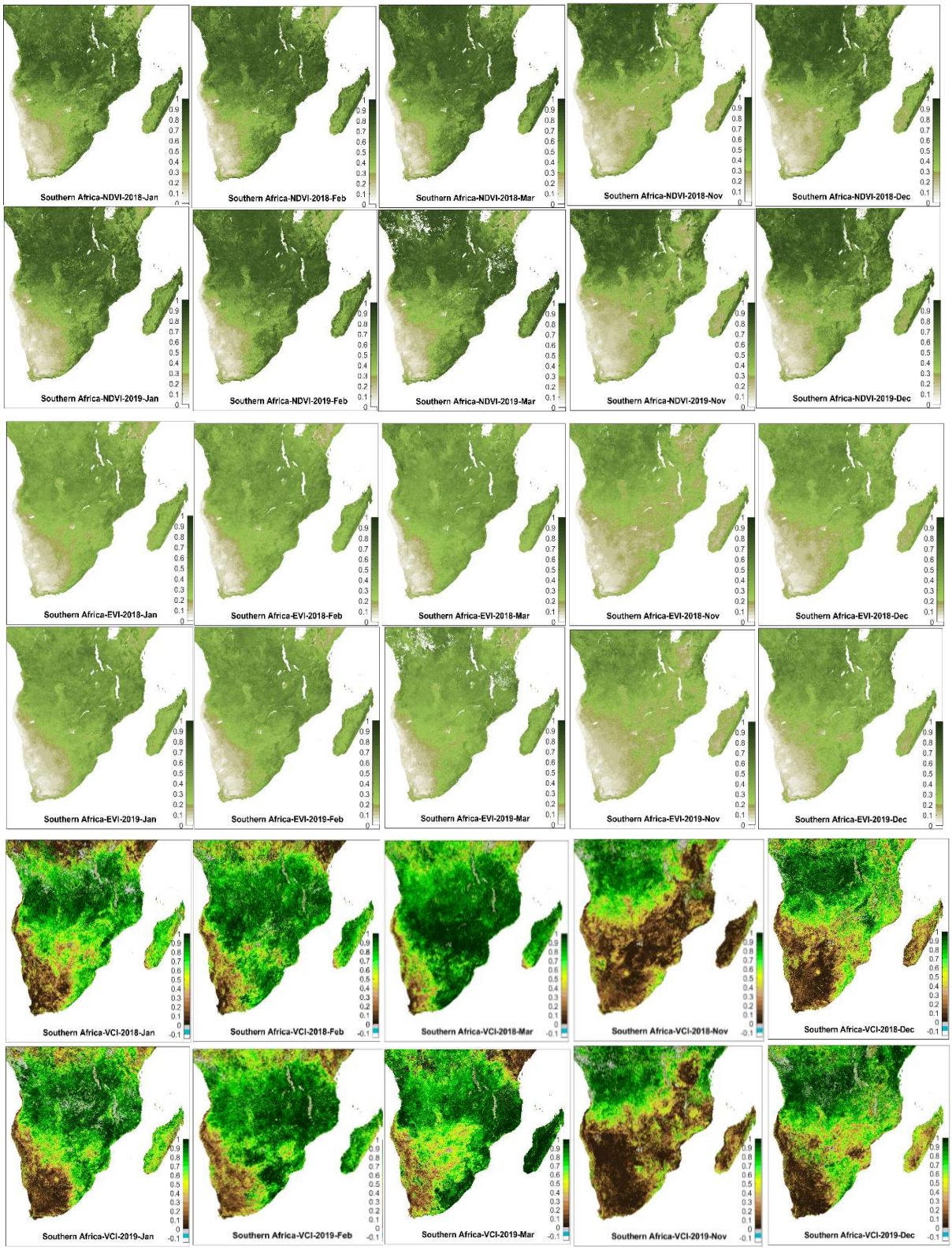

Figure 4. NDVI, EVI and VCI indices for Southern Africa in the wet and warm seasons (November 2018 to March 2019).

In the two years of the study period, the difference in values of VCI between the maximum and minimum is greater than 0.5. The monthly maps of VCI for these two years are presented in Appendix A (**Figure 1A** and **Figure 2A**).

 DOI: https://doi.org/10.60620/mzh6-cy13

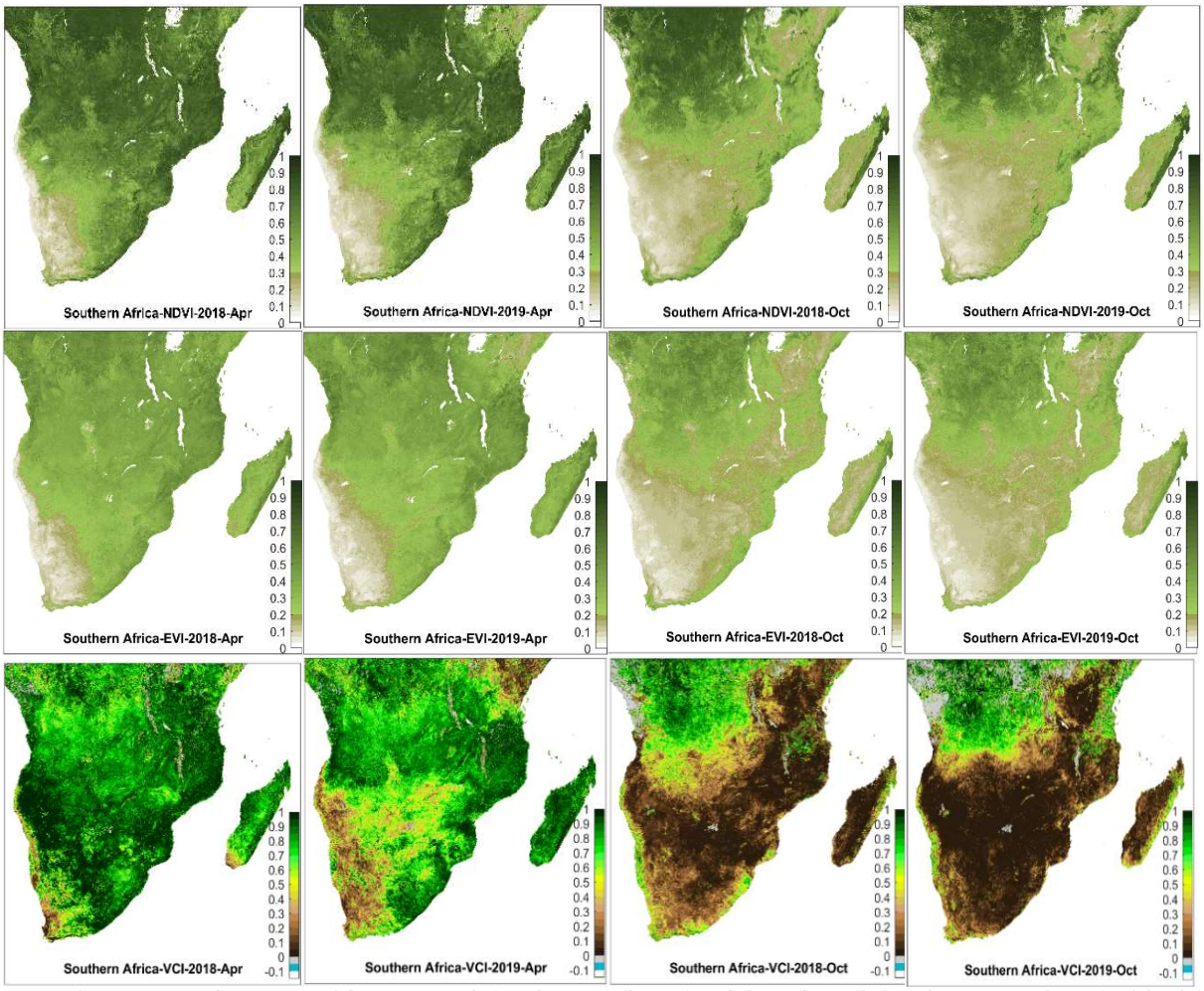

Figure 5. NDVI, EVI and VCI maps of the start month (April 2018 and 2019) and the end month (October 2018 and 2019) of the dry season.

4. Discussion and conclusions

The results obtained for the three indices used in this work to assess drought in SA are in good agreement with previous results found in the literature. The lowest values of NDVI, EVI and VCI occur in periods without rainfall, which leads to the drying of the vegetation and, in turn, reduces the near-infrared reflectance. In periods with high rainfall, values of the three indices are higher, due to the growth and existence of dense vegetation (Carlson & Ripley, 1997; Heath et al., 2016; Weier & Herring, 2000).

Usually, outside the desert region, the rainy and hot season of the study region corresponds to the period defined between the months of November and March. In this period the vegetation is usually quite "green". However, this study reveals dry vegetation in 2018 and 2019, with VCI values close to 0.4 in the month of November, (**Figure 5**). The rainfall in the year 2019 was less than in the year 2018 and this fact was reflected in the lower values of the studied vegetation indices. In fact, during this rainy period, the value of the average VCI was greater than 0.8 in 2018 and less than 0.7 in 2019 (please, see **Figure 5**).

The dry season starts in April and lasts until October. During this period the vegetation suffers from water stress and appears much less "green". In this season, and similarly to what was observed in the wet season, 2019 was a much drier year than 2018, and this fact is evident in the vegetation indices. The average values of the VCI for the dry season are approximately equal to 0.2 in 2019 and 0.3 in 2018. The obtained results are also in good agreement with the literature in the sense that arid and semiarid regions tend to have more droughts (Nooni et al., 2022).

Additionally, in recent decades there has been a significant increase in droughts in southern Africa as a result of the increase in Global Warming Levels (Abiodun et al., 2019).
This study led us to conclude that (i) the analysed vegetation indices (NDVI, EVI and VCI) are suitable for the study of drought, especially in vast, remote regions with low density or lack of weather stations; and, (ii) VCI is the most sensitive index to detect drought, assess and analyse the effects of drought on vegetation.

5. Acknowledgements

This work is supported by Nacional Funds from FCT – Portuguese Foundation for Science and Technology, under the project UIDB/04033/2020. We are grateful to NASA for making available the MODIS/TERRA NDVI and EVI data from the portal EARTHDATA.

6. References

Abiodun, B. J., Makhanya, N., Abatan, A., & Oguntunde, P. G. (2019). Future projection of droughts over major river basins in Southern Africa at specific global warming levels. August. DOI: https://doi.org/10.1007/s00704-018-2693-0

Anderson, L. O., Lotorre, M. L., Shimabukuro;, Y. E., Arai;, E., & Júnior, O. A. de C. (2016). Sensor MODIS : Uma abordagem geral.São José dos Campos. Incluye Información de La SE Función Pública, January 2003, 58.

Carlson, T. N., & Ripley, D. A. (1997). On the relation between NDVI, Fractional Vegetation cover, and leaf area index. Remote Sensing of Environment, 62(3), 241 – 252. DOI: https://doi.org/10.1016/S0034-4257(97)00104-1

Didan, K. (2015). MOD13A3 MODIS/Terra vegetation indices monthly L3 global 1km SIN grid V006 (Data set) NASA EOSDIS Land Process. In Nasa. DOI: https://doi.org/doi.org/10.5067/MODIS/MOD13A3.006

Edwards, B., Gray, M., & Hunter, B. (2019). Os impactos sociais e econômicos da seca. Australian Journal of Social, 54 (1), 22–31. DOI: https://doi.org/https://doi.org/10.1002/ajs4.52

Florenzano, teresa gallotti. (2008). 044.ASR.SRE.16 - Princípios Físicos do Sensoriamento Remoto. In Imagens de Satélite para Estudos Ambientais. https://www.agrolink.com.br/downloads/os satélites e suas aplicações.pdf

Funk, C., Harrison, L., Shukla, S., Hoell, A., Korecha, D., Magadzire, T., Husak, G., & Galu, G. (2016). Assessing the contributions of local and East Pacific warming to the 2015 droughts in Ethiopia and Southern Africa (S. C. Herring, A. Hoell, M. P. Hoerling, J. P. Kossin, C. J. S. III, & P. A. Stott (eds.)). Explaining extreme events of 2015 from a climate perspective. Special Supplement to the Bulletin of the American Meteorological Society/Vol. 97, No. 12, (pp. S75 - S80). DOI: https://doi.org/http://dx.doi.org/10.1175/BAMS-D-16-0167.1

Heath, J. T., Chafer, C. J., Bishop, T. F. A., & van Ogtrop, F. F. (2016). Post-fire recovery of eucalypt-dominated vegetation communities in the Sydney basin, Australia. Fire Ecology, 12(3), 53–79. DOI: https://doi.org/10.4996/fireecology.1203053

Huete, A., Justice, C., & Leeuwen, W. van. (1999). MODIS Vegetation Index Algorithm Theoretical Basis v3. In Environmental Sciences (Issue Mod 13).

Jury, M. (2013). Climate trends in southern Africa. 109(1), 1–11.

Larasati, D. A., Setiawan, H., & Muzayanah, M. (2020). The Utilization of Transformation of Normalized Difference Vegetation Index (NDVI) for Healthy Forest Assessment. 226(Icss), 406 – 409. https://doi.org/10.2991/icss-18.2018.84

Mateus, N. P., & António, J. F. [2]. (2020). Drought in southern Angola : An assessment of the extreme episode of 2018 2019. " Seca no sul da Angola : Uma avaliação do episódio extremo de 2018 2019. August.

Miranda, P. M. A. (2009). Meteorologia e Ambiente:Fundamentos de Meteorologia; Clima e Ambiente Atmosférico. (U.

Aberta.1269-001Lisboa-Portugal (ed.); 2o Edição).

Moreira, A. A., Guasselli, L. A., Silva Filho, L. C. P., Andrade, A. C. F., & Arruda, D. C. de. (2015). Índice de Condição da Vegetação (VCI) para mapeamento de seca no Norte do Estado de Minas Gerais. Anais XVII Simpósio Brasileiro de Sensoriamento Remoto - SBSR, João Pessoa-PB, Brasil, 25 a 29 de Abril de 2015, INPE, Vci, 1686–1692. http://marte2.sid.inpe.br/col/sid.inpe.br/marte2/2015/06.15.14.56.49/doc/p0314.pdf

Nooni, I. K., Hagan, D. F. T., Ullah, W., Lu, J., Li, S., Prempeh, N. A., Gnitou, G. T., & Sian, K. T. C. L. K. (2022). Projections of Drought Characteristics Based on the CNRM-CM6 Model over Africa. Agriculture (Switzerland), 12(4), 1 – 19. DOI: https://doi.org/10.3390/agriculture12040495

Orimoloye, I. R., Belle, J. A., & Ololade, O. O. (2021). Drought disaster monitoring using MODIS derived index for drought years: A space-based information for ecosystems and environmental conservation. Journal of Environmental Management, 284, 112028. DOI: https://doi.org/10.1016/j.jenvman.2021.112028

Parente, J., Amraoui, M., Menezes, I., & Pereira, M. G. (2019). Science of the Total Environment Drought in Portugal: Current regime, comparison of indices and impacts on extreme wild fi res. Science of the Total Environment, 685, 150 – 173. DOI: https://doi.org/10.1016/j.scitotenv.2019.05.298

Peel, M. C., Finlayson, B. L., & Mcmahon, T. A. (2007). Updated world map of the Köppen-Geiger climate classification. 1633–1644.

Shen, R., Huang, A., Li, B., & Guo, J. (2019). Construction of a drought monitoring model using deep learning based on multi-source remote sensing data. International Journal of Applied Earth Observation and Geoinformation, 79(219), 48 – 57. DOI: https://doi.org/10.1016/j.jag.2019.03.006

Uele, D. I. (2013). Impactos dos Modos de Variabilidade Climática no Cultivo do Milho em Regime de Sequeiro: Uma. 169. http://r1.ufrrj.br/wp/ppgpds/files/2015/04/DI_dissertação_versão_definitiva_27-09-2013.pdf

Weier, J., & Herring, D. (2000). Medição da Vegetação (NDVI & EVI). https://earthobservatory.nasa.gov/features/MeasuringVegetation/measuring_vegetation_4.php

WMO, W. M. O., & GWP, G. W. P. (2016). Handbook of Drought Indicators and Indices. BMJ, 1(2366), 1068–1069. DOI: https://doi.org/10.1136/bmj.1.2366.1068-b

Yamamoto, H., Miura, T., & Tsuchida, S. (2012). Advanced Spaceborne Thermal Emission and Reflection Radometer (ASTER) Enhanced Vegetation Index (EVI) products from Global Earth Observation (GEO) grid: An assessment using Moderate Resolution Imaging Spectroradiometer (MODIS) for synergistic applications. Remote Sensing, 4(8), 2277–2293. DOI: https://doi.org/10.3390/rs4082277

Appendix A

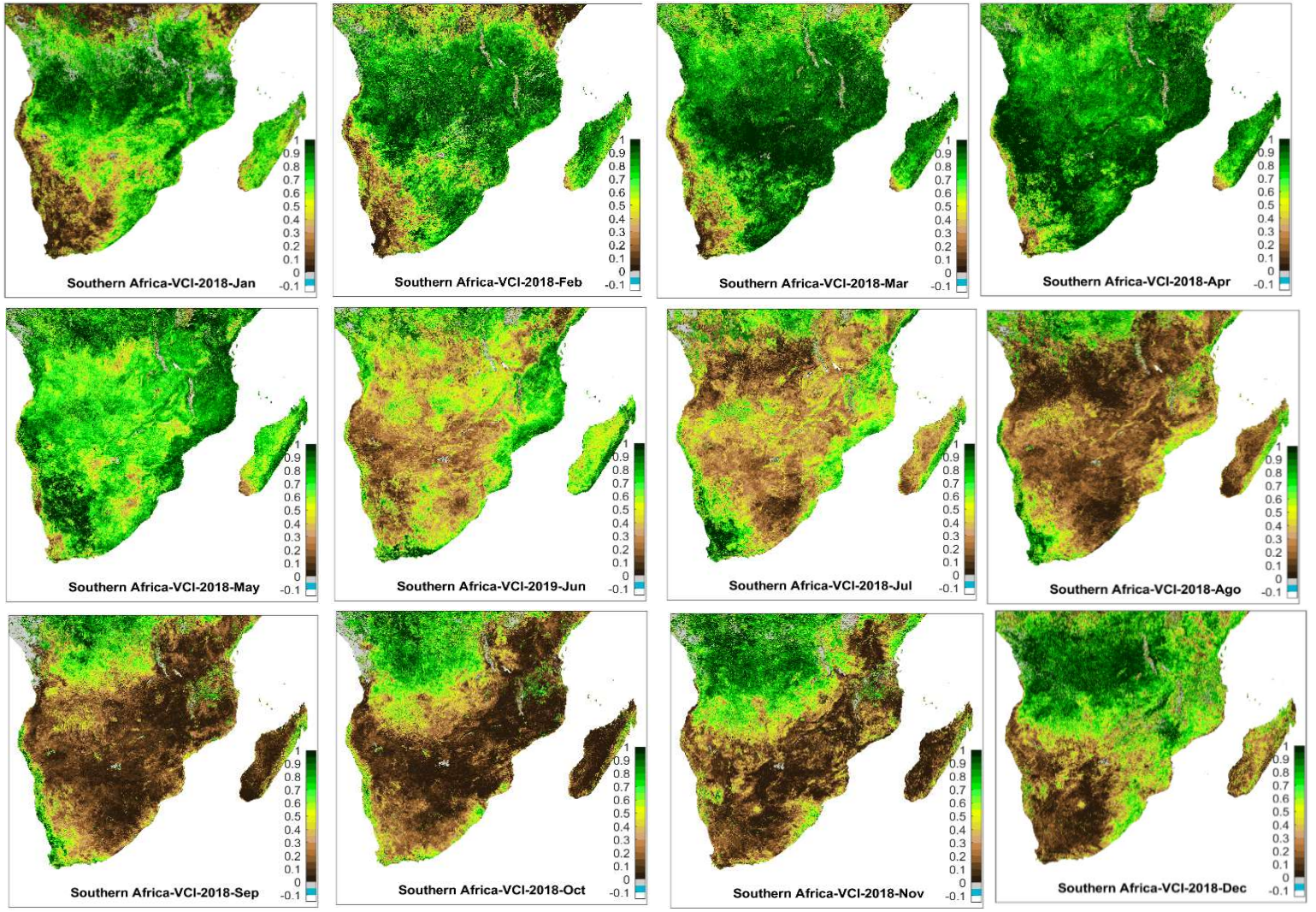

Figure 1A. Values of the VCI index of Southern Africa of the year 2018.

DOI: https://doi.org/10.60620/mzh6-cy13

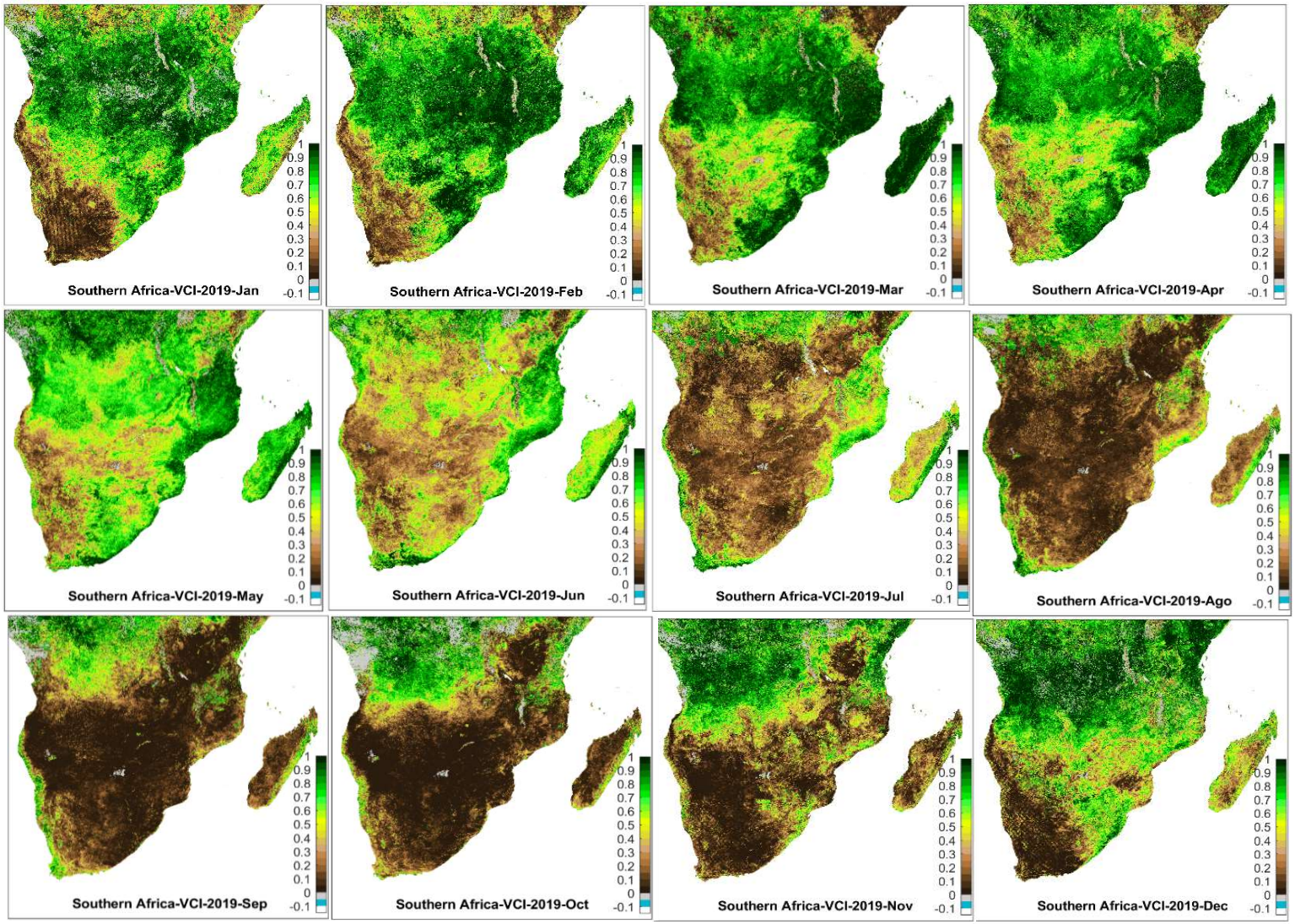

Figure 2A. Values of the VCI index of Southern Africa of the year 2019.

DOI: https://doi.org/10.60620/mzh6-cy13

The Impact of Multiple Atmospheric Rivers on The Extreme Precipitation Events in December 2022 in Portugal

Tomás Gaspar [1], Alexandre M. Ramos [2], Ricardo Deus [3], Paulo J. Pinto [3], Ricardo M. Trigo [1]

[1] *Instituto Dom Luiz, Faculdade de Ciências, Universidade de Lisboa, Portugal*
[2] *Inst. of Meteo. & Clim. Res., Karlsruhe Institute of Technology (KIT), Karlsruhe, Germany*
[3] *Instituto Português do Mar e da Atmosfera (IPMA), Lisboa, Portugal*

SUMMARY

A growing number of authors have been showing that extreme precipitation in most Western European countries is connected to Atmospheric Rivers (ARs). The recent winter of 2022 – 2023 has underlined this evidence for western Iberia, interestingly widely affected by prolonged drought periods. Here we show that the outstanding change from a dry period to an extremely wet one was driven, to a large extent, by the occurrence of consecutive ARs affecting Iberia throughout the month of December 2022. Using a method based on exceedance of Vertically Integrated Water Vapor Transport (IVT) at least 5 Ars were detected between 35°N and 45°N crossing the western Iberia coast. Additionally, using precipitation data from both reanalysis and weather stations, we show a very good match between both phenomena, i.e. the passage of several ARs and the occurrence of these extreme precipitation events.

Keywords: Atmospheric Rivers; Floods; Portugal; December 2022.

1. Introduction

Understanding the complexity of the water cycle in the atmosphere continues to be an important topic within the meteorological and hydrological communities (Gimeno et al. 2012). Besides the source and sink regions, the transport of moisture plays a key role in the atmospheric branch of the water cycle. Atmospheric Rivers (ARs) are relatively narrow regions of concentrated water vapour (WV) and strong wind responsible for intense horizontal moisture transport in the lower atmosphere (Newell et al. 1992; Ralph et al. 2006). Many authors have been showing that extreme precipitation in most Western European countries is connected to ARs (Lavers and Vilarini, 2013; Couto et al.2015) with an Atlantic origin. The recent winter of 2022 – 2023 has underlined this evidence not only for the Iberian Peninsula but also for California where back-to-back Atmospheric Rivers make landfall, interestingly two regions widely affected by prolonged drought periods in recent years. Focusing on the Iberian Peninsula, we show that the outstanding change from a dry period to a normal one was driven, to a large extent, by the occurrence of consecutive ARs affecting Iberia throughout the month of December 2022. During the recent month of December 2022, Portugal was affected by successive episodes of extreme precipitation, affecting a large part of mainland territory, including the metropolitan regions of Lisbon and Porto. According to the climate bulletin provided by the Portuguese Institute of the Sea and the Atmosphere (IPMA), December 2022 was classified as a very rainy month, with an average precipitation amount of 250.4 mm recorded, corresponding to 174% of the climatological normal value from 1971 to 2000 (IPMA, 2022). According to IPMA, several new daily maxima were established at various stations (values observed between 9:00 am on the 12th and 9:00 am on the 13th).

 DOI: https://doi.org/10.60620/ty7f-a388

This includes the absolute new maximum at the longest-recording station in Lisbon located at the old Geophysical Institute, with over 150 years of continuous records. In fact, on 13 December 2022, 120.3 mm were recorded, surpassing the previous maximum observed in 2008 with 118.4 mm (Fragoso et al., 2010).

2. Datasets and methodology

We have used an automated atmospheric river (AR) detection algorithm for the North Atlantic Ocean basin that allows the identification and analysis of the major AR events that affected the Iberian Peninsula (Ramos et al., 2015). For that, we use the ERA5 reanalysis dataset, namely the zonal and meridional components of the vertically Integrated horizontal Water Vapor Transport (IVT) flux and mean sea level pressure during extended winter months (ONDJFM). To consider the longest climatological period, we have used data for the 1959-2021 period with a temporal resolution of 6 hours and a spatial resolution of 0.25° latitude-longitude grid.

A significant number of studies identify ARs by computing the IVT following the methodology used by Lavers (2012) and Lavers and Villarini (2013). The IVT was computed taking a surface and a top level in an Eulerian framework (e.g., Neiman et al. 2008; Lavers et al. 2012):

$$IVT = \sqrt{\left(\frac{1}{g}\int_{surf}^{top} qudp\right)^2 + \left(\frac{1}{g}\int_{surf}^{top} qvdp\right)^2} \quad (1)$$

where q is the layer-averaged specific humidity ($kgkg^{-1}$); u and y are the layer-averaged zonal and meridional winds (ms^{-1}), respectively; g is the acceleration due to gravity; and dp is the pressure difference between two adjacent pressure levels.

Using a similar approach to that employed by Ramos (2015), we have identified those ARs that possibly affect the IP (35°–45°N, 10°W) using the following set of criteria:

1) We computed the IVT threshold using the maximum IVT at noon UTC for each day from our IVT dataset (1959 – 2021) along the 10°W meridian and between (35° – 45°N). According to Lavers et al., 2012, the 85th percentile is appropriate to detect the most intense. Consequently, we computed the 85th percentile of the maximum IVT distribution ($505 Kg\ m^{-1}\ s^{-1}$) and used it as the threshold value for the first step in the identification of Ars.
2) In a second phase, at each time step (every 6 hours) from our IVT dataset (1959 – 2021) we extract the maximum IVT value and their location on grid points between 35° and 45°N along 10°W.
3) If our maximum IVT from phase 2 exceeded our 85th percentile ($>505 Kg\ m^{-1}\ s^{-1}$) this particular grid cell was marked as a potential AR. We then performed a backward/forward search to identify the maximum IVT at each grid box and checked if it exceeded the IVT 85th percentile (obtained on the first step). If it did, then we added that grid to our AR central core. The core must extend over many degrees of longitude and, to obtain results consistent with studies carried out by other authors such as Ramos (2015), the length should correspond approximately to 80 continuous longitude pixels (80*0.25°=20°∼1700 km) above $505 Kg\ m^{-1}\ s^{-1}$. Then, we have an AR central core for a particular timestep, and the algorithm looked forward in time to verify if the AR central core still fulfils these conditions (phases 2 and 3). The application of these three methodological steps allows for detecting many potential ARs close to Iberia. For this analysis, only persistent events will be considered; for that, we need to consider temporal criteria. For a persistent AR event to occur (Ramos et al., 2015) it needs to fulfil the following conditions: 1) it must have at least 18h persistence (3 timesteps according to our dataset), and 2) If the separation is less than a day, it implies that we do not have two independent AR events.

In the face of successive episodes of extreme precipitation during December 2022, the occurrence of Atmospheric Rivers (ARs) was

studied using the same ERA5 reanalysis variables with hourly resolution (instead of 6 hours) and applying the same methodology as in previous works (Ramos et al., 2015). Our method detected 5 ARs during December 2022, therefore, once we have our climatological analysis from 1959 to 2021, we can conclude that December 2022 was an extremely anomalous month in comparison with climatological results for all the extended winter period (~5.7 *ARs per year*). Results for the precipitation extremes were obtained considering the same approach as Ramos (2015; 2017). Thus, we used both high-resolution regular grid datasets available for the Iberian Peninsula (IB01 and IB02). Aiming to work with the greatest temporal extension and the best spatial resolution possible we combined the two datasets, with the 1950 – 1970 period based on IB02 (PT02, Belo-Pereira et al., 2011; SPAIN02, Herrera et al., 2012), and for the period between 1971 – 2015 we used IB01 (Herrera et al., 2019). To achieve consistency in terms of spatial resolution IB02 dataset was artificially upscaled from 0.2° to 0.1° latitude-longitude grid.

To obtain the different rankings of precipitation extremes over multi-day accumulated periods, a three-step method was applied (Ramos et al., 2017). The first step consists in computing the daily normalized precipitation anomalies (*N).* The second step was applied to obtain accumulated precipitation anomalies for a certain period p (Ramos et al., 2017). Since the daily precipitation anomalies were computed in the previous step and are normalized, the sum of the normalized anomalies over multi-day periods (n) represents the accumulated precipitation anomalies (NCC). We have computed the NCC for 3, 5, 7, and 10 days of accumulated precipitation anomalies. The final step was to quantify the precipitation extreme, proceeding with the computation of the magnitude for each different accumulated precipitation anomaly period. For that, we applied the same procedure developed by Ramos (2017), i.e. the magnitude of an extreme (hereafter $\boldsymbol{R_M}$) is given daily by an index that is obtained after multiplying:

(1) The area ($\boldsymbol{A}$), in percentage, that has precipitation anomalies (over each accumulated period) above two std by;
(2) The mean value of these anomalies (hereafter $\boldsymbol{M}$) for all grid points that have precipitation anomalies above two std.

As we said before, we performed a detailed analysis of the Iberian Peninsula (IP) and for that, we considered eight different domains: the most important river basins: (1) Minho, (2) Duero, (3) Tagus, (4) Guadiana, (5) Guadalquivir and (6) Ebro); and additionally, the areas of Portugal and the entire IP. For all these domains we computed the multi-day precipitation rankings (3, 5, 7 and 10 days), resulting in a total of 32 different rankings (Ramos et al. 2017).

To study December 2022 month, because it is a recent period, we had no access to the precipitation dataset in the same grid as IB01 or IB02. Nevertheless, IPMA provided precipitation data in 114 automated EMA stations over mainland Portugal with a 10-minute temporal resolution. Therefore, we computed the accumulated precipitation (hourly, daily, and over 3 days). We have also performed a cubic interpolation of our data to derive values over all Portuguese territory instead of being confined to the marked point value at stations. Cubic interpolation is a commonly used method in the visualization of scientific data, especially for representing data continuously and smoothly (Wolberg et al., 1999).

3. Results

Our algorithm detected 5 ARs during December 2022 (an extremely anomalous month). During this month, there were episodes of intense precipitation, particularly on days 4th and 5th, 7th and 8th, 12th and 13th, and in the last days of the month, with flooding and overflowing occurring in various locations throughout the territory (IPMA, Monthly Climatological Bulletin – December 2022). In the two episodes of strong precipitation over Lisbon (days 7 – 8 and 12 – 13), on average, according to IPMA, the total amount of precipitation related to these two episodes corresponded to about 50% of the total precipitation that occurred, over Portugal, during December 2022. For the sake

 DOI: https://doi.org/10.60620/ty7f-a388

of simplicity and space limitation, we will focus our results on the extreme anomalous precipitation that occurred during the 11th – 13th December period. Daily precipitation (mm) is presented in **Figure1a–c** for the 11th, 12th, and 13th of December respectively. Overall, it was a persistent rainfall event, which was sometimes characterised by heavy rain in the North, Center, and Alto Alentejo regions, and in some locations in the Setúbal Peninsula. On December 11 (**Figure1a**) intense precipitation occurred over a widespread area of the territory, reaching the highest values over the Central region (60mm). On December 12th (**Figure1b**) the highest values of precipitation occurred mainly over the North region, reaching the highest values (90mm), especially over Gerês, Braga, Vila Real, and more to the South, Viseu.

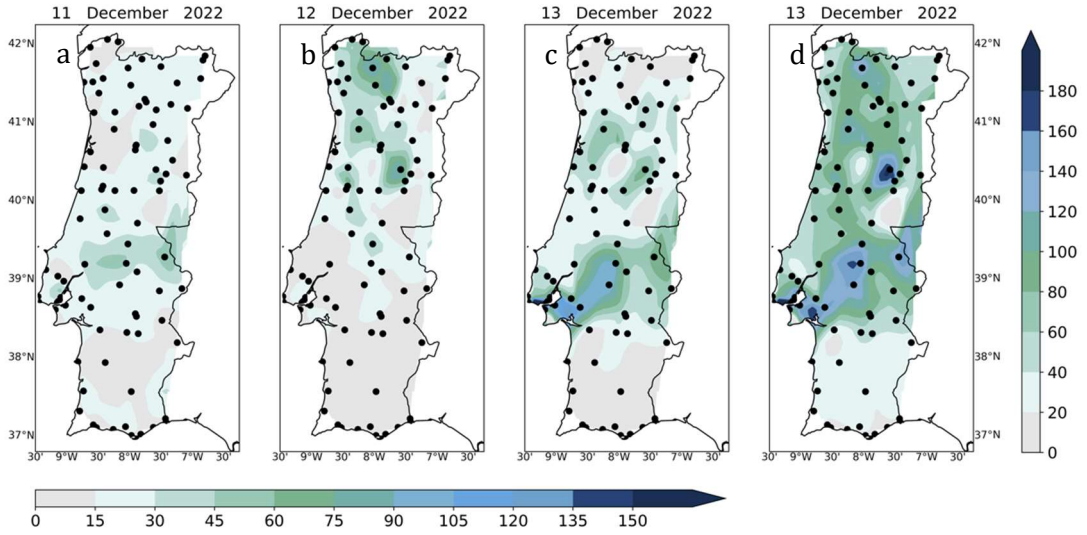

Figure 1. Daily precipitation (mm, shaded) for (a) December 11 2022, (b) December 12 2022, and (c) December 13 2022. (d) Three days of accumulated precipitation (mm, shaded) for 11-13 December 2022. The black dots show the location of the 114 stations considered.

As previously mentioned, these days were characterised by the onset of an AR, starting on December 11 at 22:00 UTC. **Figure2-left** depicts the IVT intensity ($Kg\ m^{-1}s^{-1}$; colour shading), SLP (hPA, contours) fields and the AR core (Black points) of the event at 06:00 UTC when it made landfall over the northern region, and **Figure2-right** represents the total amount of precipitation between 05:00-06:00 UTC.

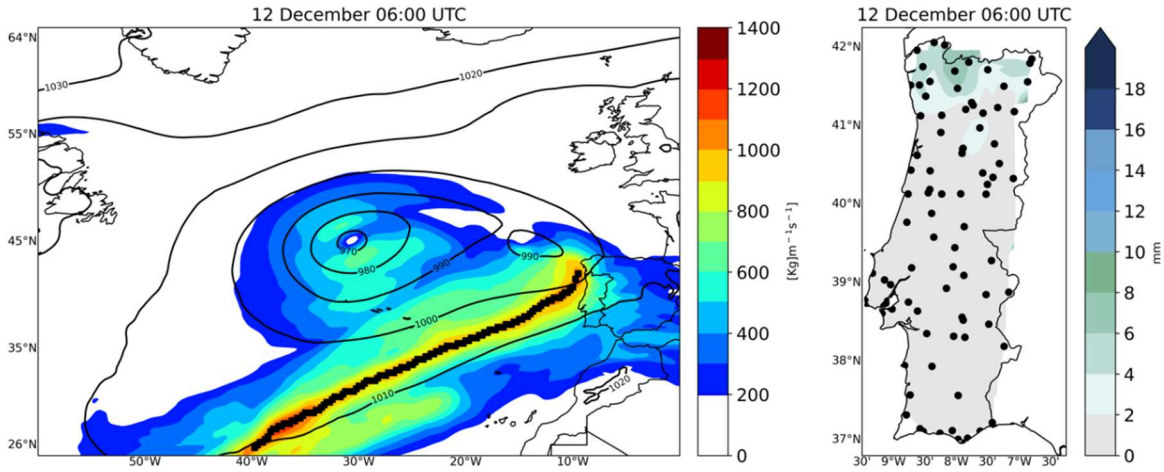

Figure 2. (left) Integrated Water Vapor Transport (IVT) intensity ($\boldsymbol{Kg\ m^{-1}s^{-1}}$), SLP (hPa; contours) fields, and Atmospheric River core detected by the Algorithm (scatters). (right) Hourly precipitation (mm, shaded) for December 12th at 06:00 UTC.

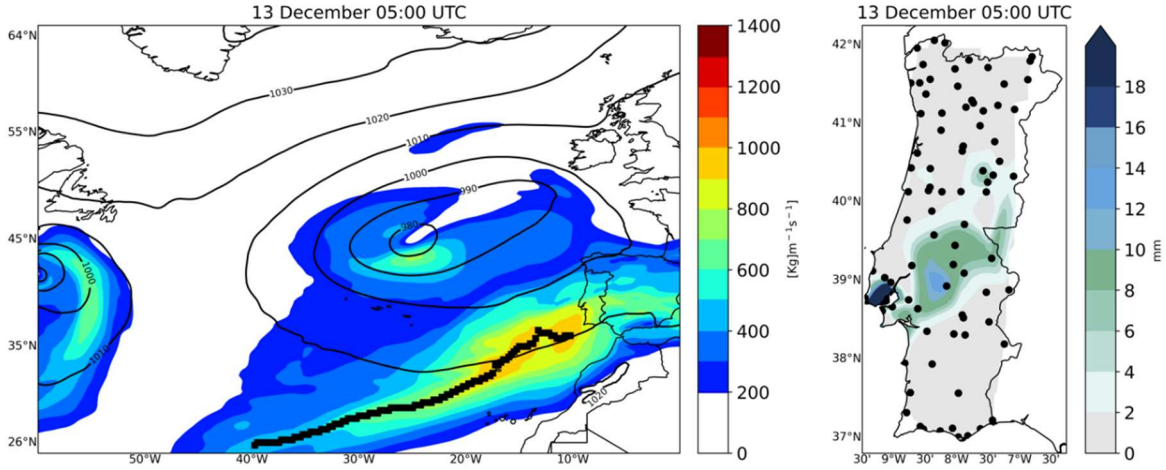

Figure 3. (left) Integrated Water Vapor Transport (IVT) intensity ($\boldsymbol{Kg\ m^{-1}s^{-1}}$), SLP (hPa; contours) fields, and Atmospheric River core detected by the Algorithm (scatters). (right) Hourly precipitation (mm, shaded) for December 13th at 05:00 UTC.

From the EMA stations, we know that no precipitation was recorded over Portugal until 05:00 UTC. Therefore, it is reasonable to assume that it started to rain precisely at the same time as the AR made landfall. By the end of the day, the atmospheric river crossed Portugal from North to South, with a decrease in intensity. Nevertheless, it was still possible to observe relatively intense precipitation mainly over the Central and Northern regions (**Figure1-b**). **Figure1-d** is the total rainfall amount for the 11 – 13 December period, and high values were recorded over the main territory with the highest values over Lisbon and Alto Alentejo established records of 168.1 mm, 147.9 mm, and 137.8 mm for the Lisboa/IPMA, Lisboa/Alges, and Alentejo/Mora stations. The extreme precipitation that occurred in Lisbon and was responsible for high social and economic losses due to flooding has, mostly occurred in the early morning of December 13th. Once again, our results help to explain this increase in precipitation. Thus, in the early morning (05:00 UTC) we had an intensification on the IVT field reaching the Portuguese coast, advected from the Atlantic Ocean (**Figure 3 - left**). This intense and channelled IVT was responsible for an extreme amount of precipitation (rainfall rate higher than "> 12 $mm\ hour^{-1}$" during several hours) over Lisbon and Alto Alentejo regions (**Figure3-rigth**). After performing a detailed analysis of the Precipitation extremes in a climatological way (1950 – 2015) we have the daily precipitation mean climatological value and respective daily std value for a particular Julian day and for each grid point over the Iberia Peninsula with a 0.1° special resolution. Considering this, we selected grid cells that include each one of the 114 stations as an attempt to merge these climatological gridded results with the precipitation dataset for December 2022. Then, we were able to compute the normalized precipitation anomalies (N) for all 114 station locations. For the sake of simplicity, we will present only the results for the 3 stations referred to above: we can conclude that the Lisboa/Algés station attained a precipitation amount (147.9 mm) that was 12.5 std above the climatological value; the Lisboa/IPMA (168.1mm) and the Alentejo/Mora (137.8 mm) stations were, respectively, at 14.5 std and 13 std above its climatological values.

Considering these specific results from stations and the analysis of this extreme precipitation episode, we can foresee that this event will likely rank very high in the multi-day extreme precipitation rankings, especially over Portugal. However, that will only occur when the precipitation data becomes available on a regular grid similar to the IB01 or IB02 datasets and the magnitude

DOI: https://doi.org/10.60620/ty7f-a388

of this episode (as described in the previous section) is calculated.

4. Conclusions

Studies such as Liberato and Trigo (2014) and Zêzere et al. (2014) have demonstrated the significant socioeconomic impacts resulting from extreme precipitation events in the IP during the extended winter months. These impacts include floods, landslides, extensive property damage, and loss of life. Furthermore, several studies have focused specifically on extreme events, including Fragoso et al. (2010), Liberato et al. (2011), Trigo et al. (2014), and Liberato et al. (2012). The most important results obtained here can be summarized as follows:

(1) This study analyzed in detail the extremely anomalous month of December 2022 in terms of precipitation. There were several episodes of intense precipitation throughout the month, particularly on the 4th and 5th, 7th and 8th, 12th and 13th, and also during the last few days of the month, which resulted in flooding and overflowing in various locations throughout the territory.

(2) We evaluated every 6h the values of IVT to determine to which extent the large rainfall amounts observed on several occasions were linked to the presence (or not) of Atmospheric Rivers (ARs) in the near North Atlantic region.

(3) Obtained results allow us to conclude that, during these days (11th, 12th, and 13th), repeated episodes of heavy precipitation gave rise to several sudden floods in various urban areas, especially in the Greater Lisbon area and some regions of Alto Alentejo, areas perfectly overlapping with the passage of an AR.

(4) New daily precipitation records were set on December 13th in several stations of Lisbon and Alentejo.

5. Acknowledgements

The financial support for attending this research was possible through the Portuguese Science Foundation (FCT) through the project AMOTHEC (DRI/India/0098/2020) and also through National funds (PIDDAC) – UIDB/50019/2020 also provided by FCT (I.P./MCTES).

6. References

Belo-Pereira, M., Dutra, E., & Viterbo, P. (2011). Evaluation of global precipitation data sets over the Iberian Peninsula. Journal of Geophysical Research: Atmospheres,116(D20). DOI: https://doi.org/10.1029/2010jd015481. Accessed 3 Apr. 2023.

Couto, F. T., Salgado, R., Costa, M. J., & Prior, V. (2015). Precipitation in the Madeira Island over a 10-year period and the meridional water vapour transport during the winter seasons. International Journal of Climatology,35(13), 3748 - 3759. DOI: https://doi.org/10.1002/joc.4243. Accessed 8 May 2023.

Fragoso, M., Trigo, R. M., Zêzere, J. L., & Valente, M. A. (2010). The exceptional rainfall event in Lisbon on 18 February 2008.Weather,65(2), 31 - 35. DOI: https://doi.org/10.1002/wea.513. Accessed 13 Mar. 2023.

Gimeno, L., Stohl, A., Trigo, R. M., Dominguez, F., Yoshimura, K., Yu, L., ... & Nieto, R. (2012). Oceanic and terrestrial sources of continental precipitation. Reviews of Geophysics,50(4). DOI: https://doi.org/10.1029/2012rg000389. Accessed 28 Oct. 2019.

Herrera, S., Gutiérrez, J. M., Ancell, R., Pons, M. R., Frías, M. D., & Fernández, J. (2012). Development and analysis of a 50-year high - resolution daily gridded precipitation dataset over Spain (Spain02). International Journal of Climatology,32(1), 74- 85. DOI: https://doi.org/10.1002/joc.2256. Accessed 27 July 2020.

Herrera, S., Cardoso, R. M., Soares, P. M., Espírito-Santo, F., Viterbo, P., & Gutiérrez, J. M. (2019). Iberia01: A new gridded dataset of daily precipitation and temperatures over Iberia. Earth System Science Data,11(4), 1947 - 1956. DOI: https://doi.org/10.5194/essd-11-1947-2019. Accessed 5 Apr 2023.

IPMA, (2022) Instituto Português do Mar e da Atmosfera, Boletim climático Portugal

Continental; dezembro 2022, https://www.ipma.pt/pt/media/noticias/documentos/2022/Boletim_clima_IPMA_dez2022.pdf. Accessed 3 Apr. 2023.

Lavers, D. A., Villarini, G., Allan, R. P., Wood, E. F., & Wade, A. J. (2012). The detection of atmospheric rivers in atmospheric reanalyses and their links to British winter floods and the large-scale climatic circulation. Journal of Geophysical Research: Atmospheres,117(D20). DOI: https://doi.org/10.1029/2012jd018027.

Lavers, D. A., & Villarini, G. (2013). The nexus between atmospheric rivers and extreme precipitation across Europe. Geophysical Research Letters,40(12), 3259-3264. DOI: https://doi.org/10.1002/grl.50636.

Liberato, M. L. (2014). The 19 January 2013 windstorm over the North Atlantic: large-scale dynamics and impacts on Iberia. Weather and Climate Extremes, 5, 16 - 28. DOI: https://doi.org/10.1016/j.wace.2014.06.002. Accessed 3 Apr. 2023.

Liberato, M. L., & Trigo, R. M. (2014). Extreme precipitation events and related impacts in Western Iberia. IAHS Publ,363, 171-176.Accessed 3 Apr. 2023

Margarida, L. R., Pinto, I. F., & Trigo, R. M. Klaus‐an exceptional winter storm over northern Iberia and southern France. DOI: https://doi.org/10.1002/wea.755. Accessed 22 May 2022.

Liberato, M. L., Ramos, A. M., Trigo, R. M., Trigo, I. F., María Durán-Quesada, A., Nieto, R., & Gimeno, L. (2013, April). Moisture Sources and Large-Scale Dynamics Associated with a Flash Flood Event in Portugal. In EGU General Assembly Conference Abstracts (pp. EGU2013-3394). DOI: https://doi.org/10.1029/2012gm001244. Accessed 3 Apr. 2023.

Neiman, P. J., Ralph, F. M., Wick, G. A., Lundquist, J. D., & Dettinger, M. D. (2008). Meteorological characteristics and overland precipitation impacts of atmospheric rivers affecting the West Coast of North America based on eight years of SSM/I satellite observations. Journal of Hydrometeorology,9(1), 22 - 47. DOI: https://doi.org/10.1175/2007jhm855.1.

Newell, R. E., Newell, N. E., Zhu, Y., & Scott, C. (1992). Tropospheric rivers? A pilot study. Geophysical research letters,19(24), 2401 - 2404. DOI: https://doi.org/10.1029/92gl02916.

Ralph, F. M., Neiman, P. J., Wick, G. A., Gutman, S. I., Dettinger, M. D., Cayan, D. R., & White, A. B. (2006). Flooding on California's Russian River: Role of atmospheric rivers. Geophysical Research Letters,33(13). DOI: https://doi.org/10.1029/2006gl026689.

Ramos, A. M., Trigo, R. M., & Liberato, M. L. (2014). A ranking of high-resolution daily precipitation extreme events for the Iberian Peninsula. Atmospheric Science Letters,15(4), 328 - 334. DOI: https://doi.org/10.1002/asl2.507. Accessed 16 July 2020.

Ramos, A. M., Trigo, R. M., Liberato, M. L., & Tomé, R. (2015). Daily precipitation extreme events in the Iberian Peninsula and its association with atmospheric rivers. Journal of Hydrometeorology, 16(2), 579 - 597. DOI: https://doi.org/10.1175/jhm-d-14-0103.1. Accessed 1 Mar. 2021.

Ramos, A. M., Trigo, R. M., & Liberato, M. L. (2017). Ranking of multi-day extreme precipitation events over the Iberian Peninsula. International Journal of Climatology, 37(2),607 - 620. DOI: https://doi.org/10.1002/joc.4726.

Trigo, R. M., Varino, F., Ramos, A. M., Valente, M. A., Zêzere, J. L., Vaquero, J. M., ... & Russo, A. (2014). The record precipitation and flood event in Iberia in December 1876: description and synoptic analysis. Frontiers in Earth Science,2, 3. DOI: https://doi.org/10.3389/feart.2014.00003. Accessed 3 Apr. 2023.

Wolberg, George & Alfy, Itzik. (1999). Monotonic cubic spline interpolation. 188-195. 10.1109/CGI.1999.777953.

Zêzere, J. L., Pereira, S., Tavares, A. O., Bateira, C., Trigo, R. M., Quaresma, I., ... & Verde, J. (2014). DISASTER: a GIS database on

 DOI: https://doi.org/10.60620/ty7f-a388

hydro-geomorphologic disasters in Portugal. Natural hazards,72, 503-532. DOI: https://doi.org/10.1007/s11069-013-1018-y.

Concurrent Marine and Atmospheric Heatwaves and Droughts and their Influence on Fire Activity in the Mediterranean Region

Raquel Santos [1], Ana Russo [2], Célia M. Gouveia [1,2]

[1] *Instituto Português do Mar e da Atmosfera (IPMA), 1749–077, Lisboa, Portugal, raquel.santos@ipma.pt*
[2] *Instituto Dom Luiz, Faculdade de Ciências, Universidade de Lisboa, Portugal*

SUMMARY

Heatwave events have been increasing during the past decades, affecting ecosystems, human health, and basic resources (e.g., water and food availability). Their occurrence also interacts with droughts, which have also become more recurrent in certain regions like the Mediterranean, impacting agriculture and reservoirs' water level and quality. When these warm and dry conditions co-occur, the probability of wildfire occurrence and severity increases.
In this work, heatwaves and drought conditions are analysed over Southern Europe, together with marine heatwaves over the East Atlantic and the Mediterranean Sea, which have been particularly affected by climate extreme episodes in the last decades. Here, we focus on the role of these events under a compound events framework, estimating their contribution to the occurrence of extreme wildfires in the region.

Keywords: Compound events, atmospheric heatwaves, marine heatwaves, droughts, fires, climate extremes.

1. Introduction

Heatwave events have been increasing in frequency, duration, and intensity over the past decades, occurring both in the ocean and atmosphere (IPCC, 2022). These events can impact human health, and terrestrial and marine ecosystems, and exacerbate the scarcity of some basic resources (Blauhut et al., 2016). These episodes are projected to continue increasing in the future, greatly influenced by anthropogenic activity (IPCC, 2022). Along with these exceptionally hot events, droughts have also increased in frequency and severity in certain regions, having a substantial influence on agricultural activity (Ribeiro et al., 2020; Bento et al., 2022) as well as the quantity and quality of water in reservoirs (Stahl et al., 2016).

The Southern region of Europe has been recurrently affected by these extreme episodes, particularly during the last few decades, along with the Mediterranean Sea and the East Atlantic (Spinoni et al, 2015; Liu et al., 2020; García-Herrera et al., 2010). When they occur simultaneously, the consequences of these hot and dry events amplify (Zscheischler et al., 2018).

The prevalence of wildfires, which cause significant ecological and economic losses, as well as loss of human lives, is one of the most severe repercussions (Ruffault et al., 2020).

Therefore, it becomes fundamental to pay special attention to the role of these compound events and synergies in fueling extreme fire outbreaks, to better
protect vulnerable ecosystems and habitats, human health, and affected resources.

Research studies have previously been conducted on the combined influence of atmospheric heat waves and droughts on fire occurrence (Ruffault et al., 2020; Gouveia et al., 2016; Ermitão et al., 2022; Sutanto et al., 2020). Here, we purpose to additionally underline the marine component and its connection to these extreme events.

2. Data and Methods

In this work, ERA5 reanalysis data from 1979 to 2022 (Hersbach et al., 2023) were used to

 DOI: https://doi.org/10.60620/wcqx-2d49

study atmospheric and sea surface temperatures and identify heatwave events, according to the definition proposed by Hobday et al. (2016), as demonstrated in **Figure 1**. Heatwave events occur when daily mean temperatures exceed the threshold (90th percentile) for at least 5 consecutive days. We use this definition to identify both marine and atmospheric episodes.

Frequency, duration, and intensity are very well-known properties to study the occurrence of heatwaves. In this work, we used the Intensity Composite Index (ICI) (Golubeva et al., 2021) to summarize the characteristics above mentioned:

$$ICI = \sum_{i=1}^{n} \sum_{d=1}^{d_i} \Delta T(i,d), \qquad (1)$$

where i=1, n is the number of heatwave events, d_i is the duration of the i-th event, and $\Delta T(i, d)$ is the intensity of the i-th event on its d-th day.

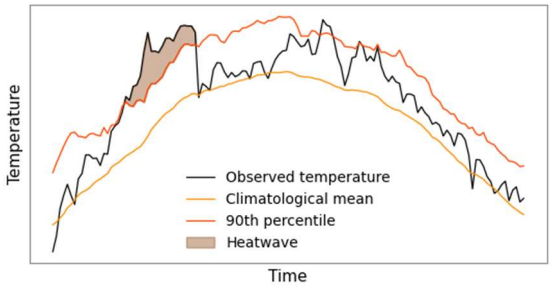

Figure 1. Schematic definition of a heatwave episode (shaded area), based on records of temperature observations (black line), 90th percentile (red line) and climatology (orange line).

The occurrence of dry episodes was assessed based on precipitation ERA5 reanalysis data (Hersbach et al., 2023), during the same period. The Standardized Precipitation Index (SPI), a commonly used index to describe meteorological dryness on various timescales, was computed, using a 12-month accumulation period (SPI-12), to determine the severity of droughts (Agnew, 2000).

To analyse the occurrence of wildfires over the region, burnt area data from 2001 to the present were extracted, and recorded by the MODIS instrument aboard the Terra and Aqua satellites (Giglio et al., 2015).

We also use land cover data from the ESA CCI (Copernicus Climate Change Service, 2019) to mask landcover areas of cropland and grassland, focusing only on the occurrence of rural fires, that may be more dependent on unfavourable climatic conditions like heatwaves and droughts.

3. Results

Figure 2a) and **Figure 2b)** show the representation of the ICI over 2022, based on 2-meter air temperatures and sea surface temperatures, respectively. This year was extremely affected by the occurrence of heatwaves in the ocean and atmosphere, as revealed by the very intense values in **Figure 2**, particularly in the Mediterranean region. **Figure 3** shows the SPI-12 index values recorded in December of 2022, for our region of study.

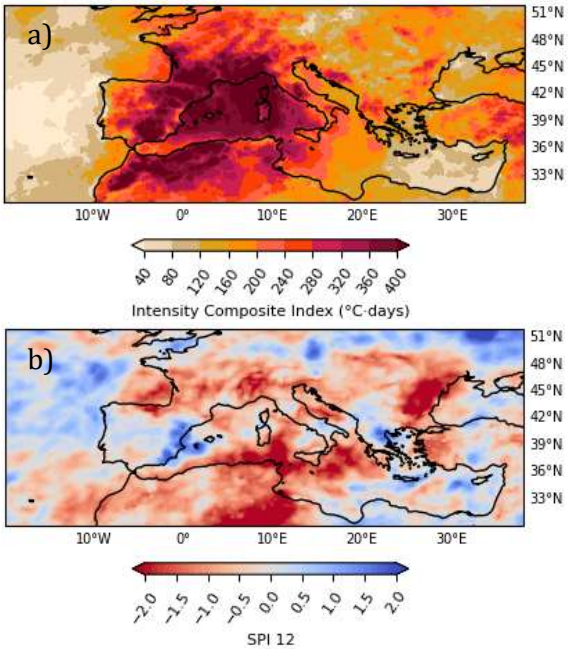

Figure 2. Intensity Composite Index, in °C·days, computed from a) 2-m air temperatures and b) sea surface temperatures, for 2022.

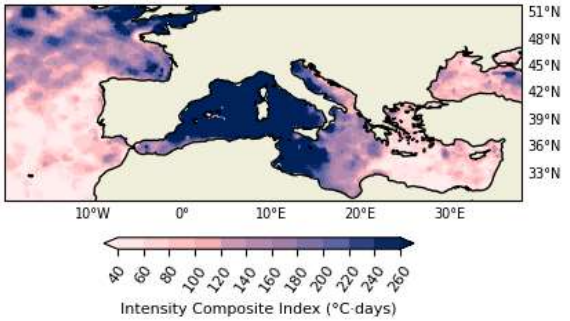

Figure 3. 12-month SPI in December of 2022.

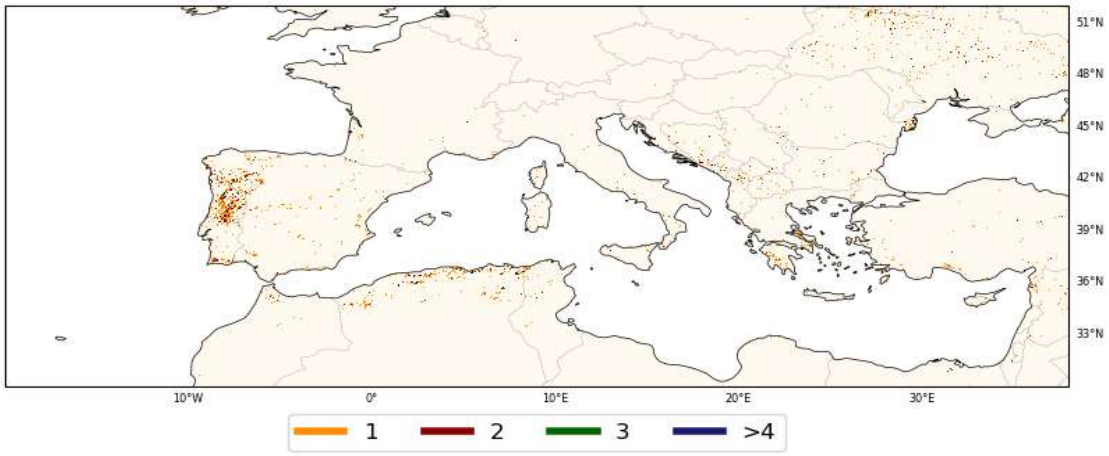

Figure 4. The frequency of rural fires occurred between 2001 and 2022.

The central part of the Mediterranean region shows to be under very dry conditions. The Iberian Peninsula was revealed to be more humid, greatly influenced by the extreme precipitation recorded at the end of the year. **Figure 4** represents the number of fires (neglecting cropland and grassland areas) that have occurred over the period 2001 – 2022.

According to the results, Portugal has been largely affected by wildfires since the beginning of the century, along with Spain and Greece, for example.

To estimate the contribution of combined heatwaves (marine and atmospheric) and droughts to the occurrence of extreme wildfires, we have chosen two different areas to study: the Iberian Peninsula and Southern Mediterranean (red box), and France and its west coast (green box), as shown in **Figure 5**.

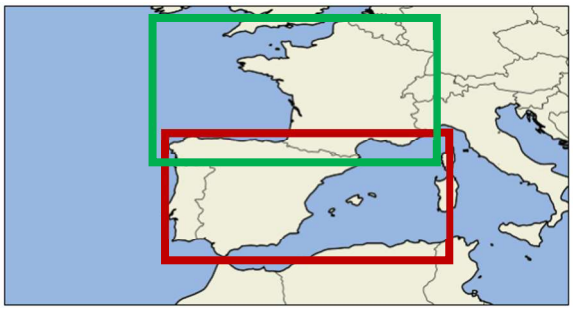

Figure 5. Red and green boxes represent the regions of study in **Figure 6**.

Pixels representing burned areas in each of these separated regions were selected each year. Following this, we calculated the mean of the atmospheric ICI and SPI12 of December over those pixels. Lastly, we annually analysed the mean marine ICI in the surrounding adjacent seas.

The results are shown in **Figure 6**. By visual inspection, there appears to be a negative correlation when examining simultaneously the cumulative intensity of atmospheric heatwaves and SPI-12 values in both Figures. In 6a), 2015, 2017 and 2022 are examples of years that show high values of mean atmospheric ICI and negative values of mean SPI-12, indicating the overall existence of very hot and dry conditions over burned areas in those years.

In addition, the mean of marine ICI over the eastern Mediterranean also recorded significant values, especially in 2022.

The west coast of France (**Figure 6b**) is characterized by lower mean values of marine ICI than the eastern Mediterranean. Nevertheless, 2022 shows to be again the most extreme year, revealing to be under the effect of strong heatwaves and droughts in this area. Years such as 2007, 2011 and 2017 also appear to be concordant when examining simultaneously the annual occurrence of wildfires, the cumulative intensity of heatwaves and SPI values.

DOI: https://doi.org/10.60620/wcqx-2d49

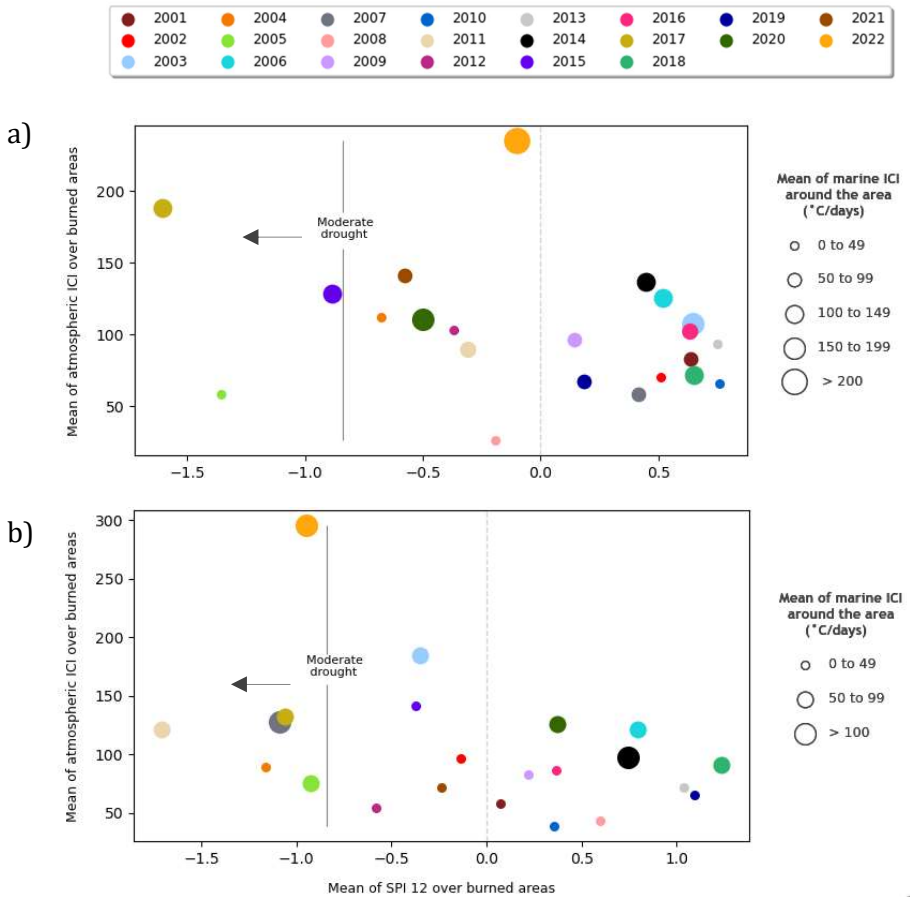

Figure 6. Scatter plot representing the mean values of SPI12 of December and atmospheric ICI, over burned pixels, in the (a) red box and (b) green box, in each year. The size of the marker is related to the severity of the marine ICI in the surrounding sea.

4. Conclusions and Future Work

By connecting the prevalence of heatwaves (both marine and atmospheric) with concurrent drought episodes, this study aims to understand how they may have contributed to the subsequent occurrence of wildfires that have significantly damaged Southern Europe over the past decades.

Our results suggest that there is an apparent consistency when examining simultaneously the annual occurrences of wildfires, total heatwave cumulative intensity (ICI), and SPI values over these areas, with 2022 being the most affected by marine and atmospheric heatwaves in both analysed areas.

We aim to continue developing this work, complementing it with the application of the Standardized Precipitation Evapotranspiration Index (SPEI) to study the occurrence and severity of droughts.

Furthermore, we will focus on the temporal evolution of atmospheric and marine heatwaves, droughts, and fires on a compound approach, while attempting to undertake a seasonal analysis.

5. Acknowledgements

This study is partially supported by the European Union's Horizon 2020 research project FirEUrisk (Grant Agr. 101003890) and by the Fundação para a Ciência e a Tecnologia (FCT) I.P./MCTES through national funds (PIDDAC) UIDB/50019/2020 IDL, DHEFEUS 2022.09185.PTDC, and 2022.01167.CEECIND.

6. References:

Agnew, C. (2000). Using the SPI to Identify

Drought. Drought Netw. News. 12.

Bento, V. A., Russo, A., Dutra, E., Ribeiro, A. F. S., Gouveia, C. M., & Trigo, R. M. (2022). Persistence versus dynamical seasonal forecasts of cereal crop yields. Scientific Reports, 12(1). DOI: https://doi.org/10.1038/s41598-022-11228-2

Blauhut, V., Stahl, K., Stagge, J. H., Tallaksen, L. M., Stefano, L. de, & Vogt, J. (2016).

Estimating drought risk across Europe from reported drought impacts, drought indices, and vulnerability factors. Hydrology and Earth System Sciences, 20(7), 2779 – 2800. DOI: https://doi.org/10.5194/hess-20-2779-2016

Copernicus Climate Change Service, Climate Data Store, (2019): Land cover classification gridded maps from 1992 to present derived from satellite observation. Copernicus Climate Change Service (C3S) Climate Data Store (CDS). DOI: https://doi.org/10.24381/cds.006f2c9a

Ermitão, T., Gouveia, C. M., Bastos, A., & Russo, A. C. (2022). Interactions between hot and dry fuel conditions and vegetation dynamics in the 2017 fire season in Portugal. Environmental Research Letters, 17(9). DOI: https://doi.org/10.1088/1748-9326/ac8be4

Giglio, L., Justice, C., Boschetti, L., Roy, D. (2015). MCD64A1 MODIS/Terra+Aqua Burned Area Monthly L3 Global 500m SIN Grid V006 [Data set]. NASA EOSDIS Land Processes DAAC. Accessed 2023-04-10. DOI: https://doi.org/10.5067/MODIS/MCD64A1.006

Golubeva, E., Kraineva, M., Platov, G., Iakshina, D., & Tarkhanova, M. (2021). Marine heatwaves in Siberian arctic seas and adjacent region. Remote Sensing, 13(21). DOI: https://doi.org/10.3390/rs13214436

Gouveia, C. M., Bistinas, I., Liberato, M. L., Bastos, A., Koutsias, N., & Trigo, R. (2016). The outstanding synergy between drought, heatwaves and fuel on the 2007 Southern Greece exceptional fire season. Agricultural and Forest Meteorology, 218, 135-145.Hersbach, H., Bell, B., Berrisford, P., Biavati, G., Horányi, A., Muñoz Sabater, J., Nicolas, J., Peubey, C., Radu, R., Rozum, I., Schepers, D., Simmons, A., Soci, C., Dee, D., Thépaut, J-N. (2023): ERA5 hourly data on single levels from 1940 to present. Copernicus Climate Change Service (C3S) Climate Data Store (CDS). DOI: https://doi.org/10.24381/cds.adbb2d47

Hobday, A. J., Alexander, L. V., Perkins, S. E., Smale, D. A., Straub, S. C., Oliver, E. C. J., Benthuysen, J. A., Burrows, M. T., Donat, M. G., Feng, M., Holbrook, N. J., Moore, P. J., Scannell, H. A., Sen Gupta, A., & Wernberg, T. (2016). A hierarchical approach to defining marine heatwaves. Progress in Oceanography, 141, 227 – 238. DOI: https://doi.org/10.1016/j.pocean.2015.12.014

IPCC, 2022: Climate Change (2022): Impacts, Adaptation, and Vulnerability. Contribution of Working Group II to the Sixth Assessment Report of the Intergovernmental Panel on Climate Change [H.-O. Pörtner, D.C. Roberts, M. Tignor, E.S. Poloczanska, K. Mintenbeck, A. Alegría, M. Craig, S. Langsdorf, S. Löschke, V. Möller, A. Okem, B. Rama (eds.)]. Cambridge University Press. Cambridge University Press, Cambridge, UK and New York, NY, USA, 3056 pp. DOI: https://doi.org/10.1017/9781009325844.

Liu, X., He, B., Guo, L., Huang, L., & Chen, D. (2020). Similarities and Differences in the Mechanisms Causing the European Summer Heatwaves in 2003, 2010, and 2018. Earth's Future, 8(4). DOI: https://doi.org/10.1029/2019EF001386

Ribeiro, A. F. S., Russo, A., Gouveia, C. M., Páscoa, P., & Zscheischler, J. (2020). Risk of crop failure due to compound dry and hot extremes estimated with nested copulas. Biogeosciences, 17(19), 4815 - 4830. DOI: https://doi.org/10.5194/bg-17-4815-2020

García-Herrera, R., Díaz, J., Trigo, R. M., Luterbacher, J., & Fischer, E. M. (2010). A review of the European summer heat wave of 2003. Critical Reviews in Environmental Science and Technology, 40(4), 267-306. DOI: https://doi.org/10.1080/10643380802238137

Ruffault J., Curt T., Moron V., Trigo R. M., Mouillot F., Koutsias N., Pimont F., Martin-StPaul N., Barbero R., Dupuy J. L., Russo A., Belhadj-Khedher C. (2020) Increased likelihood of heat-induced large wildfires in the Mediterranean Basin. Scientific Reports (Nature Publisher Group), 2020, 10.1.

 DOI: https://doi.org/10.60620/wcqx-2d49

Spinoni, J., Naumann, G., Vogt, J. v., & Barbosa, P. (2015). The biggest drought events in Europe from 1950 to 2012. Journal of Hydrology: Regional Studies, 3, 509–524. DOI: https://doi.org/10.1016/j.ejrh.2015.01.001

Stahl, K., Kohn, I., Blauhut, V., Urquijo, J., de Stefano, L., Acácio, V., Dias, S., Stagge, J. H., Tallaksen, L. M., Kampragou, E., van Loon, A. F., Barker, L. J., Melsen, L. A., Bifulco, C., Musolino, D., de Carli, A., Massarutto, A., Assimacopoulos, D., & van Lanen, H. A. J. (2016). Impacts of European drought events: Insights from an international database of text-based reports. Natural Hazards and Earth System Sciences, 16(3), 801 – 819. DOI: https://doi.org/10.5194/nhess-16-801-2016

Sutanto, S. J., Vitolo, C., di Napoli, C., D'Andrea, M., & van Lanen, H. A. J. (2020). Heatwaves, droughts, and fires: Exploring compound and cascading dry hazards at the pan-European scale. Environment International, 134. DOI: https://doi.org/10.1016/j.envint.2019.105276

Zscheischler, J., Westra, S., Van Den Hurk, B. J., Seneviratne, S. I., Ward, P. J., Pitman, A., ... & Zhang, X. (2018). Future climate risk from compound events. Nature Climate Change, 8(6), 469 - 477. DOI: https://doi.org/10.1038/s41558-018-0156-3

Formation of Pyrocumulus During a Megafire Event in Portugal Using the Coupled Atmosphere-Fire Spread Model Wrf-Sfire

Ricardo Vaz [1], Rui Silva [1], Susana Cardoso Pereira [1], Ana Cristina Carvalho [2], David Carvalho [1], Alfredo Rocha [1]

[1] *CESAM, Department of Physics, University of Aveiro,3810–193 Aveiro, ricardojorgevaz@ua.pt*
[2] *Swedish Meteorological and Hydrological Institute. Research Department. FoUmmk group. Folkborgsvägen 17, 603 80, Norrköping*

SUMMARY

Atmospheric properties are likely to be perturbed around a forest fire due to the heat and mass fluxes at the lower boundary, which may change the vertical properties of the atmosphere, namely static stability, among others. Increased instability may drastically change the dynamics of the atmosphere which eventually feedback on the fire and can lead to the formation of Pyro-cumulus (PyCu). Pyro-cumulus can generate precipitation, downdrafts, and lightning events, and have been linked with extreme fire growth, devastating firestorms, and even fire-induced tornados. Despite the significant research available on the PyCu micro-physics, little is known about the environmental controls on PyCu development. The main objective of this study is to understand the physical mechanisms and conditions favourable to the formation of PyCu during a mega-fire event that occurred in Portugal on 15 October 2017, near Figueira da Foz.

Keywords: WRF-SFIRE; Pyro convection; Wildfire.

1. Introduction

Portugal has been severely impacted by wildfires, making it the European hotspot in terms of burnt area, namely in the last two decades and often attributed to Climate Change (San-Miguel-Ayanz et al., 2021). Pyro convective events associated with wildfires have been on the rise, generated by an uptick in atmospheric instability (Senande-Rivera et al., 2022), such as in the Pedrogão Grande Fire, in June 2017, a newly arising off-season event, led by rising temperatures and decreasing water content in forest fuels (Couto et al., 2022).

Later into the 2017 fire season a large mega-fire event with widespread forest fires occurred across central Portugal, due to the proximity of hurricane Ophelia, offshore to the west, on October 15, 2017. As a consequence, insurance companies have registered 150 million euros in losses, with 51 fatalities as a consequence of wildfires (Viegas et al., 2019; Guerreiro et al., 2018).

During this event, strong south-easterly winds associated with the circulation of the tropical storm, advected dry and hot air, lowering the moisture of surface fuels and relative humidity (RH), adding up to a persistent drought that had been lasting since 2016 (Ramos et al., 2017). With a minimum central pressure of 964 hPa, southwest of the Iberian Peninsula, on October 15 at 00 UTC, the Ophelia cyclone increased its movement speed, bringing winds from the southeast, and advecting hotter North African air through its circulation. Temperatures between 34ºC to 36ºC, and RH values ranging from 10% to 20%were recorded by national weather stations, along the central coastal areas of Portugal (Simões et al., 2018). Later into the afternoon, a change in wind direction, from southeast to southwest, reduced temperatures, transporting oceanic air into

 DOI: https://doi.org/10.60620/h6cr-kr97

coastal areas and deeper inland, providing moisture for fire plumes to generate pyro-convection and fire spotting, especially in inland areas (Ramos et al., 2023). Coastal areas saw diminishing fire line intensities near night hours and, as a result, the wind became the main significant driver of fire spread (Guerreiro et al., 2018; Castellnou et al., 2018). To reproduce atmospheric conditions driving pyro-convection, one of the select fires from the 14 – 16 October 2017 multiple-event was chosen, the Quiaios Fire Complex. For that purpose, the coupled atmosphere-fire spread model Weather Research and Forecast–Spread Fire (WRF-SFIRE) was used. Results were analysed based on a thermodynamics point of view on the vertical and at the surface level.

2. Methodology

2.1. WRF-SFIRE

WRF-SFIRE is a two-way interaction, fully coupled atmosphere-fire spread-fuel moisture model, with real-time capabilities, allowing forcing elements of the atmosphere to drive the fire, and vice-versa, as they occur, transferring heat and mass, with impacts on fire progression speed and atmospheric stability (Mandel et al., 2011). This system has been previously validated (Kochanski et al., 2013), showing consistent results on the micro-scale, having been used operationally in Israel (Mandel et al., 2014) and Greece, in association with the Hellenic Fire Corps (Giannaros et al., 2020).

With WRF (Skamarock et al., 2019) being a well-known, tested, and validated mesoscale model at its core, it allows the study and simulation of the most extreme interactions between atmosphere and fires, allowing the coupled SFIRE to capitalize on these advantages as a dynamic mesoscale model. SFIRE works on a finer mesh, with higher resolution than WRF's innermost domain, where burnt fuel fractions, topography, and fuel model data are interpolated. Fire propagation is done by a level-set function, fuel fraction and time of ignition as per Mandel et al. (Osher & Fedkiw, 2005). The wind is logarithmically interpolated from the first atmospheric level into a designated reference height for the fire. It supports zero-size ignition points so no overestimation of energy release from fuel-burning processes is forced by using a radius of ignition larger than sub grid resolution. The SFIRE module is also coupled to a simple moisture model (Mandel et al., 2014), using a simple time lag differential equation for moisture content, in which time lag (1h, 10h, 100h, etc) is defined as the amount of time required for a certain fuel to reach 2/3 of its equilibrium moisture state with the environment, which is calculated based on temperature, relative humidity and how water exchanges between fuels under those conditions. This formulation is based on Van Wagner & Pickett (1985).

2.2. Simulation Setup

As initial and boundary conditions for WRF-SFIRE, ERA-5 reanalyses were retrieved from the Copernicus Climate Data Store (Hersbach et al., 2020), with hourly frequency, 0.25° horizontal resolution and distributed in 37 vertical levels between 1 hPa and 1000 hPa. Three domains, one parent, and two nested (d01, d02, d03) were discretized around the study area as per **Figure 1**.

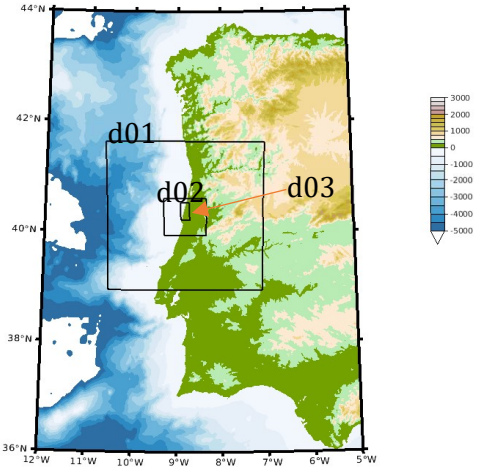

Figure 1. WRF domain nesting setup for the simulation.

Initial domain size was conservative given the proximity of a high-intensity tropical storm on the north-western edge of the domain. After some testing, computational errors, aka Courant-Friedrichs-Lewy (CFL), associated with high vertical speeds, made the simulation unstable. As an alternative, a smaller domain was used to prevent the model from directly resolving the storm, capturing only the adjacent wind field. This influenced the results as will be shown in 3.2.

DOI: https://doi.org/10.60620/h6cr-kr97

However, new results with different parametrization setups are already underway that have solved the computational errors. Each domain was attributed a resolution as follows; d01 – 7500 m; d02 – 1500 m; d03 – 300 m; sub grid – 30 m. Two simulations were performed as a means of comparison, one with fire ignition, and another with no fire.

2.3. Topographical and land use data

The land use data used in this study consists of the Corine Land Cover 2018 (CLC2018), with 44 classes and 100 m horizontal resolution, available at the Copernicus Land Monitoring Service Portal (https://land.copernicus.eu/) and remapped to the United States Geological Survey 24 (USGS24) land use classes, following Pineda et al. (2004), whilst topographical data used is the Shuttle Radar Topographic Mission (SRTM) dataset, with 90 m horizontal resolution at the equator. Both geographical datasets were ingested and interpolated for the different model domains grid by the WRF's model pre-processing system.

The fire spread module, SFIRE, requires both fuel map and topographical data with higher resolution than the one used in the atmospheric processes, integrated into the sub grid. Fuel maps with 100 m resolution were converted from the National Fuel Model into the more standardized National Forest Fire Laboratory (NFFL) 13, described by Anderson (1981) and parametrized by Rothermel (1972) and Albini (1976). Topographical data, with 25 m resolution, was obtained from the European-Digital Elevation Model (EU-DEM), v1.1. from the Copernicus Land Monitoring Service Portal.

2.4. Ignition and SFIRE initial conditions

Ignition points were retrieved from a 15th October report on the fires (Viegas et al., 2019) for two locations, Cova da Serpe, and one secondary ignition point east of Praia da Costinha, initialized at 13H30 UTC (14H30 Local Time - LT), and 14H30 UTC (15H30 LT), respectively. The fuel moisture model coupled to SFIRE was not used to initialize fuel moisture given a previous test simulation. Instead, to characterize an extreme fire progression scenario, surface fuel moisture was set at 4%, as the most extreme value over the course of the event, from (Viegas et al., 2019), as discussed later in the results.

3. Results and discussion

3.1. Fire Progression and Intensity

The Quiaios Fire complex was one of the most intense and quickly progressing fires on October 15, 2017. This complex was initially driven by the wind with pyro-convective periods (Guerreiro et al., 2018), where the power of the wind was the main driver in fire spread rather than the power of the fire, as referred to by Byram (1954). Multiple ignitions associated with this fire complex developed near Vagos and Praia de Mira, with much lesser burnt extent and impact.

The two most important ignitions were used to start the fire, in Cova da Serpe, and a resulting secondary ignition near Praia da Costinha. Isochrones of fire spread are shown in **Figure 2**. Between 14H00 to 16H00 UTC fire expansion was slower, with winds from the southwest driving the spread's direction.

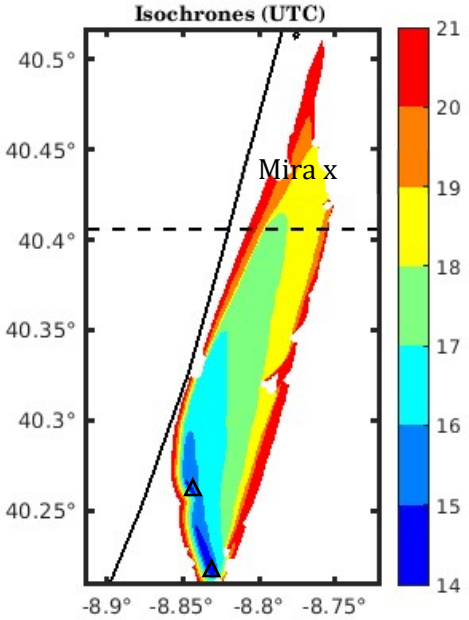

Figure 2. The simulated fire spread isochrones in hours UTC. The dashed horizontal lines denote the direction of a zonal profile, to be shown in **Figure** 4. Black triangles show ignition points.

After 16H00 UTC, (17H00 LT) both ignitions merged and fire progression speeds up significantly, peaking between 16H00 to 19H00 UTC (17H00 to 20H00 LT). After 19H00 UTC, the fire hits a standstill near Mira

DOI: https://doi.org/10.60620/h6cr-kr97

(marked in **Figure 2**), with little progression seen afterwards as winds shift to the southwest, and no more fuel is available. Compared to the real fire, in (Viegas et al., 2019), the simulated fire was significantly faster in spreading, reaching Mira 1 hour before observed.

3.2. Atmospheric surface feedback

As the fire evolved, it showed significant impacts on the surface wind speed, direction, temperature, and water vapour.

Figure 3 shows surface simulation outputs of fire intensity and ground heat fluxes, and how they affected water vapour content, temperature, and wind, compared with the no-fire simulation. During the first hours, between 13H30 to 15H30 UTC, the fire displayed little intensity fluctuations, with fire-line intensities of approximately 15000 kW/m. This corresponds to the period of slower spread mentioned previously, between 14H00 to 16H00 UTC.

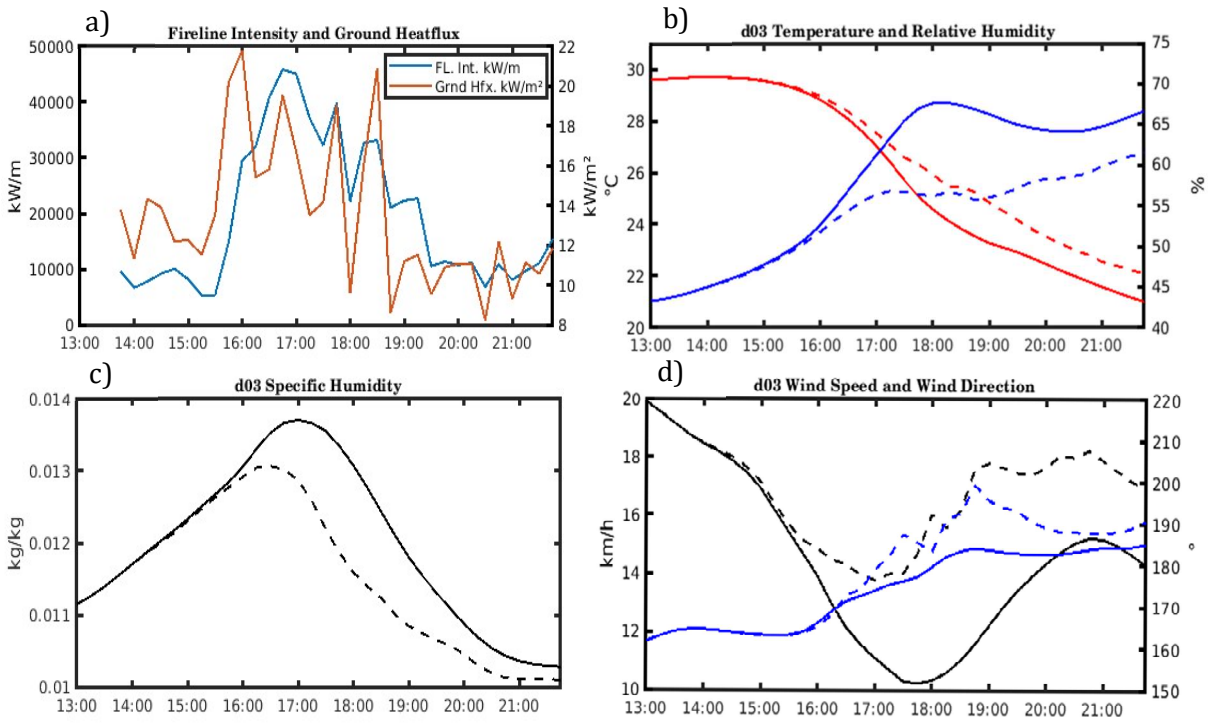

Figure 3. In a) Average fire-line intensity(kW/m) along the fire front, in every spread direction, and ground heat-flux (kW/m²) from the fire into the atmosphere between fire start and 22 UTC; b), c), and d), bold lines denote the results from the no-fire simulation while dashed lines represent the simulation with fire, and with the panels representing: b) Average surface temperature (**°C**), in red, and relative humidity (%), in blue in d03; c) Average surface specific humidity (kg/kg) in d03; d) In black, average wind speed (km/h), and in blue, the average meteorological wind direction (**°**), in d03.

Specific humidity over the surface (~20 m) displays minor to no decreases, with horizontal wind speed and direction mostly unaffected. Temperature showed small increases near 16H00 UTC as the fire grew but with little to no impact. As the two fronts merged, a very unstable and erratic period sets in between 16H00 and 19H00 UTC, with fire line intensities peaking as high as 50000 kW/m right before 16 UTC, showing pronounced fluctuations in the 10000 and 50000 kW/m range. It is after 16H00 UTC that surface water vapour content drops by nearly 0.01 kg/kg, from nearly 0.014 to 0.013, keeping the differences until later in the afternoon, when compared to a no-fire scenario. At 19 UTC, values slowly begin to converge until the end of the simulation period.

Temperatures quickly increase by roughly 1 °C as the fire intensity picks up, lowering the relative humidity to about 10%. As Ophelia tracked offshore, the simulated wind directions shifted between 160° to 185°, although this shift is much less evident than in (Viegas et al., 2019), where it is shown that as the measured winds shifted further west towards 220° – 240°, from Figueira da Foz,

the closest weather station representative of the fire.

Average wind speeds in d03 were lower than in Figueira da Foz's observations. As the weather station does not feature within the d03, comparing averaged values over land may not yield the most accurate results, given that Figueira da Foz is a coastal city, less affected by the wind attenuation from the land surface. Looking into how the fire affected surface wind, between 17H00 to 19H00 UTC, multiple shifts are shown to have occurred, in contrast to the steadier change in wind direction in the no-fire scenario. However, the fire has been shown to have anticipated and strengthened the turn to the western quadrant, increasing speed significantly and altering the synoptic wind pattern. Halting its progression past 19H00 UTC, the fire line intensity slowly subsided to 10000 kW/m, as specific humidity, wind speed, direction, temperature and relative humidity began converging into what would have been a no-fire scenario. Retrospectively looking into the surface temperatures and humidity, simulations show a large underestimation of at least 4°C and an overestimation of 30%, respectively.

The Rothermel fire spread model is highly sensitive to fuel moisture and thus, as mentioned in § 2.4, switching on the fuel moisture model coupled to SFIRE would produce major overestimations of fuel moisture, impacting fire intensity and energy fluxes, responsible for the formation of pyro-convection.

To overcome it, a set of 4% fuel moisture was used, which may have overestimated fire progression given it does not evolve with surface temperature and humidity conditions under this scenario. Given this constraint, this case study should be taken as a more idealized simulation rather than a study that accurately tries to reproduce the conditions that occurred on that day, despite being in line with the reality on many levels.

3.3. Impacts on the atmospheric vertical profiles and Pyro-cumulus formation

Looking into the atmosphere from a vertical perspective, the same pattern is observable, with most changes occurring between 16H00 to 19H00 UTC. **Figure 4a** shows a space-averaged temperature and specific humidity differences time series between fire and no fire simulations, at 3 different heights. It is visible that the fire began having a more vertical impact on the atmosphere past 16H00 UTC, as intensity peaked, with temperatures at 500m and 1500m heights increasing by around 0.1°C. Simultaneously, water vapor was advected vertically increasing specific humidity by 0.1 to 0.2 g/kg.

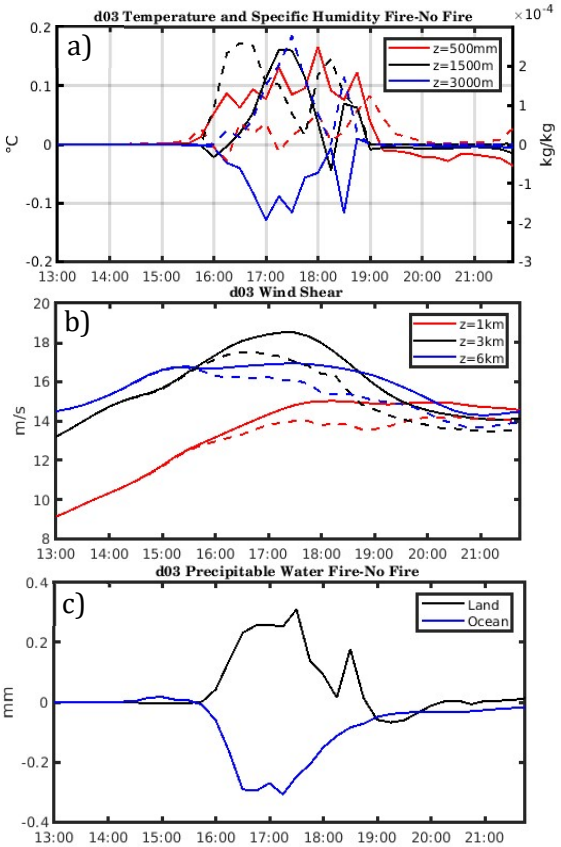

Figure 4. In b), bold denotes the results from a no-fire simulation while dashed represents a simulation with fire. a) Average temperature (°C) differences between the fire and the no fire simulation, at 500, 1500, and 3000 m heights, in d03, in bold. Average specific humidity (kg/kg) differences between fire and no fire simulation in d03, dashed. b) Wind shear at 1 km,3 km and 6 km heights, averaged over d03. c) Averaged differences between the fire and no-fire simulations in d03 for precipitable water (mm) over land and ocean.

The temperature at 1500 m had a time lag of approximately 1 hour in reacting to heat advection when compared to the 500 m height, however, moisture began increasing in this layer earlier, at the same time as the temperature began rising at 500 m height. A very small decline in temperature at 1500 m is noticeable, roughly between 15H45 and

DOI: https://doi.org/10.60620/h6cr-kr97

16H15 UTC, denoting cooler and moister air was being advected vertically at an initial stage. Looking into the 3000 m height layer, the reverse happens, with temperature decreasing by 0.1°C, also accompanied by increasing moisture. In this layer, a small, punctual increase in temperature happens soon after 18H00 UTC as moisture decreases, which may signal condensation heat release by cloud formation.

By the end of the highest fire intensity period, past 19H00 UTC, temperature and moisture normalize at all levels, except for the 500 m layer, displaying slightly cooler values. Looking into **Figure 4b**, wind shear speeds reduced as the fire grew more intense, lasting into the later hours, and peaking at 17H00 to 18H00 UTC.

Figure 3d shows the fire influencing surface wind speed, which seems to be the main reason for the diminishing vertical wind shear. High sheer values are associated with higher convective storm longevity, creating stronger and wider updrafts while regenerating the storm by forcing air to ascend back into the Level of Free Convection (LFC), releasing more latent heat. During peak intensity hours, 3 km wind shear was the most intense, nearing values of 18 m/s, displaying the potential of events of severe wind gusts (Pucik et al., 2021; Alfaro 2017).

The process of air advection is shown in the **Figure 5** series, taken along a zonal vertical profile marked in **Figure 2**. Moist air begins ascending over the sea at 15H45 UTC near - 8.55°. By 16H30 UTC, the air mass moves eastward towards land, denoting a visible temperature difference when compared to a no-fire simulation. Warmer zones are also advected ahead of the fire underneath the high moisture area. At 17H30 UTC, a cloud develops, above 3 km height, with roughly 1 km vertical extension. Strong synoptic wind from the south continues to drag the system northward as the fire front closes in warming the air vertically until the 2 km height. Shading oversaturation shows that a large column of air, warmer than 2.25°C, managed to reach as high as 1 km as heat is released from combustion, producing more vertical advection of moisture.

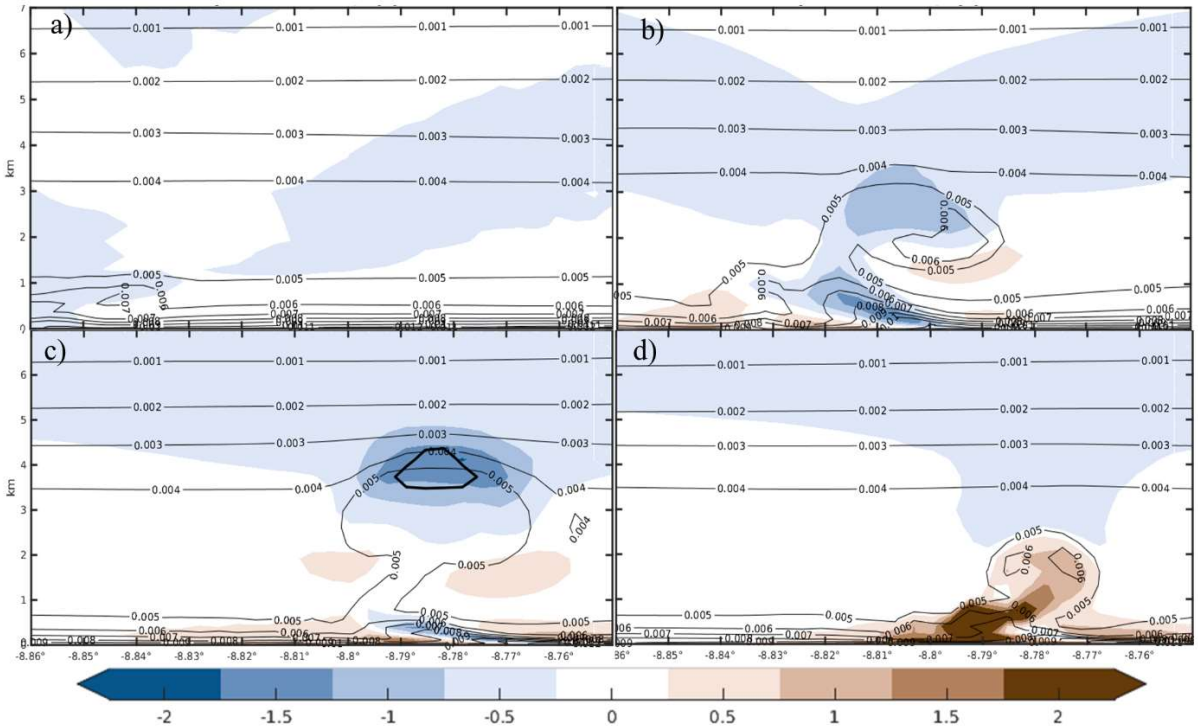

Figure 5. a), b), c), and d) show a vertical zonal profile, taken along the dashed line marked in **Figure** 2, with shaded temperature (°C) differences between the fire and no-fire simulations and specific humidity (kg/kg) contours for the fire simulation. for a) 15H45 UTC; b)16H30 UTC; c) 17H30UTC; d) 17H45 UTC. The bold black line represents the presence of hydrometeors to assess cloud formation as follows: water, snow, graupel, and ice.

Tracking back to **Figure 4 c** we can see how integrated precipitable water over land increases while decreasing from the ocean, confirming that indeed moisture was transported from the ocean into the land. Cooler and moisture-rich air lifting then gave way to the formation of scattered pyCu, as seen in **Figure 6**.

Between 17H00 to 17H45 UTC, convective clouds formed, producing precipitation at around 17H30 UTC, shown by a white column of hydrometeors reaching the surface. While no precipitation was reported, differences between simulation and reality, given by lower temperatures and higher relative humidity, provided a richer environment for convective cloud formation. Coupled with the overestimation of energy release from the surface fire, by using static fuel moisture of 4%, these factors may have contributed to the unrealistic formation of larger pyCu and potential pyCb by the later evening, as seen in **Figure 6 c**. However, it is hard to assess whether this structure continued to produce any precipitation as it most likely moved out of the range of the domain.

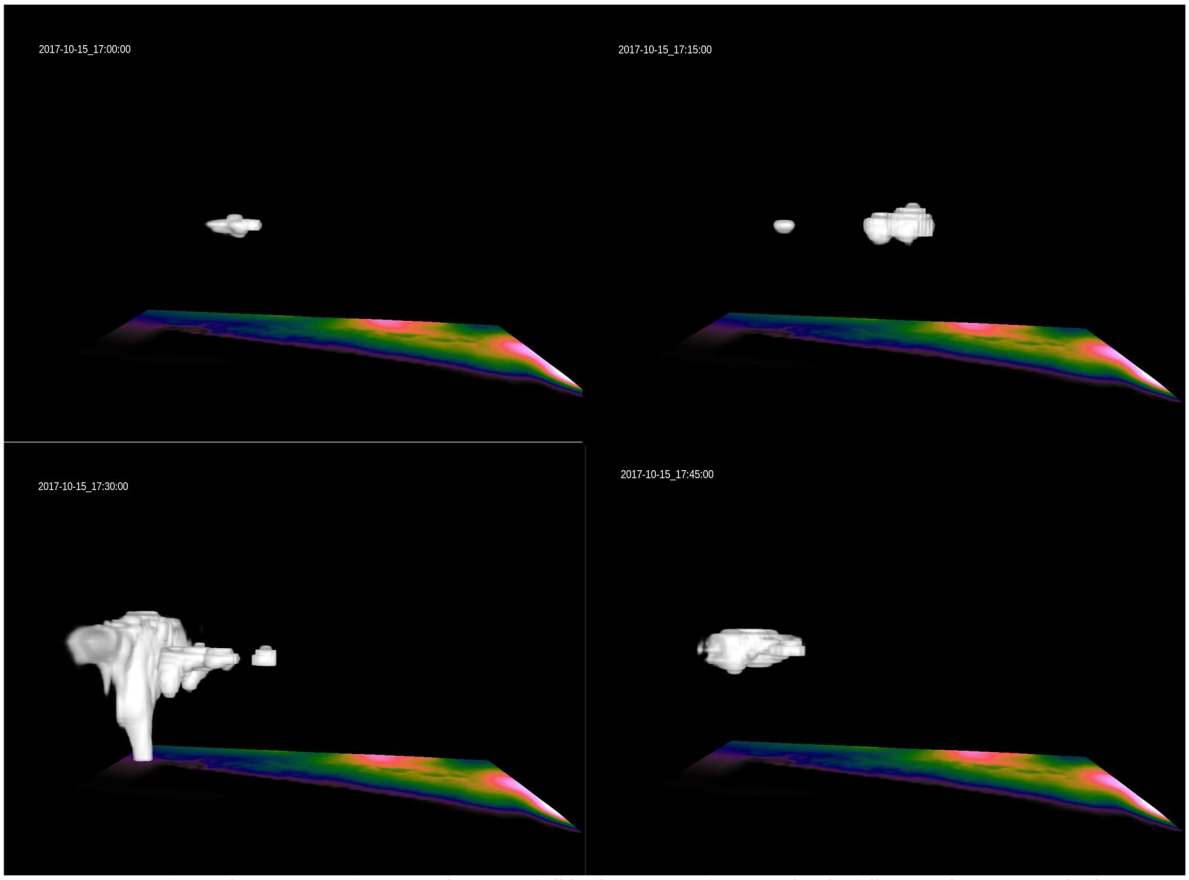

Figure 6. VAPOR (Li et al., 2019, 2023) 3D visualization of all hydrometeors forming clouds, following the same method as **Figure** 5, at a) 17H00 UTC; b) 17H15 UTC; c) 17H30 UTC; d) 17H45 UTC. In c) the extension of the hydrometeor column to the surface shows ground precipitation. These series show the evolution and formation of pyCu clouds.

Analyzing vertical profile differences from the skew-T in **Figure 7**, the inverse-shaped V is noted, similar to the soundings taken on October 15 (Guerreiro et al., 2018), although in this case, it rests upon a surface layer of high humidity, already shown to have been overestimated by the simulation. Nonetheless, above this level rests a very dry atmosphere that moistens with height, until roughly 600 hPa. This overestimation of surface moisture lowered the surface-based Lifted Condensation Level (LCL), which would otherwise be much higher. This type of "V" structure is known to promote dry microbursts as precipitation evaporates while falling and accelerates, directly affecting fire propagation (Li et al., 2023).

DOI: https://doi.org/10.60620/h6cr-kr97

Comparing **Figure 7a** to **7b**, it is seen that at the beginning of the afternoon surface temperatures were too far below the Convective Temperature (CT) to initiate lifting, with the LCL around 75 hPa lower than the Convective Condensation Level (CCL). Even though according to Lareau and Clements, cloud formation height from wildfires is best assessed from the CCL level (Wakimoto 1985),

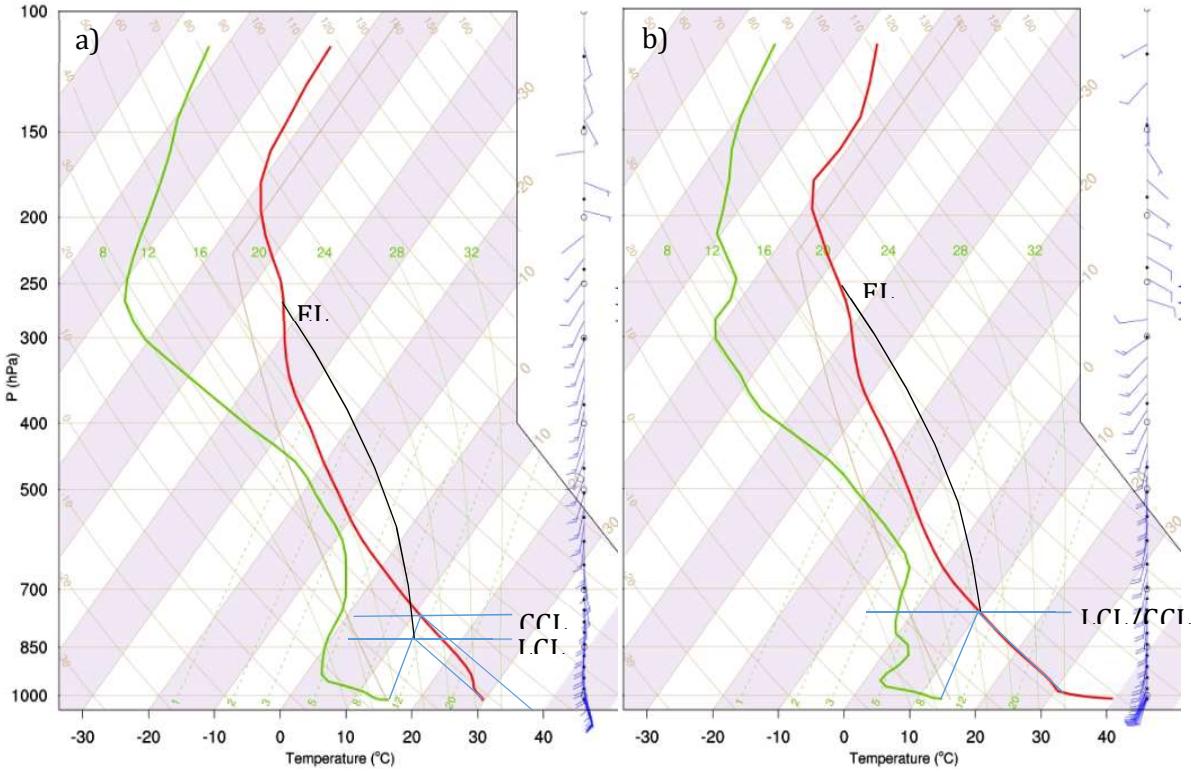

Figure 7. Skew-t vertical profiles showing dew point temperature (°C) in green and environmental temperature (°C) in red. In a) horizontal blue lines show the LLC, CCL, and Equilibrium Level (EL) heights at 13H00 UTC at -8.79°W,40.41°N. In b) the same profile is taken at 18H00 UTC as the fire line crosses this location. In this case, LCL and CCL overlap.

Figure 8 shows that the cloud base from initial pyCu development appears to be located at around 3500 m, around 1000 m higher than the CCL from **Figure 7a**.

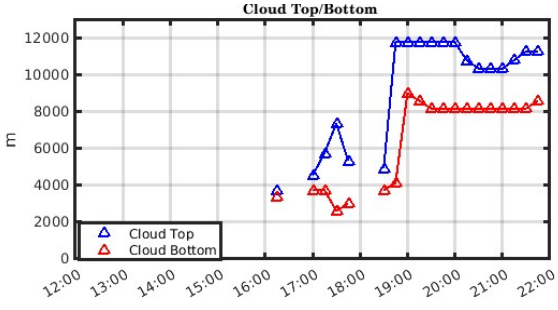

Figure 8. Cloud top and bottom heights (m), taken from hydrometeor aggregates, as in **Figure** 6, excluding rain.

However, this may be due to the height at which the colder and more vapour-rich oceanic air got advected, which seems to agree with the zonal profile from **Figure 5c**.

Furthermore, **Figure 7b** shows that as the fire approached and cooler air was transported over it, the LCL moved up towards the CCL, by increasing the environmental lapse rate to the dry adiabatic (9.8°C/km), turning the environment unstable.

Very shallow pyCu started growing between 16H00 and 17H30 UTC, up to a thickness of roughly 5 km, with the cloud base dropping to 2500 m as conditions became more favourable, coinciding with the CCL at this hour, and producing some local precipitation. After 19H00 UTC with the fire dying down due to a lack of combustible material, energy release dropped significantly and any pyro-convection collapsed. High clouds began to roll in above 8 km as the last pyCu dissipated, at 18H30 UTC.

DOI: https://doi.org/10.60620/h6cr-kr97

The entire process can be seen from a 3D perspective, in **Figure 9**, with strong southerly winds rising vertically from the fire column, forming a clockwise vortex. Zonal and vertical wind components show how moisture was transported and lifted around that vortex, also visible by the wind streamlines as they spin from the head of the fire towards the north, where cloud formation happens.

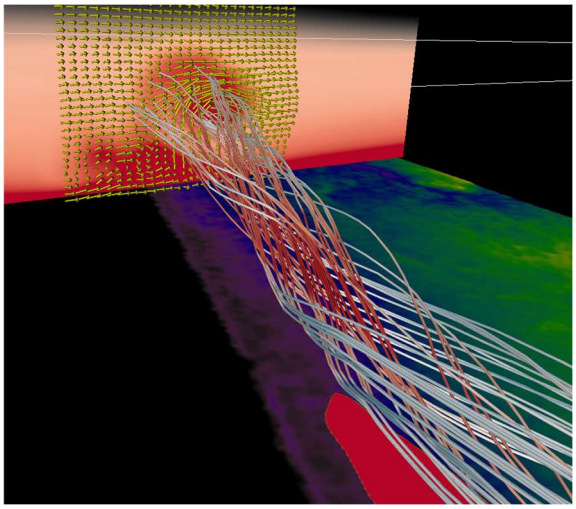

Figure 9. VAPOR Imaging of wind streamlines moving over a vortex, with red values meaning positive vertical wind speed and blue values negative, with saturation as a scale of magnitude. Arrows show the U and W components of wind. The vertical cross-section shows the specific humidity, with saturated colours being a measure of higher values. The red patch over the surface to the south shows the head of the fire area as the wind lifts the streamlines south to north.

4. Conclusion

As a case study with similarities to reality, this work sheds some light on how the formation of pyro-convection may occur near the ocean, in highly energetic and sheared environments.

Fire intensity was heavily linked to wind speed increases and shifting direction, forcing moisture and heat advection from the ocean. Temperature underestimation and surface humidity overestimation made it impossible to use the fuel moisture model to assess fuel moisture, and as such, imposing extremely low moistures (4%) may have had a big impact on energy release from fire, developing the pyCu more than what was observed in reality. The fire was shown to be able to control its weather in the vicinity, fueling cloud formation in more ways than simple surface air advection, as seen from the moisture transport between ocean and land. Fluxes in the lower troposphere, below 700 hPa, induced by the fire also show how an unstable atmosphere can be created from surface heating and upper cooling, generating an environment prone to non-mechanical lifting. Improvements to current simulations are underway and will hopefully shed a more accurate light on how the formation of these clouds and how they impact the weather. Ultimately, the Quiaios fire complex was chosen because pyro-convection was not the main driver of the fire yet a byproduct of it, making it an easier case study than, for example, the Lousã fire, which would require very accurate convection modelling by WRF-SFIRE, where pyro-convection played a critical role in fire spotting and expansion (Viegas et al., 2019).

5. Acknowledgements

Ricardo Vaz acknowledges the FCT/MCTES for the financial support for his PhD fellowship under the R&D project CLING with the reference PTDC/EME-REN/34690/2021.

The authors acknowledge the FCT/MCTES for the financial support to CESAM (UIDP/50017/2020 + UIDB/50017/2020), through national funds.

Rui Silva acknowledges the Portuguese Foundation for Science and Technology (FCT) for his PhD Grant (SFRH/BD/139020/2018).

Susana Cardoso Pereira acknowledges the EEA Grants for her researcher contract (FoRES – Development of Forests RESilience to fires in a climate change scenario, 04_Call#5_FoRES_UAveiro).

Susana Cardoso Pereira is a working member of COST Action CA 18135 – FireLINKS (WG Member CA18135 – Fire dynamics and prevention).

David Carvalho acknowledges the Portuguese Foundation for Science and Technology (FCT) for his research contract (CEECIND/00563/2020).

6. References

Albini, F. A. (1976). Estimating wildfire behavior and effects (Vol. 30). Department of Agriculture, Forest Service, Intermountain Forest and Range Experiment Station.

 DOI: https://doi.org/10.60620/h6cr-kr97

Alfaro, D.A., (2017). Low-tropospheric shear in the structure of squall lines: Impacts on latent heating under layer-lifting ascent. Journal of the Atmospheric Sciences, 74, 229 – 248. DOI: https://doi.org/10.1175/JAS-D-16-0168.1

Anderson, H. E. (1981). Aids to determining fuel models for estimating fire behavior (Vol. 122). US Department of Agriculture, Forest Service, Intermountain Forest and Range Experiment Station.19-Rothermel, R.C. (1972) A Mathematical Model for Predicting Fire Spread in Wildland Fuels; Intermountain Forest & Range Experiment Station, Forest Service, US; Vol. 115.

Byram, G.M. (1954). Atmospheric conditions related to blowup fires. Station Paper SE-SP-35. Asheville, NC, USDA-Forest Service, Southeastern Forest Experiment Station, 36 pp

Castellnou, M., Guiomar, N., Rego, F., & Fernandes, P. M. (2018). Fire growth patterns in the 2017 mega fire episode of October 15, central Portugal. Advances in forest fire research, 447-453. DOI: https://doi.org/10.14195/978-989-26-16-506_48

Couto, F. T., Santos, F. L. M., Campos, C., Andrade, N., Purificação, C., & Salgado, R. (2022). Is Portugal Starting to Burn All Year Long? The Transboundary Fire in January 2022. Atmosphere, 13(10), 1677. DOI: https://doi.org/10.3390/atmos13101677

Giannaros, T. M., Lagouvardos, K., & Kotroni, V. (2020). Performance Evaluation of an Operational Rapid Response Fire Spread Forecasting System in the Southeast Mediterranean (Greece). Atmosphere, 11(11), 1264. DOI: https://doi.org/10.3390/atmos11111264

Guerreiro, J., Fonseca, C., Salgueiro, A., Fernandes, P., Lopez-Iglésias, E., de Neufville, R., & Moura, J. M. (2018). Avaliação dos incêndios ocorridos entre 14 e 16 de outubro de 2017 em Portugal Continental. Relatório Final, 274.

Ramos, A. M., Russo, A., DaCamara, C. C., Nunes, S., Sousa, P., Soares, P. M. M., Lima, M. M., Hurduc, A., & Trigo, R. M. (2023). The compound event that triggered the destructive fires of October 2017 in Portugal. Iscience, 26(3). DOI: https://doi.org/10.1016/j.isci.2023.106141

Guerreiro, J., Fonseca, C., Salgueiro, A., Fernandes, P., Lopez-Iglésias, E., de Neufville, R., Mateus, F., Castellnou Ribau, M., Sande Silva, J.; Moura, J. M., Castro Rego, F., Caldeira, D. N. (2018). Avaliação dos incêndios ocorridos entre 14 e 16 de outubro de 2017 em Portugal Continental. Relatório Final, 274.

Hersbach, H., Bell, B., Berrisford, P., Hirahara, S., Horányi, A., Muñoz-Sabater, J., Nicolas, J., Peubey, C., Radu, R., Schepers, D., Simmons, A., Soci, C., Abdalla, S., Abellan, X., Balsamo, G., Bechtold, P., Biavati, G., Bidlot, J., Bonavita, M., … Thépaut, J. (2020). The ERA5 global reanalysis. Quarterly Journal of the Royal Meteorological Society, 146(730), 1999–2049. DOI: https://doi.org/10.1002/qj.3803

Kochanski, A. K., Jenkins, M. A., Mandel, J., Beezley, J. D., Clements, C. B., & Krueger, S. (2013). Evaluation of WRF-SFIRE performance with field observations from the FireFlux experiment. Geoscientific Model Development, 6(4), 1109–1126. DOI: https://doi.org/10.5194/gmd-6-1109-2013

Li, S., Jaroszynski S., Pearse S., Orf L., Clyne, J. (2019). VAPOR: A Visualization Package Tailored to Analyze Simulation Data in Earth System Science. Atmosphere. 10(9):488. DOI: https://doi.org/10.3390/atmos10090488

Li, S., Stas, J., Daves, J., Hallock, K., Eroglu, O., Poplawski, O., & Lacroix, L. (2023). NCAR/VAPOR: Vapor 3.8.1 (3.8.1). Zenodo. DOI: https://doi.org/10.5281/zenodo.7779648

Mandel, J., Amram, S., Beezley, J. D., Kelman, G., Kochanski, A. K., Kondratenko, V. Y., Lynn, B. H., Regev, B., & Vejmelka, M. (2014). Recent advances and applications of WRF–SFIRE. Natural Hazards and Earth System

Sciences, 14(10), 2829 – 2845. DOI: https://doi.org/10.5194/nhess-14-2829-2014

Mandel, J., Beezley, J. D., & Kochanski, A. K. (2011). Coupled atmosphere-wildland fire modeling with WRF 3.3 and SFIRE 2011. Geoscientific Model Development, 4(3), 591 – 610. DOI: https://doi.org/10.5194/gmd-4-591-2011

Osher, S., & Fedkiw, R. P. (2005). Level set methods and dynamic implicit surfaces (Vol. 1). New York: Springer.

Pineda, N., Jorba, O., Jorge, J., & Baldasano, J. M. (2004). Using NOAA AVHRR and SPOT VGT data to estimate surface parameters: application to a mesoscale meteorological model. International journal of remote sensing,25(1), 129 - 143. DOI: https://doi.org/10.1080/0143116031000115201.

Pucik, T., Groenemeijer, P., & Tsonevsky, I. (2021). Vertical wind shear and convective storms. DOI: https://doi.org/10.21957/Z0B3T5MRV

Ramos, A. M., Russo, A., DaCamara, C. C., Nunes, S., Sousa, P., Soares, P. M. M., Lima, M. M., Hurduc, A., & Trigo, R. M. (2023). The compound event that trig-gered the destructive fires of October 2017 in Portugal. IScience, 26(3), 106141.

Rothermel, R.C. A Mathematical Model for Predicting Fire Spread in Wildland Fuels; Intermountain Forest & Range Experiment Station, Forest Service, US, 1972; Vol. 115.

San-Miguel-Ayanz, Jesús., Durrant, T., Boca, R., Maianti, P., Libertà, G., Artés Vivancos, Tomàs., Oom, D., Branco, A., Tomàs. Rigo, D., & Ferrari, D. (2021). Forest Fires in Europe, Middle East and North Africa 2020. Publications Office of the European Union.

Senande-Rivera, M., Insua-Costa, D., & Miguez-Macho, G. (2022). Towards an atmosphere more favourable to firestorm development in Europe. Environmental Research Letters, 17(9), 094015. DOI: https://doi.org/10.1088/1748-9326/ac85ce

Simões, I., Pinto, P., Silva, Á., Pereira, M., Barroso, C., Santos, M.; Lopes, M., Moreira, N., Correira, S. (2018). Os Incêndios Florestais de 14 a 16 de outubro de 2017 em Portugal Continental. IPMA.

Skamarock, W. C., Klemp, J. B., Dudhia, J., Gill, D. O., Liu, Z., Berner, J., Wang, W., Powers, J. G., Duda, M. G., Barker, D. M., & Huang, X.-Y. (2019). A Description of the Advanced Research WRF Model Version 4. UCAR/NCAR. DOI: https://doi.org/10.5065/1DFH-6P97

Van Wagner, C. E. and Pickett, T. L.(1985). Equations and FORTRAN Program for the Canadian Forest Fire Weather Index System, Forestry Technical Report 33, Canadian Forestry Service, Ottawa.

Viegas, D. X., Almeida, M. F., Ribeiro, L. M., Raposo, J., Viegas, M. T., Oliveira, R., ... & Viegas, C. X. (2019). Análise dos Incêndios Florestais Ocorridos a 15 de outubro de 2017. Centro de Estudos sobre Incêndios Florestais (CEIF/ADAI/LAETA).

Wakimoto, R.M. (1985) Forecasting Dry Microburst Activity over the High Plains. Mon. Weather Rev., 113, 1131–1143.

 DOI: https://doi.org/10.60620/h6cr-kr97

Smoke Dispersion in the October 2017 Forest Fires in Mainland Portugal: Validation of Numerical Simulations

Paulo Pinto [1], João Rio [1], Carla Gama [2], André Barreirinha [1], Manuel Lopes [1], Maria José Monteiro [1], Tobias Osswald [2], Lourdes Bugalho [1], Ana Miranda [2]

[1] *IPMA. I.P., Rua C do Aeroporto, 1749–077 Lisboa, lourdes.bugalho@gmail.com*
[2] *CESAM & Departamento de Ambiente e Ordenamento, Universidade de Aveiro, Campus Universitário de Santiago, 3810–193 Aveiro.*

SUMMARY

Biomass burning is an important source of gases and particulate matter (PM) that can significantly change local, regional and global atmospheric chemistry, with an impact on air quality and human health (Crutzen & Andreae, 1990). The wildfires that occurred in 2017 in Portugal, have raised awareness towards the need for further studies on the many relevant impacts of wildfires. Climate change is increasing the environment's vulnerability to extreme events*, such as those that enhance the likelihood of forest fires. The purpose of this study is to use data from WRF-CHIMERE model simulations and validate its results for the wildfire event that occurred in October 2017 in Central mainland Portugal.*

Key Words: Wildfire smoke; Particulate matter; PM10; CHIMERE-WRF; model validation; radar data.

1. Introduction

Forest fires are one of the main natural hazards in several regions of the globe, such as the USA, Australia, and the Euro-Mediterranean region, and have devastating impacts on the economy, climate, environment, public health and loss of life.

In the Mediterranean region, forest fires are frequent, especially in the summer months, and significantly impact the landscape, vegetation, soil and air quality (Francos et al. 2018; Novara et al. 2018). Portugal has been, in this region, one of the countries with the largest burned area. The average value of the total area burnt on the Portuguese mainland as a percentage of the total area burned in the set of five countries in the Euro-Mediterranean region (Portugal, Spain, France, Italy and Greece) exceeded in several years (2003, 2005, 2010, 2013 and 2017) the 50% figure (European Forest Fire Information System reports, 2001 to 2017).

Biomass burning is a major perturbation to atmospheric chemistry, strongly contributing to the global budgets of aerosols and trace gases. As it plays a significant role in the interannual variability of the atmospheric background composition (e.g., Spracklen et al., 2007; Jaffe et al., 2008; Monks et al., 2012), the emission of greenhouse gases and long-lived aerosols will affect the radiative balance and therefore will have an impact on the climate

The smoke from wildfires can negatively influence the health and well-being of exposed people (Heil and Golhammer, 2001; Keywood et al., 2015). Vulnerable people, namely those with respiratory illnesses, are at particularly high risk from prolonged smoke exposure. To protect the health of populations, it is crucial to provide near real-time information about the area covered by the smoke from wildfires and the concentration of atmospheric pollutants.

Currently, some numerical models allow the simulation of fire emissions to the atmosphere, their dispersion, and their impact on air quality. Smoke dispersion models are used to predict the behaviour and movement of smoke in the atmosphere. By accurately predicting smoke dispersion, these models help to minimize smoke's impact on public health by allowing the adoption of population exposure mitigation measures and the environment, making it an asset to government agencies, fire management

teams and other organizations that manage wildfires, and other smoke-producing events. One of the chemical and smoke dispersion models is the CHIMERE (Menut et al., 2021), which is an Eulerian chemical transport model. The CHIMERE model has been developed and distributed since 1999 and is currently used by more than 300 registered Institutes worldwide (Menut et al., 2021), as shown in **Figure 1**.

It is crucial to validate the outputs of a model to ensure that it will present a good performance in the future. Model validation is the process of determining whether the model accurately represents the system's behaviour (Aumann, 2007). Validation can be done regularly by determining whether the model output agrees with the observed data, and conceptually, by determining whether the theory and assumptions are justifiable (Rykiel, 1996).

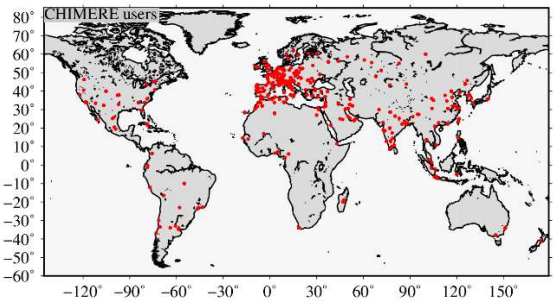

Figure 1. Distribution of users of the CHIMERE model, as of 2021. Menut et al., 2021.

However, validation is also a research process, as the origin of the difference between the model's results and the observed data can have different causes: the physics and chemistry of the model itself, the quality of the input data, the way the input data is provided to the model and also the quality of the observed data.

In this study, we intend to validate the results of the WRF-CHIMERE for a particular case study: the fires that occurred in October 2017 in Central mainland Portugal. Numerical simulations have been performed with this modelling system for the target dates, and results were compared with available observations. Data from the Portuguese air quality monitoring network (QUALAR, https://qualar.apambiente.pt/) has been used, namely PM10 and O_3 concentrations, as well as weather radar data (from IPMA, I.P.). For validation, satellite data from the FRP (Fire Radiative Power), a product of LSASAF based on SEVIRI/MSG, with a temporal resolution of 15 minutes, was also used to indicate the time and approximate location of the wildfire's ignition.

2. Methods

2.1. Modelling system

CHIMERE is an open-source multiscale chemical transport model designed to analyze pollution episodes and simulations for emission control scenarios accurately. Several external forcings are needed to run a simulation: meteorological fields, primary pollutant emissions, and chemical boundary conditions. Using meteorological information and emission flows as input, CHIMERE computes the three-dimensional concentrations of pollutants in the atmosphere (**Figure 2**). The key processes affecting the chemical concentrations are emissions, transport (advection and mixing), chemistry, and deposition.

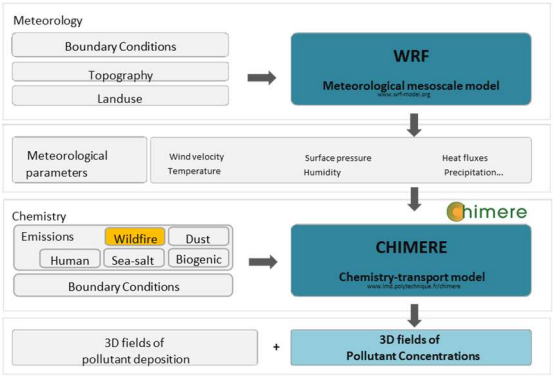

Figure 2. WRF-CHIMERE simulations run scheme.

Simulations were carried out with the forcing of meteorological conditions by the WRF model. Regarding pollutant emissions, two different scenarios were considered: (i) simulations with anthropogenic (e.g., traffic, industry, energy production, etc.), biogenic, desert dust, and sea salt emissions; and (ii) simulations with all emissions from the previous scenario, plus emissions associated with fires.

DOI: https://doi.org/10.60620/sed5-9y98

These two scenarios made it possible to distinguish between the dispersion of smoke and the presence of desert dust, which coexisted during the event, and to assess the contribution of the forest fire emissions to atmospheric pollution, considering the range of the most relevant atmospheric emission sources.

The CHIMERE model was run for two nested domains (D01 and D02), as shown in **Figure 3**. In the first domain, D01, the model has a horizontal resolution of 25 km, and the second domain has a resolution of 5 km. The simulation period was done from 6 to 20 October 2017, with 24 vertical levels (from surface to 200 hPa).

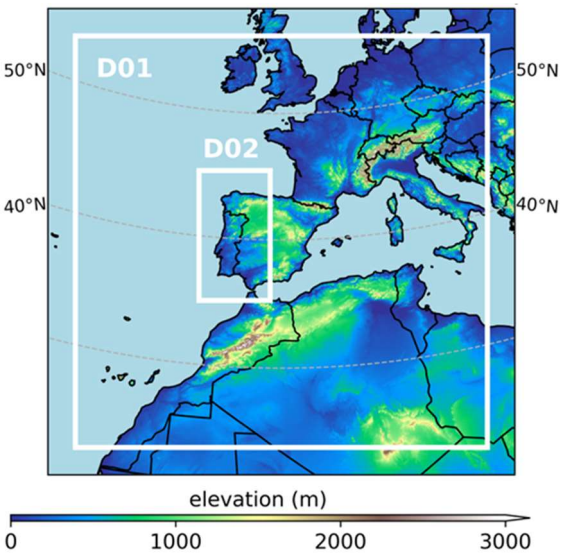

Figure 3. Spatial domains were used in this study.

2.2. Emissions from wildfires

Due to wildfires being highly variable in time and space, the calculation of emissions requires a numerical tool capable of estimating gas and particle emission flows, preferably on a kilometre scale and with an hourly time interval. This study used the APIFLAME model (Turquety et al., 2020) to estimate biomass burning emissions during October 2017.

The APIFLAME model resolves and generates input for the CHIMERE model with the desired temporal and spacing resolution, considering the following:

- Identification of burnt areas via satellite (in this case MODIS, with a resolution of 500 m);
- The type of vegetation (MODIS data, 500 m resolution), MODIS land use database, and vegetation type;
- Fuel consumption is the burnable fraction of the forest.

The input data for CHIMERE relies on this information, the emission factors associated with this information, and the height of smoke injection from wildfires, as shown in **Figure 4**.

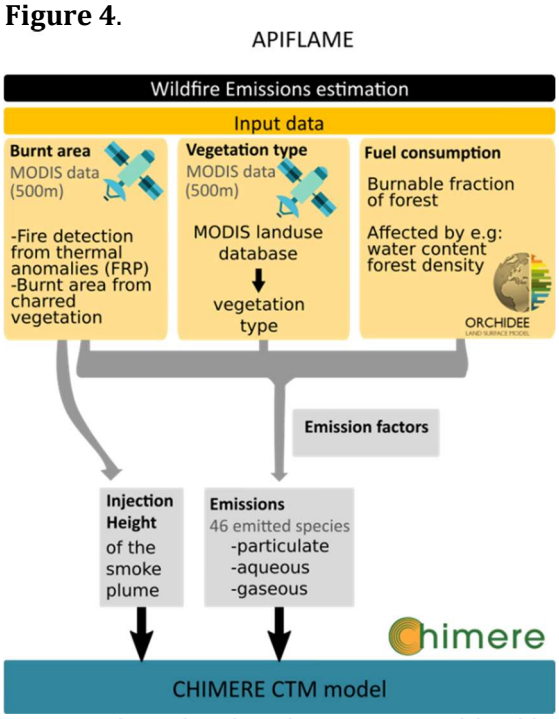

Figure 4. Scheme describing the APIFLAME model and how the data is provided to CHIMERE.

2.3. Air quality and radar data

Model results were compared with available observations, aiming at assessing model performance regarding the extent of the smoke plume and the concentrations of pollutants in the atmosphere.

Observations of particulate matter (PM10) and ozone (O_3) hourly concentrations were retrieved from surface air quality monitoring stations, from 6 to 20 October 2017. These stations are the responsibility of the Portuguese Environment Agency (APA) in coordination with the corresponding Commission for Coordination and Regional Development (CCDR). The data measured continuously at the various stations are

reported in near real-time and made available to the public through the QUALAR online database.

The comparison between modelled values and observations has been based on daily averages for PM10 and a daily maximum of eight-hour averages for O_3 concentrations, as these are the averaging periods of the Air Quality Standards defined for protecting human health, for these two pollutants.

Two Doppler meteorological radars from the IPMA network were accessed to analyze several fire plumes in the Central/North region of mainland Portugal on 15 October 2017, with the aim of early detection of plumes due to wildfires and comparison of the patterns with the output of the WRF-CHIMERE model.

FRP (Fire Radiative Power) product data, a product of LSASAF based on SEVIRI/MSG, with a temporal resolution of 15 minutes, was also used (https://landsaf.ipma.pt/en/products/fire-products/frppixel/).

2.4. Methodology for validating the CHIMERE simulations

The validation of the WRF-CHIMERE simulations was carried out:

- For daily values in the simulation period from 6 to 20 October 2017. In this case, the comparison was made between the concentration values of PM10 and near-surface ozone (O_3) and model outputs to the closest mesh point. In this paper, results are presented for four background air quality stations geolocated in the North and Central region of mainland Portugal, identified with red dots in **Figure 5**: Chamusca (CHA), Ervedeira (ERV), Montemor-o-Velho (MOV) and Douro Norte (DRN).
- For hourly values from 00UTC to 23 UTC on 15 October. In this case, the comparison was made between the simulation outputs and the pattern of smoke plumes detected by radar every 10 minutes, their location, and the height of the highest concentration of particles.

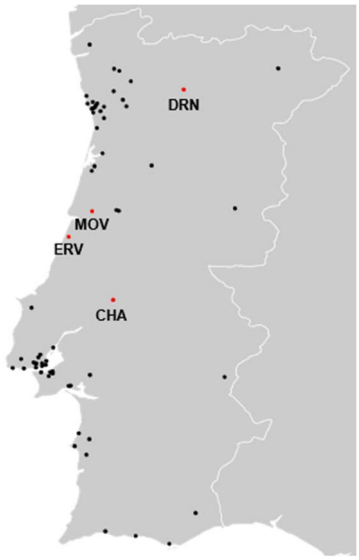

Figure 5. Air quality monitoring stations used for daily validation of WRF-CHIMERE, in red dots, simulations between 6th to 20th October 2017.

One of the radars, Arouca/Pico do Gralheiro (A/PG), is a dual polarization (DP) system located northeast of the observed plumes, with a beam around 1100 m a.m.s.l. (above mean sea level), while the other, Coruche/Cruz do Leão (C/CL), is a single polarization system located southeast of the plumes, with a beam around 200 m a.m.s.l. Low-level plane position indicators of reflectivity (PPZ) were extracted every 10 min to identify fire plume patterns. As fires intensify, heat flux increases combustion and buoyancy, and more pyrometeors are transported upward, according to Jones et al, (2010). Thus, the magnitude of low-level reflectivity observed near the fire site is a good indicator of the overall intensity of strong convective processes caused by fire. A/PG radar was additionally used to verify if the suspected patterns were originating from fire activity, based on the magnitude of the correlation coefficient that is processed in DP mode (Balakrishnan et al. (1990), Pinto et al. (2022)). Within the range of 100 km, the spatial resolution of the radar observations was 1 km or better. The evolution of plume patterns observed in the low-level PPZ was followed to compare with the CHIMERE simulations output.

Considering that one of the aspects to be validated in the simulations carried out with the WRF-CHIMERE model refers to the

 DOI: https://doi.org/10.60620/sed5-9y98

dispersion of smoke that started in the great wildfires on 15 October, it is important to know the time delay between the start of the fire and its detection with the radar and the corresponding beginning of the smoke in the simulation outputs.

To know the approximate time lapse between the start of the wildfire and the early detection by the radar in clear skies, several samples were taken from forest fires in 2016, 2017, and 2018, in Portugal, considering the official alert time by the national authorities (ICNF, Institute for Nature Conservation and Forests), **Table 1**.

Table 1. Time lag ("Desfas") between the instant of the wildfire alert (ICNF, Institute for Nature Conservation and Forests) and the instant of the first radar detection. "Ground difference" is the height from the ground level and the radar beam.

Stady Case	Date	Alert Time (ICNF, UTC)	Lat (pluma)	Long (pluma)	Radar	1ª det Radar	ground difference m	Desfas (min)
1	08-08-16	14:00	37,33	8,3	L/CC	14:10	500	10
2	07-09-16	16:00	40,64	7,8	A/PG	15:36	900	24*
3	17-06-17	13:43	39,96	8,16	C/CL	14:00	450	17
4	17-06-17	13:52	40	8,04	C/CL	14:00	200	08
5	17-07-17	14:51	39,89	7,97	C/CL	15:00	450	09
6	23-07-17	12:47	39,81	8,03	C/CL	12:50	450	03
7	19-08-17	14:18	40,25	7,51	C/CL	14:30	1200	12
8	**15-10-17**	**11:02**	**39,82**	**8,03**	**C/CL**	**11:00**	**400**	**02***
9	**15-10-17**	**07:41**	**40,16**	**8,21**	**C/CL**	**07:50**	**1150**	**09**
10	27-08-18	15:30	38,36	7,24	L/CC	15:40	1400	10
11	27-08-18	16:22	38,06	8,27	L/CC	16:36	1100	14

It can be concluded that, under clear skies, the time lag between the instant of the wildfire alert (ICNF base) and the instant of the first radar detection of the smoke associated with the same forest fire is short, nearly 20 minutes or less. This result is consistent with previous work (Bugalho et al., 2022), which compared hourly PM10 values observed at Air Quality stations and low-level radar reflectivity at those sites. Finally, to validate the delay in the onset of wildfire outbreaks from the outputs of the WRF-CHIMERE model, FRP (Fire Radiative Power) data were also used.

3. Results and Discussion

Figure 6 shows the daily accumulated PM10 biomass burning emissions estimated for 14 and 15 October 2017, based on APIFLAME output.

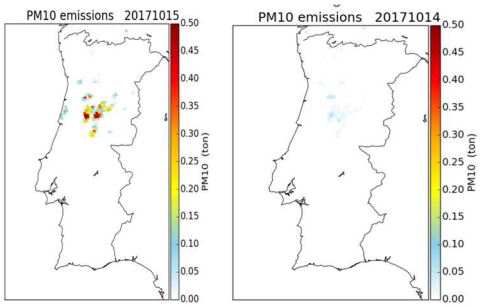

Figure 6. Daily accumulated PM10 emissions for 14 and 15 October 2017.

The impact of these emissions on air quality can be seen in **Figure 7** and **Figure 8**, which show the simulated concentrations of PM10 on 14 October 2017 at 00 UTC and on 15 October at 06 UTC, considering the whole range of the most relevant atmospheric emissions sources (**Figure 7**) and the pollution due to the forest fires emissions only (**Figure 8**). The forest fires are responsible for very high PM10 concentrations (> 100 μg/m³) in the Centre and North of Portugal.

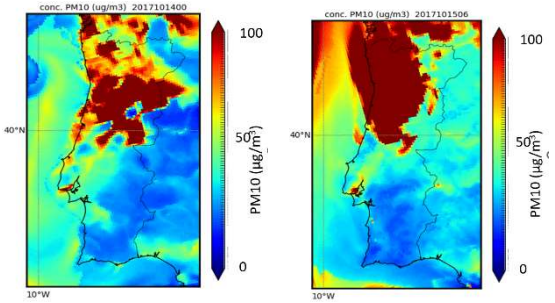

Figure 7. PM10 simulated concentrations considering the whole range of the most relevant atmospheric emissions sources, for 00 UTC on 14 October and 06 UTC on 15 October 2017.

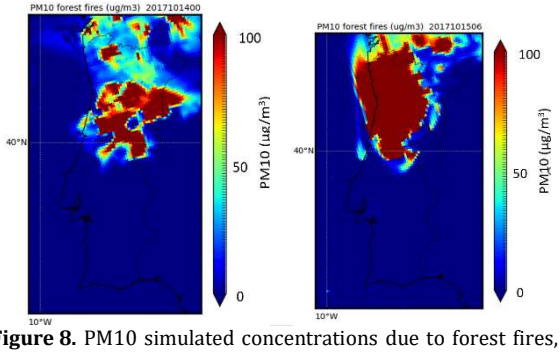

Figure 8. PM10 simulated concentrations due to forest fires, for 00 UTC on 14 October and 06 UTC on 15 October 2017.

3.1. Validation with Air Quality Stations

Air Quality stations can detect and monitor smoke episodes from large forest fires (Bugalho et al, 2022). An example can be seen in **Figure 9** for the forest fires that occurred in the district of Coimbra, where some stations in the Central Region detected high levels of particle concentration, PM10, associated with the large forest fires in June (with concentration levels of PM10 close to 200 µg m^{-3}, while the recommended limit for a daily average is 50 µg.m^{-3} (2008/50/EC)), and October 2017. In the latter, values of 1000 µg.m^{-3} in PM10 concentrations have been reached in some areas.

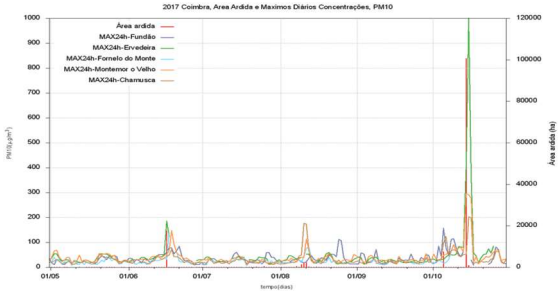

Figure 9. Observed concentrations of PM_{10} particles in the May/October 2017 period, in several air quality stations and total burnt area in the Coimbra district.

The comparison of the daily values of the output of the CHIMERE model simulations and the observed values in the stations of Chamusca (CHA), Douro Norte (DRN), Ervedeira (ERV) and Montemor-o-Velho (MOV) is shown in **Figure 10** and **Figure 11**, for PM10 and O_3, respectively. The location of these sites is available in **Figure 5**.

Figures 10–11 suggest that, overall, the model can simulate the background pollution levels in the atmosphere and the impact of forest fires on air quality, both for PM10 and O_3 (a secondary pollutant).

However, the model overestimates peaks of particle concentration (PM10) – except at the ERV station, of surface ozone (O_3) during the wildfires.

The Douro Norte station has no records of values during the fire period, from the 14th to the 17th of October, probably due to excessive pollution levels.

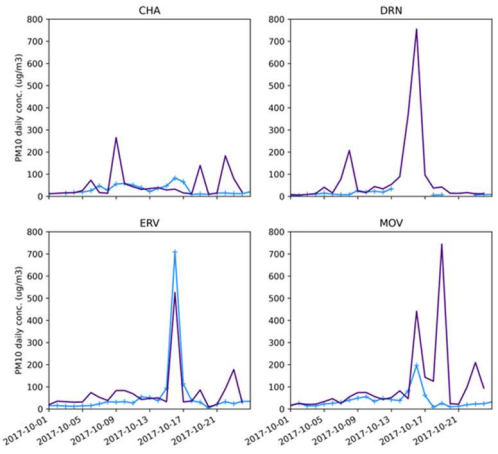

Figure 10. Observed (blue) and simulated purple) daily PM10 concentrations in selected air quality stations, during October 2017.

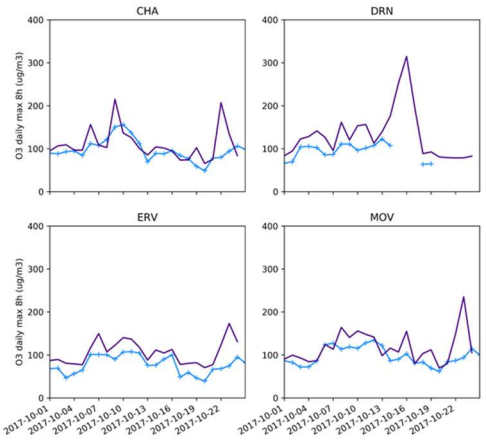

Figure 11. Observed (blue) and simulated (purple) daily O_3 concentrations in selected air quality stations, during October 2017.

3.2. Validation with Meteorological radar

To validate the hourly values of the WRF-CHIMERE simulation resulting only from the major forest fires' smoke on 15 October 2017, the start time of the smoke simulated by the model and the start time of the forest fires were compared.

Observing the hourly images of the outputs for PM10 of the WRF-CHIMERE simulation, it is visible that, on those simulations at 00 UTC, there are fires with great activity, as well as in the following hours. However, neither the radar detected fires in the region until 7:50 UTC nor the FRP (Fire Radiative Power), a product of the LSASAF, had a signal until 7:45

DOI: https://doi.org/10.60620/sed5-9y98

UTC, **Figure 12**. The first reported ignition in the region on 15 October 2017 was at 07:41 UTC (40.16N; 08.21W) in the Vilarinho Wildfire, (ICNF database). Coruche Radar data were analysed, namely the Z field (dBZ) and low elevation PPI, between 06:30-15:30 UTC (every 30 min) on 15 October 2017.

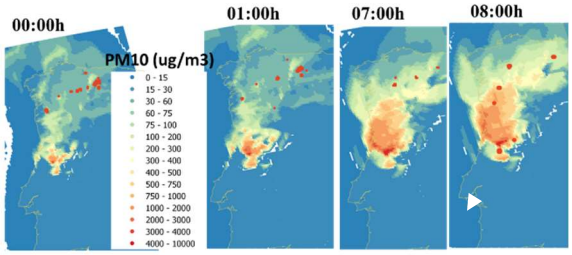

Figure 12. FRP (LSASAF/SEVIRI) for 00UTC to 08UTC shows that the first forest fire occurred after 07UTC (on the time scale shown in this **Figure**).

The animated loop on radar was analyzed and, during the night period, showed reflectivity patterns coherent with clouds being advected from the southwest, as confirmed by satellite imagery. These clouds were associated with Hurricane Ophelia's circulation, which was tracking to the northeast over the Atlantic, a few hundred km offshore the Iberian west coast.

However, several fire plumes started to be observed after 07:45 UTC. A frame extracted at 07:50 UTC from the animated loop of low-level PPI of the Z field (dBZ) showed the early detection of the Vilarinho wildfire by the Coruche radar (PPZ at 0.1°, **Figure 13**).

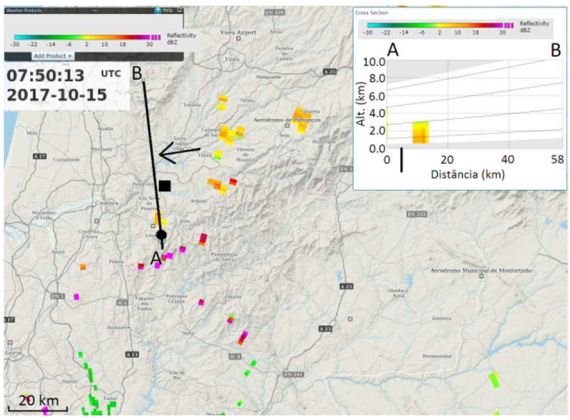

Figure 13. PPI of reflectivity, 0.1° tilt, 07:50 UTC, 15 October 2017, Coruche radar. The cross-section over the black A-B segment is represented to the right. The black dot depicts the fire ignition spot (marked as a vertical segment over the cross-section) and the black square depicts the pixel from the model whose evolution is highlighted in **Figure 15**.

The corresponding cross-section shows the smoke plume development at that time. This can be compared with a later time, 11:20 UTC, where a cross-section was also obtained (**Figure 14**) and illustrates a much taller smoke plume.

The black square in **Figures 13–14** marks a pixel from the CHIMERE model in which the evolution of the PM10 concentration was followed. The graph in **Figure 15** shows (with the blue arrow) the evolution of the PM10 concentration predicted by the CHIMERE model as a function of time for the referred pixel, located just north of the location of the ignition of the Vilarinho wildfire (represented by the black dot in **Figures 13–14**).

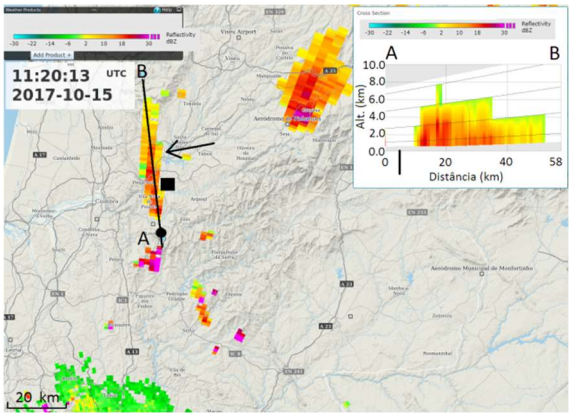

Figure 14. PPI of reflectivity, 0.1° tilt, 11:20 UTC, 15 October 2017, Coruche radar. The cross-section over the black A-B segment is represented to the right. The black dot depicts the fire ignition spot (marked as a vertical segment over the cross-section) and the black square depicts the pixel from the model whose evolution is highlighted in **Figure 15**.

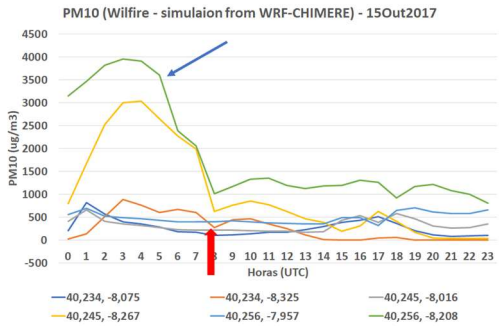

Figure 15. Hourly evolution of PM10 concentrations from the WRF-CHIMERE simulation output, with emission only from forest fires, for different indicated pixels. The red arrow indicates the detection time of the nearby fire with the radar.

Throughout this comparison, it was found a substantial lag between the reported ignition time, also confirmed by radar (plume)

observation, around 07:40–07:50 UTC, and by the FRP satellite product, and the time for which the model predicts high values of PM10 (at a much earlier time, 00 UTC, and a maximum at 03 UTC), associated with the same fire. Studying the cause of this delay we concluded that the APIFLAME model generated biomass burning emissions as daily values and hourly emission values should be used in future studies.

4. Conclusions

Analysing the evolution of smoke due to the fires of October 2017, using simulations of the WRF-CHIMERE model, the impact of these emissions on the air quality of the Central and North Region of Portugal and the chemical composition of the atmosphere is noticeable (**Figure 6** and **Figure 8**.).

The data from WRF-CHIMERE suggests a significant impact on the air quality and chemical composition of the troposphere in the northern half of mainland Portugal during the severe wildfires on 15/17 October 2017. The daily values of the simulations made with WRF-CHIMERE show that PM10 concentrations are comparable to the ones observed at several air quality stations. Overall, this study suggests that the WRF-CHIMERE modelling system is suitable for addressing the impact of forest fires on a regional scale.

The hourly validation of WRF-CHIMERE simulations highlights the importance of model validation and the need to improve the temporal allocation of fire emissions in the model APIFLAME by increasing the frequency of input data, from daily to hourly. Moreover, it is also worth noting the importance of weather radar observations in validating numerical models in the scope of forest fire research. Future work includes studying the direct and indirect effects of aerosols released into the atmosphere by wildfires, including the impacts on the chemical composition of the atmosphere (such as the changes in secondary pollutants production when direct aerosol effects are considered).

5. Acknowledgements

The authors are grateful for the financial support of the Foundation for Science and Technology, I.P., through national funds (PIDDAC), under the SmokeStorm project (PCIF/MPG/0147/2019)

6. References

Bugalho, L.; L. Mendes; M.J. Monteiro; P. Pinto; J. Rio; M.J. Lopes, (2022), Monitoring wildfire smoke dispersion using concentrations of PM10 and PM2.5. Advances in Forest Fire Research 2022 - D. X. Viegas & L.M. Ribeiro (Ed.) Chapter 1 - Decision Support Systems and Tools DOI: https://doi.org/10.14195/978-989-26-2298-9_47.

Francos, M., Úbeda, X., Pereira, P., & Alcañiz, M. (2018). Long-term impact of wildfire on soils exposed to different fire severities. A case study in Cadiretes Massif (NE Iberian Peninsula). Science of the Total Environment, 615, 664 - 671. DOI: https://doi.org/10.1016/j.scitotenv.2017.09.311

Heil, A., & Goldammer, J. (2001). Smoke-haze pollution: A review of the 1997 episode in Southeast Asia. Regional Environmental Change,2, 24- 37. DOI: https://doi.org/10.1007/s101130100021

Jaffe, D., Hafner, W., Chand, D., Westerling, A., & Spracklen, D. (2008). Interannual variations in PM2. 5 due to wildfires in the Western United States. Environmental science & technology,42(8), 2812-2818. DOI: https://doi.org/10.1021/es702755v

Jones, T. A., and S. A. Christopher, (2010). Satellite and radar observations of the 9 April 2009 Texas and Oklahoma grassfires. Bull. Amer. Meteor. Soc., 91, 455–460.

Keywood, M., Cope, M., Meyer, C. M., Iinuma, Y., & Emmerson, K. (2015). When smoke comes to town: The impact of biomass burning smoke on air quality. Atmospheric Environment, 121, 13 - 21. DOI: https://doi.org/10.1016/j.atmosenv.2015.03.050, 2015.a

Menut, L., Bessagnet, B., Briant, R., Cholakian, A., Couvidat, F., Mailler, S., ... & Valari, M.

 DOI: https://doi.org/10.60620/sed5-9y98

(2021). The CHIMERE v2020r1 online chemistry-transport model. Geoscientific Model Development, 14(11), 6781-6811. DOI: https://doi.org/10.5194/gmd-14-6781-2021

Monks, S. A., Arnold, S. R., & Chipperfield, M. P. (2012). Evidence for El Niño–Southern Oscillation (ENSO) influence on Arctic CO interannual variability through biomass burning emissions. Geophysical Research Letters, 39(14). DOI: https://doi.org/10.1029/2012GL052512, 2012.a

Novara, A., Pisciotta, A., Minacapilli, M., Maltese, A., Capodici, F., Cerdà, A., & Gristina, L. (2018). The impact of soil erosion on soil fertility and vine vigor. A multidisciplinary approach based on field, laboratory and remote sensing approaches. Science of The Total Environment, 622, 474 - 480. DOI: https://doi.org/10.1016/j.scitotenv.2017.11.272

Pinto, P., Silva, Á. P., Viegas, D. X., Almeida, M., Raposo, J., & Ribeiro, L. M. (2022). Influence of Convectively Driven Flows in the Course of a Large Fire in Portugal: The Case of Pedrógão Grande. Atmosphere, 13(3), 414. DOI: https://doi.org/10.3390/atmos13030414

Turquety, S., Menut, L., Siour, G., Mailler, S., Hadji-Lazaro, J., George, M., ... & Coheur, P. F. (2020). APIFLAME v2. 0 biomass burning emissions model: impact of refined input parameters on atmospheric concentration in Portugal in summer 2016. Geoscientific Model Development,13(7), 2981 - 3009. DOI: https://doi.org/10.5194/gmd-13-2981-2020, 2020.

Implementation of a Statistical Post-Processing Method for Significant Wave Height Forecasting

Ricardo Ramos [1], Pedro Silva [1], João Rio [1]

[1] *Instituto Português do Mar e Atmosfera, Rua C ao Aeroporto Humberto Delgado 1749-077, ricardo.ramos@ipma.pt, pedro.silva@ipma.pt, joao.rio@ipma.pt*

SUMMARY

The Portuguese Institute for Sea and Atmosphere provides the public forecast of significant wave height. The error of the forecasts can be divided into two main components: the bias and the non-systematic. The systematic error is caused by several factors, including the wrong representation of the coast or the bathymetry. This study presents the post-processing system developed at IPMA, that reduces the systematic error of the significant wave height forecast in four locations, two in Madeira and two in western Iberia.

Keywords: wave forecast; MOS, statistical models, regression model.

1. Introduction and Objectives

The Portuguese Institute for the Sea and Atmosphere (IPMA) provides on its website (www.ipma.pt) forecasts for a set of variables that characterize the state of the sea at a certain moment. These forecasts are obtained as direct outputs of numerical models of wave forecast (DMO). In the particular case of significant wave height (SWH), a variable that is of special relevance as it is used as a reference in the broadcast of IPMA's marine wave warnings, the forecasts originate from the HRES-WAM (High RESolution WAve Model) model developed by the European Centre for Medium-Range Weather Forecasts (ECMWF).

In general terms, the error in numerical model forecasts can be divided into systematic and non-systematic components (Rio 2011). The systematic part of the error arises from deficiencies/limitations inherent in the modelling process (e.g. configuration of the coastline and bathymetry) and as it influences the forecasts similarly and persistently, it is possible to improve their quality through a statistical post-processing system (Vannitsem 2008). The non-systematic error arises from situations that occur in an isolated manner (e.g. phase errors due to the approximation of a frontal surface), and it is not possible to reduce this type of error with the same approach. This work describes the methodology in the development of statistical models (MOS), that allows for forecasts of significant wave height to improve, compared to the DMO forecasts.

2. Data

In this work, hourly observations of significant wave height were used for 4 coastal buoys from the buoy network (**Table I**) managed by the Hydrographic Institute (IH) and Madeira Ports Administration (APRAM), 2 located off the coast of mainland Portugal (**Figure 1** and **Figure 2**) and 2 off the coast of the Madeira island (**Figure 3**).

Tabela I. Location the bouys

Owner	Local	Lat	Lon
APRAM	Funchal	32.61	-16.88
APRAM	Caniçal	32.71	-16.71
IH	Leixões	41.32	-08.98
IH	Sines	37.92	-08.93

 DOI: https://doi.org/10.60620/7hd4-5572

We also used hourly forecasts of the WAM-HRES model for significant wave height and a set of variables (**Table II**) that were considered to have the potential to improve the operational forecast results.

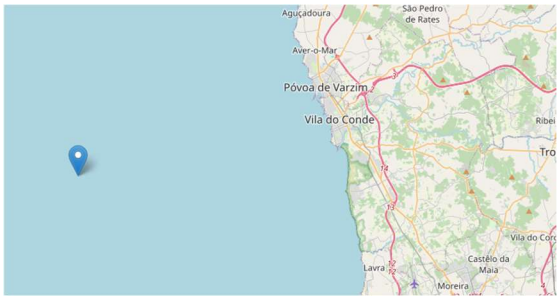

Figure 1. Bouy of Leixões

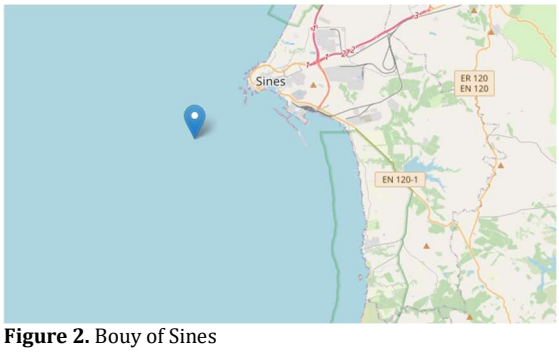

Figure 2. Bouy of Sines

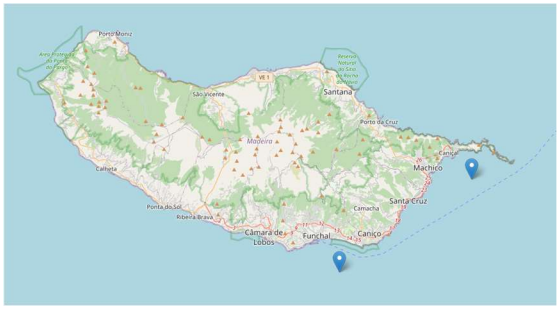

Table II. Identification of the used predictor variables.

SWH	Significant height of combined swell and wind waves(m)
SWELL	Significant height of swell (m)
VAGA	Significant height of wind waves (m)
MWD	Mean wave direction (components)
MWP	Mean wave period (s)
FF	10 meters wind speed from ECMWF atmospheric model (m/s)

Improving the forecasts of significant wave height of WAM-HRES for the southern coast of Madeira Island is of particular importance due to their poor performance as the island's configuration generates a sheltering effect on the southern coast, and the model does not have a sufficient resolution of the bathymetry to consider this effect.

3. Methodology

To achieve our objectives in the work, we made use of linear regression models, in which multiple predictors (DMO forecasts) are used to obtain a statistically predicted value (prediction). In general form, the expression (Vannitsem 2008) is given by:

$$SWH(t)mos = \alpha P1(t) + \beta P2(t) + \mu P3(t) + \theta P4(t) \quad (1)$$

where SWH(t)mos represent the statistical prediction of significant wave height for a given location, at time t, P(t)n are the values of the predictor variables (DMO forecasts) for a given time (t), and α, β, μ, and θ are the coefficients of the model.

The models evaluated in this study resulted from experiments with combinations of subsets of predictor variables from the initial set of potentially relevant predictors (**Table II**). The various evaluated variants (**Table III**) result from different combinations of predictors. In all experiments, the training period was between the first of April and the last day of May.

Table III. Predictors, steps (S) and the number of predictors (NP) used in each experience (N).

N	S	NP	Predictors
1	24	4	SWH, VAGA, SWELL, FF
2	24	4	SWH, VAGA, SWELL, MWD
3	24	3	SWH, VAGA, SWELL
4	24	4	SWH, VAGA, SWELL, MWP

3.1. DMO results

The results obtained by the DMO forecasts for the period from February to April 2022, considering hourly forecast steps from h+0 to h+24, are presented in **Table IV**.

Table IV. Results of DMO forecast for significant wave height forecasts.

Local	Viés(m)	RMSE(m)	R^2
Funchal	0,2	0,63	0,43
Caniçal	0,2	0,75	0,47
Leixões	0,01	0,29	0,91
Sines	0,16	0,26	0,91

Based on these results, it is evident that the performance of the forecasts for the points located along the coast of Madeira Island is inferior to the results obtained along the west coast of mainland Portugal.

3.2. MOS Results

The results obtained after applying the MOS to the DMO forecasts for the period from February to April 2022, considering hourly forecast steps from h+0 to h+24, are presented in **Tables V–VIII**.

Table V. All MOS results for significant wave height forecasts, for Funchal.

Experiment	Bias (m)	RMSE(m)	R^2
1	0.08	0.25	0.45
2	0.07	0.21	0.64
3	0.08	0.25	0.46
4	0.08	0.25	0.43

Table VI. All MOS results for significant wave height forecasts, for Caniçal.

Experiment	Bias (m)	RMSE(m)	R^2
1	0.13	0.36	0.22
2	0.11	0.31	0.45
3	0.13	0.34	0.3
4	0.11	0.39	0.23

Table VII. All MOS results for significant wave height forecasts, for Leixões.

Experiment	Bias (m)	RMSE(m)	R^2
1	-0.04	0.28	0.91
2	-0.11	0.27	0.91
3	-0.04	0.28	0.91
4	0.01	0.38	0.87

Table VIII. All MOS results for significant wave height forecasts, for Sines.

Experiment	Bias (m)	RMSE(m)	R^2
1	0.21	0.25	0.93
2	0.31	0.3	0.92
3	0.2	0.26	0.93
4	0.29	0.4	0.89

The best results were obtained by experiment 2, in buoys of Funchal, Caniçal and Leixões. In Funchal and Caniçal the R^2 was improved only in experiment 2, while the RMSE and Bias were reduced also.

In Leixões, experiment 2, also shows a better result than the others, but the improvement is not great. For Sines, experiment 1 introduces a minor improvement compared to the others. **Figures 4–7**, present the scatter plots of the experiments with the best MOS forecasts compared with the DMO forecast.

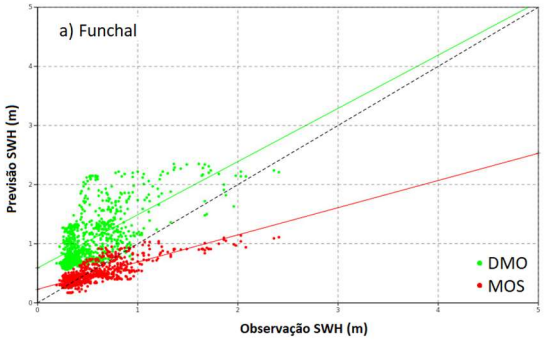

Figure 4. Results of experience 2 for Funchal, SWH forecast (DMO and MOS) vs SWH Observed.

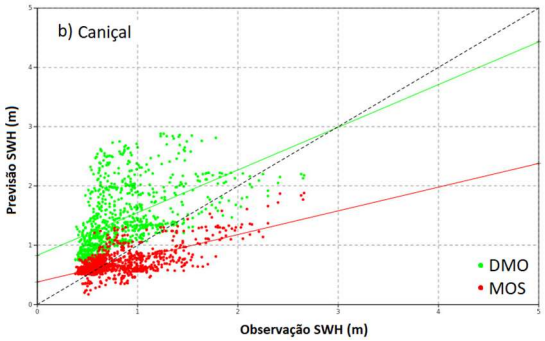

Figure 5. Results of experience 2 for Caniçal, SWH forecast (DMO and MOS) vs SWH Observed.

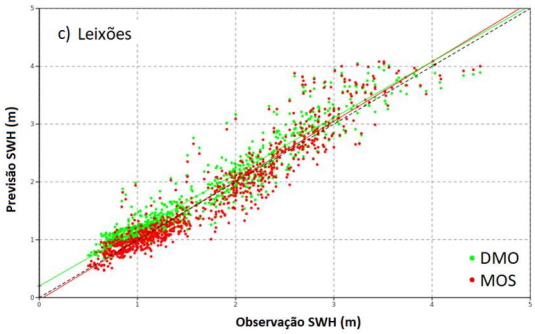

Figure 6. Results of experience 2 for Leixões, SWH forecast (DMO and MOS) vs SWH Observed.

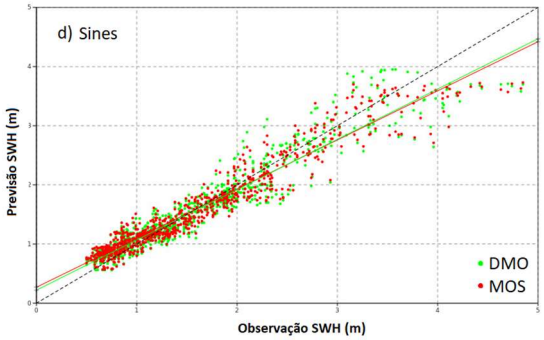

DOI: https://doi.org/10.60620/7hd4-5572

Figure 7. Results of experience 1 for Sines, SWH forecast (DMO and MOS) vs SWH Observed.

4. Final comments

The best results were obtained with experiment 2 for Funchal, Canical and Leixões and with experiment 1, for Sines (**Table IX**).

Table IX. Best MOS results for significant wave height forecasts.

Local	Bias(m)	RMSE(m)	R^2
Funchal	0.07	0,23	0,64
Caniçal	0,11	0,31	0,45
Leixões	-0,11	0,27	0,91
Sines	0,21	0,25	0,93

The statistically post-processed forecasts for the buoys at Funchal and Caniçal show lower RMSE values than those obtained with DMO. This result is obtained when the directional wave components are used as predictors in the linear regression model. Generally, the use of the mean wave period as a predictor does not bring any benefits.

In the case of the buoys in Leixões and Sines, the DMO forecast has a lower RMSE than that calculated for locations located in the Madeira Archipelago. On the mainland, the MOS forecast of significant wave height presents a similar prediction quality to DMO. This experimental study allowed for the development of the basic tools necessary to construct a post-processing system to estimate significant wave height. This work will be further developed, including the inclusion of a more extensive dataset and reformulation of the statistical models considered.

5. References

Rio, J. (2011). Implementação do MOS para as temperaturas mínimas e máximas, Nota técnica 01/2011. Instituto de Meteorologia I.P.

Vannitsem, S. (2008). Dynamical Properties of MOS Forecasts: Analysis of the ECMWF Operational Forecasting System, Institut Royal Météorologique de Belgique, Weather and Forecasting, p 1032-1043.

A Coupled Ecophysiological and Meteorological Model for the Grapevine Simulation Under Agroforestry Conditions

Isilda Cunha Menezes [1], Mário Santos [2,3,4], Lourdes Bugalho [5], Mário Gonzalez Pereira [2,6]

[1] *Centre for Environmental and Marine Studies (CESAM), University of Aveiro, Department of Environment and Planning, Aveiro, Portugal, isildacm@ua.pt*
[2] *Centre for the Research and Technology of Agro-Environment and Biological Sciences (CITAB), Inov4Agro, University of Trás-os-Montes and Alto Douro, Quinta de Prados, 5000–801 Vila Real, Portugal, mgsantos@utad.pt, gpereira@utad.pt*
[3] *Laboratory of Fluvial and Terrestrial Ecology, Innovation and Development Centre, University of Trás-os-Montes e Alto Douro, Vila Real, Portugal, mgsantos@utad.pt*
[4] *Laboratory of Ecology and Conservation, Federal Institute of Education, Science and Technology of Maranhão, Buriticupu, Brazil, mgsantos@utad.pt*
[5] *Portuguese Institute of the Sea and the Atmosphere (IPMA), Department of Meteorology and Geophysics, Lisbon, Portugal, lourdes.bugalho@ipma.pt*
[6] *Instituto Dom Luiz (IDL), FCUL, Campo Grande Edifício C1, Piso 1 1749–016 Lisboa, Portugal*

SUMMARY

A system dynamics model was developed to predict grapevine responses, within agroforestry conditions, to ongoing climate changes, namely in Mediterranean regions. The model encompasses a physiological or module or sub-model to simulate the stages of the annual vegetative cycle, a bioclimatic index sub-model to gauge climate changes, and also considers constraints such as the shade of neighbouring trees. The model uses the atmospheric radiation component to estimate the daily sunshine over a vineyard, photosynthetic activity, and vineyard growth stage evolution in shaded and/or non-shaded conditions. Several environmental in-situ variables were considered to increase the realism of the scenarios presented. Preliminary simulations were performed to show the potential of the idea presented, namely the use of tree shade to mitigate the climate change vulnerability of grapevine in the face of expected warmer environmental conditions already observed and expected for the Douro Valley, Portugal.

Keywords: Vine phenology and zoning model; Vine-tree agroforestry system; Climate change adaptation strategy; Tree shadow effect; 3D solar radiation balance.

1. Introduction

The sustainability of Mediterranean crops is particularly linked with resistance and resilience to highly variable climatic conditions, namely, the capacity to manage water shortages and extreme weather events, such as heatwaves, droughts, and storms. Autonomous or planned adaptation strategies are explored to minimize the negative impacts of observed and foreseen climate change as well as to take advantage of possible positive effects, such as changes in crop species, cultivars, sowing dates, fertilization, irrigation, drainage, land allocation, and farming systems. This challenge leads us to consider agriculture's multifunctional role and seek a balance between economic interests and changing environmental conditions (Bindi & Olesen, 2011). The impacts of solar radiation on viticulture suitability led to the establishment of novel land management paradigms, and the synergy between crops is one of the possibilities for dealing with product quality. The authors seek to explore the dynamics between two crops, a shrubby species and a tree species, specifically, the exposure of the

vineyard to microclimate changes forced by the close presence of trees. For this purpose, the authors developed and present a system dynamics model (SDM) capable of providing reliable forecasts of the vineyard cycle, information that is particularly valuable to estimate the impacts of climate change and climate adaptation actions. The model incorporates a cluster of robust modules which uses meteorological conditions to assess the development of the growing season of the grapevines and analyze a large set of bioclimatic indices. Another module considers the effects of the trees' shadow, estimating the daily sunshine duration of light over the shadow of the trees' canopy and the active photosynthetic radiation.

2. Methodology

2.1. Model Overview

The SDM comprises several modules: sunrise-sunset, light-shadow, light-orchard, phenological, and zoning. The first module simulates the hours of sunrise and sunset for each day of the study period for a specific location in the Julian calendar. The light-shadow module incorporates an accurate method to estimate the daily sunshine duration on the grapevine, based on the incident solar radiation passing over the canopy of a tree. The light-orchard module simulates the active photosynthetic radiation, based on the proportion of the orchard that is shaded by trees. This last submodule depends on the orchard configuration, and both modules consider the tree dimensions, position and distance to the grapevine as well as ground geographical characteristics, including altitude, slope, and exposure. The phenological module is based on environmental determinants for the grapevine phenological timings. This module can simulate the phenology of a large number of Vitis vinifera L. varieties. The Zoning module has a set of viticulture zoning bioclimatic indices, useful to control the change in the suitability of a particular region for grape and wine production.

2.2. Study area

To verify the capacities and performance of the model, the authors idealized an experimental conceptualization of a grapevine surrounded by four olive trees, typically used in the limits of vineyards in the Mediterranean region. For modelling and simulation purposes, we considered a typical study area in a farm in *Pinhão* village for the following reasons: (i) this village is included in the world-famous Douro Demarcated Region (DDR), in northern Portugal; and, (ii) the Portuguese Meteorological Office (*Instituto Português do Mar e da Atmosfera*, IPMA), maintains a weather station (WS) in operation in this parish. In this region, the most representative grape variety (12% of the total area) is *Touriga Franca* (Magalhães 2003), the reason why we decided to consider this variety in this research. This region's climate type, variability and evolution are well-documented (e.g., Machado, C., 2010, Sousa, 2015; Evelpidou et al., 2013, Abreu e Lima, 2014; Santos Góis, 2015; Cabral, 2017). The authors devised a conceptual experiment with a hypothetical grapevine located 3 meters from olive trees placed north, south, west, and east (**Figure 1**). The height of the hypothetical trees and vine was 4 m and 1.5 m, respectively. The experiment was designed on a horizontal terrain to simplify the process of evaluating solar radiation in the vine.

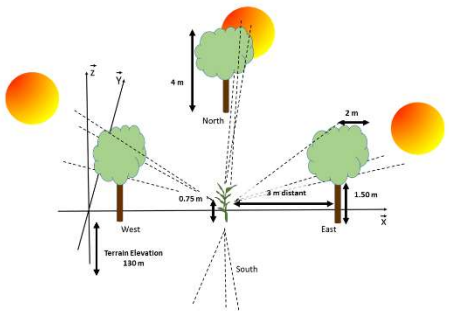

Figure 1. Scheme of conceptualization of a vine in the local near the four olive trees, placed at 3 m and located at north, south, west, and east.

2.3. Data

The DSM input data list includes time series of daily values of the following meteorological variables: accumulated precipitation, dew point temperature, maximum and minimum air temperature at 2 m height, and 10 m wind speed observed by IPMA at the *Pinhão* WS; and, surface air pressure and surface net radiation from ECMWF Era-Interim (Dee et al., 2011; Berrisford et al., 2011) in the closest grid point to the Pinhão weather station. The

simulations of the SDM to assess the influence of the shadow on the vine were performed for the annual vegetative cycle of 2004 – 2005 (hereafter 2005). The year 2005 was chosen to evaluate the effect of tree shade on the vine because it is characterized by high air temperature since April, but especially between June and September. The validation process of the phenological module also used the average dates of the main events of grapevine phenology (**Table I**) observed at Quinta de Santa Bárbara (QSB), located in Pinhão for the *Touriga Franca* variety, from 2001 to 2012, (Sousa, 2015).

Table I. Average dates of the main phenological events obtained from observed dates for the Touriga Franca variety, during the 2001 – 2012 period, in the Quinta de Santa Bárbara (QSB), located in Pinhão (Sousa, 2015), and of phenological module simulations, for the same variety, in 2005, under the shadow of a tree located 3 m from the vine at north, west or east and south.

Event	QSB	North	West/East	South
Budbrust	24/3	5/4	9/4	20/4
Flowering	24/5	17/5	25/5	27/5
Véraison	25/7	23/6	1/7	28/6
Maturity	3/9	27/7	6/8	31/7

3. Results and discussion

The average dates of the main *Touriga Franca* variety phenological states observed at QSB were compared with grapevine phenological events simulated by SDM for 2005 (**Table I**). These results allowed us to assess the ability of SDM to simulate the vine phenology's vegetative cycle in *Pinhão* and infer the influence of a shadow on the vine. The results obtained from the SDM simulations for 2005 reveal that SDM simulated a later bud break and flowering in the vine and advanced beginning of *véraison* and maturation. It is also possible to verify (**Table I**) that the shade affected the start of the physiological phases, depending on the position of the tree. The tree placed to the north of the vineyard never shades the vine, so it serves as a reference/comparison with the case of the absence of trees in the vineyard. The shade of the tree in the south was the one that most delayed the beginning of the budburst and flowering phases in the vine. The shadow of the tree to the west-east was the one that most delayed the beginning of the *véraison* and maturation phases. The validation process, although simplified, clearly allowed us to understand the influence of the trees, even if the tree in the east and west cause shade with the same duration but at different times of the day: the tree to the east at the beginning of the day; the tree to the west at the end of the day, and the tree in the south casts shade on winter days (centred at midday), but in middle summer, the height of the sun makes the sun's rays reach the vine at any time of the day.

Results obtained with the SDM simulations suggest the model's ability to simulate the phenological phases in years with extreme climatic characteristics. The dates of the phenological phases simulated for the year 2005 (**Table I**), reflect well the characteristics of the average air temperature over this year. The winter of 2004 – 2005 was colder than normal, which justifies the significant delay, namely in the budburst and flowering. However, the normal spring and warmer-than-usual summer, explain the significant anticipation of the last vegetative phases (*véraison* and maturity).

The entire year of 2005 was abnormally dry but presented greater variability in air temperature and a smaller daily temperature range during the grape maturation period. Also, these weather conditions were conducive to the development of high productivity in the vineyards with moderate vigour of the grapevine, which did not generate limitations on maturation but conditioned the oenological quality. These climatic characteristics align with the zoning module indices' results (**Table II**).

The year 2005 is representative of the most recent decades, with a higher average air temperature and earlier seasonal phases. These results are in good agreement with the findings of previous studies for the same region (Machado, 2010), reporting increasing trends in minimum, mean and maximum air temperature in the months of April to September as well as on some indices (e.g., heliothermal and cool nights). These findings suggest that climate change is observable today as well as its effects are already being noticed, urging the importance of finding adaptation measures to face climate change.

 DOI: https://doi.org/10.60620/2xqn-2728

Table II. Results of zoning module indices for the year 2005, under the influence of trees located 3 m to the north, west-east, and south.

Tree location	North	West East	South
Heliothermal index	3214	3075	3163
Cool night index (°C)	17.4	17.4	17.4
Hydrothermal index	807	734	752
Mean thermal amplitude (°C)	12.4	12.4	12.4
Growing season suitability	204	201	197
Growing season precipitation (mm)	80.1	80.1	80.1

4. Conclusion

Preliminary results demonstrate the capacity of the model to simulate the effect of tree shadow placed in different positions, in different phenological stages of the vine and zoning conditions. The SDM is still in the development and validation phase, but the results obtained demonstrate the potential and effects of consortia to solve some of the problems that Mediterranean cultures are already experiencing and that will tend to worsen in the expected future climate conditions.

5. Acknowledgements

This work is supported by Nacional Funds from FCT – Portuguese Foundation for Science and Technology, under the project UIDB/04033/2020. We are grateful to the European Center for Medium-Range Weather Forecasts (ECMWF) for providing the ERA-Interim data and to the *Instituto Português do Mar e da Atmosfera* (IPMA) for providing the *Pinhão* station data.

6. References

Berrisford, P., Dee, D., Poli, P., Brugge, R., Fielding, K., Fuentes, M., ... & Simmons, A. (2011). The ERA-Interim archive Version 2.0, Shinfield Park. Reading, 1, 23.

Bindi, M., & Olesen, J. E. (2011). The responses of agriculture in Europe to climate change. Regional Environmental Change, 11, 151-158.

Cabral, B. O. C. P. (2017). Efeitos de Estratégias de Rega Deficitária Sobre o Rendimento e Qualidade da Casta Touriga Nacional na Região do Douro. (Master dissertation, Universidade do Porto (Portugal)).

Dee, D. P., Uppala, S. M., Simmons, A. J., Berrisford, P., Poli, P., Kobayashi, S., ... & Vitart, F. (2011). The ERA-Interim reanalysis: Configuration and performance of the data assimilation system. Quarterly Journal of the royal meteorological society, 137(656), 553-597.

de Sousa, A. C. C. R. (2015). Analyzing the influence of the Douro Valley weather on the quality and yield of vintage Port (Doctoral dissertation, Universidade do Porto (Portugal)).

dos Santos Góis, N. M. (2015). Modelação fenológica da videira (Vitis vinífera L.). Integração bioclimática, genética e adaptação espácio temporal.

Evelpidou, N., Cordier, S., Merino, A., Figueiredo, T. D., & Centeri, C. (2013). Runoff erosion. Education and Culture DG. Lifelong Learning Programme.

Lima, I. M. S. D. B. D. A. (2014). Previsão de Produção da casta Touriga Franca na região do Douro com base nas Componentes de Rendimento (Doctoral dissertation, ISA).

Machado, C. I. D. S. (2010). Vulnerabilidade da Região Demarcada do Douro às alterações climáticas e efeitos sobre o ciclo vegetativo da videira: o caso do Moscatel Galego (Doctoral dissertation).

Magalhães, A. J. (2003). Plantação de uma vinha no Douro. In U. de T.-M. e Alto-Douro (Ed.), Comunicação no Seminário "Instalação da Vinha" 1,1–9.

PART II: ADVANCES IN GEOPHYSICS

 DOI: https://doi.org/10.60620/he5s-8x66

The Analysis of the Seismic Tacana Volcanic Complex in 2017 – 2018

Alan Yair Alarcón Pacheco [1]

[1] *Postgraduate in Earth Sciences, Geophysics Institute, UNAM, Avenida Universidad 3000, Mexico City, Mexico, a.alarcon@igeofisica.unam.mx*

SUMMARY

The Tacaná Volcanic Complex (TVC) is situated in the southwestern region of Mexico, specifically in the state of Chiapas and in the northwest of Guatemala, in the San Marcos Department. According to the National Center for Disaster Prevention (CENAPRED), the Tacaná volcano is ranked sixth in the relative risk assessment of volcanoes in Mexico, primarily due to its explosive activity and andesitic composition. Over the past 40,000 years, the TVC has experienced several phreatic explosions, with the most recent occurring in February 1986, which was preceded by significant seismic activity since December 1985. On September 7th, 2017, a subduction earthquake with an Mw8.2 occurred 200 km southwest of the TVC. This study confirms an increase in seismic activity in the TVC following the subduction earthquake. To determine the internal stress state of the volcano, seismic records were analyzed using a 2-minute window, focusing on volcano-tectonic (VT) events close to the TVC (with a ts-tp difference ranging from 1 to 6 seconds). A total of 13,291 VTs were detected, of which only approximately 5% were located, and had a b-value of 2.4.

Keywords: Tacana volcano, b-value, Tehuantepec, Earthquake, M8.2.

1. Introduction

The Tacaná Volcanic Complex (TVC) is located on the border between the Mexican state of Chiapas and the Guatemalan department of San Marcos, at coordinates 15°08' North latitude and 92°09' West longitude, with an elevation of 4060 meters.

During the last 40,000 years, the volcano has had eruptive activity of different types, including phreatomagmatic, strombolian, and vulcanian, that have generated ash columns, lapilli, and blocks of up to 20 km in height, distributed within a radius of 25 to 30 km around the volcano. The Secretariat of Security and Citizen Protection, in collaboration with the National Center for Disaster Prevention (CENAPRED), has classified the Tacaná volcano as the sixth volcano with the highest relative risk, which could affect nearly one million people. The last eruption of the volcano occurred on May 18, 1986, after volcano-tectonic events were recorded between 5 and 10 km southwest of the summit of the volcano, which generated pyroclastic flows and lahars that mainly affected the Mexican territory in the NW-S zone.

On September 8, 2017, a moment magnitude 8.2 earthquake occurred in the Gulf of Tehuantepec with a rupture pattern in the SE-NW direction, approximately 200 km southwest of the TVC (**Figure 1**). The main objective of this work is to determine if there was an increase in the activity of the TVC and to calculate the b-value of the Gutenberg-Richter power law.

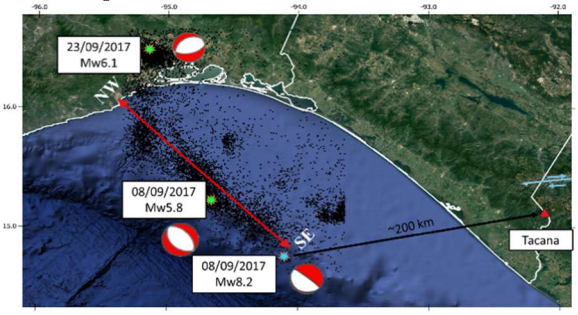

Figure 1. Moment magnitude 8.2 earthquake.

2. Geology

The Tacaná volcano is a stratovolcano that is mainly composed of volcanic rocks of andesitic composition at its base and dacitic

rocks at its upper part. In addition, intrusive igneous rocks, such as diorite and granodiorite, have been found, which were formed from the solidification of magma beneath the Earth's surface. These intrusive rocks are mainly found at the base of the volcano and in the surrounding subsurface, indicating that the process of Tacaná's formation involved the intrusion of magma through fractures in the Earth's crust, followed by its subsequent solidification and crystallization in the subsurface.

Geological studies in the Tacaná region have identified the presence of these intrusive igneous rocks by conducting geological mapping and petrographic analysis. In addition, geochemical and isotopic techniques have been used to understand the composition and origin of these rocks. A study published in the Journal of South American Earth Sciences employed petrographic and geochemical analysis to identify and classify the intrusive igneous rocks in Tacaná. The results indicated that these rocks originated from a parental magma of andesitic composition, which underwent fractional crystallization and magmatic mixing processes to form the dioritic and granodioritic rocks found in the region (Castro et al., 2019).

The Tacaná volcano is located near a triple junction between the Cocos, North American, and Caribbean plates. Various authors (Mujica-Mondragón, 1987; García-Palomo and Hernández, 1986; Macías J. L., 2005) have suggested that the formation of the Tacaná Volcanic Complex was due to two phases of intrusion, the first between 29 and 35 million years ago, and the second between 13 and 20 million years ago. Subsequently, the Tacaná Volcanic Complex was emplaced within the San Rafael Caldera approximately 100,000 years ago. Based on stratigraphic records, it is estimated that the first emissions of basaltic-andesitic lava flows occurred approximately 36,000 years ago.

According to García-Palomo et al. (2006), the Tacaná Volcanic Complex consists of four independent structures that are aligned in a NE-SW direction. It is proposed that their formation was due to a migration of volcanic activity, starting from the NE end with the Chichuj volcano, followed by the Tacanpa volcano, the Plan de las Adillas dome, and the most recent structure, the San Antonio volcano.

3. Methodology

The Tacaná Network is a seismic station network designed specifically to monitor the activity of the Tacaná volcano and provide complementary information on tectonic earthquakes in the region. The network was funded by a CONACyT project and installed in 2009 by technicians from the National Seismological Service (SSN) under the supervision of Dr Carlos Valdés.

Initially, the Tacaná network had four seismic stations located in Mexican territory. The stations are equipped with Güralp CMG-6TD triaxial broadband velocity sensors with a range of 0.3016 – 50 Hz and transmit data via radio frequency to the Tapachula Seismological Observatory, where they are retransmitted by satellite link to UNICACH and SSN for real-time monitoring.

At first, the stations transmit data at a sampling rate of 40 samples per second. However, due to the increased seismic activity of the Tacaná volcano in 2017, the sampling rate was increased to 100 samples per second from June 2018 onwards to improve the identification of P-wave arrivals. The Tacaná Network (**Figure 2**) has proven to be an important tool for monitoring volcanic activity in the region and the early detection of tectonic earthquakes.

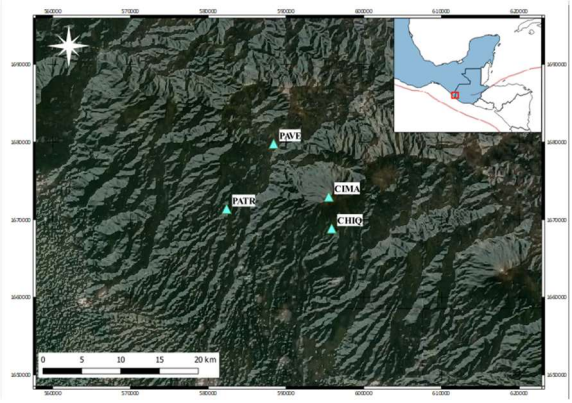

Figure 2. Tacana Network Stations.

A request was made by Dr Denis Legrand to UNICACH and the Servicio Sismológico Nacional to obtain records. The records were provided in hourly intervals, which were

 DOI: https://doi.org/10.60620/vet6-kt90

stacked to generate 24-hour files for each station.

Subsequently, the records from the PAVE, PATR, and CHIQ stations were manually and simultaneously reviewed to identify volcano-tectonic events (**Figure 3**) and obtain a catalogue of seismicity in the area from January 2017 to December 2018.

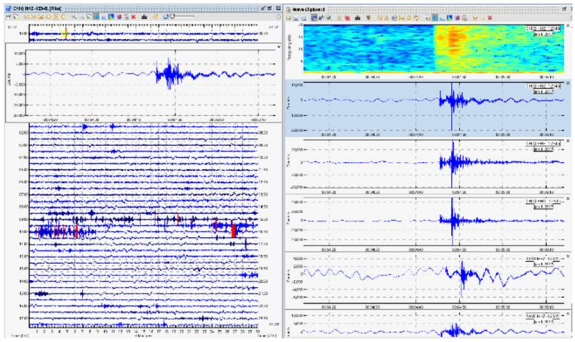

Figure 3. Deployment of stations in SWARM for event identification. The left-hand display corresponds to the recording from the CHIQ station. On the right-hand side, the display shows the vertical and horizontal components of the recordings from CHIQ, PAVE, and PATR stations, along with a spectrogram display using a 2-minute window. This allowed for better discrimination of volcanic-tectonic event signals from anthropogenic noise signals and/or signals unrelated to the volcano.

After creating the catalogue, hypocentral locations of the volcano-tectonic events were determined using SEISAN software, with the maximum height of the CVT as a reference and the cortical velocity model of Jiménez et al. (1999).

Once the locations were obtained, the maximum likelihood methodology proposed by Aki (1965) was used to determine the slope of the Gutenberg-Richter law with greater reliability.

The formula proposed by Aki (1965) allows for a more reliable determination of the slope of the Gutenberg-Richter law (1).

$$b = \frac{\log_{10} e}{< M > - M_{\min}} \qquad (1)$$

Where the b-value corresponds to the slope, $\langle M \rangle$ is the average magnitude for n earthquakes, and $M_{\min}$ is the minimum magnitude of the catalogue.

4. Results

4.1. TVC Activity 2017

Considering all the events in **Figure 4**, a progressive decrease in activity can be observed from January to August 2017. Subsequently, there was a surge in activity recorded after the Mw8.2 earthquake that occurred on September 7th, 2017. The highest number of recorded events was identified in November 2017, although a swarm of 64 recorded and located events was observed in December 2017.

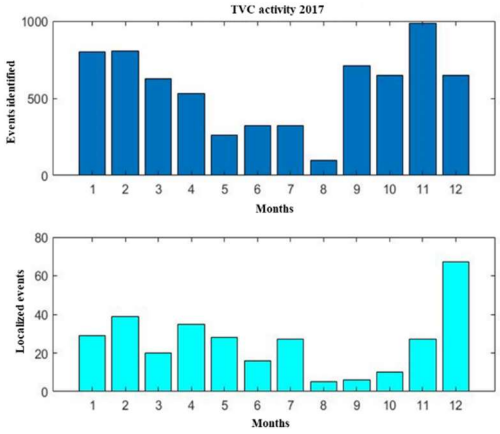

Figure 4. Bar chart of the temporal distribution of seismic activity at Tacaná in 2017. Blue bars represent events with low amplitude values and/or unclear P-wave arrivals, the localization for these events is not possible. The cyan bars represent events that met the criterion of having clear body wave arrivals, allowing for localization with a minimum of one station and a maximum of three stations. The month with the highest number of localized volcanic-tectonic events was the swarm identified in December.

The seismicity found is shown in the depth profiles of **Figure 5** and on the map of **Figure 6**, highlighting four areas where seismicity was clustered, both in their distribution in plan and in-depth values. The ellipse represented by the letter A is oriented in a NE direction to the Tacaná Volcano, located on the outer part of the Sibinal caldera. The ellipse represented by the letter B is the seismicity within the Sibinal caldera. The ellipse with the letter C is the seismicity found between the structures of the Tacaná and San Antonio volcanoes and the Ardillas dome. Finally, the seismicity enclosed by the circle represented with the letter D is mainly located between the Ardillas dome and the Tacaná volcano.

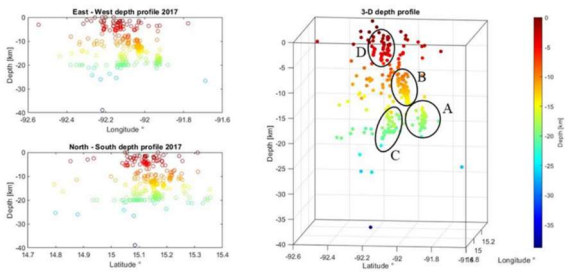

Figure 5. 2D and 3D depth profiles of VT locations for 2017 are shown in the following figures. (A) displays the swarm that occurred in late December 2017. (B) shows the VTs located within the Sibinal Caldera. (C) shows the VTs that occurred between the Tacaná and San Antonio volcanoes. Lastly, (D) shows the shallow VTs related to the Plan las Ardillas dome and the Tacaná volcano.

The seismic swarm in December consists of VTs that have a depth ranging from 15 km to 20 km. There is no clear migration of depth over time, except for the December swarm, which is slightly deeper and was highlighted in ellipse A in **Figures 5 and 6**.

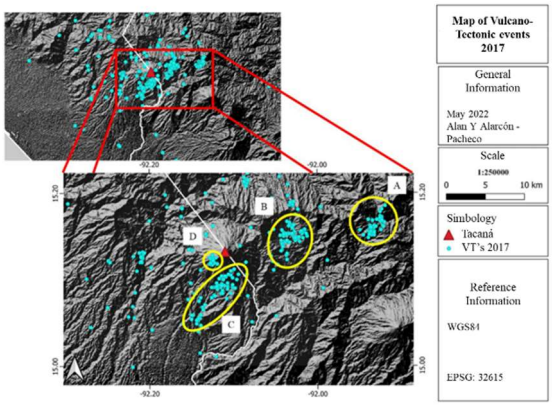

Figure 6. Map of the spatial distribution of the seismicity found for 2017.

Another point that was analyzed was the accuracy of the model used. **Figure 7a** and **Figure 7b** show an average error of 2.4 km in the NS and EW directions, respectively, while the average error in the vertical direction is 3.65 km (**Figure 7c**).

The average number of stations used for a location was 3, as shown in **Figure 7d**. An average azimuthal gap of 307° was also obtained (**Figure 7e**), with an average location error for a minimum of 4 phases of 0.02 seconds, as shown in **Figure 7f**.

These errors are related to the proximity of the stations, as well as the number of stations used for the location of VTs (a maximum of 3 stations).

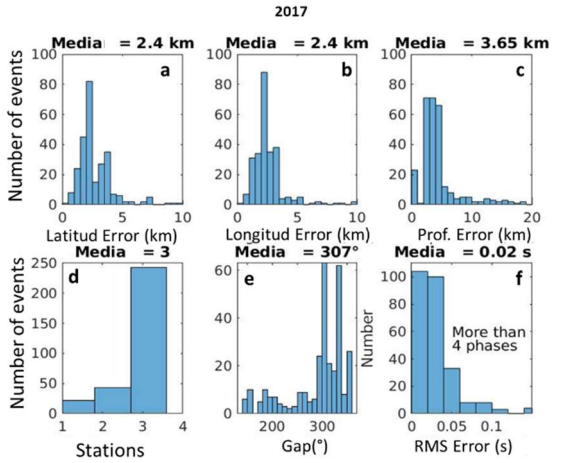

Figure 7. (a) Histogram of the error in the NS direction. (b) Histogram of the error in the EW direction. (c) Histogram of the error associated with the vertical component. (d) Histogram representing the average number of stations used for the location. (e) Histogram representing the azimuthal gap of earthquakes to the distribution of stations. (f) Histograms of the root mean square (RMS) of earthquake locations.

4.2. TVC Activity 2018

For 2018 (**Figure 8**), a total of 6526 events were identified, most of which were only distinguishable again at the CHIQ station. Of these, 240 events were observable in at least two stations, or body wave arrivals were clear enough to ensure azimuthal location.

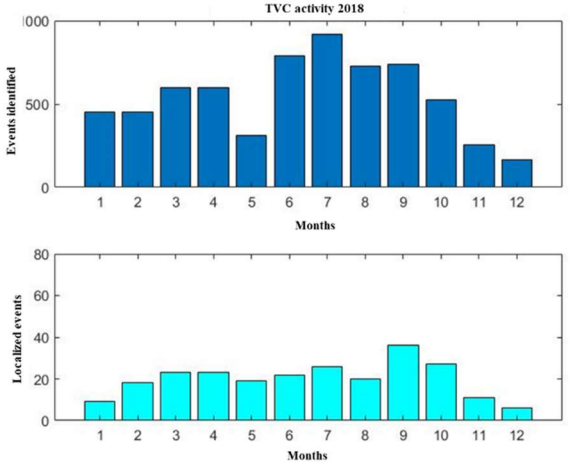

Figure 8. Bar graph of the temporal distribution of seismic activity at Tacaná in 2018. Blue bars represent events with small amplitude and/or unclear P-wave arrivals, the localization for these events is not possible. The cyan bars represent events that met the criterion of having clear body wave arrivals, allowing for localization with a minimum of one station and a maximum of three stations.

A significant concentration of seismicity can be observed in two regions indicated by circles in **Figure 9** and **Figure 10**. Circle A is located on the south flank of the volcano, which includes the San Antonio Volcano, Plan de las Ardillas Dome, and Tacaná Volcano

DOI: https://doi.org/10.60620/vet6-kt90

within the first 10 km of depth. Circle B is located on the northeast flank of Tacaná volcano, in the Sibinal Caldera within the first 10 to 15 km.

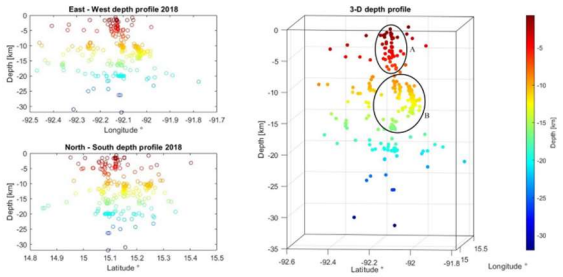

Figure 9. 2D and 3D depth profiles of the VTs locations for 2018 are shown in (A) and (B), respectively. (A) VTs are associated with the structures of the San Antonio Volcano, Plan de las Ardillas dome, and Tacaná Volcano. (B) VTs are located on the NE flank of the Tacaná volcano, within the Sibinal Caldera.

Regarding depths, most of the events were found within the first 15 km. Unlike the depth profiles shown in **Figure 5**, the VTs for 2018 were caused by a variation in surface stresses. The VTs highlighted in ellipse B were observed and located mostly within the months of March and April, while the VTs located in ellipse A of **Figure 9** and **Figure 10**.

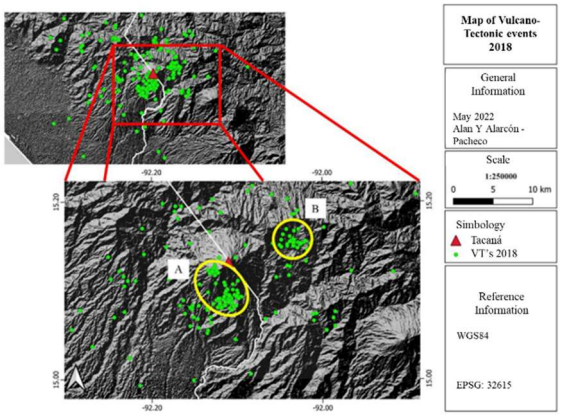

Figure 10. Map of the spatial distribution of seismicity found for 2018.

The localization errors for 2018 are shown in **Figure 11**; the histogram related to the errors in the horizontal components is displayed in **Figure 11a** and **Figure 11b** with average errors of 4.4 km and 4.2 km in the NS and EW directions, respectively, while the average error in the vertical direction shown in **Figure 11c** is 5.61 km. The average number of stations used for localization was 3, as shown in **Figure 11d**; an average azimuthal gap of 292° was obtained (**Figure 11e**) with an average error in the locations with a minimum of 4 phases of 0.09 seconds, as shown in Figure 11f.

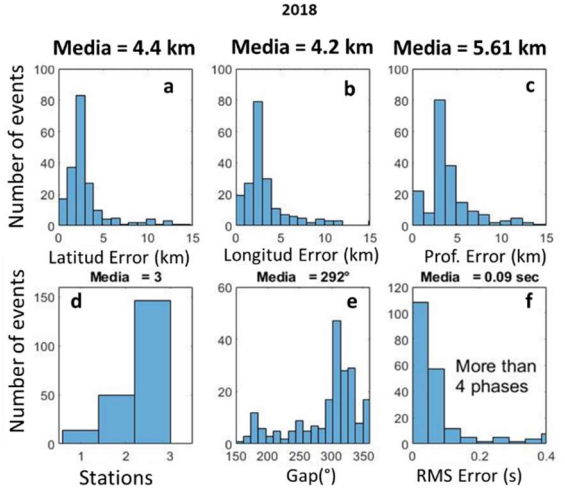

Figure 11. (a) Histogram of error in the NS direction. (b) Histogram of error in the EW direction. (c) Histogram of error associated with the vertical component. (d) Histogram representing the average number of stations used for the location. (e) Histogram representing the azimuthal gap of the earthquakes to the station distribution. (f) Histograms of the root mean square (RMS) of the earthquake locations.

The catalogues obtained for the years 2017 and 2018 contain 309 and 252 VTs respectively, which allows us to obtain a single Gutenberg-Richter law graph with a total of 561 VTs. The completeness magnitude (Mc = 2.8) yielded a b value of 2.4. **Figure 12** shows the fitting line for the points after the completeness magnitude. It can be noted that the fit is not perfect, indicating that the total number of VTs is still small. This is due to the need for a larger time window of more than two years to obtain a better estimation of the b-value.

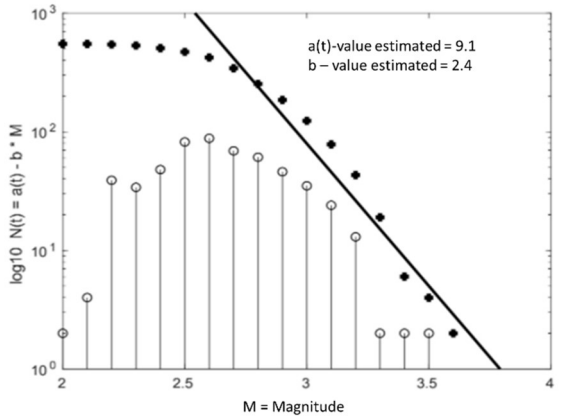

Figure 12. Cumulative (black dots) and non-cumulative (white dots) Gutenberg-Richter law for the years 2017 and 2018 with a b-value of 2.4 (Graph made by Dr Denis Legrand).

5. Conclusions

A large number of events were identified, many of them with very small amplitudes. The majority of these events are only visible at the CHIQ station; however, it is not possible to identify the P-wave arrival, resulting in 95.87% (13,291) of events that cannot be located. If the missing events could be located and calculated, this would allow for a different value of the completeness magnitude, which would vary the points that will be part of the parameter calculation, resulting in a better estimation as the method used to calculate the parameters yields the best probability that fits the observed data.

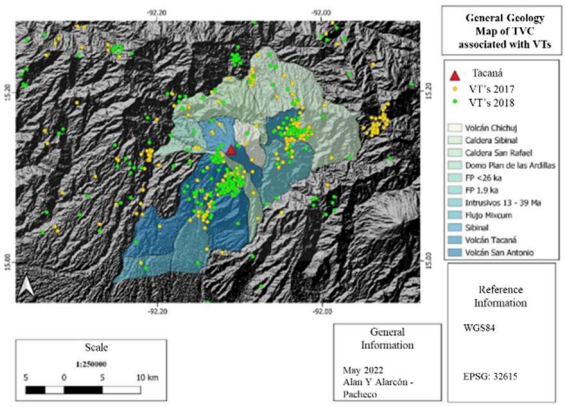

Figure 13. Map of the study area with the locations of the seismicity found in 2017 and 2018 with the stations.

Within the obtained locations, it can be observed that the spatial distribution of seismicity is located to the NE of the Tacaná volcano, corresponding to the Sibinal Caldera, and this seismicity remains constant throughout the period covered in this study. Additionally, the swarm that occurred in December 2017 consisted of 64 events located 15 km NE of the volcano, with a duration of 9 days. It can be assumed that the locations of the VTs bear some similarity in spatial distribution reported during the precursor activity associated with the phreatic eruption on May 8, 1986 (CENAPRED, 2015). The highest number of located VTs are located in the NE for 2017 and 2018 as shown in **Figure 13**.

The analysis of histograms of the average errors of the locations of both latitude (2.4 km for 2017 and 4.4 km for 2018), longitude (2.4 km for 2017 and 4.2 km for 2018), and depth (3.65 km for 2017 and 5.61 km for 2018) shown in **Figure 7** and **Figure** 11 are significant errors considering the dimensions of the volcanic edifice; taking into account that the dimensions of the volcano in its EW cross-section are approximately 6.1 km while in its NS cross-section is approximately 7.2 km, this may be due to the cortical velocity model used by Jiménez et al. (1999), which was originally obtained for the Chichón volcano. Another factor that affected the locations is the sampling rate at which the records were obtained; from January 2017 to June 2018, the sampling rate was 40 samples per second, which prevents a more precise identification of the arrival time of body waves.

Previous studies conducted in different regions have indicated that, for active volcanic zones, a high calculated b-value ($b \geq 1.3$) is due to the increase in stress caused by rock fracturing as a result of magma intrusion (Rodríguez et al., 2021; McNutt, 2005). The obtained b-value ($b = 2.4$) falls within the maximum reported range of 1.4 to 3.5 for active volcanoes (Roberts et al., 2015). An example of this is Mount Etna, a volcano with basic lava that showed b-value values between 1.5 and 2.5 during eruptions on the East flank in the period from July to August 2001 and from October 2002 to January 2003 (Roberts et al., 2015; Privitera et al., 2006). Another example of the application of the Gutenberg-Richter law parameters calculation is the submarine eruption of the Hierro volcano in October 2011 with a b-value between 1.5 and 2.0.

The number of located events used for the Gutenberg-Richter law (**Figure 12**) represents 4.13% of the total identified and unidentified events. This allows us to infer that the number of VTs used for the calculation of the Gutenberg-Richter law is too small. Furthermore, we see that the seismicity is distributed in three different zones and has been mixed for the calculation of the b-value due to the lack of data, but this may generate errors in the final b-value.

6. Acknowledgements

SSN data was obtained by the Servicio Sismológico Nacional (México), station maintenance, data acquisition and distribution are thanks to its personnel.

 DOI: https://doi.org/10.60620/vet6-kt90

Thanks to UNAM-Institute of Geophysics, UNICACH for providing seismic records. To my undergraduate thesis advisor Dr Denis Legrand, to my thesis committee members: Dr Arturo Iglesias, Dr Carlos Valdés, M.C. David Escobedo Zenil, and M.C. Javier Lermo Samaniego. To the guidance of Ing. Daniel González, Ing. Adriana González, and Dr Victor Hugo Espíndola from the National Seismological Service, and my friend Alondra Rodríguez for her unconditional support. And to the unconditional support and motivation of Dr Elsa Leticia Márquez Flores from the Institute of Geophysics and my companion on this adventure, Engineer Karla Guadalupe Ramírez Vega. And last but not least, many thanks to APMG, IPMA, and the people of Portugal for their attention and care.

7. References

Alarcón, Alan., (2022). Estudio de la sismicidad de 2017 – 2018 del volcán de Tacaná. [Tesis de Licenciatura, Universidad Nacional Autónoma de México].

Allen, R. V. (1978). Automatic earthquake recognition and timing from single traces. Bulletin of the Seismological Society of America, 68(5), 1521–1532.

Aki, K. (1965). Maximum likelihood estimate of b in the formula log N = a- bM and its confidence limits, Bull. Earthq. Res. Inst. Tokyo Univ.43, 237–239.

Bormann, P. y J. Saul (2008). The new IASPEI standard broadband magnitude mB. Seismological Research Letters Vol. 79, No 5, pp. 698-705.

Caballero, G., Espinasa, R., Nieto, A., Hernández, A. & Castañeda, E. (2015). Informe del Monitoreo del Volcán Tacaná 2015.

Caballero, G. (2018). Análisis de cocientes espectrales usando telesismos para la determinación de zonas de atenuación en el volcán Tacaná. [Tesis para optar por el grado de Maestra en Ciencias, Universidad Nacional Autónoma de México].

Caballero, G. (2019). Informe del Monitoreo del Volcán Tacaná 2019. Recuperado de: http://www1.cenapred.unam.mx/DIR_INVESTIGACION/2020/1er_Trimestre/FRACCION_XLI/RV/Monitoreo_de_la_actividad_de_los_volcanes_Citlaltepetl_SanMartin_Tuxtla_Ceboruco_Tacana_y_Chichon.pdf

Condori, Cristobal & pérez, Leandro. (2015). Análisis de la variación espacio-temporal del valor sísmico de b en el Valle del Cauca, suroccidente de Colombia. GEOS. 35. 16.

De La Cruz Martínez, V., & Hernández Zuñica, R., (1986). Geología del Volcán Tacaná, Chis. Geotermia, Rev. Méx., Geoenergía, 2, 5-21, 1986.

De La Cruz Reyna, S., Tacaná (México/Guatemala). (1986 a): Local seismicity continues, SEAN Bull., 11, 2, 4-5, 1986a.

De La Cruz Reyna, S., Tacaná (México), (1986 b). Earthquake swarm then small phreatic eruption, SEAN Bull., 11, 4, 14, 1986b.

Garcia-Palomo A, Macias J L, Arce J L, Mora J C, Hughes S, Saucedo R, Espindola J M, Escober R, Layer P, (2006). Geological evolution of the Tacana volcanic complex, Mexico/Guatemala. In: Rose W I, Bluth G J S, Carr M J, Ewert J W, Patino L C, Vallance J W (eds), Volcanic hazards in Central America, {Geol Soc Amer Spec Pap}, 412: 39-57.

Genschel, U. y Meeker, W.Q. (2010). A Comparison of Maximum Likelihood and Median- Rank Regression for Weibull Estimation. Quality Engineering, 22(4): 236–255.

Gutenberg, B. y C. F. Richter (1956). Magnitude and energy of earthquakes. Annali di Geofisica, 9, pp. 1-15.

Gutenberg, B., and C. F. Richter (1944). Frequency of earthquakes in California, Bull. Seismol. Soc. Am. 34, 185–188.

Gutenberg, B., and C. F. Richter (1954). Seismicity of the Earth, Second Ed., Princeton University Press, Princeton, New Jersey, 310 pp.

Hanks, T. C. y H. Kanamori (1979). A moment magnitude scale. Journal of Geophysical Research 84, pp. 23480-23500.

Havskov, J., De la Cruz-Reyna, S., Singh, S. K., Medina, F., & Gutiérrez, C. (1983). Seismic activity related to the March-April, 1982 eruptions of El Chichon Volcano, Chiapas, Mexico. Geophysical Research Letters, 10(4), 293 – 296. DOI: https://doi.org/10.1029/GL010i004p00293

Havskov, Jens, & Ottemöller, L. (2010). Routine data processing in Earthquake seismology. DOI: https://doi.org/10.1007/978-90-481-8697-6

Hernández, C. (2005). Análisis de la percepción del riesgo en los volcanes Chichón y Tacaná, Chiapas. [Tesis de Licenciatura, Universidad Nacional Autónoma de México]. Repositorio institucional de la Universidad Nacional Autónoma de México. http://132.248.9.195/ptb2005/01026/0347104/Index.html.

James Clarke, Ludmila Adam, Kasper van Wijk, (2021). LP or VT signals? How intrinsic attenuation influences volcano seismic signatures constrained by Whakaari volcano parameters, Journal of Volcanology and Geothermal Research, Volume 418, 107337, ISSN 0377-0273. DOI: https://doi.org/10.1016/j.jvolgeores.2021.107337.

Kanamori, H. (1977), The energy release in great earthquakes, J. Geophys. Res., 82(20), 2981 – 2987, DOI: https://doi.org/10.1029/JB082i020p02981.

López, C. (2002). Sismicidad en la región del volcán Tacaná, Chiapas, durante septiembre de 1997 y su evaluación en el riesgo volcánico. [Tesis para optar por el grado de Ingeniero Geofísico, Universidad Nacional Autónoma de México].

López, Víctor., (2021). Estudio de la sismicidad del volcán Chichón, Chiapas, México durante el año 2017. [Tesis de Licenciatura, Universidad Juárez Autónoma de Tabasco].

Lamb, O. D., Angelis S. De, Wall R. J., Lamur A., Varley N. R., Reyes-Dávila G., Arámbula-Mendoza R., Hornby A. J., Kendrick J. E., and Lavallée Y. (2017), Seismic and experimental insights into eruption precursors at Volcán de Colima, Geophys. Res. Lett., 44, 6092–6100. DOI: https://doi.org/10.1002/2017GL073350.

Lee W, Bennet R, Meaghu K (1972) A method of estimating magnitude of local earthquakes from signal duration. U.S. Geological Survey Open File Report, 28 pp.

Legrand, D., & Comte, D., (2003). Análisis multi-fractal de la sismicidad del norte de Chile. Universidad de Concepción, Departamento de Geofísica, Santiago, Chile.

Legrand, Denis & Barrientos, Sergio & Bataille, Klaus & Cembrano Perasso, Jose & Pavez, A., (2011). The fluid-driven tectonic swarm of Aysen Fjord, Chile (2007) associated with two earthquakes (Mw=6.1 and Mw=6.2) within the Liquiñe-Ofqui Fault Zone. Continental Shelf Research. 31. 154-161. 10.1016/j.csr.2010.05.008.

Legrand, Denis & Iglesias, Arturo & Singh, Shri Krishna & Cruz-Atienza, Victor & Yoon, C & Dominguez, Luis & Valenzuela, R & Suárez, Gerardo & Castro-Artola, Oscar. (2021). The influence of fluids in the unusually high-rate seismicity in the Ometepec segment of the Mexican subduction zone. Geophysical Journal International. 226.10.1093/gji/ggab106.

Legrand, Denis & Marroquín, G. & DeMets, C. & Mixco, L. & García, A. & Villalobos, M. & Ferrés, Dolors & Gutiérrez, E. & Escobar, D. & Torres, R. & Hernandez, Douglas. (2020). Active deformation in the San Salvador extensional stepover, El Salvador from an analysis of the April–May 2017 earthquake sequence and GPS data. Journal of South American Earth Sciences. 104. 102854. DOI: https://doi.org/10.1016/j.jsames.2020.102854.

Lutgens, F. K., Tarbuck, E. J., & Tasa, D. G. (2016). Foundations of earth science (8th ed.). Pearson.

Macías, J., (2005). Geología e historia eruptiva de algunos de los grandes volcanes activos de México. Boletín de la Sociedad Geológica Mexicana, ISSN 0366-1784, Tomo 57, No. 3, 2005, pags. 379-424. 57. 10.18268/BSGM2005v57n3a6.

 DOI: https://doi.org/10.60620/vet6-kt90

Macias J L, Arce J L, García-Palomo A, Mora J C, Layer P W, Espindola J M, (2010). LatePleistocene flank collapse triggered by dome growth at Tacana volcano, Mexico/Guatemala, and its relationship to the regional stress regime. Bull Volc, 72: 32- 53.

Macías, J.L., Espíndola, J.M., García-Palomo, A., Scott, K.M., Hughes, S., and Mora, J.C., (2000), "Late Holocene Peléan style eruption at Tacaná Volcano, Mexico–Guatemala: Past, present, and future hazards", Bulletin of the Geological Society of America, 112 (8): 1234-1249.

Macias J L, Espindola J M, Garcia-Palomo A, Scott K M, Hughes S, Mora J C, (2000). Late Holocene Pelean-style eruption at Tacana volcano, Mexico and Guatemala: past, present, and future hazards. Geol Soc Amer Bull, 112: 1234-1249.

McNutt, S.R., (2005). Volcanic seismology. Annu. Rev. Earth Planet. Sci. 32, 461–491 Montenegro, Verónica & Spagnotto, Silvana & Legrand, Denis & Caselli, Alberto. (2021). Seismic evidence of the active regional tectonic faults and the Copahue volcano, at Caviahue Caldera, Argentina. Bulletin of Volcanology, 83. DOI: https://doi.org/10.1007/s00445-021-01442-7

Mora J C, Macias J L, Garcia-Palomo A, Arce J L, Espindola J M, Manetti P, Vaselli O, Sanchez J M, (2004). Petrology and geochemistry of the Tacana volcanic complex, Mexico/Guatemala: evidence for the last 40 000 yr of activity. Geof Internac, 43: 331-359.

Murcia, H. & Macías, J., (2014). Volcaniclastic sequences at the foot of Tacaná Volcano, southern México: Implications for hazard assessment. Bulletin of Volcanology. DOI: https://doi.org/76.10.1007/s00445-014-0835-5.

M. Shearer, P. (2009). Introduction to Seismology. 2a edición. New York: Cambrigde University Press. Privitera, Eugenio & Cocina, Ornella & Bonanno, A. & Gresta, Stefano. (2006). Seismogenic Stress Fields During an Inter-Eruptive Period. A Case History: Mt. Etna Volcano, 2001-2002. AGU Fall Meeting Abstracts.

Richter, C. F. (1935). An instrumental earthquake magnitude scale. Bulletin of the Seismological Society of America. Vol. 25, No1, pp. 1-32.

Rodríguez-Pérez, Q., Monterrubio-Velasco, M., Zúñiga, F. R., Valdés-González, C. M., & Arámbula-Mendoza, R. (2021). Spatial and temporal b-value characterization at Popocatépetl volcano, Central Mexico. Journal of Volcanology and Geothermal Research, 417, 107320. DOI: https://doi.org/10.1016/j.jvolgeores.2021.107320.

Shi, Yaolin & Bolt (1982). The standard error of the Magnitude-frequency b value. BSSA. 72.1677 - 1687. DOI: https://doi.org/10.1785/BSSA0720051677.

Scholz, C. (1968). The frequency-magnitude relation in microfracturingin rock and its relation to earthquakes, Bull. Seismol. Soc. Am. 58,399–415.

Schorlemmer, D., S. Wiemer, and M. Wyss (2005). Variations in earthquake-size distribution across different stress regimes, Nature 437. DOI: https://doi.org/10.1038/nature04094

SSN (2022): Servicio Sismológico Nacional, Instituto de Geofísica, Universidad Nacional Autónoma de México, México. URL: http://www.ssn.unam.mx DOI: DOI: https://doi.org/10.21766/SSNMX/SN/MX

Stein, S., Wysession, M. (2003), An Introduction to Seismology, Earthquakes, and Earth Structure. Blackwell Publishing, 1a Edición, EUA. Tsuboi, S., K. Abe, K. Takano y Y. Yamanaka (1995). Rapid determination of Mw from broadband P waveforms. Bulletin of the Seismological Society of America. Vol. 85, No 2, pp. 606-613.

Utsu, T. (1965). A method for determining the value of b in the formula log N =a - bM showing the magnitude-frequency relation for earth-quakes, Geophys. Bull. Hokkaido Univ. 13, 99–103 (in Japanese withEnglish summary).

Valdés, C., González, G., Arcimega, A., Nava, E., Gutiérrez, C., Santoyo, M. (1995).

Sismicidad del volcán Popocatépetl a partir del 21 de diciembre de 1994 al 30 de marzo de 1995. Estudios realizados durante la crisis de 1994 – 1995. SINAPROC, CENAPRED, UNAM. Ed. Especial. Secretaría de gobernación. Pp. 129 – 138.

Veith, K.F. y G.E. Clawson (1972). Magnitude from short period P-wave data. Bulletin of the Seismological Society of America. Vol. 62 No 2, pp. 435-452.

Whitmore, P. M., S. Tsuboi, B. Hishorn y T. J. Sokolowsky (2002). Magnitude-dependent correction for Mwp. Science of Tsunami Hazards Vol. 20, No 4, pp. 187 – 192.

 DOI: https://doi.org/10.60620/vet6-kt90

Density Variations, Thermodynamic Properties and Earthquakes in the Horseshoe Basin

Maria Rosa Alves Duque [1]

[1] *Universidade de Évora, Departamento de Física, Escola de Ciências e Tecnologia, Rua Romão Ramalho 59, Évora, mrad@uevora.pt*

SUMMARY

This work considers the hypothesis of heating of materials and water in the Region of the Bank of Gorringe and Horseshoe Basin before the earthquake of February 28, 1969. For this purpose, data from the magnetic field obtained in Magnetic Observatories of the Iberian Peninsula were analysed, and anomalies were observed, including strong variations in the magnetic declination. A simple model was used to obtain the effect of heating two different media (peridotite and gabbro) in physical contact, with different thermal and mechanical properties. The results include compression of peridotite by gabbro and shear stresses in the contact of the two materials.

Keywords: Geoid height; magnetic anomalies; thermal properties; mechanical properties, thermal stresses.

1. Introduction

In the early morning of February 28 in 1969, a seismic crisis began with epicentres located in the SW of Cabo de São Vicente (Portugal). In a time interval of less than three hours, five earthquakes of magnitude 8, 5.6, 3.9, 4.4 and 3.8 were registered by seismic stations. The events mentioned caused 13 deaths and considerable damage. On that day, a total of 32 seismic events occurring in the region were registered by seismic observatories (Pena et al, 2014).

Some answers to surveys carried out after the earthquake of February 28 include descriptions of phenomena that may be associated with changes in the terrestrial magnetic field. This work analyses data registered 54 years ago. Geoid height data with models from 1984, 1996 and 2008 are also used.

2. Geoid Height values

Geoid height values for the region were obtained using EGM models 1984, 1996 and 2008. The results obtained for latitude values 36.00°N and 36.36°N can be seen in **Figure 1a** and **Figure 1b**.

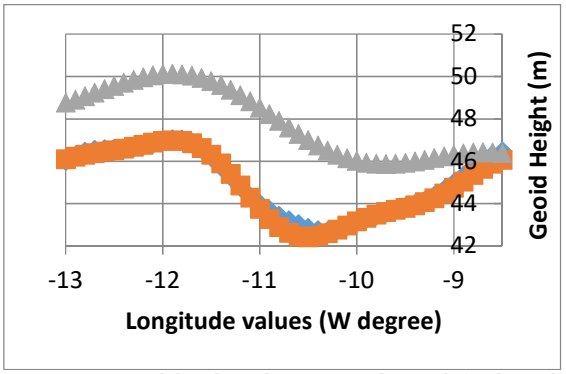

Figure 1a. Geoid height values were obtained for latitude 36°N- green-1984, red-1996 and blue-2008.

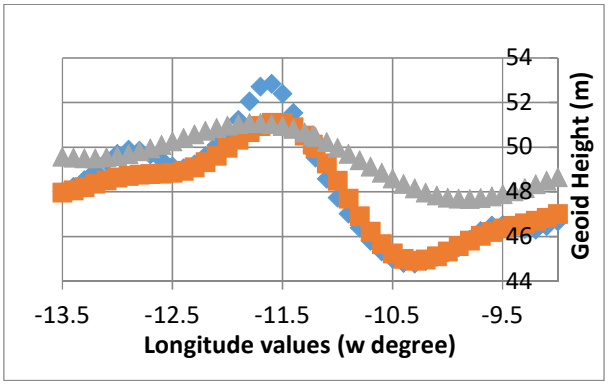

Figure 1b. Geoid height values were obtained for latitude 36.36°N- green-1984, red-1996 and blue-2008.

Figure 1a shows clearly that values decrease in all longitude values from 1984 to 1996 but the values change with longitude. An increase is visible in longitude values from -10.4° to -11.0° in 2008 (blue points).
An increase in geoid height values is seen in **Figure 1b** for longitude values from -11.3° to -12.0° in 2008 (blue points). It is possible to see also that values decrease in all longitude values from 1984 to 1996. The decreasing value changes with longitude in both latitudes. The greatest values are obtained in **Figure 1a** (≈5 m) between longitude values -10.5° and -11.0°.
The changes found in geoid height values at latitude 36.00°N are difficult to explain, particularly the blue points between -10.4° and -11.0°. A possible explanation for density alteration is temperature changes in the region.

3. The geomagnetic field

Magnetic field data used in this work were obtained from Geomagnetic Observatories located in the Iberian Peninsula and the Canary Islands. The data consist of average time values of the horizontal and vertical components of the magnetic field and the magnetic declination, recorded at the Observatories and inserted in Annales of the years 1969 and 1968.

3.1. The year 1969

Figure 2a shows the average monthly values of the horizontal component of the geomagnetic field measured in the Coimbra Geomagnetic Observatory during the year 1969 (blue points). Orange points show the values obtained using the IGRF model for Coimbra in the year 1969.

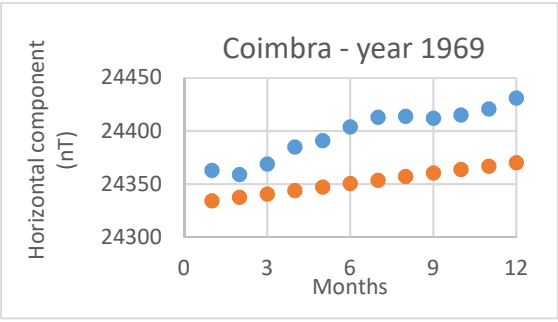

Figure 2a. Average monthly values of the horizontal component measured in Coimbra Observatory (blue points) and values obtained with the IGRF Model (red points).

It is possible to see that the values measured are higher than the values obtained with the model IGRF. February is the month with a value near that obtained with the model.
Figure 2b shows identical anomalies to those observed in Coimbra. In this case, the data were obtained in Toledo Observatory from July 1968 to June 1969. The anomalies of the horizontal component of the geomagnetic field are present in all data presented. November 1968 is the month with a value close to the value obtained with the IGRF model. February 1969 is also a value close to that obtained with the IGRF model.

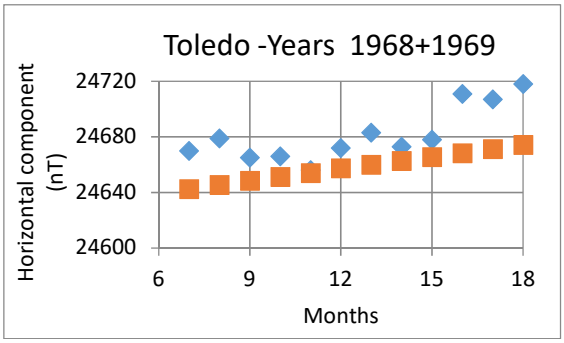

Figure 2b. Average monthly values of the horizontal component measured in Toledo Observatory from July 1968 to June 1969 (blue points) and values obtained with the IGRF Model (red points).

Table I shows the values of the horizontal component of the geomagnetic field measured in February 1969 in different observatories and the values obtained with the IGRF model. Only in one station (Tenerife), the value measured is lower than the value obtained with the IGRF model.

Table I. Values of the horizontal component of the geomagnetic field in May 1969. Dif is the difference between the values measured and modelled by the IGRF model.

Observatory	Measured	IGRF	Dif
Coimbra	24391	24352	39
Toledo	24707	24655	52
San Fer.	26406	26205	201
Almeria	26289	26249	40
Tenerife	28762	29160	-398

The analysis of the values measured in February 1969 shows that the lower value of the horizontal component of the geomagnetic field is associated with three strong anomalies that occurred in that month. In November 1968 a strong anomaly occurred at the end of October and the first days of November.

DOI: https://doi.org/10.60620/d57m-k250

3.2. February and May 1969

Seismic records show the occurrence of earthquakes of high magnitude on 28 February (M=7.9) and 5 May (M=5.4) in 1969. **Figure 3a** shows hourly average values of the horizontal component of the geomagnetic field in a time interval from February 25 to February 27 (blue points). Red points are average values obtained on quiet days registered by the Observatory. It is possible to identify some hours with increased values (blue points) of the geomagnetic data. **Figure 3b** shows the same type of data obtained for the time interval from May 3 to May 5. In this case, the positive anomalies are present in the three days studied but the increase is lower than in February. The negative anomaly found on February 27 is not visible in May.

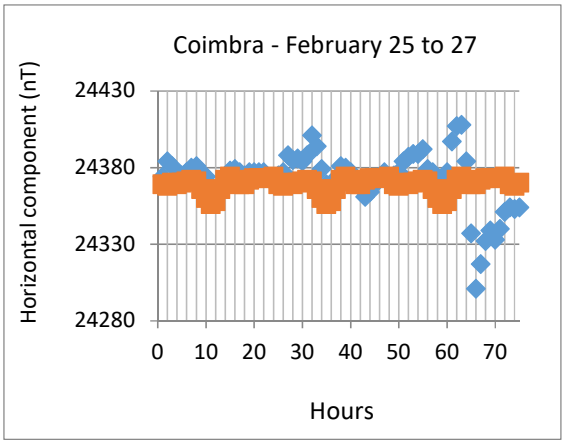

Figure 3a. Average hourly values of the horizontal component o the geomagnetic field (blue points). Average values for quiet days (red points).

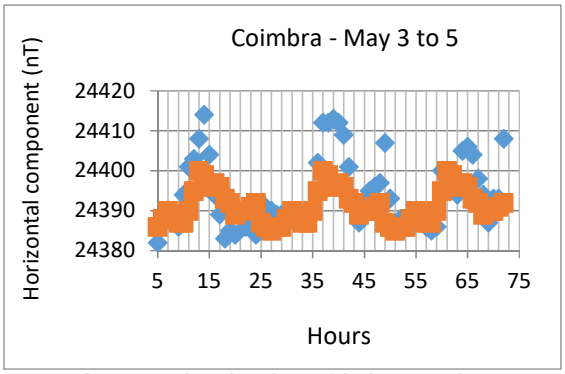

Figure 3b. Average hourly values of the horizontal component of the geomagnetic field (blue points). Average values for quiet days (red points).

The vertical component of the geomagnetic field shows lower values than those obtained on quiet days on February 25, 26 and in the morning of 27. A strong positive anomaly appears only on February 27 (**Figure 4a**) with the maximum values at hour 18. Small anomalies occurring in small time intervals may be seen in **Figure 4b**.

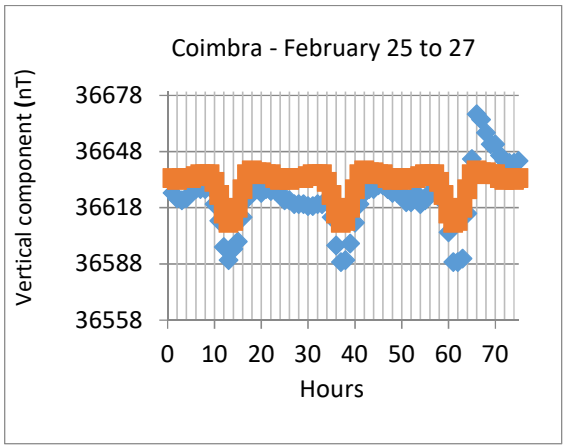

Figure 4a. Average hourly values of the vertical component of the geomagnetic field (blue points). Average values for quiet days (red points).

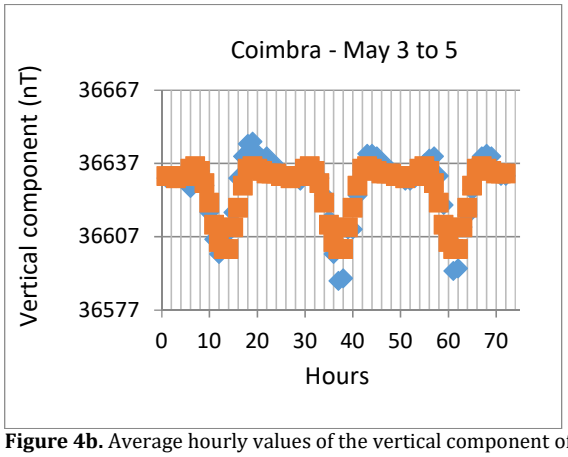

Figure 4b. Average hourly values of the vertical component of the geomagnetic field (blue points). Average values for quiet days (red points).

The inclination of the magnetic field in **Figure 5a** (25 to 27 February) is lower than the average values found on quiet days. An exception is found on day 27 with a strong positive anomaly. In the last days of February 1969, the horizontal component of the geomagnetic field was higher than the values measured in quiet days, but the vertical component and the inclination of the geomagnetic field are lower than the values obtained in quiet days. On the afternoon of day 27, a positive anomaly occurred in the vertical component and the inclination of the field. This type of anomaly was not observed on May 3 to 5 (**Figure 5b**).

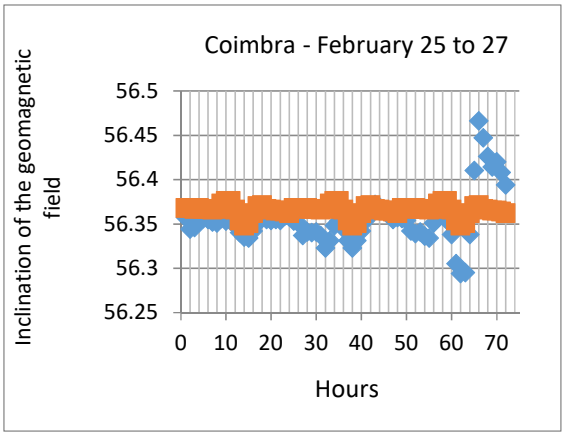

Figure 5a. Average hourly values of inclination of the geomagnetic field (blue points). Average values for quiet days (red points).

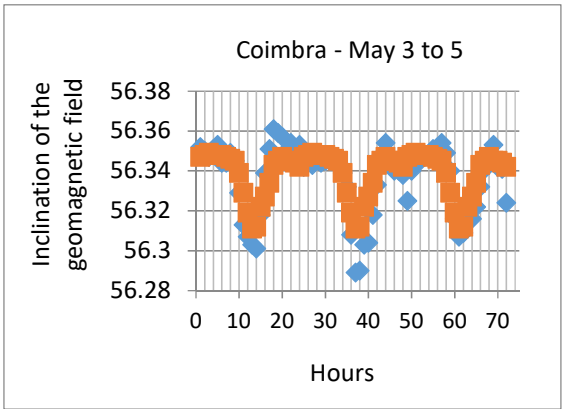

Figure 5b. Average hourly values of inclination of the geomagnetic field (blue points). Average values for quiet days (red points).

4. Thermodynamic properties

The variations found in geoid height values in the Horseshoe Bain and the Gorringe Bank suggest heating episodes separated from time intervals with decreasing temperatures.

It is thought that in the region referred the main type of formations are peridotites with intercalations of gabbros. These types of rocks show different thermal and mechanical properties when subjected to the same heat source.

A study considering a body formed by two different materials with the same volume but with different thermal properties heated by the same heat source was made (Duque, 2023). **Table II** presents the main properties of the constituent materials of the body.

In the initial state, the temperature of the two materials is equal. T_0=10°C. The two materials will be heated simultaneously. Because they have different densities and specific heat capacity values, the temperature increase will be different in both materials. T_{1A}=45°C, T_{1B}=89.7°C≈90°C.

Table II. Some properties of the structure studied.

	Material A	Material B
Density	3200 kg m^{-3}	3000 kg m^{-3}
Specific heat	1.26 KJ.kg^{-1}.K^{-1}	0.59 KJ kg^{-1} K^{-1}
Thermal expansion coefficient	3.5×10^{-5} K^{-1}	4.8×10^{-5} K^{-1}

The temperature difference between the two materials originates temperature gradients and heat flow by conduction in the horizontal direction. The horizontal flow of heat near the border between the two materials must be equal. Using the Fourier law, we will have

$$\text{Grad } T_A.K_A = \text{Grad } T_B.K_B \qquad (1)$$

Using as thermal conductivity values, K_A=4.0 W.K^{-1}.m^{-1} (peridotite rock) and K_B = 2.3 W.K^{-1}.m^{-1} (gabbro rock) it is possible to obtain the temperature value in the contact zone of the two materials, T_{in}=61.4°C. **Table III** contains temperature values obtained in materials A and B and the contact zone after different intervals of heating, considering constant values of C_p, mass, and thermal conductivity.

Table III. Temperature values in materials A and B and the contact zone of the two materials.

T_A (°C)	T_B (°C)	T_{in} (°C)
45	90	61
80	170	113
106	231	152
200	443	289
316	707	459

The values of this Table show that the difference between the temperature values of materials A and B increases with the increase in temperature values. The thermal gradient near the contact zone of the two materials is higher in material B than in material A.

Due to the increase in temperature, the materials will tend to expand. If they are confined, they will suffer an increase in pressure. Because they are subjected to different temperature variations and because they have different expansion coefficients, the volume variations will be different.

DOI: https://doi.org/10.60620/d57m-k250

If the materials are confined, they will not be able to expand and pressure variations will happen. The results obtained will depend on the value of the volumetric elasticity/ compressibility modulus of the materials (**Table IV**). The effect of the temperature increase was not considered, and the values presented are considered constant values.

Table IV. Values of mechanical properties used in the work.

Property	Material A	Material B
Bulk modulus (Pa)	75.3×10^{9}	44.4×10^{9}
Young modulus (Pa)	1.1×10^{11}	$0.8\ 10^{11}$
Torsion modulus (Pa)	0.44×10^{11}	0.30×10^{11}
Poisson coefficient -υ	0.25	0.20

The pressure will increase in the two materials but near the border between them, the pressure is higher in material A than in material B.

Due to the increase of temperature in material A (decrease in material B) near the contact zone of the two materials, σ_3 (the thermal stress in the vertical direction) presents a gradient value with a positive signal in material A (the stress increases near the contact zone) and negative signal (the stress decreases near the contact zone B).

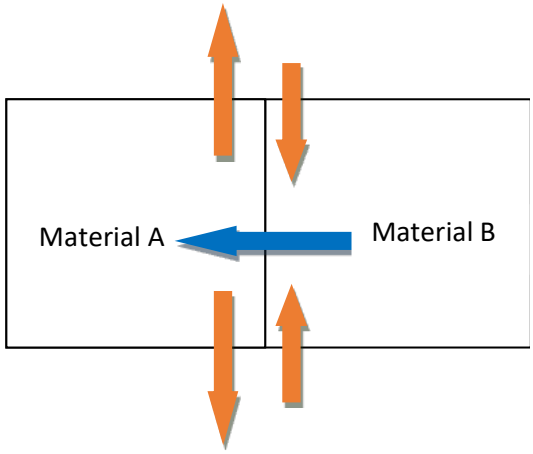

Figure 6. Thermal stresses originated from the contrast of thermal properties of the materials subjected to heating.

It is observed a horizontal compression is exerted by material B on material A. Its value increase with temperature increase.

Shear stresses appear near the boundary between the two materials (**Figure 6**).

Table V shows that stresses due to heating are higher in material B than in material A but in the region near the contact zone of the two materials thermal stresses are higher in material A than in material B.

Table V. Thermal stresses.

σ_A(MPa)	σ_B(MPa)	σ_{bA}(MPa)	σ_{bB}(MPa)
60	28	87	82
120	256	176	165
164	354	241	226
465	693	478	446
524	1115	772	722

At the boundary between the two materials, there is a decrease in the thermal stress in the vertical direction in material B relative to material A. The decrease increases with the heating process (temperature values used).

5. Some final comments

The variation of mechanical properties with temperature was not considered in this work. Water was not introduced in the model. The introduction of water into the model will decrease the temperatures and also pressure increases and thermal stresses.

As the degree of fracture and the transmissivity between them may be different in both materials, the amount of water introduced may also be different on the two sides, originating changes in the results obtained.

6. Future work

Thermal episodes of heating in the region could give rise to compression and deformation phenomena and may eventually reach the rupture of materials.

Anomalies of the geomagnetic field seem to be present sometime before the occurrence of some earthquakes in the region before and after February 28 A great increase of the vertical component and in the declination and inclination of the geomagnetic field were detected on the afternoon of February 27.

The velocity at which the increase took place was very high and alterations in the electric field are expected but that is a work to be done in the future.

7. Acknowledgements

Data obtained in San Fernando Observatory were provided by Real Instituto y Observatorio de La Armada in San Fernando (Spain).

8. References

Instituto Geofísico da Universidade de Coimbra, (1972). "Observações Meteorológicas, Magnéticas e

Sismológicas. Ano de 1969 – 2ª Parte: Magnetismo Terrestre", Volume CVIII, Coimbra.

Instituto Geografico y Catastral, (1971). Anuarios del Servicio de Geomagnetismo y Aeronomia, Año de 1969, Madrid.

Instituto Geografico y Catastral, (1970). Anuarios del Servicio de Geomagnetismo y Aeronomia, Año de 1968, Madrid.

J. Pena, , J. Costa Nunes and F. Carrilho, (2014). Catálogo Sísmico de Portugal Continental e Região Adjacente,1961-1969 IPMA, Lisboa, Portugal, 2014.

Haenel, R., Rybach, L. and Stegena, L. (eds), (1988), Handbook of Terrestrial Heat-Flow Density determination, 499-453, Holland, Kluwer Academic Publishers.

Turcotte, D. L., Schubert, G. (2002), Geodynamics (2nd ed.), New York, Cambridge University Press.

Coelho, P., (2017). Tabelas de Termodinâmica (4ª edition), LIDEL-Edições Técnicas. ISBN 978-989-752-262-8.

Duque, M. R., (2023). Problems associated with the contrast between thermal and mechanical properties of materials. Brazilian Journal of Development, v.9.n.1, 3362-3370.

 DOI: https://doi.org/10.60620/d57m-k250

Preliminary Results of the Macroseismic Survey on the 28 February 1969 (7.9 Ms) Earthquake that Occurred at SW St. Vincent Cape

Célia Marreiros [1]; Paulo M. Alves [1], Carlos S. Oliveira [2], Susana Custódio [3], Fernando Carrilho [1]

[1] *Instituto Português do Mar e da Atmosfera, Lisboa, Portugal, celia.marreiros@ipma.pt, paulo.alves@ipma.pt, fernando.carrilho@ipma.pt*
[2] *Instituto Superior Técnico, CERIS, Lisboa, Portugal, csoliv@civil.ist.utl.pt*
[3] *Instituto D. Luís, Faculdade de Ciências, Universidade de Lisboa, Lisboa, Portugal, sicustodio@fc.ul.pt*

SUMMARY

On 28 February 1969, a 7.9 Ms earthquake occurred 180 km SW of St. Vincent Cape, which was felt with maximum intensity VIII, in the south of Portugal. It was felt in mainland Portugal, Madeira, Spain, Morocco, Andorra, and France. This earthquake is the most important in Europe in the 20th century if we consider the combination of the magnitude and the macroseismic effects. In February 2019, the Instituto Português do Mar e da Atmosfera (IPMA), the Instituto Superior Técnico (IST), the Faculdade de Ciências da Universidade de Lisboa (FCUL) and the Instituto Dom Luiz (IDL) launched an international survey at the 50th anniversary of the earthquake published in several languages, on internet, for the citizens report the earthquake observed effects. It was observed a significant collaboration between the population and the schools in this initiative allowed the collection of thousands of answers to complement the existing data.

Keywords: Macroseismic, survey, EMS-98, Earthquake, 1969.

1. Introduction

The earthquake of 28 February 1969 had a surface wave magnitude of 7.9 Ms and occurred at ~180 km of SW St. Vincent Cape, Portugal. The map of **Figure 1** shows the location of the epicentres of the earthquakes with a magnitude greater than 5, which occurred in the European region according to the Global Instrumental Catalogue from ISC from 1904 to 2018 (ISC-GEM earthquake catalogue, 2022).

The red stars indicate the 6 strongest earthquakes with magnitudes greater or equal to 7.7 Mw. Three of them (1941, 1969 and 1975) occurred in the Atlantic between Azores and Iberia and had macroseismic effects in Portugal.

Table I shows the magnitude and the intensity for the 6 earthquakes with a magnitude greater or equal to 7.7 Mw. Comparing the combination of the magnitude and the macroseismic intensity, we find that the 1969 earthquake is the most important in the 20th century in Europe region.

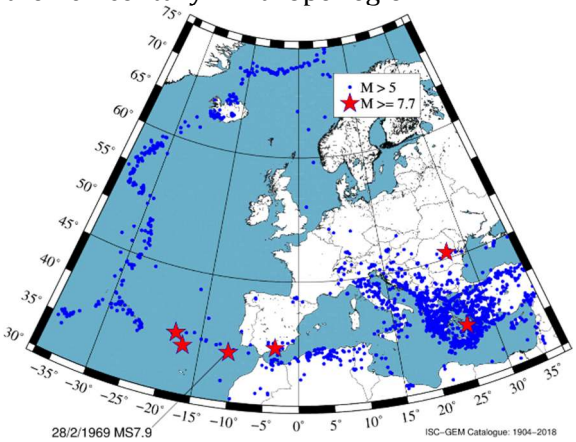

Figure 1. Map with the location of the epicentres of the earthquakes with a magnitude greater than 5, that occurred in the European region according to the Global Instrumental

Catalogue from ISC from 1904 to 2018 (37.5°W ≤ Lon ≤ 37.5°E; 30°N ≤ Lat ≤ 75°N; Mw ≥ 7.7).

Table I. Strongest earthquakes with magnitudes greater or equal to 7.7 Mw, that occurred in the European region according to the Global Instrumental Catalogue from ISC from 1904 to 2018.

Year	Mw	Intensity	Region
1941	7.84	VI	Gloria F., Atlantic
1954	7.8	VI	Granada, Spain
1969	7.8	VIII	Gorringe, Atlantic
1975	7.8	IV	Gloria F., Atlantic
1940	7.74	IX	Vrancea, Romenia
1956	7.7	IX	Amorgos, Greece

The earthquake of 28 February 1969 occurred at 03:41 (local time) and was felt as far as 1300 km. The earthquake was felt in Portugal, Spain, Morocco, Andorra, and France. The maximum macroseismic intensity was VIII at the Algarve region in the south of Portugal's mainland (SMN, 1969).
Comparing the combination of the magnitude and the macroseismic intensity, we find that the 1969 earthquake is the most important in the 20th century in Europe region.
In the days after the occurrence of the earthquake, the newspapers published photos with some effects of this event.
Figure 2 shows vehicles parked next to the buildings with damages in Lisbon that were published in the "Diário Popular" newspaper on 28 February 1969.
The 50th anniversary of the earthquake was an opportunity to perform a last survey related to it. Seismologists and engineers from Portuguese seismic service and academic institutions collaborated to launch an international survey at the end of February 2019 for citizens reporting the 1969 earthquake observed effects. There were two main purposes for this initiative. Firstly, collect the data that remain in the memory of the population and preserve it. Nowadays it is much easier to collect and deal with huge amounts of data that wasn´t possible fifty years ago. In some important regions, the collected data were not exhaustive. Secondly, it was important to test the online questionnaire "Did you feel an earthquake?" with an event with real damage. Although, the online questionnaire of IPMA was available to routinely collect macroseismic data until the present day there was no significant data from damaging earthquakes.

Figure 2. Vehicles parked next to the buildings with damages in Lisbon (Diário Popular, 28/2/1969).

2. Method and data

To publicize the survey was created a webpage with the link to the questionnaire, information about the earthquake and the seismic network, etc. The survey was published in Portuguese, Spanish and French. Also, Facebook and Instagram pages were created to publicize the survey and ask people to answer the questionnaire. In addition, the survey was publicized on the social networks of IPMA. The Portuguese media also helped to disseminate the survey. A school contest (with a prize) was organized, inviting the students to interview their older relatives. Other institutions joined the initiative, like the Instituto Geográfico Nacional of Spain (IGN), the European Mediterranean Seismological Centre (EMSC) and many others.
The 1969's earthquake macroseismic questionnaire was implemented on IPMA´s webpage using the software package LimeSurvey. Answers in a free text or macroseismic questionnaire mode were allowed. The 1969´s earthquake macroseismic questionnaire was based on: 1) the EMS-98 scale (Grünthal, 1998); 2) the IPMA´s macroseismic web questionnaire (*Sentiu um Sismo*, IPMA), with some specific questions added related to the type of report (direct, interview or indirect), trust level (total or partial), effects on electricity and phone networks and type of movements.
The 1969's earthquake web survey answers were received from 20/2/2019 to

 DOI: https://doi.org/10.60620/tze1-b883

30/3/2021. The DataBase of the LimeSurvey stored 7555 records but many of them are incomplete or empty, 41.4% of them are complete. **Figure 3** shows the distribution of the mode of access to the survey received from 20/2/2019 to 30/3/2021. Many of the accesses to the survey (54%) were made using the link to the webpage (http://sismo1969.ipma.pt).

Regarding the complete answers: 94% are in questionnaire mode and 6% are in free text mode. From 20/2/2019 to 30/3/2021, 3128 answers are completed and submitted with success.

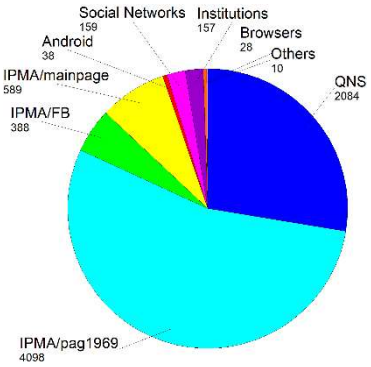

Figure 3. Distribution of the accesses to the survey from 20/2/2019 to 30/3/2021.

Many of the answers were received from the end of February to the end of May 2019 (more answers were received in the 3 first months). Most of the answers (88%) are direct reports via questionnaire. Most of the respondents (94%) have a high level of trust in the report. Concerning the level of trust of the respondents it was considered that the responses are true because fake, truthless, phoney and/or impolite responses are usually excluded by a quality control that is applied to the responses (Alves *et al*., 2012). Nevertheless, it is not impossible to respond to the questionnaire with coherent and plausible fake responses, which is not common.

Portugal's mainland received 3014 responses (589 sites) and Madeira Island (9 sites) received 10 responses. The map (**Figure 4**) shows the distribution of the responses by the site on Portugal's mainland. The size and the colour of the circles indicate the number of responses. The site with more responses is Alvalade in Lisbon with 123. The closest reports were received from Sagres (Vila do Bispo) located ~180 km away from the earthquake epicentre. In addition, were received responses from 24 sites from Spain, Morocco and Andorra.

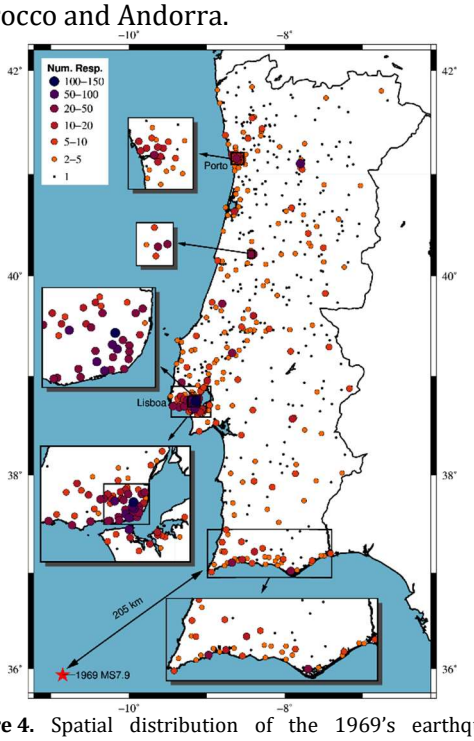

Figure 4. Spatial distribution of the 1969's earthquake questionnaire responses received from Portugal's mainland.

Some aspects of the responses can be highlighted. For instance, 99% were from observers that were inside buildings, 79% of the observers were sleeping and awaked by the earthquake, 45% reported that doors and windows rattled, 54% reported that occurred building damages, 8% reported that they were extremely frightened, and 0.2% reported that occurred masonry buildings collapse.

The Portuguese seismic service has an algorithm developed and implemented to make a quick analysis of the reported effects and convert them into degrees of seismic intensity. The results are the median of values of intensities obtained per site (Alves *et al*., 2012; Marreiros *et al.*, 2020).

3. Results

The maps of **Figure 5a, Figure 5b** and **Figure 5c** show the results of intensities per Macroseismic Data Point (MDP) using the automatic routine with the answers received until the end of March 2021.

The 1st map shows results considering all the answers organised by MDP. The 2nd map shows results considering a minimum of 3 answers by MDP. The 3rd map shows results

considering a minimum of 10 answers by MDP.

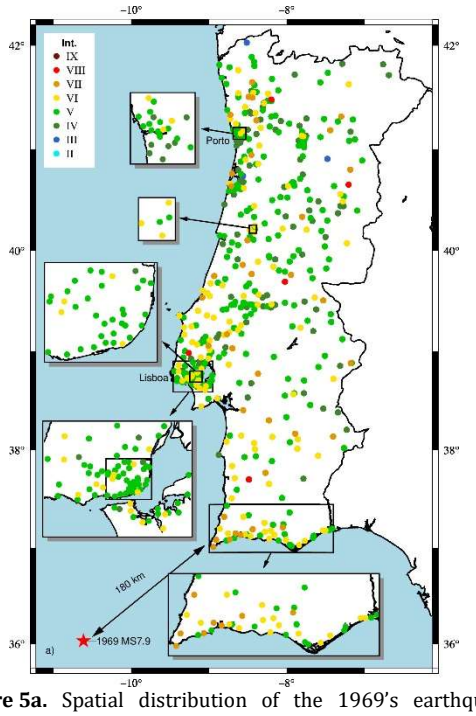

Figure 5a. Spatial distribution of the 1969's earthquake macroseismic intensities at Portugal mainland with all data.

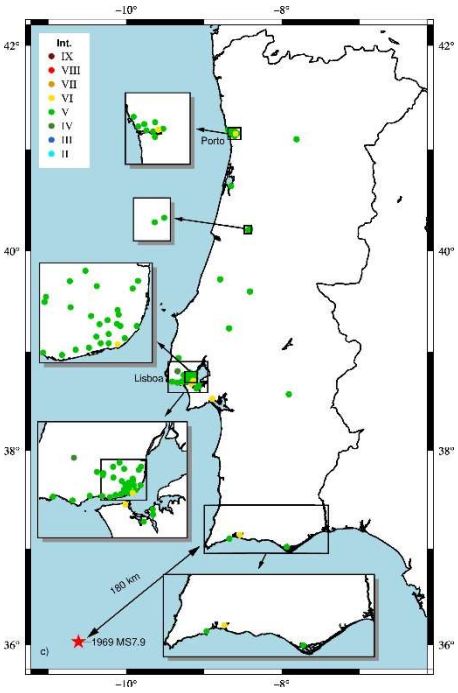

Figure 5c. Spatial distribution of the 1969's earthquake macroseismic intensities at Portugal mainland with min 10 responses per MDP.

The most affected region was the southwestern Algarve, with the seismic vibration attenuated to the northeast, with significant local variations.

The map of **Figure 5b** shows the best balance between the number of responses per MDP and the number of MDPs with macroseismic

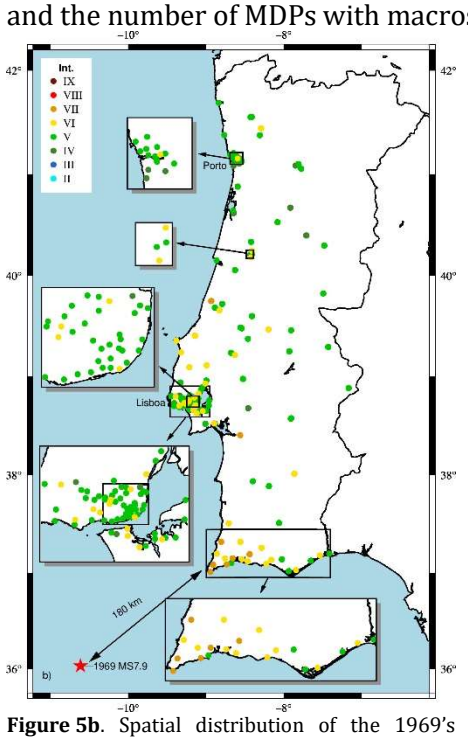

Figure 5b. Spatial distribution of the 1969's earthquake macroseismic intensities at Portugal mainland with min 3 responses per MDP.

intensity estimated. For this map is presented the histogram in **Figure 6**.

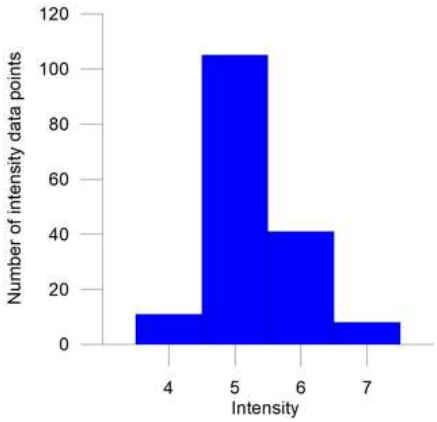

Figure 6. Histogram showing the "Number of intensity data points" versus "Intensity" for the 1969's earthquake and for MDPs with a minimum of 3 responses.

4. Final Remarks

Figure 7 shows the 1969's earthquake distribution of intensities that were published in the Seismological Yearbook of Portugal in 1969 (SMN, 1969).

The comparison of **Figure 7** and **Figure 5b** shows some interesting aspects. The data obtained will complement the existing lack of information in some regions, such as Lisbon,

DOI: https://doi.org/10.60620/tze1-b883

among others. The distribution of intensities agrees with the expected attenuation in the territory.

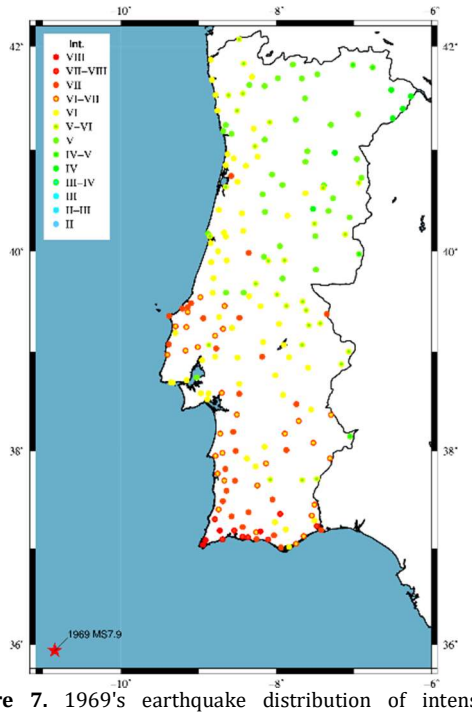

Figure 7. 1969's earthquake distribution of intensities published in the Seismological Yearbook of Portugal in 1969.

However, it is noticeable that the values now obtained are at least one degree lower than the macroseismic values published in the Seismological Yearbook of Portugal in 1969. The reason for that can probably be found in the macroseismic scales used now and then.

The scale used in 1969 was the Mercalli version of 1931 and it was common to assign the intensity considering the highest effects observed in the site. This work it is used the macroseismic scale EMS-98 and one important aspect of it is assigning the intensity according to the most common effects on a given site. It is expected in this given site that some effects typical of higher intensities can be present, but they are not representative of what happened commonly in that site. So, it is important to consider which scale is based on the evaluation in each case.

The collaboration of the population and schools allowed us to collect thousands of responses with the macroseismic questionnaire "Did you feel the 1969 earthquake?".

Also, new technologies, such as mobile devices, allowed the acquisition of an amount of quantifiable and unquantifiable data, which was still in the memory of the population. Many citizens still remember well this earthquake and most are between 60 and 70 years old. The free text mode allowed many observers to report what they experienced and from these reports, a consistent amount of data was related to less known phenomena as sounds, lights and smells that seemed to be common in earthquakes equal to or greater than 1969´s earthquake magnitude. The information in these reports will be presented soon.

The 1969's earthquake macroseismic questionnaire made it possible to perform a test with the automatic evaluation algorithm with real data, which includes damages to buildings. Although this damage analysis routine is now implemented in the operational routine of the IPMA, it has become clear that the rapid assessment using the collection of information through the Internet necessarily has to be complemented with *in-situ* observations by experts to guarantee that there is reliable information in the catalogues for further studies, namely, seismic risk studies.

Lastly, it is important to mention that this work presents results of the evaluation of macroseismic intensities based on new data collected 50 years after the 1969 earthquake occurrence, it is not a re-evaluation of previous intensities related to the event.

5. References

Alves P.M., Marreiros C. & Carrilho F. (2012) New Developments on Automatic Macroseismic Evaluation Based on Internet Questionnaires at I.M., I.P. The 15th World Conference on Earthquake Engineering (15WCEE), Lisboa, Portugal, pp.10.

Anuário Sismológico de Portugal - 1969 (1970), nº 23, Serviço Meteorológico Nacional

Grünthal, G. (1998). European Macroseismic Scale 1998 (EMS-98). Cahiers Centre Europeen Geodynamique Seismologie Luxembourg 15,1–99.

ISC-GEM earthquake catalogue (2022), DOI: https://doi.org/10.31905/d808b825.

Marreiros, C., Alves, P., Carrilho, F. (2020), The macroseismic questionnaire "Did you feel an earthquake?" and its automatic evaluation, International meeting - 40 years of the 1980 Azores earthquake: a week of reflection.

www.ipma.pt/pt/geofisica/informe/

 DOI: https://doi.org/10.60620/tze1-b883

Advancements in the LouMu Project – Muography for Geophysical Surveys

Pedro Teixeira [1], Alberto Blanco [2], Bento Caldeira [1], Bernardo Tomé [2], Isabel Alexandre [3], João Matos [4], João Costa [8], Jorge Silva [5], José Borges [1], Josué Figueira [1], Lorenzo Cazon [6], Luis Afonso [2], Luis Lopes [2], Magda Duarte [7], Mário Pimenta [2], Mourad Bezzeghoud [1], Paolo Dobrilla [2], Pedro Assis [2,3], Raul Sarmento [2], Rui Oliveira [1], Sofia Andringa [2], Vanessa Pais [8]

[1] *Physics Department (ECT), Institute of Earth Sciences (ICT/IIFA), Earth Remote Sensing Laboratory (EaRSLab), University of Évora, Rua Romão Ramalho n.º 59, 7000–671 Évora, pmmt@uevora.pt*
[2] *Laboratory of Instrumentation and Experimental Particle Physics (LIP), Av. Prof. Gama Pinto, 2, 1649-003 Lisboa*
[3] *Instituto Superior Técnico (IST), Av. Rovisco Pais, 1, 1049–001 Lisboa*
[4] *Nacional Laboratory of Energy and Geology (LNEG), Campus de Aljustrel, Bairro da Vale d' Oca, Apartado 14, 7601–909 Aljustrel, Portugal*
[5] *Physics Department (DF), University of Coimbra, Rua Larga, 3004–516 Coimbra, Portugal*
[6] *Instituto Galego de Física de Altas Enerxías (IGFAE) – Universidade de Santiago de Compostela, Rúa de Xoaquín Díaz de Rábago, 15705 Santiago de Compostela, Spain*
[7] *University of Minho, Gualtar Campus, CP3, 3.02, 4710–057 Braga, Portugal*
[8] *Mina de Ciência - Lousal Ciência Viva Center, Avenida Frédéric Velge, 7570–006, Lousal, Portugal*

SUMMARY

The LouMu Project is an ongoing collaboration between the Laboratory of Instrumentation and Experimental Particle Physics, the Institute of Earth Sciences – University of Évora and the Lousal Ciência Viva Center, and also with the support of the Nacional Laboratory of Energy and Geology. In this collaboration, the potential of the muography technique is being explored in the Lousal Mine. The end goal is to create the conditions for the use of muography as a novel method for geophysical surveys in Portugal.
This communication intends to summarize and briefly describe the work involved in the LouMu Project while presenting the advancements done so far in this ongoing work.

Keywords: Muography, Geant4, Geophysical survey, Lousal Mine, Corona Fault.

1. Introduction

Muography is an imaging technique that uses muons, elementary charged particles created in the atmosphere, to enable non-invasive and remote observations. It uses detection methods and equipment to measure the crossing of muons. The muon flux, which only a fraction of it crosses the surveyed targets and reaches the detectors, is attenuated differently depending on the density of the materials. The denser the matter the fewer muons will be detected crossing it. The detection measurements are stored in direction maps, called muographs, and show the average density distribution from the surveyed targets. The technique has been around in the world for some decades and used in different fields of science (Bonechi et al., 2020; Kaiser, 2019) but has not been used in Portugal until now.

The LouMu Project wants to develop the muography technique for the first time in Portugal and make it available for applications in geophysics. It is a

collaboration between the Laboratory of Instrumentation and Experimental Particle Physics (LIP), the Institute of Earth Sciences University of Évora and the Lousal Ciência Viva Center, and the Nacional Laboratory of Energy and Geology (LNEG). The first test muography implementation is being carried out in an underground environment in the Lousal Mine.

The project work is divided into the creation of simulations and development of muography analysis tools, geophysical work to study the terrain above the telescope, the development of muon telescopes and the application of muography in the Lousal Mine, and also outreach activities, like presentations and visits to the telescopes in the mine. The muography survey using the muon telescope in the mine started in April of 2022 and it is still ongoing. The muon data can be analysed in real-time, but the geophysical results and the muography final results are still in preparation and will be published in the future.

2. Lousal Mine

The muography application of this project is taking place inside the Waldemar Gallery, the uppermost gallery of the Lousal Mine, located in the Alentejo region of Portugal. The mine is no longer active and is now a place of visit at the Lousal Ciência Viva Center. The Lousal Mine was chosen to receive the first application of muography because it has a well-supported infrastructure and well-known geology, making it ideal to be a test site for this initial application. After the mining activity ended in 1988, the Lousal Mine was rehabilitated as a science museum, offering tours to visitors in the museum and the rehabilitated mining complex. After the beginning of the project collaboration, in 2018, the muography and the muon telescopes have become part of the museum exhibition, helping in the dissemination of information about the technique and the project to the public. The goal is to do a geological survey of the terrain between the telescope and the surface with muography and improve the existing information with new data while evaluating the performance of the telescope and the muography analysis tools. A geophysical survey in the same area done with standard methods will give a reference against which to compare the muography results.

3. Muon Telescope

To test the electronics in the mine humidity and temperature underground conditions, a prototype was installed in 2019 inside the gallery. With this initial test, a bigger and fully functional muon telescope was designed and assembled.

The LouMu muon telescope, nicknamed CorePix, was developed in the LIP detectors laboratory in Coimbra, where it stayed for several months collecting data to test and calibrate the muon detectors. It was moved to the Lousal Mine in April of 2022 and placed in storeroom nº 4 of the mine gallery, as seen in **Figure 1**. The muography data acquisition started the week after.

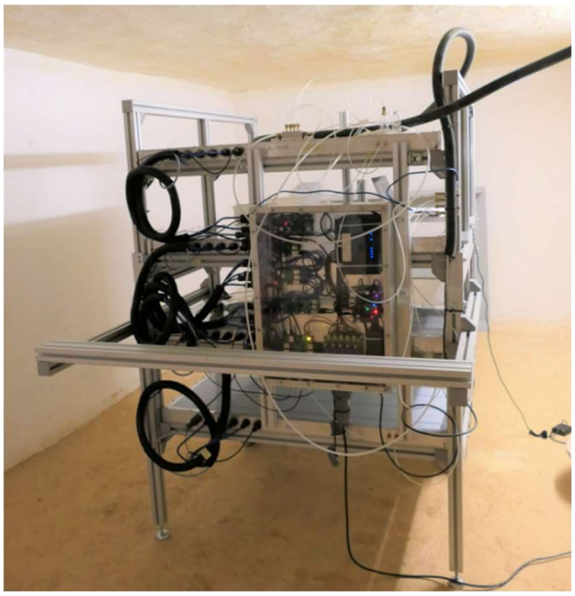

Figure 1. CorePix muon telescope placed and working inside the storeroom nº 4 of the Waldemar gallery.

The CorePix is equipped with 4 Resistive Plate Chambers (RPC), a type of gaseous

DOI : https://doi.org/10.60620/1y7h-f307

muon detector, with a size 1 m×1 m square shape, and the entire structure of the telescope has a height of about 1.60 m. The gas is sent to the RPCs with a low flux, from a container outside the mine, to prevent leakage into the environment. The RPCs are particle detectors that contain a mixture of a gas, which when ionized by the passage of a muon originates an avalanche of electrons that produces an electrical signal.

Consecutive detections in the different plane detectors give the direction of the muon trajectory and all detections are stored in a muon transmission map. After processing the data in the maps, we obtain muographs, which are similar to X-rays, but instead, it shows the average density distribution based on the attenuation of the muon transmission caused by the quantity of matter, geologic structure and density differences in the surveyed area. **Figure 2** gives a base idea of the muography functioning.

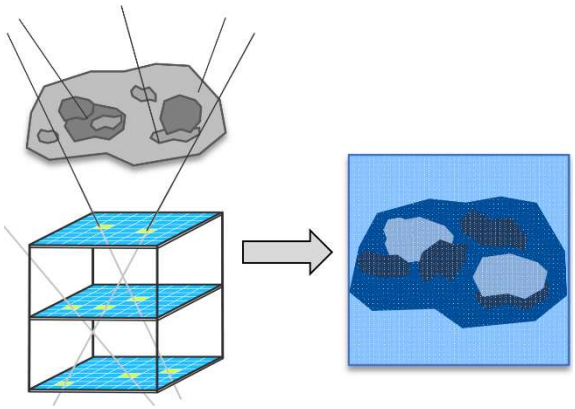

Figure 2. Illustration of the muography working basis, which results in muographs of the surveyed targets.

4. Simulations and Survey Targets

Muography simulations are made in Geant4 software (Agostinelli, *et al.*, 2003), which was designed to simulate the properties and interactions of all physical particles. A simulated scenario is built, and a muon flux is injected into the simulation, resulting in simulated muographs. They are used to predict what can be distinguished by the detectors and the exposure time needed to have enough muon statistics to create the muographs and also serve to compare with the survey results, analysing the differences and discovering what was previously unknown.

The current simulation approach uses a geometry based on the present location of the muon telescope – the gallery around the storeroom nº 4, an area of 60 m by 60 m. A regional fault (Corona Fault) crosses the location and because it has a structure and density different from the geology around it, it is, at the time, the main detection target of the survey.

Two places have been identified and considered as good observation points because of the existence of density contrasts in the terrain above the mine. As mentioned, the current position, near the middle of the 270 m long gallery, has the regional fault and is the best spot to first test the muography.

The second position is on the southern part of the gallery, close to the exit and has extensive massive sulphides in the geological strata, which are masses of iron mineral ore of higher density than the rocks where it is deposited and is a possible position that can be used in the future of the project.

The exposition time needed to do muography in this subterranean environment close to the surface, ranges from some days to some weeks, depending on the size of the target and the rocks' density contrast.

5. Muography Survey

The Corona Fault that can be seen in the area being surveyed is a subvertical N5E direction fault characterized by rock fracking and weathering, caused by movement related to the regional Late Variscan geologic activity. Due to the fault zone having a lower average density than the bordering and more compact rock geology, it presents a density contrast that can be seen in the muographs.

The muography surveyed area is an inverted square-shaped pyramid with the top vertex focused on the telescope. The base of the

pyramidal surveyed area has a size of 30 m by 30 m at the surface level, around 19 m above the gallery ground level. The maximum aperture angle from where the muons can arrive at the telescope and be detected is 60° and the muon flux that reaches the depth of the telescope is around 10 to 12 per cent of the muon flux registered at the surface level.

The first muograph that was obtained (**Figure 3**) had an exposure time of 2 months and the fault zone corridor was very clear (yellow/green), showing higher muon counts from its direction, as expected, due to the geological constraints that characterize the area in the study.

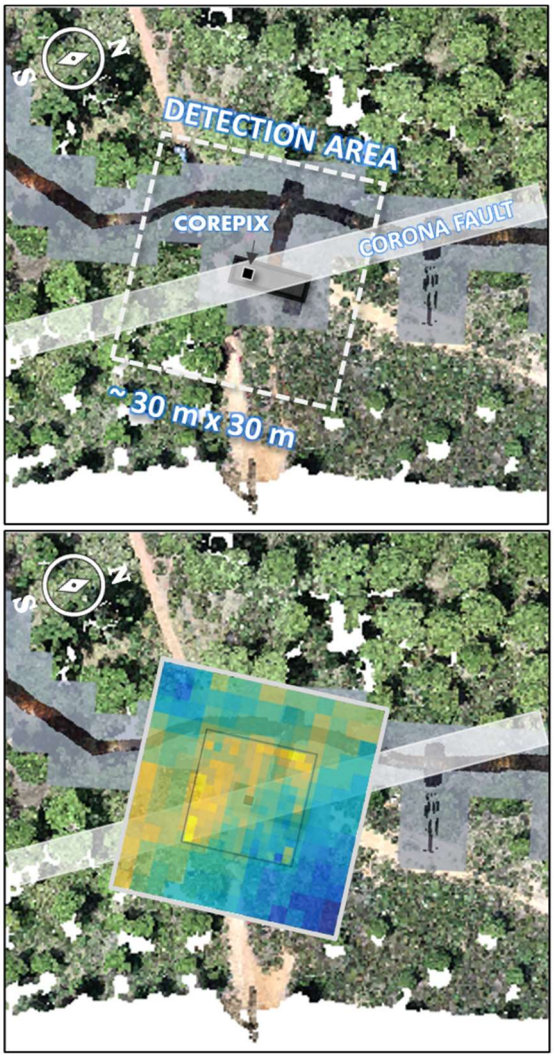

Figure 3. Above: Frame of the surveyed area above the telescope in a digital model obtained from photographing the surface (photogrammetry) and the gallery (ground lidar); Below: muography map showing the geological fault zone superimposed on the digital surface.

The fault zone orientation (almost N–S) that can be seen on the muograph seems the same as the fault orientation given by the geological map (represented as a white rectangle), but the fit for the location does not coincide perfectly. It is something that needs further study.

Because of the geological movement happening across the fault, two different geological settings exist on each side of it the studied area, creating a density contrast that is also measurable (Teixeira, et al., 2022; Teixeira, et al., 2023).

Sometime later, the telescope was moved from its initial position, where the fault zone was vertically above it, and placed in a different position, still inside the storeroom but the fault zone is seen from a different angle to the side. This way the data from the two observations can be combined to have a better view of the survey target. This part is still in the process and will be finished soon.

6. Ground Survey

One uncommon aspect of this muography implementation is the ground survey that's being carried out with standard geophysical techniques to complement and cross-reference the muography data.

A detailed characterization of the terrain is required to compare the muographic information from the observation with the expected results, so that the attenuation caused by topographical differences can be normalized.

To do that, the methods that are being used in the area under study, above the CorePix position, are the following:

- The differential GPS to direct measure coordinates in the field;
- The photogrammetry scans the surface and generates a digital elevation model of the surface and the ground lidar to 3D scan of the Waldemar Gallery. Both digital clouds were combined in a single model by

DOI : https://doi.org/10.60620/1y7h-f307

georeferencing them with shared GPS coordinate points. This way, it is possible to position the exact location of the telescope and other features of interest within the gallery, where GPS coordinates cannot be obtained directly;

- The collection of rock samples to have a direct measurement of the density of the rocks;
- Finally, the seismic refraction and the ground penetrating radar survey the ground below the surface so the underground features known and unknown to exist in the area can be seen.

All the geological and geophysical information obtained from the ground survey can be combined to create a 3D geological model to use as a reference in the muography data analysis and this will be done after the data processing is finished.

7. Outreach Activities

Outreach activities and dissemination of information about the muography technique represent a major aspect of the LouMu Project.

The inclusion of the telescopes in the mine public tours, organized by the science museum, offers a great opportunity for education and activities done with the general public. Lectures in middle and high schools are another interesting aspect that brings the technique into contact with younger students and teachers. And participation in conferences with oral presentations and article publications brings knowledge about the project to the researchers and the academic public of the relevant areas, which mostly are physics, particle physics, geology, and geophysics. And for a more indirect way to reach people, the LouMu website was created, filled with information about the project, so that interested people can see the most interesting pictures and learn more details at their own pace. The website is hosted in the LIP servers and hyperlinked to the Lousal Ciência Viva Center's webpage (LouMu Webpage, 2022).

8. Final Remarks

The work of the LouMu Project is still in progress but the test phase is almost reaching its programmed finish date. The data and results obtained so far show great potential in continuing and implementing the technique in other places and possibly different scenarios.

Our focus is the application of the muography technique and all that it involves: the simulations, the analysis tools and the telescope. With the standard geophysical techniques, a geological model will be created to be used as a reference for the analysis of the muographs.

In the end, a 3D density model of the studied terrain will be reconstructed as a combined result from the muography survey and the geological reference information, which will contribute with fidelity and precision. This will tell how well the muography implementation was and what direction it needs to take to establish it as an available probing technique for geophysics in Portugal.

9. Acknowledgements

This R&D project is financed by National Funds through the FCT – Foundation for Science and Technology, reference EXPL/FIS-OUT/1185/2021. The FCT also funds the PhD scholarship, integrated into the LouMu, reference PD/BD/150490/2019, and within the scope of ICT, the project with reference UIDB/04683/2020.

10. References

Agostinelli, S., Allison, J., Amako, K. A., Apostolakis, J., Araujo, H., Arce, P., ... & Geant4 Collaboration. (2003). GEANT4—a simulation toolkit. Nuclear instruments and methods in physics research section A: Accelerators, Spectrometers, Detectors and Associated Equipment, 506(3), 250-303.

Bonechi, L., D'Alessandro, R., & Giammanco, A. (2020). Atmospheric muons as an imaging tool. Reviews in Physics, 5, 100038.

Kaiser, R. (2019). Muography: overview and future directions. Philosophical Transactions of the Royal Society A, 377(2137), 20180049.

LouMu Webpage https://pages.lip.pt/loumu/en/loumu/, last accessed in 2022/04/17.

Teixeira, P., Afonso, L., Andringa, S., Assis, P., Bezzeghoud, M., Blanco, A., ... & Tomé, B. (2022). Muography for Underground Geological Surveys: Ongoing Application at the Lousal Mine (Iberian Pyrite Belt, Portugal).

Teixeira, P, et al. (2023). Muography applied in Underground Geological Surveys: ongoing work at the Lousal Mine (Iberian Pyrite Belt, Portugal), submitted and accepted to publish in a Springer Journal.

 DOI : https://doi.org/10.60620/1y7h-f307

Characterization of the Gravitational Mass Movements by Seismic Signals

Karla Guadalupe Ramírez Vega [1], Elsa Leticia Flores Márquez [2], Emma Suriñach Cornet [3]

[9] *Posgrado en Ciencias de la Tierra, UNAM, Circuito Instituto S/N, Coyoacán 04510, México, karlup@comunidad.unam.mx*

[10] *Departamento de Geomagnetísmo y Exploración, Instituto de Geofísica, UNAM, Circuito Instituto S/N, Coyoacán 04510, México, leticia@igeofisica.unam.mx*

[11] *Department RISKNAT Avalanches Research Group–Institut Geomodels. DPY. Dinàmica de la Terra i de l'Oceà, Facultat de Ciències de la Terra. c/Martí i Franquès s/n, Universitat de Barcelona (UB). Barcelona 28008, Spain*

SUMMARY

Gravitational mass movements are a very hazardous phenomenon that has captured the attention of many scientists. Some organizations and universities have installed seismic sensors to record the signals generated by these events, intending to be able to describe their dynamics. The principal tools that have been used for their study are the spectral analysis, where the Short–Time Fourier Transform, Wavelets and the Wigner distributions have some limitations because of the assumptions of linearity and stationarity of the studied signals.

We are introducing the Hilbert–Huang transform in the gravitational mass movements analysis because it has been developed for analyzing non-linear and non-stationary data. This transform is based on the decomposition of the seismic signal into intrinsic mode functions (IMF). The Complete Ensemble Empirical Mode Decomposition with Adaptative Noise (CEEMDAN) is a variant of the original Empirical Mode Decomposition proposed by Huang to perform the Hilbert–Huang transformation. We search for a relation of the IMF´s of the seismic signals generated by lahars, snow avalanches and rock fall with the dynamics of these phenomena.

Keywords: Gravitational Mass Movements, Seismic Signals, Empirical Mode Decomposition, Hilbert-Huang Transform, and Non-linear, Non-stationary data.

1. Introduction

Several authors have applied different techniques for the analysis of gravitational mass movements (GMM), to understand their dynamics and to prevent the possible fatality of this GMM populations (Vilajosana et al., 2008; Pérez-Guillén, 2016; Vázquez, 2016).

The most popular technique used for this purpose is the short-time Fourier transform (STFT), which has produced good advances in the characterization of the GMM, not only in time but also in frequencies by using the spectrogram and the power spectrum techniques.Despite the advances in the analysis of signals made with de STFT, there are some limitations in the Fourier transform application due to the non-linearity and non-stationarity of the data (Reyes, 2009). For this reason, we introduce the Hilbert–Huang transformation, developed by Norden E. Huang (Huang et al., 1998) for the analysis of non-linear and non-stationary data.

2. Background

The mass movement term has been defined by some authors, as the movement of lithological material downslope, driven by gravity, where a volume of water could be involved (Cruden & Varnes, 1996; Vargas, 2000). Soeters & Van Westen (1996), describe GMM as the product of changes in geomorphological, hydrological, and geological conditions, due to geodynamic

processes, vegetation, land use and human activities.

GMMs are classified from different approaches and follow different characteristics. Vargas (2000) classifies them according to the mobilized material and the type of movement. The groups we are interested in, are falls, landslides and collapses, flows, and avalanches where rock falls, and lahars are part of them.

Two important characteristics have been observed in the seismic signals generated by avalanches and in their corresponding spectrograms obtained by the STFT (Suriñach et al., 2000; Suriñach et al., 2020; Suriñach and Flores-Márquez, 2022). In the time signal an exponential increase in amplitudes is observed as the moving mass approaches the sensor (**Figure 1a**), which later decays rapidly with time, and sometimes can present new increases due to new dense material next to the front of the mass approaches. In the spectrogram, we can observe an exponential shape because of the increase in the amplitude and the frequency ranges (**Figure 1b**), although this second characteristic is not easy to find in all GMM.

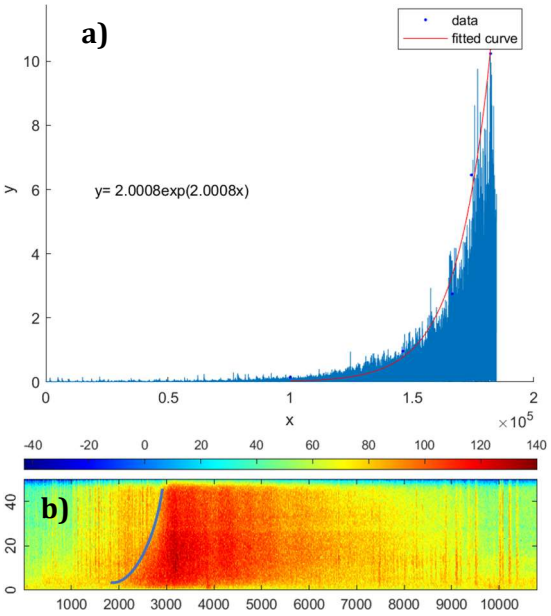

Figure 1. a) Image that exemplifies the exponential increase in the amplitudes of the seismic signal generated by GMM, b) and in the spectrogram.

Authors such as Vilajosana (2008), Pérez-Guillén (2016) and Roig-Lafon (2021) have sectioned the spectrograms according to the characteristics of the amplitude and frequency resulting from the relative position between the mass and the sensor. We use the classification proposed by Roig – Lafon (2021), who considers four sections: SON (signal on set), SBO (body over the sensor), STA (signal tail) and SEN (signal end), where SON and SBO are the sections, we are analyzing because of the information they contain, (**Figure 2**).

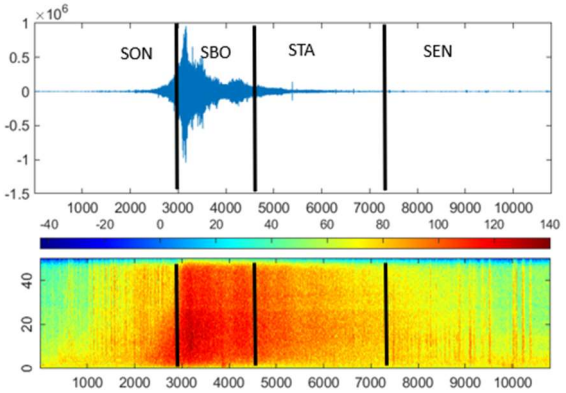

Figure 2. Sections in the spectrogram and seismic signal. The classification proposed by Roig – Lafon (2021).

The analysis of these sections by using the Hilbert–Huang transform (HHT), allows us to characterize the seismic signals generated by rock falls, lahars, and snow avalanches, because we can compare our results with the previous already published and obtain different methodologies. This comparison will allow us to assess if Complete Ensemble Empirical Mode Decomposition with Adaptative Noise (CEEMDAN) is good enough to obtain information on the signal, or if it is even better than other previously applied methodologies such as STFT.

3. Methodology

The HHT is a method developed by Dr Norden E. Huang (Huang et al., 1998) to analyze nonlinear and non-stationary data. It consists of a complete, orthogonal, local and adaptative spectral decomposition basis, which allows this decomposition to be exact, the amplitudes to be positive and to deal with the nonlinear and non-stationary characteristics of the data.

The HHT consists of two steps, the first is the application of the Empirical Mode Decomposition (EMD) that consist of the decomposition of the original signal *x[n]* into a finite and sometimes small number of intrinsic mode functions (IMF). The second, is

DOI: https://doi.org/10.60620/bda4-qh85

the application of the Hilbert transform (HT) to each of these functions, where the result is a time–frequency–amplitude representation, where the instantaneous frequencies, as a function of time, allow the identification of hidden structures more efficiently.
To be considered an IMF, a signal must satisfy two conditions (Torres et al., 2011):

1. In the whole data set, the number of extrema and the number of zero crossings must either equal or differ at most by one.
2. At any point, the mean value of the envelope defined by the local maxima and the envelope defined by the local minima is zero.

They are built by the following numerical procedure described by Huang et al. (1998) and illustrated in **Figure 3**:

1. Identify all extrema of *x[n].*
2. Interpolate to find the minima and maxima envelopes.
3. Compute the mean.
4. Extract the detail, in that way, we obtain a new signal *c[n]*.
5. Verify if *c[n]* satisfies the conditions of intrinsic mode functions. If it satisfies them, set *c[n]* as an IMF and obtain a residual *r[n].*
6. Iterate until the final residue *r[n]=x[n]–c[n]* is a monotone signal.

This method can experience problems in some cases, such as the presence of oscillations of very disparate amplitude in mode, or the presence of very similar oscillations in different modes, named “mode mixing” (Colominas et al., 2011). For this reason, authors like Torres et al. (2011) and Colominas et al. (2011) introduce the CEEMDAN which is a variation of the original method that overcomes this mixing problem and achieves a complete decomposition with no reconstruction error with a better spectral mode separation. The method is described by the following algorithm (Colominas et al., 2011):

1. Decompose by EMD I realizations $x[n] + \epsilon_0\omega^i[n]$ to obtain their first mode and compute:

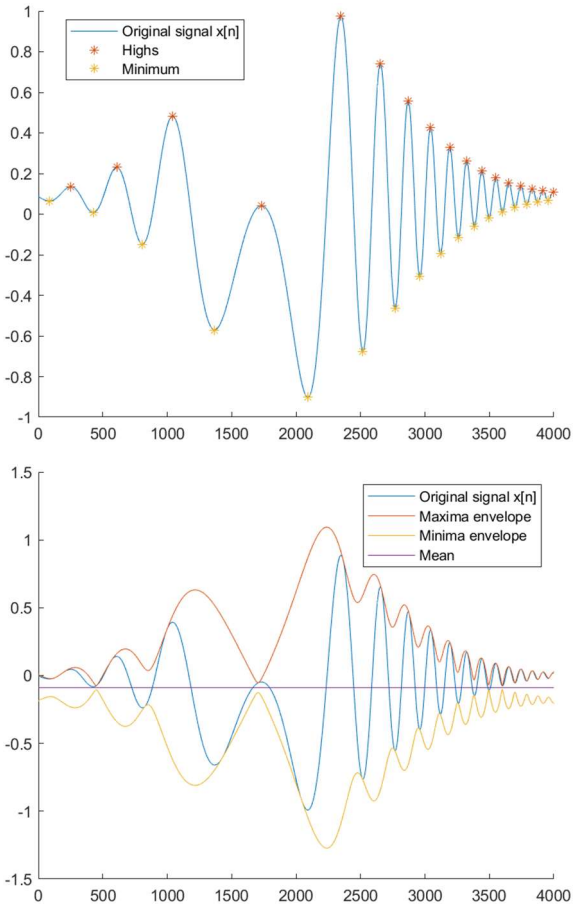

Figure 3. Illustrations that describe the empirical mode decomposition procedure, according to the algorithm proposed by Huang et al. (1998).

$$\widetilde{IMF_1}[n] = \frac{1}{I}\sum_{i=1}^{I} IMF[n] \qquad (1)$$

2. At the first stage (k = 1) calculate the first residue as:

$$r_1[n] = x[n] - \widetilde{IMF_1}[n] \qquad (2)$$

3. Decompose realizations $r_1[n] + \epsilon_1 E_1(\omega^i[n]), i = 1 \ldots I$, until their first EMD mode and define the second mode:

$$\widetilde{IMF_2}[n] = \frac{1}{I}\sum_{i=1}^{I} E_1(r_1[n] + \epsilon_1 E_1(\omega^i[n])) \qquad (3).$$

4. For k = 2, ..., K calculate the kth residue:

$$r_k[n] = r_{k-1}[n] - \widetilde{IMF_k}[n] \qquad (4).$$

5. Decompose realizations $r_k[n] + \epsilon_k E_k(\omega^i[n]), i = 1 \ldots I$, until their first EMD mode and define the (k+1)th mode as:

$$\widetilde{IMF_{k+1}}[n] = \frac{1}{I}\sum_{i=1}^{I} E_1(r_k[n] + \epsilon_k E_k(\omega^i[n])) \qquad (5).$$

6. Go to step 4 for the next k.

Where $x[n]$ denotes the original signal, n is the number of samples, $r[n]$ is the residue, the operator $E_j(.)$ produced the j-th mode obtained by EMD. The white noise is represented as ω^i with $\mathcal{N}(0,1)$ known as Gaussian white noise, ϵ_0 is the initial standard deviation, i represents the number of realizations and k is the residue number.
The residual satisfies that:

$$R[n] = x[n] - \sum_{k=1}^{K} \widetilde{IMF_k} \qquad (6).$$

4. Study Sites

For this work, we have used data from three different sites, the signals generated by lahars come from the Colima volcano (VC) in Mexico, the snow avalanche signals come from the Valleé de la Sionne in Switzerland and the rock fall signals are from the Monserrat massif in Spain. The description of each site is as follows.

4.1. Colima volcano

The Colima volcano is an andesitic stratovolcano, located between 19.514° and 19.58° N, and 103.62° and 103.626° W, with an elevation of 3850 m above sea level. It is in the western portion of the Trans-Mexican Volcanic Belt, which is known as the Colima Central Graben and in the southern portion of the Colima Rift (López-Loera et al., 2011). It is part of the Colima Volcanic Complex (CVC), aligned with the Cántaro and Nevado stratovolcanoes (**Figure 4**).

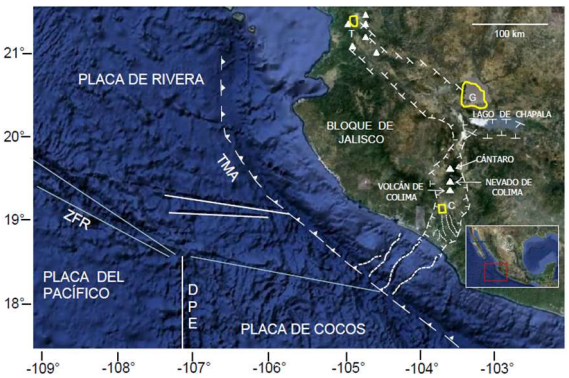

Figure 4. The volcanoes that constitute the volcanic complex of Colima are observed; Cantaro, Nevado and Colima. (Taken from López - Loera et al., 2011).

The Colima volcano is one of the most active volcanoes in Mexico and North America with explosive activity, it has an approximate volume of 10 km^3 and consists of alternating pyroclastic flow and fall deposits, as well as andesitic spills that have reached up to 15 km from the crater (Macías, 2005). The slope of the Colima volcano varies from 40° to 10° and it is 1640 m higher than the surrounding area. The main ravines are located on the E – S – W flanks of the cone, the most active being the San Antonio, Montegrande, Muerto, Arena, La Lumbre and Córdoba ravines, where only La Lumbre and Córdoba are permanent drainages. These ravines are in the southern part of the volcano and are characterized by loss of material that can be easily eroded (Vázquez, 2016). La Lumbre and Montegrande ravines present the highest frequency of lahar activity. In La Lumbre there is a lower occurrence, but the lahars are of larger magnitude than in Montegrande, where the lahars are smaller, but occur more frequently, reporting up to three lahars per year. These ravines are monitored by RESCO (Seismic Telemetric web of the Colima state, Mexico) with various types of sensors, including broadband three-component seismometers.

4.2. Vallée de la Sionne, Switzerland.

The Vallée de la Sionne (VdlS) is an experimental site built in 1997 by the Swiss Federal Institute for the Study of Snow and Avalanches (SLF) to obtain experimental data that would allow modelling of the dynamics of snow avalanches and thus learn more about their dynamics (Pérez-Guillen, 2016; Lafon, 2021). Lafon (2021) describes the geology as a region characterized by the presence of carbonate rocks in the highest parts, as well as limestone and marl belonging to the upper and lower Cretaceous, which are found in a Jurassic schist basement. The main cover consists of glacial sediments from the last glacial period that occurred in the Pleistocene, as well as carbonate moraines and clay matrix.
Various research groups from Switzerland, England, Spain, France, and Australia have collaborated to install different sensors to obtain data for snow avalanche analysis.
Because of the infrastructure of the different caverns built in the VdlS, they installed various types of sensors, such as broadband three-component seismometers with different sensitivities and eigenfrequencies, as well as airborne infrasound sensors

 DOI: https://doi.org/10.60620/bda4-qh85

(Vilajosana, 2008; Pérez-Guillén, 2016; Roig-Lafon, 2021).

4.3. Massif of Monserrat, Spain.

The Monserrat massif is located 40 km northwest of Barcelona, where the local authorities have carried out a rock clearance using explosives to prevent future tragic scenarios. The geophysical team of the geodynamics department of Barcelona University (Vilajosana et al., 2008) installed two seismic stations in the area, consisting of Lennartz, type LC 4-3D, brand seismometers with an eigenfrequency of 1 Hz and a Nanometrics Orion data logger. **Figure 5** shows the position of the stations and the location of the explosions.

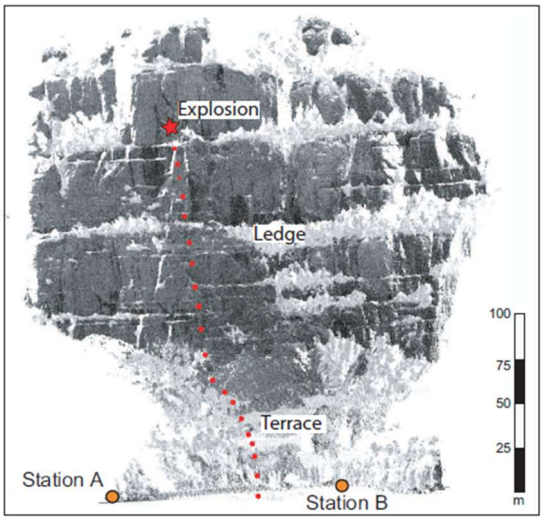

Figure 5. Location of seismic stations A and B and the explosion zone. The fall trajectory (red dots) and impact areas are also indicated (Figure taken from Vilajosana et al., 2008).

5. Results

For this work, we used 7 snow avalanche signals, 3 lahar signals and 2 rockfall signals, as shown in **Table I**.

Each signal was processed in the same way, with small variations depending on its sampling frequency.

A large number of samples of the seismic signals generated by lahars caused some difficulties in the processing with the CEEMDAN algorithm.

Then we decided to analyze the IMF of snow avalanches and lahars by sections (see **Figure 2**), just the SON (**Figure 6** and **Figure 7**) and SBO (**Figure 8** and **Figure 9**) sections.

Table I. Signals used and their characteristics.

GMM	Identifier	Sample frequency	Samples	Duration
Snow avalanches	Pow 5	200 sps	24000	120 s
	Pow 15	200 sps	14702	74 s
	Wet 3	200 sps	25000	125 s
	Wet 6	200 sps	25001	125 s
	Wet 17	200 sps	70000	350 s
	Trans 4	200 sps	50000	250 s
	Trans 11	200 sps	52501	262 s
Lahars	Lahar 2012	100 sps	380000	3800 s
	Lahar 2013	100 sps	710000	7100 s
	Lahar Patrio	100 sps	1080001	10800 s
Fall rock	Monserrat abajo	200 sps	12001	60s
	Monserrat arriba	200 sps	12001	60s

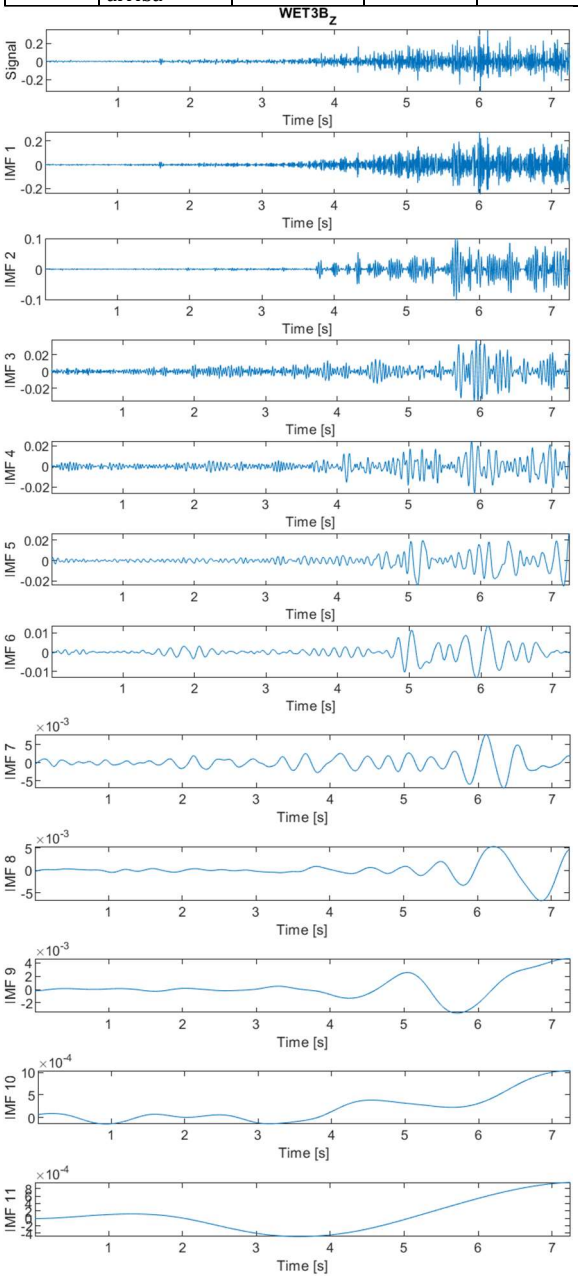

Figure 6. Snow avalanche Wet 3 modes, section SON, component Z.

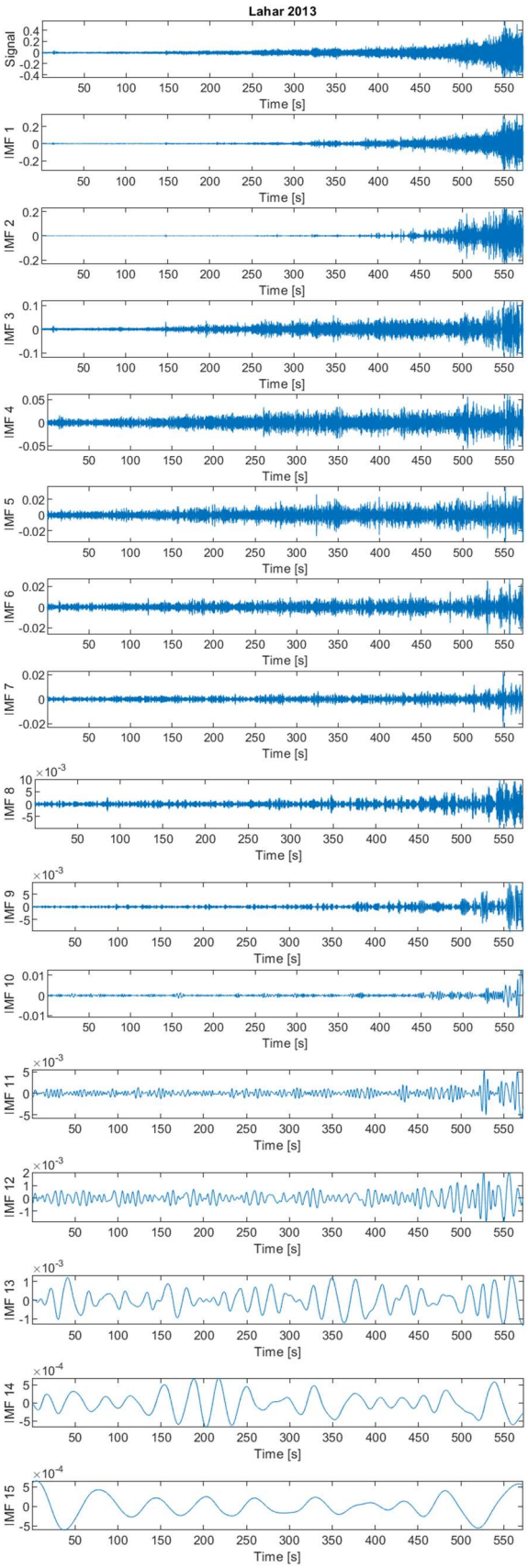

Figure 7. Lahar 2013 modes, section SON, all the components.

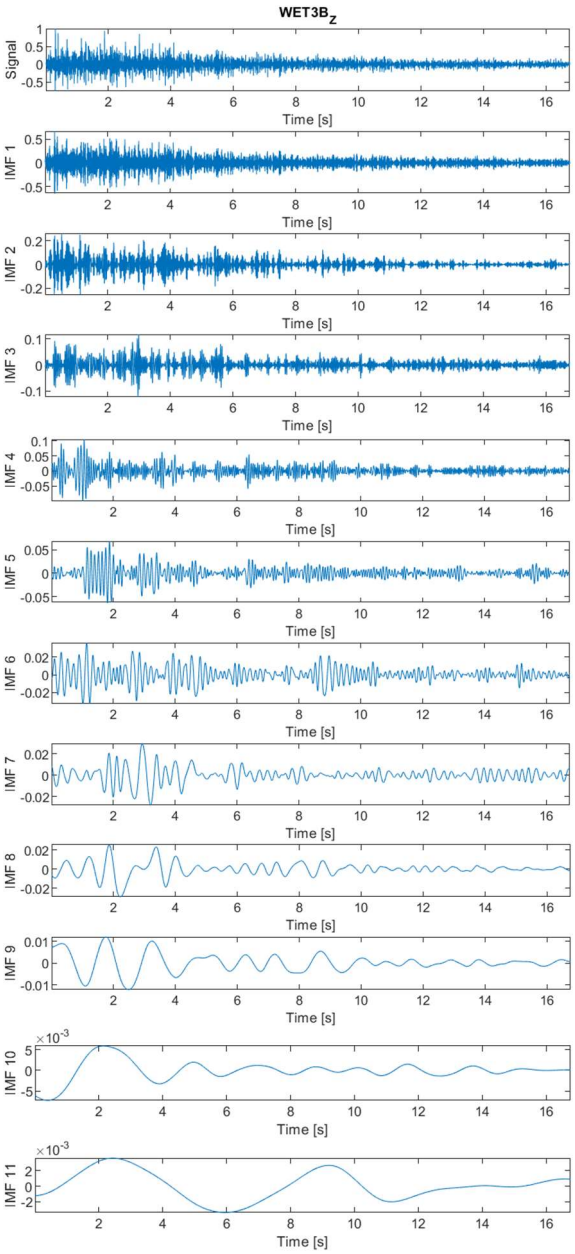

Figure 8. Snow avalanche Wet 3 modes, section SBO, component Z.

This allowed less computational time processing and a clear view of the IMF characteristics of each type of GMM. Due to the characteristics of the signals generated by rock fall, its seismic signals were analyzed without sectioning (**Figure 10**). Below we show some IMFs of the different types of GMM and the SON and SBO sections. With the IMF we have been able to find important similarities between lahars and the different types of snow avalanches and characteristic behaviours that we had not observed in other types of signals from previous bibliography.

 DOI: https://doi.org/10.60620/bda4-qh85

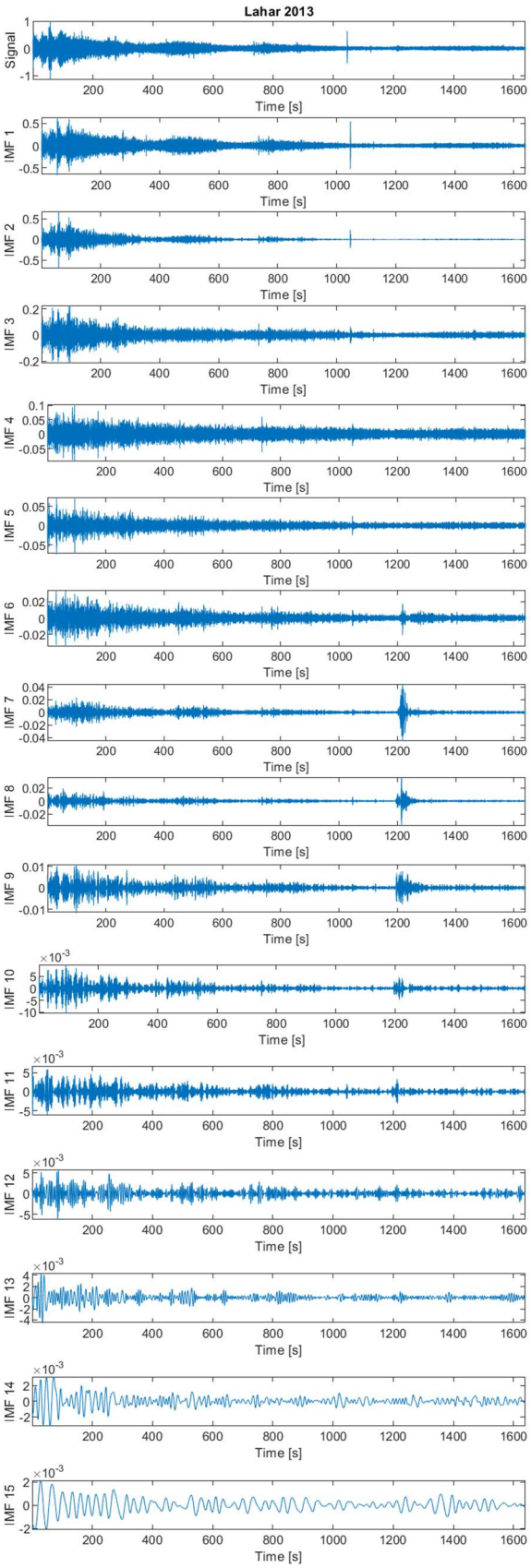

Figure 9. Lahar 2013 modes, section SBO, all the components.

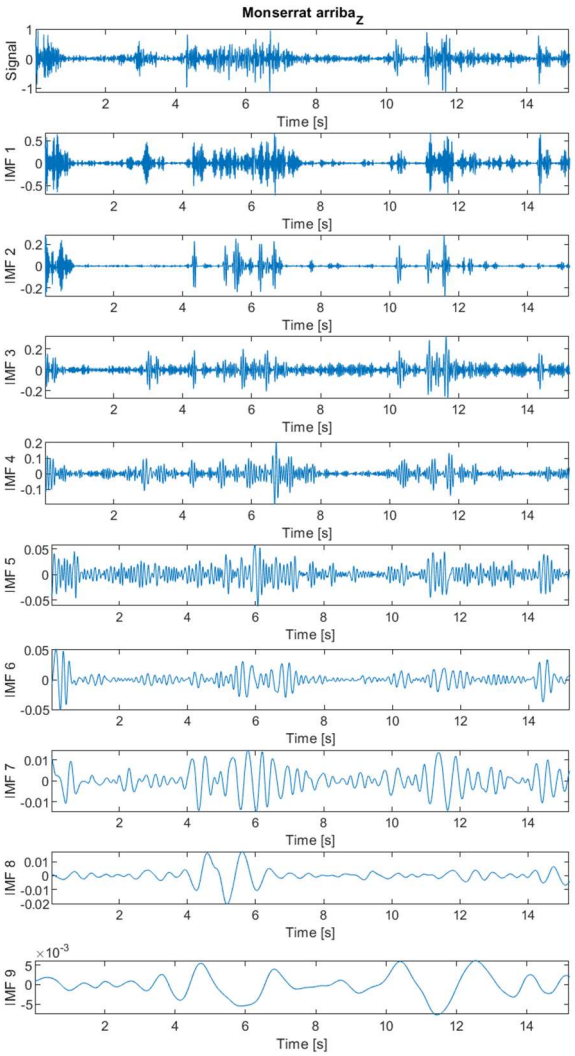

Figure 10. Monserrat arriba modes, component Z.

Following the work of Pereira de Souza, N. (2007) and Martínez C. D. (2017), we obtained the Fourier spectra for each of the modes and displayed them on the same graph, linearly and logarithmic, in this way we were able to make comparisons between lahars, avalanches and rock falls (**Figures 11 – 15**).

We observe that the avalanche spectra (**Figure 11**) do not show much similarity for the SON section. While in the lahar spectra (section SON, **Figure 12**), we observe great similarities for all the modes.

For the SBO section, we observed more interesting things in the case of avalanches. In this section, the spectra show a great similarity for the first modes.

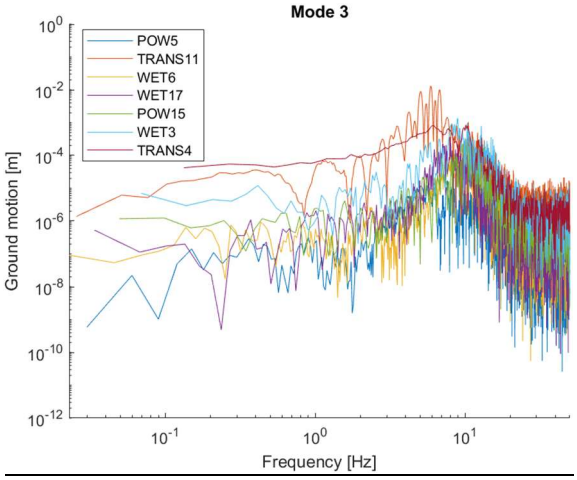

Figure 11. Avalanche spectra mode 3, SON section.

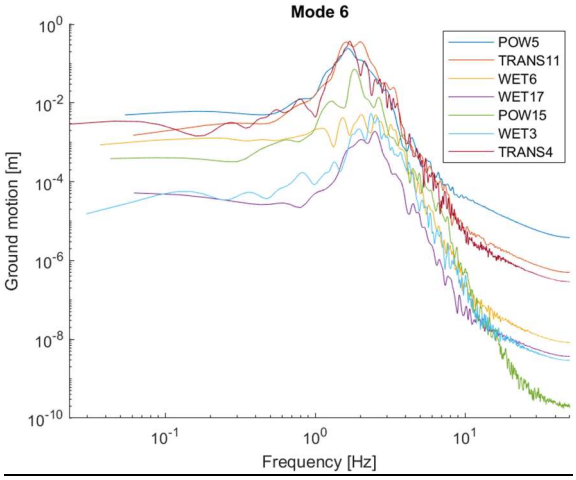

Figure 14. Avalanche spectra mode 6, SBO section.

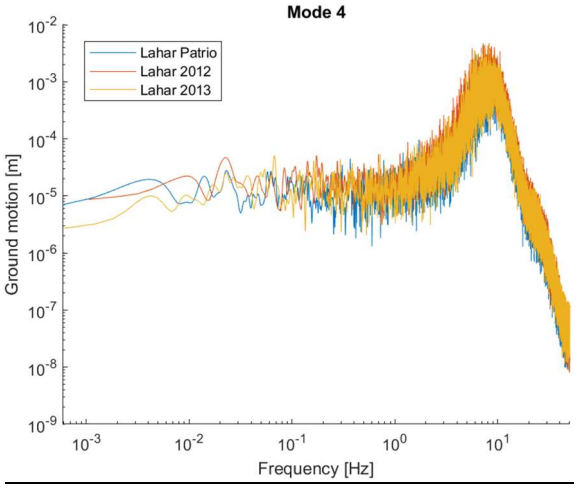

Figure 12. Lahar spectra mode 4, section SON.

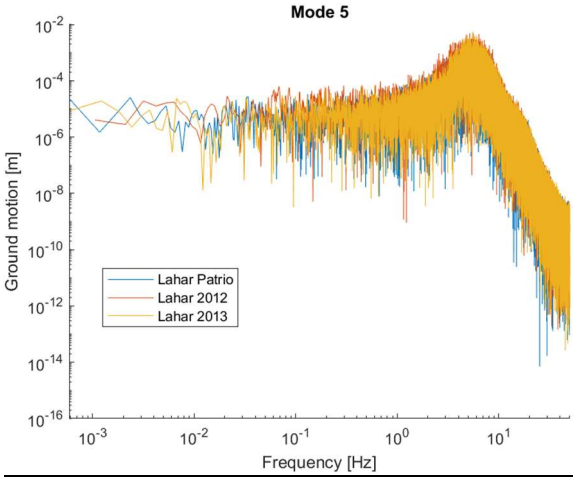

Figure 15. Lahar spectra mode 5, section SBO.

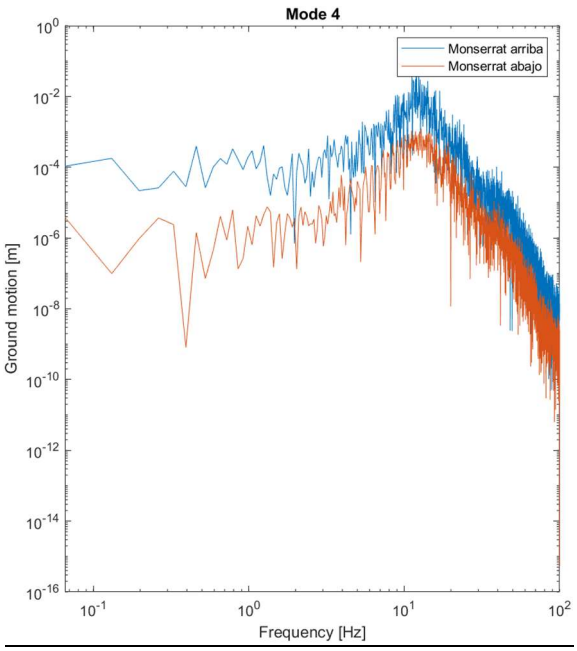

Figura 13. Monserrat arriba – abajo spectra, mode 4.

Additionally, in mode 6 (**Figure 14**), we could notice that at high frequencies, the avalanches show a very similar trend according to the type of avalanche, that is, we noticed a grouping of the spectra for the wet avalanches and the transitional ones, being the powder ones those that do not show this behaviour. We should compare more signals to conclude that the classification of snow avalanches can be seen in the avalanche spectra. For the SBO section of the lahars, we could observe similar behaviour in all of them (**Figure 15**), as well as in the spectra of the rockfall modes (**Figure 13**).

6. Discussions

The results obtained so far have allowed us to observe unknown and in other cases expected characteristics of the seismic signals generated by GMM. The expected characteristic was the similarity between the

 DOI: https://doi.org/10.60620/bda4-qh85

modes and the spectra obtained from the seismic signals of the different types of GMM when processed with EMD.

As we observed in **Figures 6 – 10**, it appears a very well-defined wave train with a defined frequency and amplitude for the three types of GMM. The frequency ranges go from 10 – 50 Hz for lahars (Cole et al. 2009) and 1 – 45 Hz for avalanches (these values depend on the type and the section of the avalanche (Pérez – Guillén, 2016).

An explanation for this is the description of the method itself, which says that the signals are expressed as a sum of modulated amplitude and frequency components. The thing that makes interesting this result is that the trend of frequencies observed in IMFs, is not previously depicted in consulted bibliographies (Pereira et al., 2007; Reyes, 2009; Colominas et al., 2011; Martínez, 2017). For this reason, we think this behaviour is typical of the seismic signals generated by GMM.

From the analysis of the SBO section modes obtained from the signals generated by lahars, we can notice a greater amplitude in the first seconds of almost all the IMF, even those with the lowest frequency, where only the last 2 – 4 modes do not show these characteristics. This increase in amplitude is related to the difference in the densities of the materials that make up a lahar and the way they move. Although the SBO sections are divided in the spectrogram, the IMF obtained allows the identification of two sections inside. These sections could be distinguishing the passage of the front, with more dense materials and over the sensor, and after the lesser dense materials with smaller amplitudes.

In the case of snow avalanches, the method could be used to develop possible guides that quickly classify events from the power spectrum (Fourier transform) according to the spectral characteristics of the different types of avalanches, since we noticed that the IMF have many similarities in time and frequency depending on the type of avalanche that generated the signal.

7. Conclusions

The EMD is a method that has allowed us to observe the IMF of the GMM and the way they behave in time and frequency. The great challenge is to effectively relate everything that we have observed with the complex physical phenomenon that GMM involves, for which it is necessary to continue working with more signals from different events in this way, we will understand what information these seismic signals provide.

8. References

Cole, S., Cronin, S., Sherburn, S., Manville, V. (2009). Seismic signals of snow-slurry lahars in motion: 25 September 2007, Mt Ruapehu, New Zealand. Geophysical Research Letters, 36. DOI: https://doi.org/10.1029/2009GL038030.

Colominas, M., Schlotthauer, G., Flandrin, P., Torres, M. E. (2011). Descomposición empírica en modos por conjuntos completa con ruido adaptativo y aplicaciones biomédicas. XVIII Congreso Argentino de bioingeniería.

Cruden, D. M., Varnes, D. J. (1996). Landslide types and processes, transportation research board. U. S. National Academy of Sciences, Special Report, 247: 36 – 75.

Huang, N.E., Shen, Z., Long, S.H., Wu, M.C., Shih, H. H., Zheng, Q., Yen, N., Tung, C. C. and Liu, H. H. (1998). The empirical mode decomposition and the Hilbert spectrum for nonlinear and non-stationary time series analysis. Proceedings of the Royal Society A: Mathematical, Physical and Engineering Sciences, 454-1971, 903-955.

López – Loera, H., Urrutia – Fucugauchi, J., Alva – Valdivia, L. (2011). Estudio aeromagnético del complejo volcánico de Colima, occidente de México – implicaciones tectónicas y estructurales. Revista Mexicana de Ciencias geológicas. 28(3).

Macías, J. L. (2005). Geología e historia eruptiva de algunos de los grandes volcanes activos de México. Boletín de la Sociedad Geológica Mexicana. 379-424(3).

Martínez, C. D. (2017). Interpretación de la respuesta sísmica de los suelos blandos del Valle de México a través de la Transformada Hilbert – Huang. [Tesis de maestría, Universidad Nacional Autónoma

de México]. https://repositorio.unam.mx/contenidos/3495160.

Pereira de Souza, N., Abry, P., Loiseau, P., Cejka, J.C., Custaud, M. A., Frutoso, J., Gharib, C. and Flandrin, P. (2007). Empirical mode decomposition to assess cardiovascular autonomic control in rats. Blackwell Publishing Ltd. Fundamental & Clinical Pharmacology. 21, 481 – 496. DOI: https://doi.org/10.1111/j.1472-8206.2007.00508.x

Pérez-Guillén, C. (2016). Advanced Seismic Methods Applied to the study of snow avalanche dynamics and avalanche formation. [Tesis para obtener el grado de doctora, Universidad de Barcelona, Barcelona].

Reyes, F. (2009). Algoritmos de atributos sísmicos para el mejoramiento de la resolución. [Tesis de doctorado, Universidad Nacional Autónoma de México].

Roig – Lafon, P. (2021). Identification of snow avalanche release areas and flow and flow characterization based on seismic data studies. [Tesis de doctorado, Universidad de Barcelona]

Soeters, R., Van Westen, C., J., (1996). Slope Instability recognition, analysis and zonation. Landslides: Investigation and mitigation

Suriñach, E., Sabot, F., Furdada, G., Vilaplana, J. M. (2000). Study of Seismic Signals pf Artificially Released Snow Avalanches for Monitoring Purposes. Physics and Chemistry of the Earth (B). 25(9). 721 – 727.

Suriñach, E., Flores – Márquez, E. L., Roig – Lafon, P., Fundada, G., Tapia, M. (2020). Estimation of Avalanche Development and Frontal Velocities Based on the Spectrogram of the Seismic Signals Generated at the Vallée de la Sionne Test Site. Geosciences (10). DOI: https://doi.org/10.3390/geosciences10030113

Suriñach, E., Flores – Márquez, E. L. (2022). A template to obtain information on gravitational mass movements from the spectrograms of the seismic signal generated. European Geosciences Union. General Assembly 2022. DOI: https://doi.org/10.5194/egusphere-egu22-8600

Torres, M. E., Colominas, M., Schlotthauer G., Flandrin, P. (2011). A complete ensemble empirical mode decomposition with adaptative noise. IEEE.

Vargas Cuervo, G. (2000). Criterios para la clasificación y descripción de movimientos en masa. Colombia: Boletín de Geología.

Vázquez, R. (2016). Estudio en la dinámica de lahares con base en el monitoreo de eventos en el volcán de Colima: estimación de parámetros para el desarrollo de un sistema de alerta temprana. [Tesis de doctorado, Universidad Nacional Autónoma de México].

Vilajosana, I. (2008). Seismic detection and characterization of snow avalanches and other mass movements [PhD Thesis, Universidad de Barcelona].

Vilajosana, I., Suriñach, E., Abellán, A., Khazaradze, G., García, D., y Llosa, J. (2008). Rockfall induced seismic signals: a case study in Monserrat, Catalonia. Natural Hazards and Earth System Sciences.

 DOI: https://doi.org/10.60620/bda4-qh85